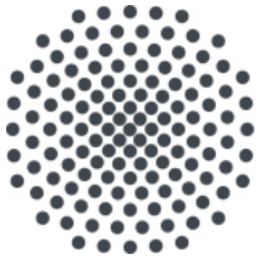

Universität Stuttgart

Fakultät 3

Influence of Morphology on Electrochemical Redox Processes in Semiconducting Polymers

Von der Fakultät Chemie der Universität Stuttgart zur Erlangung der Würde eines Doktors der Naturwissenschaften (Dr. rer. nat.) genehmigte Abhandlung

vorgelegt von

Kirsten Bruchlos

aus Böblingen

Hauptberichterin:	Prof. Dr. Sabine Ludwigs
Mitberichter:	Prof. Dr. Frank Gießelmann
Prüfungsvorsitzender:	Prof. Dr. Joris van Slageren
Tag der mündlichen Prüfung:	14.05.2019

Institut für Polymerchemie

2019

Eidesstattliche Erklärung

Hiermit versichere ich, dass ich die vorliegende Arbeit mit dem Titel

Influence of Morphology on Electrochemical Redox Processes in Semiconducting Polymers

selbstständig verfasst habe und keine anderen als die angegeben Quellen verwendet habe. Aus fremden Quellen entnommene Passagen und Zitate sind als solche kenntlich gemacht.

Declaration

I hereby certify that the dissertation with the title

Influence of Morphology on Electrochemical Redox Processes in Semiconducting Polymers

is entirely my own work except where otherwise indicated. Passages and quotes from other sources have been clearly indicated.

Kirsten Bruchlos

2019

Summary

The thesis focuses on the electrochemical characterisation of redox processes in two classes of semiconducting polymer films, namely the π-conjugated poly(3-hexylthiophene) (P3HT) and the redox copolymer polyvinyltriphenylamine-*co*-polystyrene (PVTPA-*co*-PS). The focus has been set especially on the influence of the inner structure of the polymer films, which is defined by the semi-crystalline nature of the π-conjugated P3HT or generated by the electrochemically induced cross-coupling of the polymer chains in case of the redox copolymer PVTPA-*co*-PS respectively.

In the first part of the thesis the influence of the thin film morphology of the semicrystalline poly(3-hexylthiophene) (P3HT) on its electrochemical behaviour is studied. Since P3HT is one of the most commonly used donor materials in organic photovoltaics, the influence of film preparation and morphology on the optical and electronic properties had been studied intensively in literature. [1, 2] It had been shown by the organic electronics community that the absorption properties, the optical band gap as well as the charge carrier mobilities in field effect transistors and the power conversion efficiency in organic solar cells are strongly depending on the semicrystalline nature of P3HT. [3, 4] In contrast to this, the electrochemistry community has mostly focused on influences of molecular weight or regioregularity rather than on controlled thin film morphologies. [5] Therefore the aim of this work is to establish a direct correlation of film morphology to the electrochemical properties. To do so, P3HT thin films of various controlled morphologies were prepared by crystallisation from solution and by post-annealing methods like solvent vapour annealing, thermal annealing and high temperature rubbing. For the structure resolution methods like atomic force microscopy (AFM), transmission electron microscopy (TEM) and polarised optical microscopy (POM) are combined with spectroelectrochemical methods like *in-situ* absorption spectroscopy with cyclic voltammetry (CV). The characterisation reveals a strong dependency of the anodic redox wave in the CV to the film morphology with a characteristic subsignal that can be

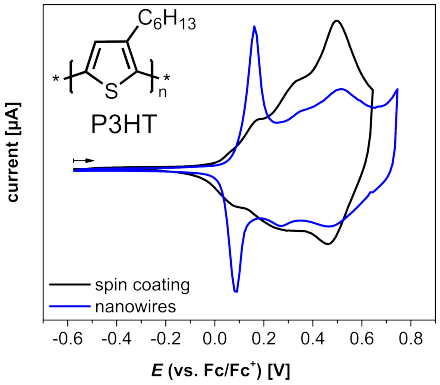

attributed to the crystalline domains in the polymer film. As the influence of the morphology is strongest on the oxidative redox wave at low potential, the HOMO energy level of the studied P3HT samples, which is crucial for its application in organic solar cells, is also significantly altered by the morphology of the polymer film.

In addition to P3HT homopolymer films, binary donor acceptor blend films have been studied. For application in organic solar cells typically P3HT:$PC_{61}BM$ (phenyl-C61-butyric acid methyl ester) blends are used. It had been shown in literature that the power conversion efficiency of such P3HT:$PC_{61}BM$ solar cells can be significantly improved by thermal post-annealing. [6] This is usually explained by the increased phase separation in the blend which leads to continuous pathways for the charges to be dissipated to the electrodes. The electrochemical characterisation of as-cast and annealed P3HT:$PC_{61}BM$ films reveals that the oxidative wave at low potential in the cyclic voltammogram of P3HT becomes suppressed by the intermixing with the fullerene acceptor material which results in a decrease of the HOMO level of several hundreds of meV. By thermal annealing the oxidative wave at low potential in the voltammogram is regained and the resulting HOMO level in the blend becomes comparable to the undisturbed P3HT. Since the LUMO level of the $PC_{61}BM$ acceptor material is not influenced by the annealing procedure, the electrochemical band gap of the thermally annealed blend is decreased with respect to the non-annealed blend.

In the second part of the thesis the influence of the cross-linking density of a series of polyvinyltriphenylamine-*co*-polystyrene (PVTPA-*co*-PS) copolymers with varying triphenylamine (TPA) content on the electrochemical and chemical doping behaviour is studied. Redox polymers containing triarylamine groups are promising energy storage materials due to their high charge density, solution processability and high film stability in common electrolytes. [7] The electrochemical behaviour of PVTPA and its copolymers is interesting since it undergoes an irreversible oxidative coupling reaction of the TPA-groups to tetraphenylbenzidine groups (TPB) which can be induced either chemically or electro-

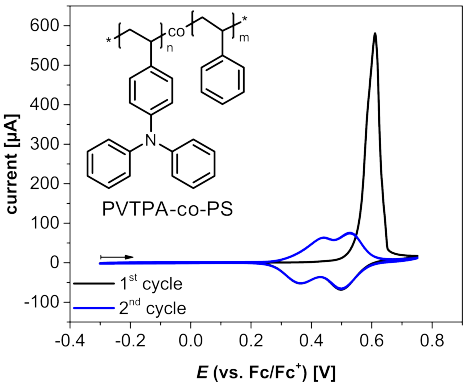

chemically, leading to cross-linking of the polymer chains. [8] The cross-linked TPB units are redox active themselves.

The cross-linking process and the charging/ discharging of PVTPA and PVTPA-*co*-PS are studied by means of spectroelectrochemistry to identify all coexisting redox steps and to attribute characteristic absorption bands to the CV signals.

During the electrochemically induced cross-linking and charging/ discharging of the polymer films, counter ion intercalation and expulsion occurs to maintain electroneutrality. The characterisation of ion intercalation/ expulsion during the electrochemical redox processes has been performed by electrochemical quartz crystal micro balance (EQCM) measurements with varying cross-linking density and varying ion sizes.

To study the charge storage properties of PVTPA-*co*-PS *supercapacitor* devices were prepared and studied by electrochemical impedance spectroscopy (EIS), cyclic voltammetry (CV) and galvanostatic charging/ discharging (GCD) cycles. The PVTPA-*co*-PS copolymers show capacitive and faradaic charge storage behaviour with specific energy densities and specific power densities of 10^1 - $10^2\,\mathrm{J\,kg^{-1}}$ and $10^1\,\mathrm{W\,kg^{-1}}$ respectively.

Chemically doped TPA-containing polymers may provide a possible replacement for poly(3,4-ethylenedioxythiophene)-poly(styrenesulfonate) (PEDOT:PSS) as the hole transport layer in organic solar cells, which currently suffer from a decrease in lifetime for example due to the acidity of the PEDOT:PSS layer. Therefore, in addition to the electrochemically induced cross-linking and doping, the chemical cross-linking and doping was performed via dip doping and vapour doping with iron(III) chloride and iron(III) tosylate as dopants. The doping process was monitored by absorption spectroscopy and conductivities of up to $10^{-4}\,\mathrm{A\,V^{-1}\,cm^{-1}}$ were measured by 4-point probe (4pp) measurements.

Zusammenfassung in deutscher Sprache

Im Rahmen dieser Doktorarbeit wurden die elektrochemischen Redox-Prozesse in halbleitenden Polymerfilmen des π-konjugierten Poly(3-hexylthiophen) (P3HT) und des Redox-Copolymers Polyvinyltriphenylamin-*co*-Polystyrol untersucht. Hierbei wurde der Fokus insbesondere auf den Einfluss der inneren Strukturierung der Polymerfilme gelegt. Im Falle des P3HT wird die innere Strukturierung durch die teilkristalline Natur des π-konjugierten Polymers definiert, während im Fall des PVTPA-*co*-PS Redox-Copolymers die Strukturierung durch eine elektrochemisch induzierte Quervernetzungs-Reaktion erzeugt wird.

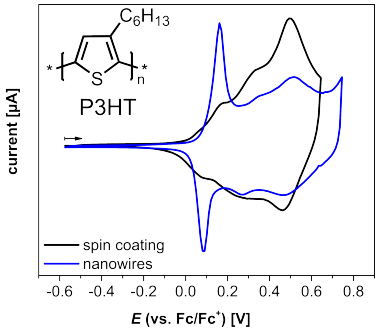

Im ersten Teil der vorliegenden Arbeit wurde der Einfluss der Dünnschicht-Morphologie des teilkristallinen Poly(3-hexylthiophens) auf das elektrochemische Verhalten untersucht. Da P3HT eines der am häufigsten untersuchten Donormaterialien für die Anwendung in organischen Solarzellen ist, wurden die Einflüsse der Proben-Präparation und der Morphologie auf die optischen und elektronischen Eigenschaften intensiv in der Literatur untersucht. [1, 2] Es konnte gezeigt werden, dass die Absorption, die optische Bandlücke und die Ladungsträger-Mobilitäten in Feldeffekt-Transistoren sowie die Energieumwandlungs-Effizienz in Solarzellen eine deutliche Abhängigkeit von der Teilkristallinität von P3HT zeigen. [3, 4] Im Gegensatz hierzu liegt der Fokus der bisher literaturbekannten elektrochemischen Untersuchungen auf den Einflüssen des Molekulargewichts und der Regioregularität. [5] Das Ziel dieser Arbeit ist es daher eine direkte Korrelation der Dünnschicht-Morphologie von P3HT auf die elektrochemischen Eigenschaften zu untersuchen. Hierfür werden P3HT Filme verschiedener, kontrollierter Morphologien mittels Kristallisation aus Lösung und Nachbehandlungs-Methoden wie Lösungsmittel-Dampf Tempern, thermischer Nachbehandlung und Hochtemperatur-Ausrichtung hergestellt. Zur Strukturaufklärung und elektrochemischen Untersuchung wurden Analysemethoden wie Rasterkraftmikroskopie (AFM), Transmissionselektronenmikroskopie (TEM), Polarisationsmikroskopie (POM), Absorptions-Spektroskopie und Zyklovoltammetrie (CV) verwendet. Es wurde eine starke Abhängigkeit der anodischen Redox-Halbwellen des Voltammograms von der Film-

Morphologie beobachtet, wodurch ein charakteristisches CV-Signal den kristallinen Domänen des Polymerfilmes zugeordnet werden kann. Da der Nieder-Oxidationsbereich des Voltammograms am stärksten durch die Film-Morphologie beeinflusst wird, zeigt sich ebenfalls ein signifikanter Morphologie-Einfluss auf das HOMO Grenzorbital, welches für die Anwendung von P3HT in organischen Solarzellen von essentieller Bedeutung ist.

Zusätzlich zu P3HT Filmen wurden auch binäre Donor-Akzeptor Blend Filme untersucht. Für die Anwendung in organischen Solarzellen wird P3HT üblicherweise als binäre Mischung mit Phenyl-C_{61}-Buttersäuremethylester ($PC_{61}BM$) verwendet. In der Literatur konnte gezeigt werden, dass die Energieumwandlungs-Effizienz von P3HT:$PC_{61}BM$ Solarzellen durch einen thermischen Nachbehandlungsschritt signifikant erhöht werden kann. [6] Dieser Effekt wird üblicherweise durch eine verbesserte Phasen-Separation in dem binären Blend erklärt, wodurch durchgehende Donor- bzw. Akzeptor-Kanäle zu den jeweiligen Elektroden ausgebildet werden und die Ladungsableitung verbessert wird. Die elektrochemische Untersuchung von unbehandelten und thermisch nachbehandelten P3HT:$PC_{61}BM$ Filmen zeigt, dass die oxidativen Redox-Halbwellen von P3HT bei niedrigen Oxidationspotentialen im Voltammogram durch die Beimischung des Fullerens unterdrückt werden, wodurch das HOMO Grenzorbital um einige hundert meV verschoben wird. Durch die thermische Nachbehandlung von P3HT:$PC_{61}BM$ können die oxidativen Halbwellen bei niedrigen Oxidationspotentialen wieder gewonnen werden und das daraus resultierende HOMO Grenzorbital liegt im Bereich von ungestörtem P3HT. Da die LUMO Grenzorbitale des $PC_{61}BM$ nicht durch die thermische Nachbehandlung beeinflusst werden, wird die elektrochemische Bandlücke durch die thermische Nachbehandlung insgesamt verkleinert.

Im zweiten Teil dieser Arbeit wird der Einfluss der Quervernetzungs-Dichte einer Reihe von Polyvinyltriphenylamin-*co*-Polystyrol (PVTPA-*co*-PS) Copolymeren mit variierenden Wiederholungseinheits-Verhältnissen auf das elektrochemische und chemische Dotierungs-Verhalten untersucht. Redox-Polymere, welche Triarylamin-Gruppen enthalten, sind vielversprechende Ladungsspeicher-Materialien, da sie eine hohe Ladungsdichte aufweisen,

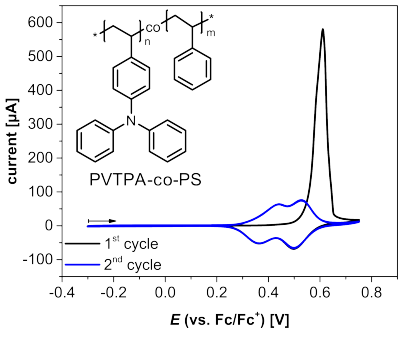

aus Lösung prozessiert werden können und eine hohe Film-Stabilität im vernetzten Zustand besitzen. [7] Das elektrochemische Verhalten von PVTPA und seinen Copolymeren ist insbesondere aufgrund einer irreversiblen oxidativen Kupplungs-Reaktion, in der die TPA-Gruppen zu TPB-Gruppen (Tetraphenylbenzidin) dimerisieren, interessant. [8] Die oxidative Kupplung kann sowohl elektrochemisch als auch chemisch induziert werden und führt zu einer Quervernetzung der Polymerketten, wobei die gebildeten TPB-Gruppen wiederum elektrochemisch redox-aktiv sind.

Die Quervernetzungs-Reaktion und Ladungs-/ Entladungs-Prozesse von PVTPA und PVTPA-*co*-PS wurden mit Hilfe von *in-situ* Spektroelektrochemie untersucht, um die nebeneinander vorliegenden Redox-Prozesse zu identifizieren und charakteristische Absorptions-Banden den Redox-Halbwellen im Voltammogram zuordnen zu können.

Während der elektrochemisch induzierten Quervernetzungs-Reaktion und der Ladungs-/ Entladungs-Prozesse der Polymerfilme, findet eine Ionen-Einlagerung bzw. -Auslagerung statt um die Elektroneutralität zu bewahren. Die Untersuchung dieser Ionen-Bewegungen während der elektrochemischen Redox-Reaktionen in Abhängigkeit der Quervernetzungs-Dichte und Ionengröße wurde mittels elektrochemischer Quartzkristall Mikrowaage (EQCM) durchgeführt.

Um die Ladungsspeicher-Eigenschaften von PVTPA und PVTPA-*co*-PS zu untersuchen, wurden so-genannte *supercapacitor* Zellen gebaut und mittels Zyklovoltammetrie (CV), elektrochemischer Impedanzspektroskopie (EIS) und galvanostatischen Ladungs-/ Entladungs-Zyklen (GCD) charakterisiert. Die untersuchten Polymere zeigen sowohl kapazitive als auch faradaysche Ladungsspeicherung mit spezifischen Energiedichten und Leistungsdichten von 10^1 - $10^2\,\mathrm{J\,kg^{-1}}$ bzw. $10^1\,\mathrm{W\,kg^{-1}}$.

Chemisch dotiertes PVTPA bzw. PVTPA-*co*-PS ist ein interessantes Elektrodenmaterial um PEDOT:PSS als Lochtransport-Schicht in organischen Solarzellen zu ersetzen, da die Lebenszeit momentan verwendeter organischer Solarzellen durch die Azidität der PEDOT:PSS Schicht leidet. Im Rahmen dieser Doktorarbeit wurden die chemisch induzierte Quervernetzung und Dotierung von PVTPA und PVTPA-*co*-PS mit Eisen(III)-Chlorid und Eisen(III)-Tosylat als Dotierungsmittel untersucht. Der Dotierungs-Prozess wurde mittels Absorptions-Spektroskopie verfolgt und mit Hilfe von *4-point probe* Messungen Leitfähigkeiten der dotierten Polymerfilme von bis zu $10^{-4}\,\mathrm{A\,V^{-1}\,cm^{-1}}$ erhalten.

Publications

Scientific Paper

Li Liu, Pierre Eisenbrandt, Thomas Roland, Matthias Polkehn, Pierre-Olivier Schwartz, Kirsten Bruchlos, Beatrice Omiecienski, Sabine Ludwigs, Nicolas Leclerc, Elena Zaborova, Jérémie Léonard, Stéphane Méry, Irene Burghardt, Stefan Haacke, *Phys. Chem. Chem. Phys.*, **2016**, 18536-18548.

Dimitar I. Kutsarov, Ilija Rašović, Alexandros Zachariadis, Argiris Laskarakis, Maria A. Lebedeva, Kyriakos Porfyrakis, Christopher A. Mills, Michail J. Beliatis, Brett Fisher, Kirsten Bruchlos, Sabine Ludwigs, Stergios Logothetidis, S. Ravi P. Silva, *Adv. Electron. Mater*, **2016**, *2*, 1600362.

Johannes C. Hänle, Kirsten Bruchlos, Sabine Ludwigs, Andreas Köhn, Sabine Laschat, *Chem. Plus. Chem.*, **2017**, *82*, 1197-1210.

Peter Reinold, Kirsten Bruchlos, Sabine Ludwigs, *Polym. Chem.*, **2017**, *8*, 7351-7359.

Kirsten Bruchlos, Daniel Trefz, Amer Hamidi-Sakr, Martin Brinkmann, Jürgen Heinze, Adrian Ruff, Sabine Ludwigs, *Electrochimica Acta*, **2018**, *269*, 299-311.

Tiziana Benincori, Sergio Gámez Valenzuela, Miriam Goll, Kirsten Bruchlos, Claudia Malacrida, Serena Arnaboldi, Patrizia Romana Mussini, Monica Panigati, Juan T. López Navarrete, M. Carmen Ruiz-Delgado, Giulio Appoloni, Sabine Ludwigs, *Electrochimica Acta*, **2018**, *284*, 513-525.

Iris Wurzbach, Christian Rothe, Kirsten Bruchlos, Sabine Ludwigs, Frank Giesselmann, *J. Mater. Chem. C*, **2019**, *7*, 2615-2624.

Oral Presentations

Kirsten Bruchlos, Daniel Trefz, Adrian Ruff, Martin Brinkmann, Sabine Ludwigs, *Influence of the Crystallisation Conditions of P3HT Thin Films on the Electrochemical Behaviour*, **2017**, *ECHEMS 2017*, Milano Marittima

Poster Presentations

Kirsten Bruchlos, Adrian Ruff, Florian S. U. Fischer, Sabine Ludwigs, *In-situ Spectroelectrochemical Characterization of Polymer:Fullerene Blend Films for Photovoltaic Applications*, **2014**, *Electrochemistry2014*, Mainz

Kirsten Bruchlos, Daniel Trefz, Adrian Ruff, Florian S. U. Fischer, Sabine Ludwigs, *In-situ Spectroelectrochemical Characterization of P3HT and P(NDI2OD-T2) Films with Controlled Thin Films Morphology*, **2015**, *WEEM2015*, Bad Herrenalb – including oral presentation

Peter Reinold, Kirsten Bruchlos, Sabine Ludwigs, *Conjugated Redox Polymers via Click Functionalization*, **2016**, *International Symposium Organic Electronics: Recent Developments and Challenges*, Stuttgart

Peter Reinold, Kirsten Bruchlos, Sabine Ludwigs, *Conjugated Redox Polymers via Click Functionalization*, **2016**, *Electrochemical Energy Conversion and Storage*, Stuttgart

Scientific Projects

EU Project *Smartonics*, within the *Seventh Framework* Program FP7 / 2007-2013, *grant 310229*
– including periodic oral presentations (Berlin: April 2015, Thessaloniki: July and November 2015, Potsdam: January 2016) and reports

Danksagung

Die vorliegende Arbeit entstand im Zeitraum von November 2014 bis Januar 2018 im Institut für Polymerchemie der Universität Stuttgart. Im Folgenden möchte ich mich bei allen bedanken, die durch zahlreiche fachliche Disskusionen und durch ihre Unterstützung im Labor maßgeblich zum Gelingen dieser Arbeit beigetragen haben.

Frau *Prof. Dr. Sabine Ludwigs* danke ich für die Aufnahme in ihren Arbeitskreis sowie die kontinuierliche, fachliche Betreuung die meinen wissenschaftlichen Lebensweg seit meiner Bachelorarbeit 2012 und Masterarbeit 2014 geprägt haben. Insbesondere bedanke ich mich für das in mich gesetzte Vertrauen bei der Betreuung zahlreicher interdisziplinärer Forschungsprojekte. Durch die internationalen Kooperationen erhielt ich nicht nur einen tieferen Einblick in verschiedene Facetten der organischen Halbleiterforschung, sie ermöglichten mir auch den inspirierenden Austausch mit Wissenschaftlern verschiedenster Fachrichtungen aus aller Welt, wodurch ich mich auch persönlich weiterentwickeln konnte.

Herr *Prof. Dr. Frank Gießelmann* und Herr *Prof. Dr. Joris van Slageren* danke ich herzlich für die Übernahme des Zweitgutachtens und des Prüfungsvorsitzes.

Für finanzielle Unterstützung im Rahmen des *Smartonics*-Projektes (Seventh Framework Programm FP7/2007-2013, grant agreement no 310229) danke ich der *Europäischen Union* sowie der *Procope France-Germany (DAAD)* für die Übernahme von Reisekosten.

Internationale Kooparations- und Projektpartner haben maßgeblich zum Gelingen dieser Promotion beigetragen:

Mein besonderer Dank gilt *Dr. Martin Brinkmann* vom *Institut Charles Sadron, CNRS Straßburg* und seinen Doktoranden für die herzliche Aufnahme in ihre Gruppe und die inspirierende Diskussionen während meiner Aufenthalte in Straßburg. *Dr. Amer Hamidi-Sakr*, *Dr. Morgane Diebold* und *Vishnu Vijayakumar* danke ich im Speziellen für die Hilfe im Labor und die unzähligen Stunden, die sie für mich am Transmissionselektronenmikroskop

verbracht haben.

Ich möchte allen Kooperationspartner im Rahmen des *Smartonics*-Projektes für die freundliche Aufnahme und lebhaften wissenschaftlichen Diskussionen danken. Insbesondere gilt mein Dank *Prof. Dr. Joannis Kallitsis* und *Dr. Katerina Andreopoulou* von der *Universität Patras*, *George Paloumbis* von *Advent Technologies* und *Dr. Kyriakos Porfyrakis* von der *Universität Oxford* für die Bereitstellung von funktionalisierten P3HT- und Fullerenderivaten. Desweiteren möchte ich *Dimitar Kutsarov* von der *Universiät Surrey* für Solarzellen-Messungen danken.

Dr. Hubert Perrot von der *Sorbonne Universität* in Paris danke ich für seine Hilfe bei EQCM Messungen und die maßgefertigten Quarz-Kristalle.

Dr. Johannes Hänle und *Prof. Dr. Sabine Laschat* von der *Universität Stuttgart* danke ich für die intensive Zusammenarbeit, durch die ich einen tieferen Einblick in die Welt der Farbstoffe erhalten konnte.

Dr. Li Liu und *Prof. Dr. Stefan Haacke* vom *CNRS Straßburg* danke ich für die spannende Kooperation im Bereich der oligomeren Thiophen-Donor-Akzeptor-Systeme.

Für die enge wissenschaftliche Kooperation und lehrreichen Diskussionen im Bereich der chiralen Thiophen-Oligomer Elektrochemie danke ich *Prof. Dr. Patrizia Mussini* und *Dr. Serena Arnaboldi* von der *Universität Mailand*.

Ich möchte mich bei allen Mitgliedern des Arbeitskreises für die wunderbare Atmosphäre und die vielen gemeinsamen Aktionen und Ausflüge bedanken. Die letzten drei Jahre haben mich nicht nur fachlich sondern vor allem persönlich sehr geprägt.

Dr. Klaus Dirnberger danke ich für die fachliche Betreuung und dafür, dass seine Türe stets für Fragen oder Probleme aller Art offen steht.
Für ihre großartige Unterstützung sowohl im Labor als auch bei allen organisatorischen

Problemen möchte ich mich herzlich bei *Beatrice Omiecienski* bedanken. Bei *Corinne Rost-Schmidt* möchte ich mich für die Synthese der PVTPA-*co*-PS Copolymeren und die GPC-Messungen bedanken. *Simon Tannert* danke ich für seine Hilfe bei allen Computer-Problemen sowie für das Erstellen der *origin*-Skripte, die mir die Datenverarbeitung enorm erleichtert haben.

Mein besonderer Dank gilt meinen beiden Mentoren *Dr. Steffen Link* und *Dr. Adrian Ruff* für die Betreuung meiner Bachelor- und Masterarbeit. Ihre unermüdliche Geduld im Labor und fachliche Unterstützung haben wesentlich zum Gelingen dieser Arbeit beigetragen. *Dr. Gisela Schulz* und *Jun.-Prof. Dr. Anna Schenk* danke ich für ihre Hilfe bei der Betreuung verschiedener Projekte und bei administratorischen Problemen.

Meinen Bachelorstudenten *Fabian Moczko* und *Lisa Eisele* sowie meinen Praktikanten *Lluis Martinez Gallo*, *Felix Goerigk* und *Lukas Stein* danke ich für ihre hilfreiche Mitarbeit bei verschiedenen Projekten im Rahmen meiner Promotion.

Meinen Mit-Doktoranden *Dr. Florian Fischer*, *Dr. Martin Scheuble*, *Justus Back*, *Dr. Miriam Goll*, *Dr. Christian Rothe*, *Dr. Daniel Trefz*, *Philipp Gutrod*, *Dr. Peter Reinold*, *Yannic Gross*, *James Borchert*, *Carsten Dingler*, *Jochen Kuhlmann*, *Matthias Wieland*, *Claudia Malacrida*, *David Gepperth* und *Sherri Liu* möchte ich für die gemeinsame schöne Zeit danken.

Meinen Kommilitonen *Daniel Rudolph*, *Jens Schmid*, *Nico Kress*, *Andrea Nuñez*, *Iris Wurzbach*, *Clarissa Dietrich* und *Kristina Schneider* danke ich für die schönen gemeinsamen Studienjahre und ihre Unterstützung innerhalb sowie außerhalb des Labors und Hörsaals.

Mein größter Dank gilt meiner Familie, die stets an mich geglaubt und mich während meines gesamten Studiums und der nachfolgenden Promotion unterstützt haben.

List of Abbrevations

3-HT	3-hexylthiophene
4pp	four-point-probe
AFM	atomic force microscopy
AIBN	azobisisobutyronitrile
a.u.	arbitrary unit
CB	chlorobenzene
CE	counter electrode
CV	cyclic voltammetry
DCM	dichloromethane
DSC	differential scanning calorimetry
EDLC	electrochemical double-layer capacitor
EIS	electrochemical impedance spectroscopy
EQCM	electrochemical quartz crystal micro balance
EQE	external quantum efficiency
F4TCNQ	2,3,5,6-tetrafluoro-7,7,8,8,-tetracyanoquinodimethane
Fc/Fc$^+$	ferrocen/ ferrocenium
FF	fill factor
GCD	galvanostatic charging/ discharging
GPC	gel permeation chromatography
HOMO	highest occupied molecular orbital
ITO	indium tin oxide
LCD	liquid crystal display
Li-BTFSI	lithium bis(trifluoromethane)sulfonimide
LUMO	lowest unoccupied molecular orbital
MeCN	acetonitrile
M$_n$	number average molecular weight
M$_w$	weight average molecular weight

NBu_4BF_4	tetrabutylammonium tetrafluoroborate
NBu_4PF_6	tetrabutylammonium hexafluorophosphate
$NHex_4PF_6$	tetrahexylammonium hexafluorophosphate
NMR	nuclear magnetic resonance
o-DCB	1,2-dichlorobenzene
OFET	organic field effect transistor
OLED	organic light emitting diode
OPV	organic photovoltaics
P3AT	poly(3-alkylthiophene)
P3DDT	poly(3-dodecylthiophene)
P3HT	poly(3-hexylthiophene)
P3MT	poly(3-methylthiophene)
PA	polyacetylene
PAN	polyacrylonitrile
PC	polycarbonate
$PC_{61}BM$	phenyl-C61-butyric acid methyl ester
PCE	power conversion efficiency
PDI	polydispersity index
PDMS	polydimethylsiloxane
PEDOT	poly(3,4-ethylenedioxythiophene)
PET	poly(ethylene terephthalate)
PLED	polymer light emitting diode
PMMA	poly(methyl methacrylate)
PNDI2OD-T2	poly[N,N'-bis(2-octyldodecyl)-1,4,5,8-naphthalindicarboximid-2,6-diyl]-alt-5,5'-(2,2'-bithiophen)
POM	polarised optical microscopy
PPV	polyphenylenevinylene
PS	polystyrene
PSS	polystyrenesulfonate

PTFE	polytetrafluoroethylene
PVTPA	polyvinyltriphenylamine
PVTPA-co-PS	polyvinyltriphenylamine-co-polystyrene
r2r	roll-to-roll
RE	reference electrode
rpm	revolutions per minute
TEM	transmission electron microscopy
TEMPO	2,2,6,6-tetramethylpiperidinyl-N-oxyl
THF	tetrahydrofuran
TPA	triphenylamine
TPB	tetraphenylbenzidine
UPS	ultraviolet photoelectron spectroscopy
UV-vis	ultraviolet-visible
W	free exciton bandwidth
WE	working electrode
w/w	weight by weight

Contents

1. Introduction

One of the most challenging tasks of humankind in the 21st century is the compatibility of an increasing energy consumption of the growing global population and ongoing technological and industrial progress on the one hand and the environment and climate protection on the other hand. According to the *U.S. Energy Information Administration* the global energy consumption is expected to increase by approximately 28 % in the period from 2015 to 2040. The main contribution to this increase is caused by the economical growth of emerging countries like China and India. The main sources to cover this energy demand are expected to be renewable energy sources like solar energy, wind power, hydro power and geothermal energy, and nuclear power with approximate annual growth of 2.3 % and 1.5 % respectively. [9] This increasing energy demand is met by the growing awareness of environment and climate protection. In 2014 the *European Union* agreed on the so-called *2030 climate and energy framework* whose main objective is a reduction of green house gasses to 80 - 95 % below the level of 1990. As secondary objectives, the utilization of fossil fuels is supposed to be reduced to avoid high energy costs on oil and gas imports which would hamper the european economy and to reduce the dependency of the EU on imports from politically unstable regions. [10] On the international stage the *Paris Climate Treaty*, which aims to prevent a global warming of more than 2 °C, was signed in 2015 from the *United Nations Framework Convention on Climate Change*. [11]

One of the key industrial sectors in the 21st century is the semiconductor industry. According to the *U.S. Department of Commerce* and the *International Trade Administration* the USA, Japan and the Netherlands are the global market leaders with combined about 90 % of the global semiconductor production. Due to increased sales volume of electronic devices like smartphones, computers and multimedia devices, the expected annual growth of the global semiconductor production is approximately 3.5 %. In addition a steady long term growth of the semiconductor industry is expected in the future to provide the infra structure for the so-called *Internet of Things* which describes internet connected devices like smart grids, smart cities and automatic manufacturing. [12] A main challenge to satisfy the increasing demand for semiconductors are the high costs for the purification and high temperature production of commonly used silicon based products. In the last two decades the field of

organic semiconductors gained huge interest in the scientific community due to its potential to replace silicon. Since the charge transport in organic semiconductors is caused by the molecular structure rather than a crystal lattice, the properties of organic semiconductors can be tuned by the molecular design during synthesis. In addition, organic semiconductors are flexible and soluble which enables cheap and simple processing techniques like printing or roll-to-roll coating. [13, 14] The main field of application of organic semiconductors are organic photovoltaics (OPV) [15–18], organic field effect transistors (OFET) [19–21], organic light emitting diodes (OLED) [22, 23], thermoelectrics [24, 25], elecrochromic windows [26, 27], actuators [28–30] and charge storage devices [31–33].

In the following a short introduction into the basic theory of the charge transport mechanisms in π-conjugated and redox polymers is given in chapter 1.1.1 and 1.1.2. The two organic electronic devices which are relevant for this thesis, namely organic solar cells and energy storage devices, are discussed afterwards in chapters 1.2.1 and 1.2.2.

1.1. Charge Transport in Conducting Polymers

In the last century, polymers became a fundamental material in all areas of everyday live. Due to the tailor-made properties and cheap synthesis in large scale, polymers replace conventional materials like wood, steel and glass. [34, 35] Some typical representatives of such polymers are polystyrene (PS), polycarbonate (PC), poly(ethylene terephthalate) (PET), polyacrylonitrile (PAN), polyurethane, poly(methyl methacrylate) (PMMA) and polydimethylsiloxane (PDMS). A common feature of these polymers is that they are all electrical insulators.

In 1977 Alan J. Heeger, Alan G. MacDiarmid and Hideki Shirakawa discovered metallic behaviour in polyacetylene (PA) after exposure to halogen vapour. The conductivity of the doped polyacetylene could be increased over seven orders of magnitude from 10^{-4} $\mathrm{S\,cm^{-1}}$ to 10^{3} $\mathrm{S\,cm^{-1}}$. [36, 37] Since then, the research in the field of conducting polymers gained huge interest and led to the award of the Nobel Prize in chemistry to Heeger, McDiarmid and Shirakawa in 2000 for their discovery of a novel material class. [38]

The advantages of conducting polymers compared to silicon are the light weight, the flexibility and the possibility to tune the properties by changing the molecular design by means of organic synthesis. [39–41] By up-scaling of the organic synthesis the material production

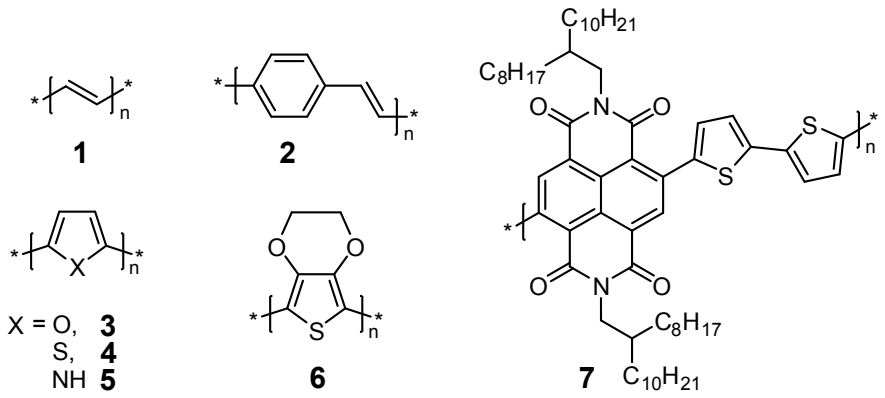

Figure 1.1: Molecular structures of polyacetylene (**1**), poly(*p*-phenylenevinylene) (**2**), polyfuran (**3**), polythiophene (**4**), polypyrrole (**5**), poly-3,4-ethylenedioxythiophene (**6**) and poly[N,N'-bis(2-octyldodecyl)-1,4,5,8-naphthalindicarboximid-2,6-diyl]-alt-5,5'-(2,2'-bithiophen) (**7**).

cost can be reduced and since the semi-conductors are soluble, the device production can be performed by means of cheap solvent deposition techniques like inkjet printing or roll-to-roll processing instead of expensive *Czochralski* process (high temperature process used for the production of monocrystalline silicon of high purity) or high vacuum deposition respectively. [42–44]

In general the field of semi-conducting polymers can be subdivided into two groups: the π-conjugated polymers and the redox polymers. [39, 45] In the following both material classes with their unique charge transport mechanisms will be discussed in chapters 1.1.1 and 1.1.2.

1.1.1. π-conjugated Polymers

Traditional polymers used for various applications as packaging or engineering material are insulating materials. They usually consist of chains or networks of mainly sp^3-hybridised carbon which results in σ-bonds in the polymer backbone. $C{=}C$ double bonds or aromatic units are typically electronically isolated (e.g. poly(ethylene terephthalate)) or located in side chains (e.g. polystyrene). In contrast, π-conjugated conducting polymers consist of sp^2-hybridised carbon atoms which results in alternating σ- and π-bonds in the polymer backbone. [46] The simplest molecular structure of such a π-conjugated polymer backbone is polyacetylene (**1** in Fig. 1.1) which is also historically the first studied semi-conducting polymer and is seen as the *first generation* of π-conjugated polymers. [38, 47] In the fol-

lowing years the research focus shifted from polyacetylene towards systems with aromatic heterocycles in the polymer backbones like poly(*p*-phenylenvinylene) (**2** in Fig. 1.1), polyfuran (**3** in Fig. 1.1), polythiophene (**4** in Fig. 1.1) and polypyrrole (**5** in Fig. 1.1). [46] These so-called *second generation* of π-conjugated polymers possess better thermal and oxidation stability, higher conductivity and higher absorbance which makes these materials suitable for the production of organic optoelectronic devices like organic solar cells (OPV), light-emitting diodes (OLED) and organic field-effect transistors (OFET). [48–50] Two of the most important members of the *second generation* π-conjugated polymers regarding the commercial availability and usage in organic optoelectronic devices on large scale are poly(3-hexylthiophene) (P3HT) and poly(3,4-ethylenedioxythiophene) (PEDOT). Since P3HT is discussed in detail in chapter 4, for now the focus is set on PEDOT.

The molecular structure of PEDOT is shown in Fig. 1.1 **6**. The ethylenedioxy bridge attached to the two β-positioned carbon atoms causes a planarised, all-*trans* configuration of the monomer units due to non-covalent attractive interactions of the oxygen atoms in the side groups and the sulphur atoms in the aromatic rings. [51] In addition the free electron pairs of the oxygen atoms cause PEDOT to be electron rich compared to the non-substituted polythiophene or the alkyl side-chain β-substituted P3HT which significantly influences the electronic properties of PEDOT. The oxidation potential is lower and therefore the HOMO energy level is increased which results in an improved thermodynamic stability of the oxidised state. In addition, PEDOT is almost transparent in the oxidised state which makes it a suitable material to replace metallic semi-conductors as electrode materials. One significant disadvantage for the use of PEDOT as an electrode material is the poor solubility in organic solvents or water. By using the water-soluble polyelectrolyte polystyrenesulfonate (PSS) to neutralise the positive charge of PEDOT, the generated PEDOT:PSS composite becomes not only highly conductive through a self-doping effect but also water-soluble. [52, 53] By treating PEDOT:PSS with solutions of organic salts like methylammonium halogenides, Yu et al. observed conductivity values of up to $2100\,\mathrm{S\,cm^{-1}}$. [54]

A common feature of all semi-conducting polymers mentioned above is that they are *p*-type conductors. [55] For sake of completeness Fig. 1.1 **7** shows the molecular structure of poly[N,N'-bis(2-octyldodecyl)-1,4,5,8-naphthalindicarboximid-2,6-diyl]-alt-5,5'-(2,2'-bithiophen) (PNDI2OD-T2) which is a promising material for the application in organic

electronics and especially in organic field effect transistors. PNDI2OD-T2 is a member of the so-called *third generation* [46] π-conjugated polymers which are characterised by their common feature of a copolymerisation of donor-units (here: bithiophene) and acceptor-units (here: naphthalindicarboximid). In case of PNDI2OD-T2 the acceptor-unit dominates and therefore this polymer becomes a *n*-type conductor with charge carrier mobilities up to $6.4\,\mathrm{cm^2\,V^{-1}\,s}$. However, the charge carrier mobility of PNDI2OD-T2 is anisotropic and highly depending on the aggregation texture of the polymer chains which makes the precise morphological control crucial for the application in organic electronic devices. It should also be mentioned that despite the molecular structure of a π-conjugated polymer, the charge transport mechanism in PNDI2OD-T2 complies more with the charge transport processes observed in redox polymers instead. The general mechanism is discussed in chapter 1.1.2. In brief, this unusually electronic behaviour can be explained by a localisation of the charges followed by a hopping-process and has been studied in-depth in literature. [56–58]

Charge transport mechanism in π-conjugated polymers

To date, the charge transport mechanism in π-conjugated polymers is widely understood and can be explained by a detailed analysis of the interaction of the molecular orbitals. [47, 59, 60]

The basic idea goes back all the way to the 1860s when Kekulé studied the nature of the chemical bonds in benzene. Due to his discovery that all hydrogen atoms are equal and all *C-C* bonds have the same length, Kekulé concluded that the π-electrons in the benzene molecule are delocalised across the whole molecule. With this conclusion the concepts of π-electron conjugation and aromaticity were born. Continuing this line of thought, it has been proposed that such free electron movement not only occurs in cyclic conjugated π-systems but also along poly-conjugated chains. In accordance with this, it has been known that the physico-chemical properties of unsaturated small hydrocarbon chains change with increasing number of conjugated double bonds. A shift of the absorption maximum towards larger wavelengths (bathochromic effect) and an increase in the extinction coefficient (hyperchromic effect) have been observed. This lead to the interpretation that the difference between single and double bonds diminishes with increasing prolongation of the conjugated π-system. As a conclusion, it has been proposed that for an infinitely prolonged π-conjugated hydro-

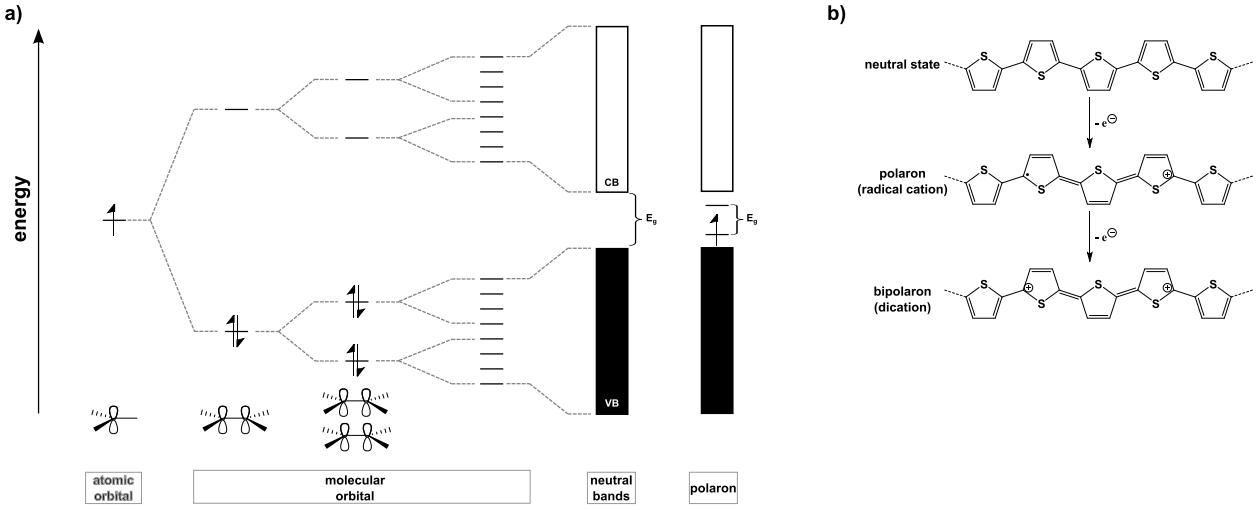

Figure 1.2: **a)** Schematic illustration of the energetic merging of the frontier orbitals of π-conjugated polymers with increasing conjugation length from left (isolated atomic orbitals) to right (continuous valence and conducting bands in polymer chains); adapted from [47] and [60]; **b)** molecular structures of polythiophene chain sections in the neutral, radical cation (polaron) and dication (bipolaron) form respectively.

carbon chain the bond length alternation should vanish and the π-electrons be completely delocalised.

In the following the impact of the infinite prolongation of the π-conjugated chain on the molecular orbitals is discussed on polyacetylene as a model molecule. The evolution of the molecular orbitals with increasing chain length is shown in Fig. 1.2 **a** from left to right. In the far left an isolated sp^2-hybridised carbon atom, which is the basic building block of polyacetylene, is shown. The p_z-orbital of this carbon atom is occupied by one unpaired electron illustrated by the upward harpoon arrow. As soon as two sp^2-hybridised carbon atoms interact to form an ethylene molecule, the two p_z-orbitals are split into a binding (π) and an anti-binding (π^*) orbital and the two electrons fill in the energetically lower lying orbital to form a shared π-bond. The π^*-orbital remains empty. Therefore the π- and π^*-orbitals are the HOMO and LUMO orbitals respectively. In the next step two ethylene molecules interact. Again, the degenerated π- and π^*-orbitals of both molecules split and form two respective π- and π^*-orbitals with discrete energy levels. The π-orbitals are filled completely and the π^*-orbitals remain empty. With increasing chain length the number

of π- and π^*-orbitals increase as well. Since every orbital has a discrete energy level, the energetic distance between the orbitals decreases. In addition, the gap between HOMO and LUMO levels decreases. For an infinite chain length the discrete molecular orbitals merge and can be described analogous to the band model used for metallic conductors with the electron occupied π-orbitals as valence band and the empty π^*-orbitals as conducting band respectively. The frontier orbitals (HOMO and LUMO) correspond to the upper and lower edge of the valence and conducting band respectively. The energetic difference between HOMO and LUMO is the band gap (E_g). For organic semi-conductors E_g is usually in the range of 1 - 3 eV. Since in the electronic ground state the valence band is filled completely and the conducting band is empty, no mobile charge carriers are present. Therefore in the neutral state, which corresponds to the electronic ground state, semi-conductors are insulating. In metallic semi-conductors charge carriers can be elevated from the valence band to the conducting band by energetic excitation (thermal or radiation) whereby the material becomes conducting. In case of organic semi-conductors the conducting species is generated by means of chemical or electrochemical doping. In contrast to the excitation process in metallic semi-conductors, the doping process initiates a redox reaction in which an anionic (n-type, reduction) or cationic (p-type, oxidation) species is generated respectively. In Fig. 1.2 **b** a section of a polythiophene chain is shown. In the neutral state the whole polymer backbone consists of a benzene-like aromatic electron structure. During the oxidation to the radical cation an unpaired electron and a positive charge are generated which are stabilized by delocalisation over multiple thiophene rings. Hereby, the benzene-like structure is partially changed to a quinoid-like structure. With increasing doping level the unpaired electron is also removed to form the dication species. The partially quinoid-like structure in the doped polymer chain can be described as a mobile pseudo-particle, the so-called *polaron* (single charge) and *bipolaron* (two times charged). The quinoid-like structures generate an additional π- and π^*-orbital in the band gap whereby the effective band gap shrinks and as a result the material becomes conducting. Since the conductivity of organic semi-conductors is generated by ionic pseudo-particles (polaron, bipolaron) the conductivity/ number of mobile charges is a function of the doping level. [47, 59, 60]

1.1.2. Redox Polymers

The second class of conducting polymers are the so-called redox polymers. A classification of these polymers into their subgroups is made by means of the position of the redox-active group in the polymer backbone or the side chain and of the organic or inorganic nature of the redox group. [61] Within the scope of this thesis the focus is set only on semi-conducting, organic redox polymers with the redox group as a side-group attached to a non-conducting polymer backbone. Some typical representatives of such polymers are derivatives of poly(9-vinylcarbazole) (Fig. 1.3 **1**), poly(vinyltriphenylamine) (Fig. 1.3 **2**) and poly(vinyl-*p*-benzoquinone) (Fig. 1.3 **3**). [62–64]

In contrast to the π-conjugated polymers, the polymer backbone is isolating with individual redox-active groups attached to it. The redox-active groups are either electron-donating (donor material) or electron-withdrawing (acceptor material). Since every individual redox group can carry a charge, the charge density in redox polymers is significantly higher than in π-conjugated polymers where the charges are delocalised over segments of the polymer chains. In addition, due to the localisation of the charges on isolated redox groups, the electrochemical properties of these polymers are solely defined by the properties of the individual redox groups. This is in contrast to the electrochemical properties of π-conjugated polymers which are defined by the interaction and energetic distribution of the redox sites resulting in non-Nernstian waves in the cyclic voltammograms. As a consequence the redox potentials in redox polymers are sharply defined and the transition between redox states is fast. Therefore redox polymers are promising materials for application in energy storage devices (batteries or supercapacitors), sensors, electrochromic devices, actuators and biofuel cells. [61]

Charge transport mechanism in redox polymers

The charge transport mechanism in redox polymers is completely different to the mechanism in π-conjugated polymers described in chapter 1.1.1. Since the charge bearing redox groups are isolated from each other, the charges can not be moved through a delocalisation along a shared π^* conducting band, but have to be transported via a hopping mechanism between the redox groups which is also described as a mixed valence transport process. The two important parameters for the conductivity are the number of charge carriers and their mobility.

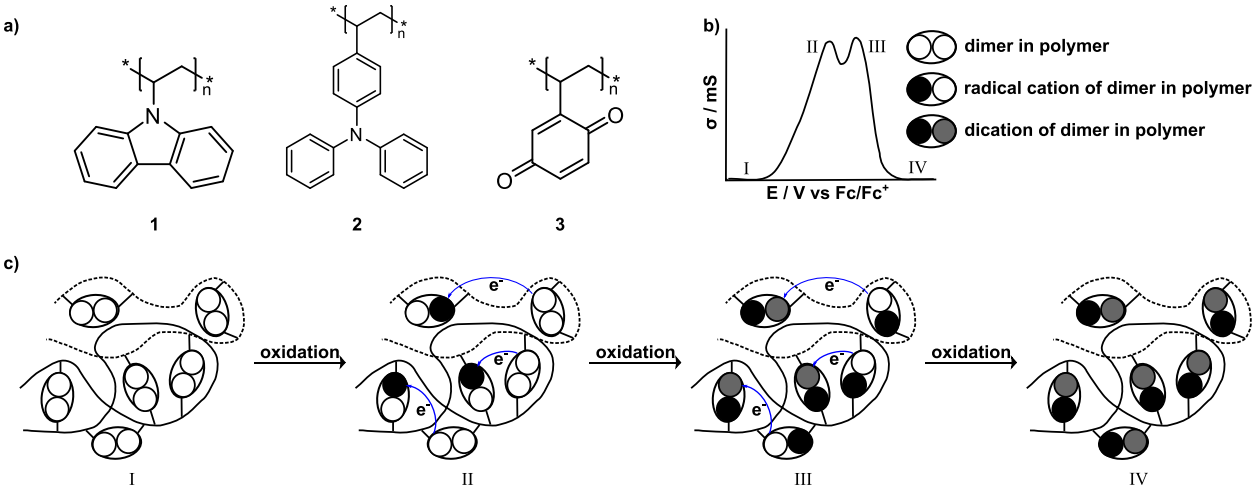

Figure 1.3: **a)** Molecular structures of poly(9-vinylcarbazole) (**1**), poly(vinyltriphenylamine) (**2**) and poly(vinyl-*p*-benzoquinone) (**3**); **b)** and **c)** schematic illustration of the charge transport mechanism in a redox polymer with the conductivity profile and the schematic illustration of the involved charged species respectively; adapted from Yurchenko et al. [8].

For a better understanding of the charge transport mechanism, in the following the mixed valence hopping processes in poly(vinyltriphenylamine) (PVTPA) are described in detail. In Fig. 1.3 **b** and **c** the potential dependent conductivity profile and the redox states of the redox groups in the polymer chains are illustrated schematically. Poly(vinyltriphenylamine) undergoes a cross-linking reaction upon oxidation in which pairs of the initial redox groups dimerise (see chapter 5.3.1) and form larger redox groups which can bear two charges each. The respective redox states are indicated by coloured circles in Fig. 1.3 (neutral: empty/empty; radical cation: black/empty; dication: black/ grey). In the neutral PVTPA polymer (**I** in Fig. 1.3 **b** and **c**) no conductivity is observed. This is due to the fact that in the electronic ground state (neutral state) no free charges are present. With increasing degree of electrochemical doping (**II**); here depicted by an increase in oxidation potential; the conductivity increases. This can be explained by the injection of charge carriers through the formation of the radical cation species. Due to the mixed valence state of the redox sites (co-existence of radical cations and neutral redox sites), electron hopping between redox sites of different oxidation state occurs. The conductivity maximum is reached at the half charged state, when the number of charges and free redox sites is equal. [8] Upon further increase

of the oxidation potential the conductivity profile passes through a local minimum due to a decreased mobility of the charge carriers caused by electrostatic repulsion of the increased number of charge carriers. As soon as the oxidation potential of the second oxidation step to the dication is reached, the conductivity increases again and passes a second maximum at the half charged state where the number of radical cations and dications are equal (**III** in Fig. 1.3). Again the charge carrier transport occurs via hopping processes between redox sites of different oxidation states. In the completely charged state (**IV** in Fig. 1.3) no free redox sites are available anymore and eventually the polymer becomes insulating again.
Compared to π-conjugated semi-conducting polymers, redox polymers generally possess a narrower conductivity potential window and the overall conductivity value is lower. Thus these materials are not suitable for the application as electrode material but due to their high charge density redox polymeres are promising materials for energy storage devices. In addition, especially for the application in batteries, the disadvantageous low conductivity can be compensated by intercalation of the redox polymers in conducting matrices like carbon nanotubes [61] or graphene [65].

1.2. Organic Electronic Devices

In the following chapter two of the main organic electronic devices for the application of semi-conducting polymers are introduced in detail. The two devices, namely the organic solar cell and organic energy storage devices, have been chosen since they can be seen as the showcase devices for the polymers studied in this thesis. In chapter 4 the influence of the thin film morphology on the electrochemical behaviour and the frontier orbital energy levels of P3HT and P3HT:PCBM blends, which are state-of-the-art materials of choice for the application in the photoactive layer in organic solar cells, is studied. In the second main subject of this thesis in chapter 5 the influence of the cross-linking density of the redox PVTPA-*co*-PS copolymers on the electrochemical behaviour and energy storage capacity for potential application in energy storage devices is studied.

1.2.1. Organic Solar Cells

Over the last decades, silicon based photovoltaic devices have dominated the solar cell industry due to their high efficiency and the high abundance of silicon in the earth's crust. This

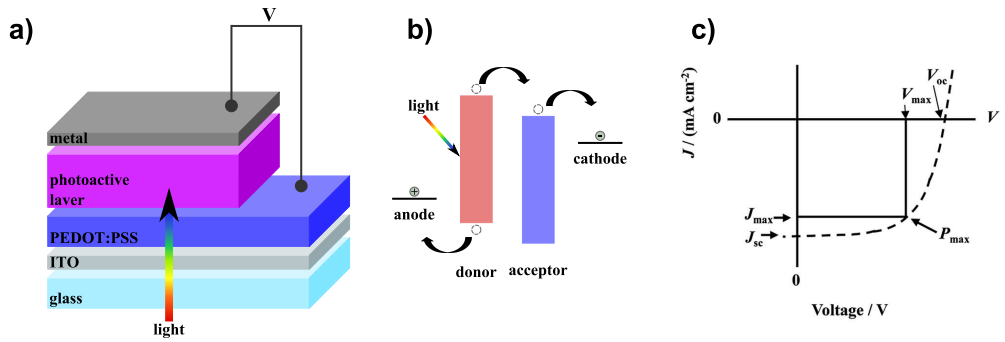

Figure 1.4: Schematic illustration of the energy conversion processes within a bulk heterojunction solar cell; **a)** multi layer structure with metal cathode (dark grey), photoactive layer (violet), PEDOT:PSS layer (dark blue), ITO anode (light grey) and glass substrate (light blue); adapted from [69]; **b)** energy band diagram of the charge generation in the photoactive layer and consecutive charge dissipation to the respective electrodes; adapted from [6]; **c)** schematic potential dependent current density profile; reprinted with permission from Yan et al. [18], Copyright (2014) RCS.

first generation solar cells reached power conversion efficiencies (PCE) up to 25 % which is close to the theoretical maximum value of 31 % for a single junction device. However, due to the high manufacturing costs of crystalline silicon caused by the required high purity grades which require complex thermal purification procedures, the power generation with silicon based solar cells can not compete with conventional energy sources. [66] For this reason in the last 25 years, large scientific effort has been spent on the development of new, cheap photovoltaic devices. In this effort organic semi-conductors have turned out to be promising materials due to their light weight, flexibility and for they do not require laborious high-temperature purification procedures. Since these so-called *second generation* solar cells, which contain small organic semi-conductors, still required expensive vacuum deposition techniques, soon the focus shifted towards conducting polymers which can be large area deposited by solvent processing techniques like printing or roll-to-roll (r2r) deposition, whereby the manufacturing costs can be reduced significantly. [6, 18, 66–68]

As an other advantage of using conducting polymers instead of silicon, the optical band gap can be tuned by the molecular design and the absorption coefficient is high, wherefore the photoactive layer thickness can be reduced to about 100 nm. [6, 67] The general structure

of such an organic solar cell is schematically illustrated in Fig. 1.4 **a**. The photoactive layer (violet layer in Fig. 1.4 **a**), in which the light is harvested, consists of a donor acceptor system. Photons with an energy equal or exceeding the band gap of the donor acceptor system get absorbed and bound electron-hole pairs, so-called excitons, are generated. The exciton diffusion length, meaning the distance over which the excitons can diffuse in their limited lifetime before recombination, is in the range of 5 nm to 20 nm for organic materials. [6, 67] Due to the small exciton diffusion length effective charge separation followed by charge dissipation to the respective electrodes, usually metal layers as cathode and ITO coated glass or foils as anode (dark grey and light grey layers in Fig. 1.4 **a**), only occurs in close proximity to the donor acceptor interface. Therefore organic solar cells are usually prepared as either thin bilayer structures or as so-called bulk heterojunction cells in which the donor acceptor blend microphase separation is tuned to be in the range of the exciton diffusion length. To avoid short circuit current an additional hole transport, electron blocking layer of the polyelectrolyte PEDOT:PSS (blue layer in Fig. 1.4 **a**) is applied in-between the photoactive layer and the anode. The PEDOT:PSS layer furthermore acts as a protection layer which prevents oxygen and ITO nanoparticle diffusion into the photoactive layer. [6]

To gain deeper insight into the energy conversion processes in the photoactive layer a detailed review of the involved frontier orbitals is necessary. [6] The orbital energy diagram of the light energy conversion to electrical charges in a bulk heterojunction solar cell is schematically illustrated in Fig. 1.4 **b**. In the first step the incident light is absorbed by the photoactive layer. In case of a P3HT:PCBM donor acceptor system, which can be seen as a model system for organic bulk heterojunction solar cells, the light is primarily absorbed by the donor material. Thereby electrons from the donor HOMO become excited to the donor LUMO which results in the formation of excitons. The photon absorption efficiency η_{A} is dependent on the photoactive layer thickness in proportion to the absorption length and the optical band gap. Due to the low dielectric constants of organic molecules the excitons are strongly electrostatically bound and have short lifetimes. The exciton diffusion efficiency η_{diff} describes the proportion of excitons reaching the donor acceptor interface before recombination. Due to an energy offset between the donor LUMO and the lower lying acceptor LUMO charge separation takes place at the interface if the orbital energy offset is larger than the exciton binding energy. This charge separation process is described by the exciton

dissociation efficiency η_{diss}. After the exciton dissociation at the donor acceptor interface the free electrons and holes are dissipated towards the cathode and anode respectively via hopping processes. The charge carrier transport efficiency η_{tr} is limited by charge loss processes through recombination at the interface and charge trapping in isolated donor or acceptor phases without continuous pathways to the electrodes. As a last step, at the electrode surfaces the charges are transferred from the donor HOMO and the acceptor LUMO to the anode and cathode respectively. The charge collection efficiency η_{cc} is mainly influenced by the contact resistances at the interfaces and the work functions of the respective materials. The efficiency of the energy conversion process in the photoactive layer is described by the external quantum efficiency: [18]

$$EQE \;=\; \eta_{\mathrm{A}}\;\eta_{\mathrm{diff}}\;\eta_{\mathrm{diss}}\;\eta_{\mathrm{tr}}\;\eta_{\mathrm{cc}} \tag{1}$$

whereby η_{diff} and η_{tr} are significantly influenced by the morphology of the bulk heterojunction solar cell.

The second key parameter for the characterisation of organic solar cells is the power conversion efficiency (PCE) which can be determined from the potential dependent current density curve (see Fig. 1.4 **c**) of a solar cell device under standardised light irradiation. The short-circuit current ($\mathrm{J_{sc}}$) and the open circuit voltage ($\mathrm{V_{oc}}$), which are mainly influenced by the EQE and the effective band gap respectively, can be extracted from the axes intersections. The power conversion efficiency is calculated according to the following equation: [6, 18, 70, 71]

$$PCE \;=\; \frac{J_{\mathrm{sc}}\;V_{\mathrm{oc}}\;FF}{P_{\mathrm{in}}} \tag{2}$$

with FF being the so-called fill factor and P_{in} being the incident light input power. An other important parameter that can be determined from the current density curve is the maximum power (P_{max}) which defines the pair of values (J_{max} and V_{max}) that result in the highest JV product. The fill factor is defined by the proportion of P_{max} and the product of $J_{sc}\,V_{oc}$ and can be used as a measure for the deviation of the current density curve from the ideal behaviour. In the ideal case the current density curve becomes rectangular and FF equals 1. [6, 18, 70, 71]

In the early years of organic solar cell research scientific interest was mainly focused on poly(phenylene vinylene) (PPV) as the donor material. However, due to the higher absorp-

tion as well as hole conducting properties, the focus shifted towards poly(3-hexylthiophene) (P3HT) as the donor material of choice. [72] Due to their high electron affinity and *n*-conducting properties, fullerene derivatives are commonly used as acceptor materials in organic electronic devices. In particular, phenyl-C61-butyric acid methyl ester ($PC_{61}BM$) which has been first synthesised in 1995 by Hummelen et al. [73] is still the state of the art acceptor material for both commercial and scientific organic solar cell production. [6] One substantial disadvantage of $PC_{61}BM$ is the low absorbance in the visible spectrum, whereby the acceptor material does not significantly contribute to the light harvesting and to J_{sc} in the solar cell. Consequently, larger derivatives like $PC_{71}BM$ and $PC_{84}BM$ as well as indene functionalised fullerene derivatives (e.g. $IC_{xx}MA$, $IC_{xx}BA$ and $IC_{xx}TA$ of different fullerene sizes) have been synthesised in order to increase the spectral range and the acceptor strength. However, the improved optical properties of $PC_{84}BM$ and the indene functionalised derivatives are counterbalanced by poor solubility in organic solvents, which is why $PC_{61}BM$ and $PC_{71}BM$ are still the most commonly used acceptor materials in organic solar cells. [18]
Even though the development of low band gap polymers have lead to PCE values over 10 % in recent years, P3HT:PCBM (C_{61} and C_{71}) remains the donor acceptor system of choice due to the simple synthesis and commercial availability of the materials. [74] In literature, PCE values between 3 % and 6 % are commonly reported [75] depending on characteristic polymer parameters like the regioregularity [74] and the molecular mass [76] as well as the thermal post treatment of the solar cell devices [77]. In addition, a lot of effort has been spent on the optimisation of the device design, like the intercalation of plasmonic nano particles [78] or the usage of ternary blend systems with functionalised hybrid materials like zinc phthalocyanine functionalised single walled carbon nanotubes and reduced graphene oxide [79].

1.2.2. Energy Storage Devices

A second important application of conducting polymers are energy storage systems. In contrast to the photovoltaic devices described above, where the photon energy is transformed into electric charges, the energy transformation in energy storage systems is between chemical energy and electric charges. Nowadays, the commercially used and most studied energy storage system is the family of lithium ion batteries. [7, 61] This type of battery has been presented by M. Whittingham [80] in 1976 and has been commercialised by *SONY* in the

1990s. Due to their high energy density, the lithium ion battery is the energy storage system of choice for the application in mobile electronic devices like mobile phones and laptops. However, these batteries also possess some significant drawbacks which limit their usage in novel devices like smart clothing, smart packaging and sensors. The main requirements to be matched by new battery systems are flexibility, avoiding of toxic materials, a high abundance of the raw materials, usability of renewable natural resources, fast charging times and the cost-efficient production. [7, 61] Even if some examples of flexible lithium ion battery devices have been published, due to the complex treatment required to transform the electrode material to nanomaterials, these devices are not ready to be commercialised yet. [81] In addition, lithium ion batteries rely on toxic cobalt or nickel salts as cathode material and need elaborate overcharge protection to avoid thermal runaway. [7]

One promising approach is to replace lithium ion batteries by organic batteries whose electrode materials consist of redox active polymers. [64] Due to the intensive research effort that has been spent in the field of conducting polymers, numerous redox active polymers have been reported in literature in the last 25 years and are available through known synthesis routes. The advantages of these polymer materials is, that the redox properties can be adjusted by the molecular design and the introduction of functional groups which allows for fine tuning of the cell potential of the battery system. In addition the flexibility and solubility of these polymer materials allow for the large-scale production by means of cheap and simple techniques like roll-to-roll or inkjet printing. Moreover, even if the monomer synthesis is mainly based on fossil crude material, sustainable procurement of the monomer materials from renewable sources may be possible in future. [7, 61]

The first polymer batteries have been based on π-conjugated polymers like polypyrrole and polyaniline and have been commercialised by *VARTA* and *BASF* in the late 1980s. [62] Due to bad charging/ discharging behaviour and fluctuations of the cell potentials caused by the delocalisation of the charges along the π-conjugation which results in dependency of the cell potential on the degree of doping, the production has been stopped soon though. In 2002 Nakahara et al. [82] introduced an organic battery based on redox polymers. These polymers consist of either redox groups attached onto non-conjugated backbones or of conjugated backbones with localised charged states. These materials combine the advantages of polymeric materials with the presence of distinct, degree of doping independent redox potentials

which results in constant cell potentials and improved charging/ discharging properties. [7] In case of the battery system presented by Nakahara et al. the electrode material consists of a polymethacrylate backbone grafted with TEMPO redox groups. [82]

The basic set-up of all types of electrochemical energy storage systems is similar. The three main components are the electrolyte, the anode and the cathode. In some battery cells an additional membrane is inserted to act as a separator between the two electrodes. The electrolyte is responsible for the ion exchange and to counter balance charges at either electrodes. Therefore a high ion conductivity of the electrolyte is essential. To avoid internal short cuts, the electric conductivity of the electrolyte should be as low as possible though. Commonly the classification of the electrodes is defined by the discharging redox processes. Thus, the negatively and positively polarised electrodes are referred to as anode and cathode respectively. In addition, battery cells are differentiated into primary (single use) and secondary (rechargeable) cells depending on the reversibility of the redox processes. [7] For this thesis the focus is set on secondary cells only.

For the general description of the basic operating principle of battery cells, the redox processes in a common lithium ion cell are discussed before the polymer battery configuration is introduced.

In Fig. 1.5 **a** the discharging processes in a lithium ion battery are shown. The anode consists of graphene layers with intercalated lithium atoms. Upon the discharging of the cell, the lithium atoms are oxidised to Li^+ ions and migrate through the electrolyte to the cathode. The electrons are dissipated towards the cathode by the external electric circuit. The cathode consists of a lithium-ion-containing material like $Li_{1-x}CoO_2{}^{x-}$. During the discharging of the cell the cathode material is reduced by the electrons from the electric circuit to form $LiCoO_2$. Upon the re-charging of the cell, shown in Fig. 1.5 **b** all ion transport and redox processes take place in the opposite direction. The reason for the intercalation of the lithium atoms in-between the graphene layers of the anode material is the immobilisation and separation of the lithium atoms which inhibits the formation of metal dendrites upon the re-charging of the cell. For lithium ion batteries, the intercalation and expulsion processes during the charging/ discharging cycles cause mutation of the crystal lattices and the graphene layers which results in slow kinetics and high heat built-up. The slow ion diffusion during the Li^+ intercalation is also the limiting factor of the lithium ion battery performance. [7]

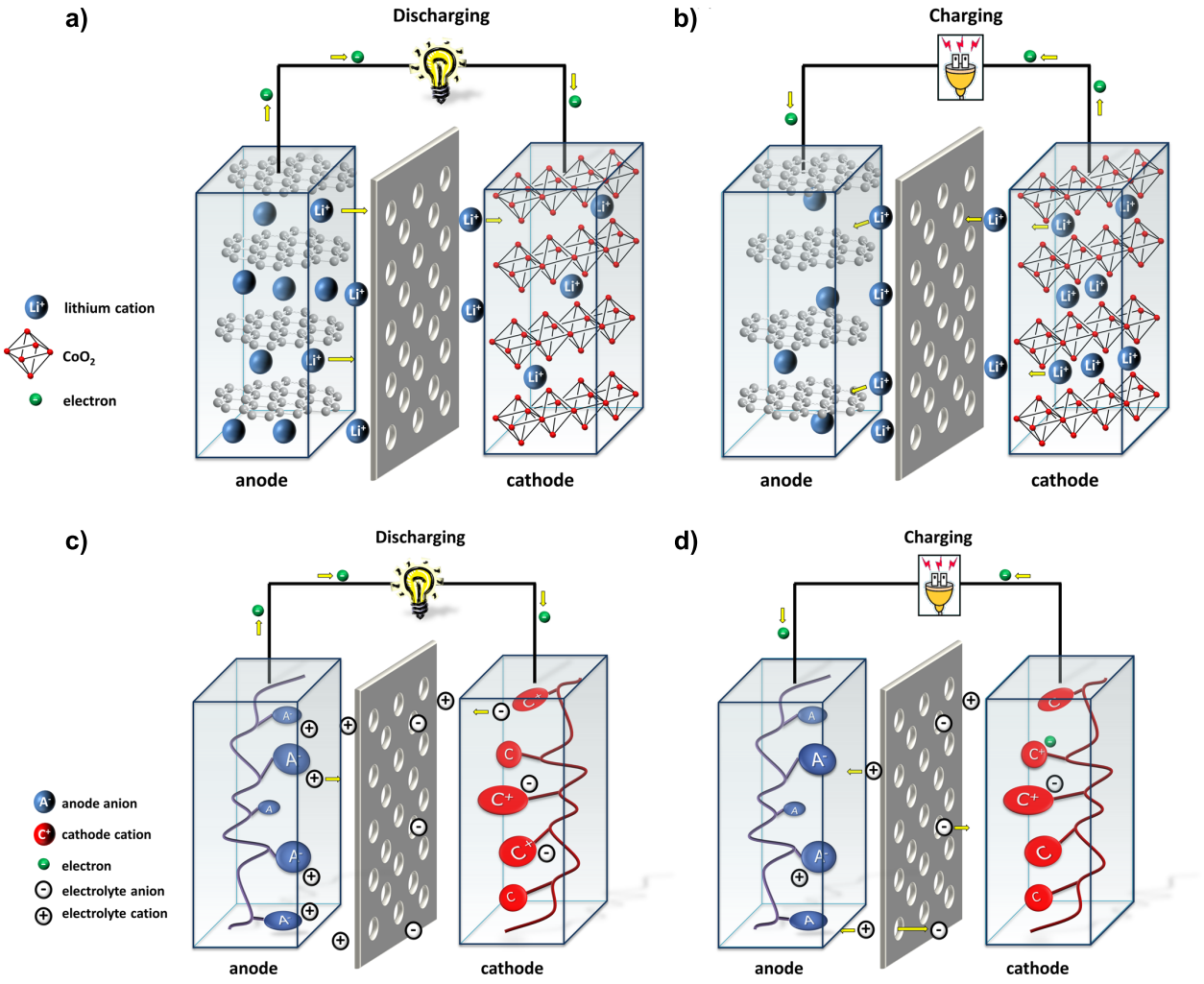

Figure 1.5: Schematic illustration of the redox processes during charging and discharging of a lithium ion (**a** and **b**) and an all-organic polymer (**c** and **d**) battery. Reprinted with permission from Muench et al. [7], Copyright (2016) ACS.

In organic batteries the anode and cathode materials consist of an *n*-type and a *p-type* conductor respectively. The polymers are usually processed in their neutral form which means that organic batteries have to be charged initially. Fig. 1.5 **d** shows the charging process in which the cathode material is oxidised and the anode material is reduced by applying an external current flow. The charges are immobilised in the respective polymer matrices at each electrode and are counter balanced by the intercalation of the counter ions from the electrolyte. This charging process is limited by the complete oxidation/ reduction of the cathode/ anode material or the complete consumption of the conducting salt ions respectively. To optimise the cell performance, the theoretical charge density of both electrodes

should be equal. Upon the discharging of the organic battery cell, shown in Fig. 1.5 **c**, electrons are dissipated from the anode to the cathode via the external electric circuit. Both polymers are transferred into their respective neutral form and the counter ions are expelled from the polymer matrices to the electrolyte. In case of the organic batteries the limiting factor is the migration of the counter ions of the conducting salt and the electron transfer kinetics of the polymer redox reactions. For this reason, electrolytes with high conducting salt concentrations are used to ensure good availability of ions. Since the charge storage in organic batteries occurs via fast and simple redox reactions without significant structural alteration of the electrode materials, the rate performance and cycle life are superior to common lithium ion batteries. [7]

2. Objectives

The aim of this thesis is the electrochemical characterisation of electro-active π-conjugated and redox polymers to gain deeper insights into the basic redox processes and to evaluate possible applications of these organic semi-conductors in organic electronic devices.

Poly(3-hexylthiophene)

Poly(3-hexylthiophene) (P3HT) is one of the most commonly used donor materials in organic optoelectronic devices. Due to its semi-crystalline nature, the thin film morphology of P3HT possesses an important influence on the device characteristics. Therefore the thin film morphology of P3HT and its influence on physicochemical properties like the charge carrier mobility [19, 83] and optical properties [2] have been studied intensively in the last 25 years. Especially the absorption behaviour of P3HT has gained huge scientific interest, since it shows a significant morphology dependency by undergoing a bathochromic shift upon aggregation which causes also a shift in the optical bandgap. [84]

A similar dependency of the bandgap on the P3HT thin film morphology is expected for the electrochemical bandgap. The electrochemical determination of the bandgap by means of solid state cyclic voltammetry is a powerful tool, since it not only provides the effective bandgap but also the individual frontier orbital energy levels. The influence of the film morphology on the electrochemical redox behaviour is only sparsely reported on in literature. For the oxidation of P3HT, broad current signals which consist of superimposing subsignals are commonly described in literature. It has also been shown that the regioregularity of the P3HT batch influences the number of the superimposing subsignals which also results in a shift of the oxidation potential and therefore of the HOMO energy level. The origin of the superimposing subsignals is usually attributed to the coexistence of domains of different conjugation lengths in the P3HT films. However, no direct correlation of electrochemical redox waves to the inner structure of the P3HT films could be made, since the film morphologies in these studies were uncontrolled and numerous polymer batches with varying regioregularities but also different molecular weights and molecular weight distributions were used.

In this thesis, a systematic characterisation of the morphological influence on the electrochemical redox behaviour of P3HT is performed by using different deposition and post-

treatment methods like crystallisation from solution, solvent vapour annealing and high temperature rubbing, to prepare thin films of varying textures and degrees of crystallinity of the same P3HT batch. Since P3HT is usually used as a donor material in binary donor acceptor blend systems, not only the morphological influence on the redox behaviour of neat P3HT films but also of P3HT:$PC_{61}BM$ donor acceptor blend films is studied.

Polyvinyltriphenylamine

Molecules containing the triphenylamine (TPA) redox group have gained huge scientific interest for the application in various organic electronic devices due to their optical, electrochemical and electronic properties. [85] In recent years the focus shifted from small molecules towards polymers containing the triphenylamine redox group. [23] The main advantage of TPA-containing polymers compared to their small molecular relatives, is an increased organic film stability due to inter- and intra-chain cross-linking of the polymers induced by either chemical or electrochemical oxidation. The cross-linking density herein can be tuned by the synthesis.

The aim of this work is to perform a systematic characterisation of the optical, electrochemical and electronic properties of the polyvinyltriphenylamine (PVTPA) polymer and to study the influence of the cross-linking density. Therefore, polyvinyltriphenylamine-polystyrene (PVTPA-*co*-PS) copolymers are studied. Styrene as the second monomer has been chosen since it is chemically closely related to vinyltriphenylamine, which is favourable to ensure successful random copolymerisation, but redox inactive. The main objectives are to study the influence of the PVTPA-to-PS repeating unit ratio on the successful cross-linking reaction of the redox groups and the charging/ discharging behaviour in the cross-linked films, which involves swelling and shrinking of the polymer films due to the counter ion intercalation/ expulsion with accompanied solvent uptake/ release.

In addition to the basic electrochemical characterisation, the general usability of PVTPA and PVTPA-*co*-PS for the application in organic electronic devices as energy storage material and as novel electrode material are studied.

In general, triarylamine derivatives are state-of-the-art electrode materials in organic energy storage systems. [86] As a first test towards the application in real battery devices, the charge storage properties of PVTPA and PVTPA-*co*-PS copolymers are characterised by means

of so-called *supercapacitor* devices, since they require neither elaborate device preparation techniques nor the usage of a fitting *n*-type conducting counter electrode material.
As a second possible application in organic electronic devices, PVTPA and PVTPA-*co*-PS are interesting materials as novel transparent electrode coatings, since they can be solution processed before oxidative cross-linking is induced which results in stable polymer films in their conductive state. Therefore, in addition to the electrochemical doping, also the chemical doping of PVTPA and PVTPA-*co*-PS with different oxidative dopants in either solution and gas phase is studied. The aim is to optimise the doping parameters to gain polymer films of maximum conductivity.

3. Experimental Part

Parts of the experimental work on the electrochemical characterisation and chemical doping of the PVTPA-*co*-PS copolymers have been contributed by *Felix Goerigk* and *Lukas Stein* within the scope of their research internships and by *Fabian Moczko* and *Lisa Eisele* within the scope of their bachelor theses, respectively. The synthesis of the PVTPA-*co*-PS copolymers has been performed by *Corinne Rost-Schmidt*.

3.1. Materials

3.1.1. Polymers

The molecular structures of the polymers used in this thesis are shown in Fig. 3.1. Poly(3-hexylthiophene) (P3HT) (**1** in Fig. 3.1) batch *EF430802* (M_w = 112 kg mol^{-1}, PDI = 2.4, regioregularity 95 %) was purchased from *Merck* and was used without further purification. Polyvinyltriphenylamine-*co*-Polystyrene (PVTPA-*co*-PS) copolymers (**2** in Fig. 3.1) with varying repeating unit ratios have been synthesised by *Corinne Rost-Schmidt* via free radical polymerisation. For the synthesis details see chapter A.3. Poly(3,4-ethylenedioxythiophene)-poly(styrenesulfonate) (PEDOT:PSS) (**3** in Fig. 3.1) was purchased from *Sigma Aldrich* as a 1.1 wt% suspension in water and was homogenised by ultra sonification prior to the film deposition.

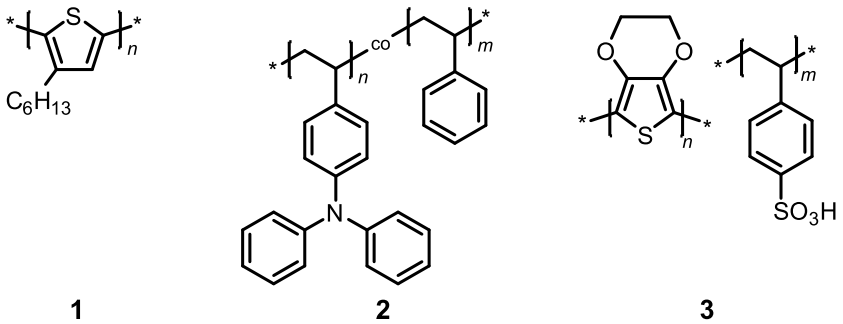

Figure 3.1: Molecular structures of poly(3-hexylthiophene) [P3HT] (**1**), polyvinyltriphenylamine-*co*-polystyrene [PVTPA-*co*-PS] (**2**) and poly(3,4-ethylenedioxythiophene)-poly(styrenesulfonate) [PEDOT:PSS] (**3**).

3.1.2. Chemicals

Table 3.1: Overview of the used solvents.

solvent	grade	distributor	abbreviation
acetone	p.a., $\geq$ 99.5 %	Sigma Aldrich	
acetonitrile	anhydrous, $\geq$ 99.8 %	Sigma Aldrich	MeCN
anisole	anhydrous, $\geq$ 99.7 %	Sigma Aldrich	
carbon disulfide	anhydrous, $\geq$ 99.9 %	Sigma Aldrich	CS_2
chlorobenzene	anhydrous, 99.8 %	Sigma Aldrich	CB
chloroform	anhydrous, $\geq$ 99 %	Sigma Aldrich	$CHCl_3$
1,2-dichlorobenzene	anhydrous. 99 %	Sigma Aldrich	*o*-DCB
dichloromehtane	anhydrous, $\geq$ 99.8 %	Sigma Aldrich	DCM
isopropanol	p.a., 99.8 %	Sigma Aldrich	
tetrahydrofuran	HPLC grade	*MBraun SPS-800* drying system	THF
toluene	anhydrous, 99.8 %	Sigma Aldrich	
water	demineralised	internal supply line	H_2O

The solvents, conducting salts and other chemicals used in this thesis are listed in tables 3.1 and 3.2.

For the preparation of polymer solutions the used solvents were stored in a nitrogen filled glove box. Solvents used for the preparation of organic electrolytes (MeCN, THF and DCM) have been dried by filtering through a column of activated AlO_x and degassed by freeze-pump-thaw cycling or argon purging (bubbling of argon through the solvent for at least 30 min) prior to the electrochemical experiments. All conducting salts were stored under vacuum in a desiccator to avoid the uptake of moisture.

[6,6]-phenyl C61 butyric acid methyl ester ($PC_{61}BM$), Iron(III) chloride ($FeCl_3$), Iron(III) *p*-toluenesulfonate hexahydrate ($Fe(Tos)_3$) and 3-hexylthiophene (3-HT) were used without further purification.

Table 3.2: Overview of the used conducting salts and other small molecules.

conducting salts	distributor	abbreviation
lithium bis(trifluoromethane)sulfonimide	Sigma Aldrich	Li-BTFSI
lithium perchlorate	Sigma Aldrich	$LiClO_4$
potassium hexafluorophosphate	Sigma Aldrich	KPF_6
tetrabutylammonium hexafluorophosphate	Sigma Aldrich	NBu_4PF_6
tetrabutylammonium tetrafluoroborate	Sigma Aldrich	NBu_4BF_4
tetrahexylammonium hexafluorophosphate	Sigma Aldrich	$NHex_4PF_6$
other chemicals	distributor	abbreviation
3-hexylthiophene	Sigma Aldrich	3-HT
iron(III) chloride	Sigma Aldrich	$FeCl_3$
iron(III) *p*-toluenesulfonate hexahydrate	Sigma Aldrich	$Fe(Tos)_3$
[6, 6]-phenyl C61 butyric acid methyl ester	Sigma Aldrich	$PC_{61}BM$

3.1.3. Substrates

The gold electrodes for the electrochemical experiments in solid state were prepared by evaporation deposition using a *UNIVEX 350 G* setup from *Oerlikon Leybold Vacuum*. Glass slides from *Glasbearbeitung Henneberg & Co.* were first coated with a 5 nm thick chromium layer to ensure good adhesion of the subsequent 50 nm thick gold layer. These substrates were also used for the preparation of P3HT spherulites by means of solvent vapour annealing in CS_2. For the *in-situ* spectroelectrochemical measurements indium tin oxide (ITO) substrates from *PGO Präzisions Glas & Optik GmbH* with a low specific surface resistance ($R \leq 20\,\Omega\,sq^{-1}$) were used. The glass substrates from *Glasbearbeitung Henneberg & Co.* without further modification were also used for absorption spectroscopy of polymer films in transmission and for the chemical doping of PVTPA-*co*-PS films.

3.2. Sample Preparation

3.2.1. Preparation of Polymer Solutions

The polymer solutions for film deposition by spin coating were prepared in a nitrogen filled glove-box. P3HT was dissolved in chloroform, toluene or *o*-dichlorobenzene while solutions of PVTPA-*co*-PS were prepared in toluene or chloroform. The polymer solutions in chloroform, toluene and *o*-dichlorobenzene were stirred at least over night at 40 °C, 100 °C and 80 °C respectively. For the preparation of P3HT spherulites by means of solvent vapour annealing the solution in toluene was stirred at 100 °C and filtered hot through a 0.2 µm PTFE (polytetrafluoroethylene) syringe filter. The P3HT:fullerene blend solutions were prepared by intermixing of the respective polymer and fullerene stock solutions. PEDOT:PSS was purchased as an aqueous suspension which was homogenised by ultrasonification prior to the film deposition.

3.2.2. Substrate Cleaning

The substrates were cut prior to the cleaning process in pieces of 1 cm *x* 1 cm (glass substrates for the chemical doping and absorption spectroscopy), 1 cm *x* 1.5 cm (Au electrodes) or 0.8 cm *x* 1.5 cm (ITO electrodes) respectively. As a first cleaning step the substrates were ultra sonificated in *i*-propanol, demineralised water and acetone (10 min each). Afterwards the substrates were dried by using an argon airbrush. Afterwards the ITO and glass substrates were treated in an oxygen plasma chamber from *Diener electronic* for 10 min while the Au electrodes were cleaned mechanically by using a *snow jet*. In this surface cleaning technique the substrate is mounted to a heat plate and the temperature is set to 220 °C. By scanning the substrate surface with a narrow stream of dry ice from a CO_2 high pressure vessel, impurities are removed mechanically due to the sublimation of the dry ice stream.

3.2.3. Film Deposition Techniques

Drop Casting

Drop casting is the simplest film preparation method since the polymer solution is just dropped onto the substrate and left to dry. In general drop casting does not allow for a precise control of the film thickness and leads to inhomogeneous films which hampers

the reproducibility of the experiments. Therefore film preparation by drop casting is only favourable for experiments in which precise control of the polymer film mass is crucial and the film morphology is neglectable. In this thesis drop casting was used for the preparation of polymer supercapacitors (exact mass of the polymer needed to calculate the charge storage capacity) and as a comparison for P3HT samples of controlled morphologies. Drop casting from chloroform solution was performed at room temperature and the polymer covered substrates were afterwards placed in a constant air stream to improve the drying.

Spin Coating

The method of spin coating is commonly used to deposit polymer films of controlled thickness and morphology. In this deposition technique the substrate is mounted to a rotating stage. During the evaporation of the solvent the generated polymer film shrinks until it reaches its equilibrium thickness. The film thickness can be tuned by the choice of the solvent, the concentration and the rotation velocity. In general, spin coating is the favoured deposition method since it leads to homogeneous polymer films but due to the centrifugal force excess of the polymer solution is floated off the substrate and therefore wasted. In this thesis, polymer films were prepared by spin coating unless otherwise stated. The spin coating was usually performed in a nitrogen filled glove-box with a *Delta 6RC* spin coater from *Suess MicroTec*. For the spin coating of aqueous solutions a *WS-400-6NPP-LITE* from *Laurell Technologies* was used. Typical spin coating parameters for P3HT and PVTPA-*co*-PS solutions in various solvents are summarised in Table 3.3.

Blade Coating

Blade coating is a useful and material-saving deposition method for the preparation of large-area films. In this technique the substrate is mounted to a heatable stage with a movable blade hovering above the substrate surface. The distance between substrate and blade and the movement speed of the blade are adjustable. The polymer solution is applied at the substrate-blade gap and by moving the blade across the substrate the polymer solution is spread to form a homogeneous film. The evaporation of the solvent can be improved by an increase of the substrate temperature. The thickness of the polymer film can be tuned by the concentration and the blade-substrate distance. In this thesis blade coating was used for the

Table 3.3: Typical spin coating parameters for the film preparation of various substances from different solvents.

substance	solvent	concentration	revolutions per minute	duration [s]
P3HT [a]	$CHCl_3$	$5\,mg\,mL^{-1}$	2 000	30
P3HT	anisole:$CHCl_3$	0.05 wt%	2 000	300
P3HT	toluene	$6\,mg\,mL^{-1}$	4 000	50
$PC_{61}BM$ [a]	$CHCl_3$	$5\,mg\,mL^{-1}$	2 000	30
P3HT:$PC_{61}BM$ [a]	$CHCl_3$	$5\,mg\,mL^{-1}$	2 000	30
PVTPA-*co*-PS	$CHCl_3$	$5\,mg\,mL^{-1}$	2 000	180
PVTPA-*co*-PS [a]	toluene	$5\,mg\,mL^{-1}$	2 000	90
PEDOT:PSS	H_2O	1.1 wt%	1 000	300

[a] an additional rotation step with 6000 rpm for 15 s was applied afterwards to ensure complete drying of the film.

preparation of P3HT films for high temperature rubbing. The P3HT films were deposited from *o*-dichlorobenzene solution ($5\,mg\,mL^{-1}$). During the blade coating process the substrate temperature was kept at 170 °C to improve the solvent evaporation. The sample preparation was performed under ambient conditions on a custom-made set-up at the *Institut Charles Sadron* in Strasbourg.

3.2.4. Crystallisation in Solution

Crystallisation of P3HT nano wires was performed according to Ihn et al. [87] The polymer is dissolved in a mixture of a good and a bad solvent in the heat. Upon controlled cooling of the solution P3HT starts to precipitate in fibre-like structures. X-ray and electron diffraction characterisation by Ihn et al. revealed crystallisation of the P3HT chains in the so-called *edge-on* texture with strong π-π stacking along the fibre axis. [87] In this work P3HT was dissolved in anisole/$CHCl_3$ (4:1 by volume) at 70 °C for 72 h and afterwards cooled down to room temperature (20 °C) with a cooling rate of $25\,K\,h^{-1}$. The deposition of the P3HT nano wires was performed by spin coating (2000 rpm for 300 s).

3.2.5. Solvent Vapour Annealing

Solvent vapour annealing is a versatile tool for the preparation of polymer thin films of controlled morphologies. In literature, this method has been used to create spherulitic poly(3-alkylthiophene) films with highly ordered crystalline lamellar in the *edge-on* texture [2] or to induce micro-phase separation in block-copolymer templates [88, 89]. In this work solvent vapour annealing was used as a post treatment method to prepare spherulitic P3HT samples. The sample preparation procedure is based on previous work by *Dr. Edward Crossland* who studied the influence of the recrystallisation conditions on the nucleation density of the P3HT spherulites to further study the 3-dimensional anisotropy of the charge transport. [83, 84]

The initial polymer film was spin coated from toluene solution ($6\,\mathrm{mg\,mL^{-1}}$) onto ITO or gold substrates (4000 rpm for 50 s). Prior to the spin coating the solution was stirred at 100 °C for 4 h and filtrated hot through a PTFE syringe filter (0.2 µm). The edges of the substrates were cleaned by using a chloroform soaked cotton-wool tip to remove the inhomogeneous margins of the polymer films and the samples were kept under vacuum in a desiccator over night. Solvent vapour annealing in CS_2 was performed in a custom-made annealing chamber described in Ref. [90] and [91]. In brief, the polymer film is exposed to a gas stream of controlled temperature and solvent vapour pressure. The sample temperature is kept slightly below the temperature of the surrounding atmosphere to ensure condensation of the solvent vapour into the polymer film. Upon increasing partial pressure of the solvent vapour the polymer film swells. As soon as a solution-like state of the polymer film is reached, the

Table 3.4: CS_2 vapour annealing procedure for the preparation of spherulitic P3HT (batch *EF430802* from *Merck*) samples.

action	duration [min]	CS_2 partial pressure	comment
↗	2	91.5 %	
—	5	91.5 %	swelling
↘	0.1	86 %	
—	20	86 %	recrystallisation
↘	1	0 %	drying

solvent partial pressure is decreased and held constant so that the polymer chains have time to recrystallise. In this work, the temperatures of the gas stream and the substrate were kept at 22 °C and 19 °C respectively. The overall volume stream was set to 20 sccm and a typical annealing procedure for P3HT (batch *EF430802* from *Merck*) is given in Table 3.4.

3.2.6. High Temperature Rubbing

High temperature rubbing is a post annealing method to induce large-area orientation of organic molecules. In contrast to other deposition or post annealing methods, high temperature rubbing of P3HT results in the so-called *face-on* texture in which the π-π stacking direction is perpendicular to the substrate surface. Hamidi-Sakr et al. studied the influence of the rubbing temperature on the film morphology of P3HT and observed that the grade of alignment, which can be characterised by the dichroic ratio from the polarised absorption spectra in parallel and in perpendicular to the rubbing direction, increases with increasing rubbing temperature. In addition the authors showed that the exciton bandwidth, which can be used as a measure for the degree of crystallinity in the polymer film, decreases (indicating increasing crystallinity) with increasing rubbing temperature. [92]
Fig. 3.2 shows a schematic illustration of the rubbing set-up. The substrate with the polymer

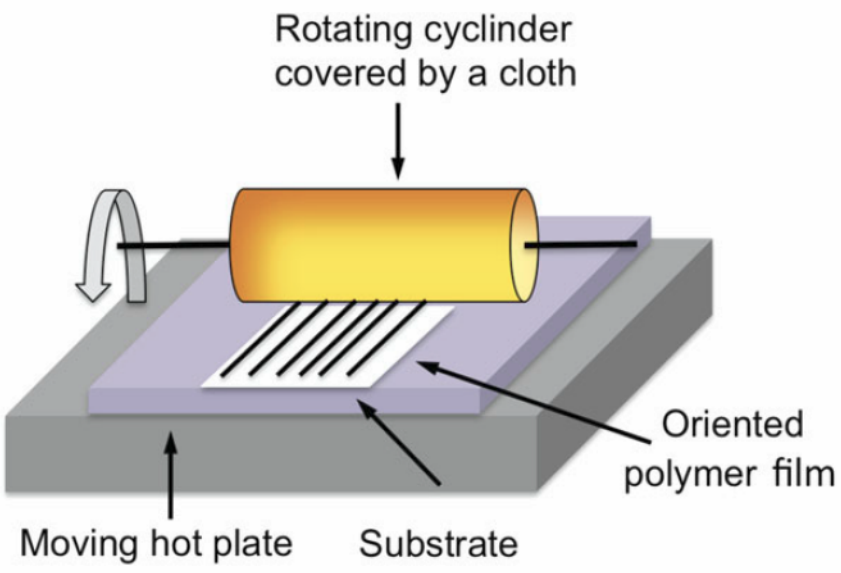

Figure 3.2: Schematic illustration of the high temperature rubbing setup; image reprinted with permission from Brinkmann et al. [93], Copyright (2014) Wiley

film is mounted to a movable hot stage. During the rubbing process a rotating cylinder of tunable rotation speed is pressed onto the polymer film which is moved lateral. The rotating cylinder is covered in a micro-fibre cloth. Due to the shear force caused by the rotation of the cylinder and lateral movement of the substrate the polymer chains align along the rubbing direction. The quality of the alignment is dependent on the sample temperature. [92]
For this work, film deposition was performed by blade coating from a *o*-DCB solution ($5\,\mathrm{mg\,mL^{-1}}$) onto ITO substrates at 170 °C. The high temperature rubbing was performed in a nitrogen filled glove-box with a custom-made set-up at the *Institut Charles Sadron* in Strasbourg. During the rubbing process the substrate temperature was kept at 230 °C and the rotating cylinder (approximately 350 rpm) was covered with a micro-fibre cloth (polyester 85 %, polyamide 15 %). The rubbing process was performed as one single rubbing cycle.

3.2.7. Supercapacitors

The polymer film deposition for the supercapacitor samples was performed by drop casting from aqueous solution (PEDOT:PSS, 1.1 wt%) or chloroform solution (PVTPA-*co*-PS, $10\,\mathrm{mg\,mL^{-1}}$) respectively, since the exact mass of the polymer film is needed for the calculation of the specific capacitance, specific energy and specific power. The devices were built in a symmetric geometry and characterised in a custom-made glass cell by means of electrochemical impedance spectroscopy (EIS), cyclic voltammetry (CV) and galvanostatic charging/discharging cycles (GCD). In case of the PVTPA-*co*-PS samples the oxidative cross coupling reaction was performed in a separate voltammetry cell beforehand.

3.2.8. Chemical Doping

Chemical doping of the PVTPA-*co*-PS copolymers with iron(III) chloride ($FeCl_3$) and iron(III) *p*-toluenesulfonate ($Fe(Tos)_3$) as oxidants was performed by dip-doping and by vapour-doping. The PVTPA-*co*-PS films were spin coated from chloroform solutions ($5\,\mathrm{mg\,mL^{-1}}$) onto square-shaped glass substrates. The spin coating parameters are listed in Table 3.3. Glass substrates were chosen since the characterisation of the chemically doped polymer films was carried out by absorption spectroscopy and four-point-probe (4pp). Therefore a transparent, non-conducting substrate is required. Before the chemical doping was carried out the film thickness was measured by atomic force microscopy. The absorption spectra of

Table 3.5: Characteristic parameter for the characterisation of PEDOT:PSS and PVTPA-*co*-PS copolymers supercapacitors.

parameter	PEDOT:PSS	PVTPA-*co*-PS copolymers
solvent	H_2O	$CHCl_3$
concentration	1.1 wt%	$10\,mg\,mL^{-1}$
electrolyte	0.1 M $LiClO_4/H_2O$	0.1 M LiBTFSI/MeCN
EIS	1 V; 100 kHz - 5 mHz	0.5 V; 100 kHz - 5 mHz
CV [a]	$10\,mV\,s^{-1}$ - $100\,mV\,s^{-1}$	$10\,mV\,s^{-1}$ - $100\,mV\,s^{-1}$
GCD [b]	100 µA/−100 µA	1 µA/−1 µA

[a] measured with scan rate steps of $10\,mV\,s^{-1}$ and one cycle for each scan rate.
[b] each measurement was performed with cuttoff potentials of 0 V and 1 V.

the initial polymer films were recorded directly before the doping process and immediately after drying of the doped polymer films the spectra and 4pp were measured to avoid uptake of moisture by the hygroscopic dopants.

Dip-Doping

Dip-doping is a simple chemical doping method in which the polymer covered glass substrate is dipped into a solution of the dopant in an orthogonal solvent with respect to the polymer solubility. Afterwards the sample is cleaned from dopant excess and dried. In this work $FeCl_3$ and $Fe(Tos)_3$ solutions in MeCN with concentrations in the range of $0.5\,mg\,mL^{-1}$ up to $10\,mg\,mL^{-1}$ and doping durations of 5 min to 30 min were used. After the dip-doping process the samples were washed with pure MeCN to remove excess of the dopant and dried in an argon stream.

Vapour-Doping

Vapour-doping of PVTPA-*co*-PS films with $FeCl_3$ was carried out in a custom-made *in-situ* spectroscopy-vacuum cell adapted from Yamamoto et al. [94]. A schematic illustration of the set-up is shown in Fig. 3.3. The vacuum cell consists of a glass tube with two dismountable quartz glass windows and an attached reservoir for the solid dopant. The polymer solution ($10\,mg\,mL^{-1}$ in chloroform) is spin coated onto one of the quartz glass windows in a way that

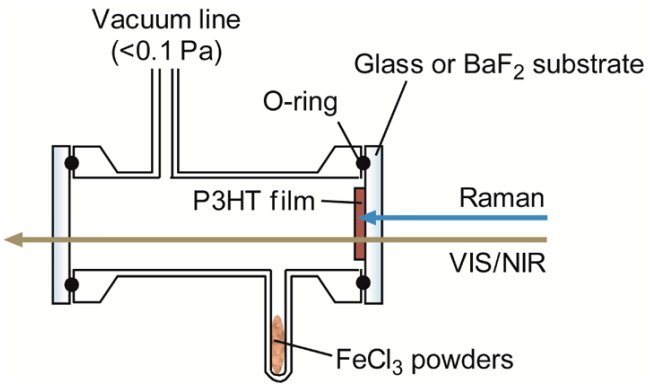

Figure 3.3: Schematic illustration of the vapour doping setup; image reprinted with permission from Yamamoto et al. [94], Copyright (2015) ACS Publications.

the light path of the spectrometer traverses both quartz windows but not any other glass part of the cell or the dopant reservoir. The sealed doping cell is set under high vacuum and when a constant pressure of 10^{-3} mbar is reached the valve to the vacuum pump is closed to avoid constant draining of the dopant vapour.

3.3. Methods

3.3.1. Cyclic Voltammetry

Cyclic voltammetry is a powerful tool to study the electron transfer processes in redox reactions. [95–100] During the voltammetric scan an external field is applied between the working and counter electrodes and simultaneously monitored between the working and reference electrode. The electric circuit is completed through the ionic conductance in the electrolyte. Due to internal resistance of the electrolyte, the applied field has to be modulated by the potentiostat until the measured potential in the cell equals the potential set by the programmed procedure. The time depending applied potential in a typical voltammetric scan is shown in Fig. 3.4 **b**. Originating from the starting potential (E_{start}) the applied potential is linearly increased/ decreased (anodic/ cathodic scan) with a defined scan rate (v) until the turning potential (E_λ) is reached. Afterwards the potential is decreased/ increased with the same scan rate until the stop potential (E_{stop}) is reached. In a complete voltammetric cycle the starting and stop potential are identical. For an electrochemically reversible one-electron transfer the resulting potential dependent current is shown in Fig. 3.4 **c**. The

voltammogram reveals a redox half wave in each the forward (oxidative) and backward (reductive) scan. From the peak potentials of the oxidation and reduction half wave (E_{pa} and E_{pc}) the half wave potential ($E_{1/2}$) can be calculated according to Eq. 3. For a reversible, diffusion controlled electron transfer process the half wave potential can be calculated by the *Nernst equation* and is used as a good approximation for the formal potential (E_0) of the redox process:

$$E_{1/2} = \frac{|E_{\mathrm{pa}} + E_{\mathrm{pc}}|}{2} \approx E^0 + \left(\frac{RT}{nF}\right) \ln \left(\frac{D_{\mathrm{red}}}{D_{\mathrm{ox}}}\right)^{1/2} \tag{3}$$

with the diffusion coefficients of the reduced and oxidised species (D_{red} and D_{ox}), the gas constant (R), the absolute temperature (T), the faraday constant (F) and the stoichiometric number of electrons involved in the redox reaction (n).

In case of polydisperse materials a redox half wave is the superposition of the overlapping redox waves of every individual redox process of each redox site (depending on the molecular weight, the planarisation of the polymer chains and the order of the electron transfer process). Therefore the CV signals in polymers are usually broad and can exhibit several local current maxima. As a result, it is usually not possible to determine the half wave potential of a redox process in a polymer. The only characteristic parameter which can be extracted is the so-called onset potential which represents the potential at which the electron transfer reaction starts initially. The onset potential is determined by the intersection of two tangents on the current base line and the redox half wave. From the oxidation and reduction onset potentials the HOMO and LUMO frontier orbital energy levels can be calculated according to Eq. 4 and 5 respectively:

$$E_{\mathrm{HOMO}} = -({E_{\mathrm{onset}}}^{\mathrm{ox}} + 5.1)\ [eV] \tag{4}$$

$$E_{\mathrm{LUMO}} = -({E_{\mathrm{onset}}}^{\mathrm{red}} + 5.1)\ [eV] \tag{5}$$

with 5.1 being a correction factor which corresponds to the energy of the ferrocen/ ferrocenium redox couple; used in this thesis as reference for measurements in organic electrolytes; in the Fermi scale. [101] The effective band gap (E_g) can be calculated from the HOMO and LUMO levels according to Eq. 6:

$$E_{\mathrm{g}} = |E_{\mathrm{HOMO}} - E_{\mathrm{LUMO}}| \tag{6}$$

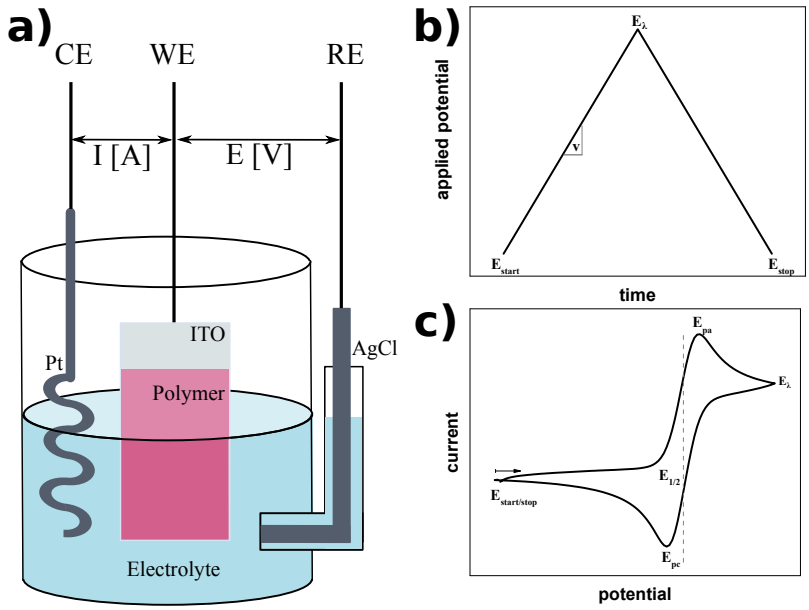

Figure 3.4: **a)** Schematic illustration of a three-electrode CV setup with the analyte deposited onto the working electrode; with a platinum spiral as counter electrode (CE), a Ag/AgCl pseudo reference electrode (RE) and a polymer covered ITO substrate as working electrode (WE); **b)** time dependent applied potential for one anodic voltammetric scan with the scan rate (v) and **c)** resulting potential dependent current for a one-electron redox reaction with the start potential (E_{start}), stop potential (E_{stop}), turning potential (E_{λ}), half wave potential ($E_{1/2}$) and anodic/cathodic peak potential (E_{pa}/E_{pc}).

The electrochemical measurements were performed with *PGSTAT101* and *PGSTAT204* potentiostats from *Metrohm* in custom-made three-electrode glass cells. As counter electrodes platinum spirals or plates were used. Since conventional reference electrodes are only defined for aqueous electrolytes, Ag/AgCl pseudo reference electrodes (RE); meaning silver wires coated with silver chloride; were used and the potentials were calibrated against the internal standard of the ferrocen/ferrocenium redox couple afterwards. As working electrodes (WE) either gold or ITO substrates were used for polymer film characterisation and for measurements in solution platinum or gold disk electrodes were used. The measurements were conducted under inert conditions under argon atmosphere and in pre-dried electrolytes.

3.3.2. *in-situ* Spectroelectrochemistry

In-situ spectroelectrochemistry is a versatile method for the characterisation of redox processes since it combines the electronic information derived from the electrochemical experiment with chemical information from the spectroscopy. Typical tasks are the determination of concentrations of redox species for example in sensors, the characterisation of reaction mechanisms and the identification of redox species and intermediates. [102, 103] In case of π-conjugated polymers like polythiophenes the formation of the charged species (radical cation and dication) results in a bathochromic shift. Since the characteristic absorption bands of all involved redox species (neutral, radical cation and dication) are in the UV-vis-NIR range, the transformation of the respective redox species can be easily studied by means of simple absorption spectroscopy. The measurement can be performed either in transmission or reflection. In Fig. 3.5 the schematic illustrations of a transmission cell (**a**) for polymer films and a reflection cell (**b**) for the characterisation of dissolved analytes are shown.

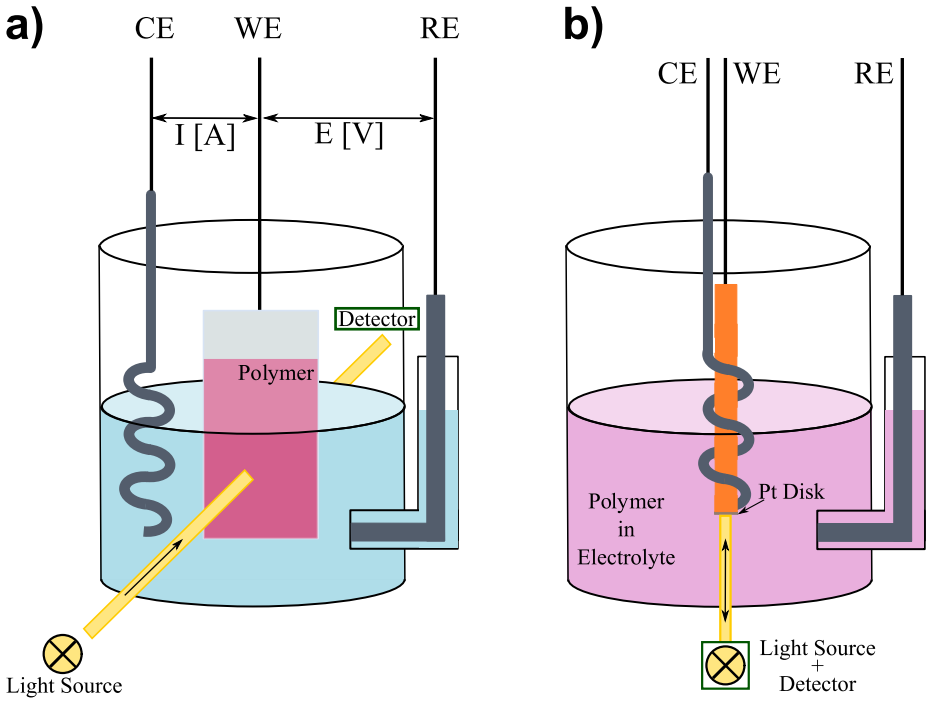

Figure 3.5: Schematic illustration of *in-situ* spectroelectrochemical cells for measurements in transmission (**a**) and in reflection (**b**) for polymer films or solutions respectively; with platinum spirals as counter electrodes (CE), Ag/AgCl pseudo reference electrodes (RE) and either ITO or a platinum disk as working electrode (WE).

The *in-situ* spectroelectrochemical experiments were conducted by using *PGSTAT101* or *PGSTAT204* potentiostats from *Metrohm* and a modular *MCS621 Vis III* spectrometer from *Zeiss* equipped with a *CLH 600 F* halogen lamp. The light path was directed through optic fibres from *Ocean Optics*. To decrease the background light intensity the *in-situ* experiments were performed in a closed optic box. The spectra of a ITO substrate or the polished platinum disk, which acts as a mirror, immersed into the respective electrolytes were used as reference spectra. Platinum spirals or plates were used as counter electrodes (CE) and silver chloride coated silver wires as pseudo reference electrodes (RE). The potentials were calibrated against the ferrocen/ferrocenium redox couple as internal standard. As working electrodes polymer coated ITO substrates for measurements in solid state or a platinum disk electrode for measurements in solution were used respectively. The measurements were performed under inert conditions (dried electrolyte solvents and argon atmosphere).

3.3.3. Electrochemical Quartz Crystal Microbalance

The electrochemical quartz crystal micro balance (EQCM) is a device for the *in-situ* monitoring of mass changes of a studied solid sample during an electrochemical charging/ discharging process. Therefore EQCM is a powerful tool for the characterisation of ion intercalation and expulsion during a voltammetric experiment. Due to the charging of the analysed material during the forward voltammetric scan the respective counter ions from the supporting electrolyte are intercalated into the sample to ensure electrostatic charge neutrality. Upon the discharging of the analyte in the backward scan of the voltammogram the previously intercalated counter ions are expelled from the sample. In case of trapping of the counter ions in confined samples like polymer films the electrostatic neutrality can be restored by additional intercalation processes of respective ions from the electrolyte which leads to complex multi-ion movement processes. In addition, the ion intercalation processes lead to an uptake of solvent due to the solvent shell surrounding the ions in the electrolyte.
The EQCM measurements are carried out in solid state with the analyte deposited onto a working electrode which consists of a quartz crystal covered with a gold layer. In Fig. 3.6 the schematic illustrations of an EQCM cell (**a**) and a typical EQCM working electrode (**b**) are shown. The working electrode is mounted horizontally in the cell with two sealing rings underneath and above to ensure a tight fit and to avoid leakage of the electrolyte which is

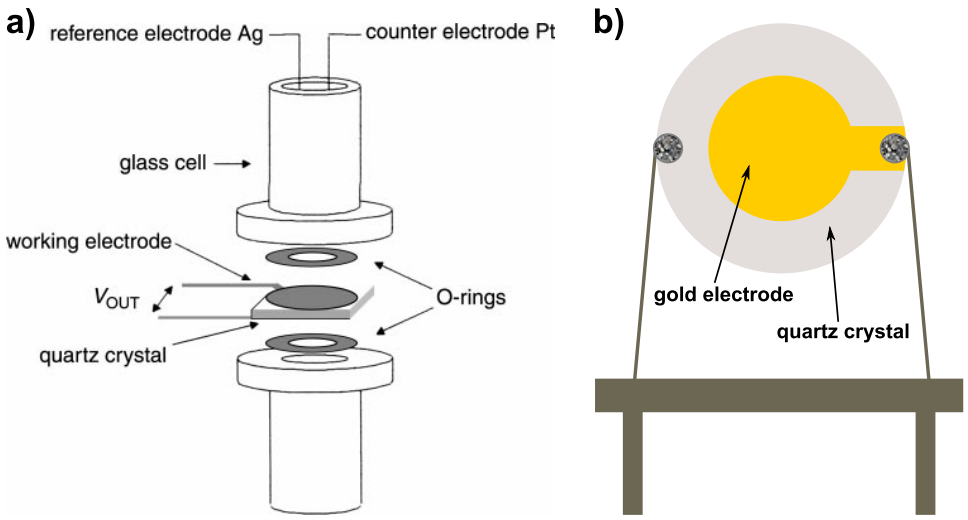

Figure 3.6: **a)** Schematic illustration of an EQCM setup (image reprinted with permission from Soavi et al. [104], Copyright (2000) Royal Society of Chemistry); **b)** schematic illustration of a gold covered quartz crystal.

only filled in the top part of the cell. The counter and reference electrodes are immersed into the electrolyte filled upper compartment.

During the electrochemical experiment the quartz crystal is set into oscillation by applying an alternating electric field, which results in a transverse shear wave in the quartz substrate. The mass-dependency of the frequency is described by the *Sauerbrey equation* (Eg. 7):

$$\Delta f = -\frac{2{f_0}^2}{A\sqrt{\rho_\mathrm{q}\mu_\mathrm{q}}} \cdot \Delta m \tag{7}$$

with Δf and Δm being the frequency and mass changes respectively. The other parameters of the *Sauerbrey equation* are the resonant frequency of the quartz crystal (f_0), the active area (A), the density of quartz (ρ_q) and the shear modulus of quartz (μ_q). The latter parameters are usually cumulated to the so-called sensitivity coefficient of the quartz crystal (C_f) to simplify the *Sauerbrey equation* to Eq. 8: [104–106]

$$-\Delta f = C_\mathrm{f} \cdot \Delta m \tag{8}$$

For the used commercially available 6 MHz crystals C_f equals 0.0815 Hz cm^2 ng^{-1}.

The EQCM characterisation of PVTPA-*co*-PS copolymer films was carried out with an *Autolab EQCM 7321* device from *Metrohm*. The working electrodes which were also purchased from *Methrohm* consist of quartz crystals with a resonance frequency of 6 MHz covered with

gold. As counter and reference electrodes a gold coil and a silver chloride coated silver wire were used. Since the used EQCM cell does not provide a junction for a connection to the Schlenk line, the measurements were performed under ambient conditions with an argon gas stream directed into the cell through a plastic tube.

3.3.4. Impedance Spectroscopy

Electrochemical impedance spectroscopy (EIS) is a versatile method to study the electronic response of a redox system to an applied alternating potential. [107–110] During an electrochemical reaction or experiment the electron flow can be impeded by multiple physical or chemical procedures like slow electrode or chemical reaction kinetics and diffusion processes in general. The electrochemical cell can also be described by an equivalent electric circuit in which the electric elements represent the different procedures. In general, an electrochemical experiment can be performed in either direct current (dc) or alternating current (ac) mode. In case of an applied potential in the dc mode the resistance (R) of the system is defined by Ohm's law:

$$V = I \cdot R \tag{9}$$

with the applied potential (V) and the resulting current (I). The respective element in the equivalent circuit is a resistor. In the ac mode the polarity of the applied field is reversed as a function of frequency (f). The applied potential as well as the resulting current can be described as wave functions. Due to impedance of the electrons the current wave is shifted with respect to the potential wave:

$$I(t) = A \cdot sin(2\pi f t + \Theta) \tag{10}$$

with A being the maximum amplitude, t the time and Θ the phase shift. In the electrochemical cell the phase shift is caused by non-ohmic resistors like capacitors and inductors. Analogously to Ohm's law for the dc mode, the overall impedance of the electrons in an ac system is described by equation 11.

$$V = I \cdot Z \tag{11}$$

with the impedance (Z) which includes both ohmic and non-ohmic elements of the equivalent circuit. Z can be expressed as a complex number with the resistance being the real component and the sum of capacitance and inductance being the imaginary component.

Therefore, by analysing the frequency dependence of the absolute impedance ($|Z|$), the real and imaginary components of Z and the phase shift (Θ) the individual electron impeding procedures in an electrochemical cell can be identified.
The EIS experiments were performed with an *IM6* potentiostat from *Zahner* in either two- or three-electrode geometries in custom-made glass cells under ambient conditions. For the data analysis the *Thales* software from *Zahner* was used.

3.3.5. 4-Point-Probe

The 4-point-probe (4pp) technique was used to determine the conductivity of chemically doped PVTPA-*co*-PS copolymer films. In this technique, the polymer film is electrically connected by a probe head with four pins in a linear arrangement and equal pin-to-pin distances. An external current (I) is applied through the two outer pins and the resulting potential (V) between the two inner pins is measured. The sheet resistance (R_s) of the polymer film can be determined by using the resistance (R) calculated according to Ohm's law from the applied current and measured potential:

$$R_\mathrm{s} = R \cdot \frac{\pi}{\ln(2)} \cdot f \tag{12}$$

with f being a correction factor that takes into account the geometry of the polymer film. For square-shaped polymer film samples with the pins located in the centre of the sample, f accounts to 1. From the sheet resistance (R_s) the bulk resistance (R_b) can be calculated accordingly to Eq. 13:

$$R_\mathrm{b} = R_\mathrm{s} \cdot d \tag{13}$$

with d being the film thickness. The bulk conductivity (σ) can be calculated from the reciprocal bulk resistance according to Eq. 14: [25, 111]

$$\sigma = \frac{1}{R_\mathrm{b}} = \left(\frac{\pi}{\ln(2)} \cdot d \cdot \frac{V}{I} \right)^{-1} \tag{14}$$

For the conductivity measurements of thin PVTPA-*co*-PS films a *SP4* probe head from *Signatone* with a pin distance of 1 mm and a *2636B SourceMeter* potentiostat from *Keithley* were used. The polymer films were deposited on square-shared glass substrates and the measurements were conducted with the pins connecting to the film centre so that the geometry correction factor f equals 1. In addition the measurements were performed by applying a

series of constant currents in the same order of magnitude to confirm linear ohmic behaviour of the sample resistance.

3.3.6. Absorption Spectroscopy

UV-vis absorption spectroscopy was used as a simple but powerful tool for the characterisation of the polymer aggregation in solution and solid state and to identify chemical species correlated to electrochemical and chemical redox processes. Polarised absorption spectroscopy was performed to verify successful alignment of the polymer chains in post-treated samples.

UV-vis absorption spectra of solutions and polymer films were recorded on a stationary *Lambda 35* spectrometer from *Perkin Elmer*. For *in-situ* measurements a modular *MCS621 Vis II* spectrometer equipped with a *CLH 600 F* halogen lamp from *Zeiss* and optic fibres from *Ocean Optics* was used. Spectra of solutions and films on ITO or glass substrates were performed in transmission mode while films on gold electrodes were measured in reflection. For all measurements the respective solvent or initial substrate was used as reference.

3.3.7. Polarised Optical Microscopy

Optical microscopy and polarised optical microscopy (POM) were used as simple but powerful tools to verify homogeneity of deposited polymer thin films and to monitor the swelling and recrystallisation processes during the solvent vapour annealing treatment as well as the large area alignment after high temperature rubbing of P3HT films. For both characterisation methods the same *Axio Imager.A1* from *Zeiss* was used. In the polarised mode two additional polarisation filters were adjusted in the light path in front (polariser) and behind (analyser) the polymer film. The orientation of the two polarisation filters were set to be orthogonal so that optical isotropic samples appear dark. Polymer films with aligned polymer chains are optically anisotropic and therefore appear bright under crossed polarisers. The microscopy images were recorded with an *AxioCam IC 1* camera from *Zeiss*. The microscope was used in reflection mode for gold substrates and during the solvent vapour annealing process and in transmission mode for ITO and glass substrates.

3.3.8. Atomic Force Microscopy

Due to the resolution in the nanometer scale, atomic force microscopy (AFM) is a versatile tool for the morphological surface characterisation of polymer films. In addition, it can also be used to determine the film thickness of thin films. [112–114] The schematic illustration of an AFM is shown in Fig. 3.7. The sample is mounted to a movable stage and hold into position by a vacuum chuck. During the measurement the sample surface is scanned by a tip which is attached to the so-called cantilever. The cantilever acts as a spring which is set into oscillation. The interaction of the cantilever and the sample is monitored by the position of a laser beam which is reflected on the top side of the cantilever towards a spatial resolved photo-diode and by the changing of the cantilever frequency with respect to the resonant frequency determined prior to the measurement. The spatial resolved monitoring of the tip position results in a topographic image of the sample surface while the cantilever frequency change provides information in mechanical properties, which can be used to discriminate between different materials like donor acceptor blend systems but also between amorphous and crystalline domains of one single material.

For this thesis, a *Dimension Icon* microscope from *Bruker* was used and the data were evaluated with either *NanoScope Analysis* from *Bruker* or *Gwyddion* (free software). All measurements were performed in the tapping mode with silicon tips ($40\,\mathrm{N\,m^{-1}}$) from *µmasch*.

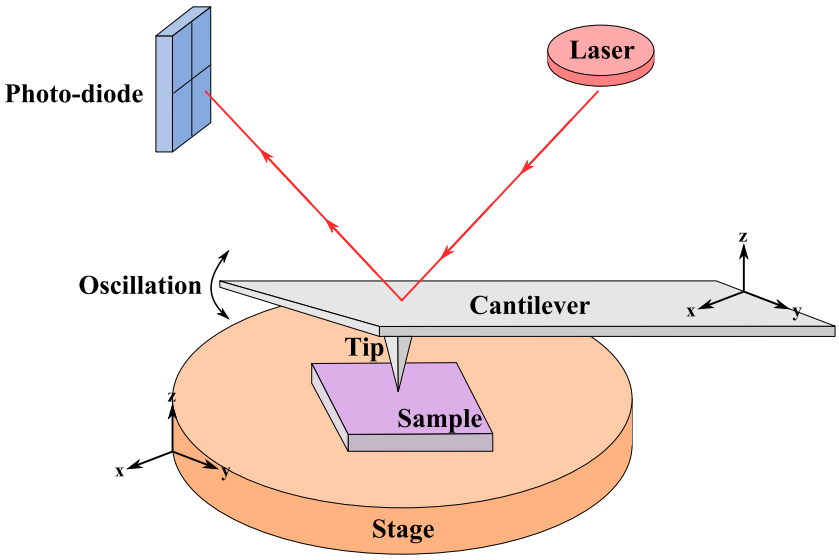

Figure 3.7: Schematic illustration of an AFM setup; image adapted from Fuoco [115].

3.3.9. Transmission Electron Microscopy

In this thesis transmission electron microscopy (TEM) was used as a characterisation method to gain detailed insights into the morphology of structured P3HT films. Compared to optical microscopy, TEM bright field images offer higher magnification due to the utilization of a focused electron beam as the imaging compound instead of visible light waves. The electron beam is emitted by a cathode due to an applied high-voltage field and focused by magnetic lenses. In contrast to atomic force microscopy which only gives morphological information on the sample surface, TEM provides information about the bulk morphology through the whole thickness of the polymer film. During the transmission through the sample, the electrons interact with the sample molecules. In case of oriented or crystalline samples the electron beam undergoes diffraction. The resulting diffraction reflexes can be described by the *Bragg equation*: [116]

$$n\lambda = 2d\sin(\theta) \tag{15}$$

with the diffraction order (n), the wavelength of the electron beam (λ), the lattice plane spacing (d) and the diffraction angle (θ).

The TEM measurements were conducted at the *Institut Charles Sadron* in *Strasbourg* by *Dr. Amer Hamidi-Sakr* and *Dr. Martin Brinkmann*. For the TEM characterisation of structured P3HT films a *CM12* microscope from *Philips* equipped with a *MVIII* ccd camera from *Soft Imaging System* was used. The measurements were performed with an acceleration voltage of 120 kV. Prior to the TEM measurements the polymer films were coated with approximately 3 nm thick amorphous carbon layers by using an *Auto 306* evaporation setup from *Edwards* with graphene electrodes. Afterwards the carbon-coated polymer films were detached from the initial substrates and attached onto copper grids. The detaching of the polymer films was performed by placing droplets of polyacrylic acid on the polymer film and letting them dry under ambient conditions for 2 h. The dried droplets were peeled off the substrate with a razor blade. Thereafter the droplets with the polymer film attached were transferred to a water bath to dissolve the polyacrylic acid, leading to free-standing polymer films which can be easily picked up with the TEM copper grids.

3.3.10. Nuclear Magnetic Resonance Spectroscopy

^{1}H and ^{13}C nuclear magnetic resonance spectroscopy (NMR) was measured by using a *Bruker Avance 250* spectrometer from *Bruker* at 250 MHz (^{1}H) and 62.5 MHz (^{13}C) respectively. The measurements were performed in deuterated chloroform ($CDCl_3$) or dichloromethane (CD_2Cl_2) at room temperature. The calibration of the spectra was performed by using the residual solvent peaks of the used $CDCl_3$ ($\delta = 7.26$ ppm) or CD_2Cl_2 ($\delta = 5.33$ ppm) respectively. [117]

3.3.11. Differential Scanning Calorimetry

Thermal analysis of the studied copolymers in chapter 5.2 was performed by differential scanning calorimetry (DSC) with a *Perkin Elmer DSC 4000*. The measurements were performed as two consecutive cycles in the temperature range of −50 °C and 200 °C with heating and cooling rates of 10 K min^{-1}. The glass transition temperatures were determined from the second heating cycles.

3.3.12. Gel Permeation Chromatography

Molecular weight distribution determination was performed by gel permeation chromatography (GPC) using an *Agilent 1260 Infinity GPC/SEC System* with three consecutive columns from *Polymer Standards Service* with pore sizes of 1000 Å, 10 000 Å and 100 000 Å and a *SECurity* UV-vis detector. The polymers were dissolved in tetrahydrofurane (3 mg mL^{-1}) and were filtered (PTFE, 0.45 µm) prior to the measurement. For the calibration polystyrene standards from *Polymer Standards Service* were used. The measurements were performed by *Corinne Rost-Schmidt*.

4. Influence of Controlled Thin Film Morphology on the Electrochemical Behaviour of P3HT

The content of the following chapter has been published in Bruchlos et al. [118] of which I am the main author. The contributions of the co-authors are experimental support by *A. Hamidi-Sakr* (hight temperature rubbing and TEM measurements), morphological interpretation by *D. Trefz*, *M. Brinkmann* and *S. Ludwigs* and electrochemical interpretation by *J. Heinze*, *A. Ruff* and *S. Ludwigs*.

4.1. Poly(3-alkylthiophenes) – State of the Art

Poly(3-alkylthiophenes) (P3AT) and in particular poly(3-hexylthiophene) (P3HT) are widely used *p*-type conducting materials in organic photovoltaic (OPV), organic field effect transistors (OFET) and organic light emitting diodes (OLED) due to their good solubility, strong absorption in the UV-vis range and high charge transport mobility. [1, 15, 67, 119] Doped P3HT is also used as electron-blocking layer in hybrid solar cells [120, 121] and in thermoelectrics (usually with 2,3,5,6-tetrafluoro-7,7,8,8,-tetracyanoquinodimethane (F4TCNQ) as dopant) [122]. In the last decades, especially the absorption behaviour and electron transport behaviour of poly(3-alkylthiophenes) have been subject of numerous studies. The electronic and optic behaviour show a strong influence of polymer characteristics as molecular weight [123–125] and regioregularity [126] but also of the thin film morphology [127–130].

Due to their semi crystalline nature, P3HT thin films consist of π-π stacked, crystalline lamellar structures (illustrated in green in Fig. 4.1) with typical π-π stacking distances of 3.6 Å - 3.8 Å [131], intermixed with disordered, amorphous domains (illustrated in orange in Fig. 4.1). The degree of crystallinity and the orientation of the polymer chains in the crystalline domains can be tuned by the film deposition conditions (solvent, deposition method, post treatment). The two most common crystallisation textures of P3HT thin films are shown in Fig. 4.1. [2] Film deposition by spin coating or drop casting from good solvents as well as solvent vapour post annealing and crystallisation from solution in a poor solvent usually leads to the formation of the *edge-on* texture. [87, 131] In the *edge-on* texture (see Fig. 4.1 **b**) the π-π stacking direction [010] and the polymer backbone direction [001] are in parallel to the substrate (in plane) and the alkyl side chain direction [100] perpendicular

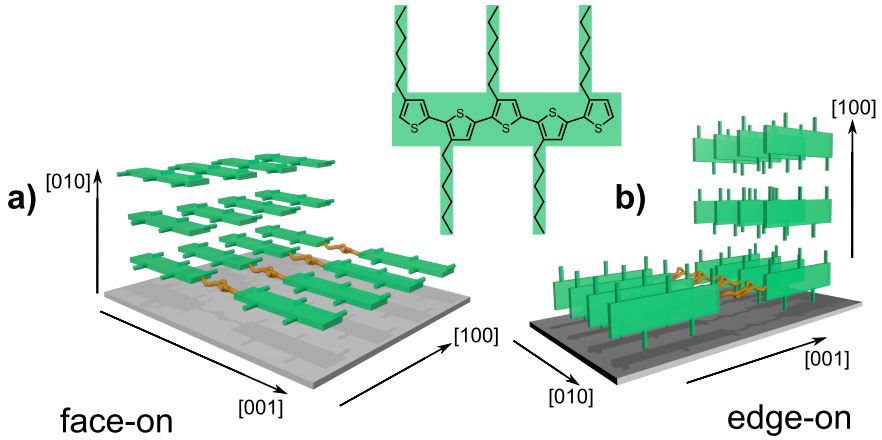

Figure 4.1: Schematic illustration of a semi crystalline P3HT thin film in *face-on* (**a**) and *edge-on* (**b**) texture with the alkyl side chain direction [100], the π-π stacking direction [010] and the polymer backbone direction [001]; crystalline domains in green and amorphous domains in orange; adapted from [2].

to the substrate surface (out of plane). By applying high temperature rubbing as a post treatment, large area alignment of P3HT chains in the *face-on* texture (see Fig. 4.1 **a**) can be achieved. [93] In this morphological texture the π-π stacking direction [010] is out of plane and the alkyl side chain direction [100] and polymer backbone [001] are in plane.

The thin film morphology also has an influence on the charge transport of P3HT. Since P3HT is a *p*-type semiconductor, the charge transport is conducted by holes. The charge carrier mobility in field effect transistors reaches up to $1\,\mathrm{cm^2\,V^{-1}\,s^{-1}}$. [19] Sirringhaus et al. observed that the charge carrier mobility of P3HT with the semi-crystalline lamella in the transistor channels oriented in the *edge-on* texture is two orders of magnitudes higher than in the *face-on* texture. [4] In general the charge transport occurs along the [010] and [001] direction. Crossland et al. observed a charge carrier mobility anisotropy between the [001] and [010] directions in the *edge-on* texture with up to 4 times faster charge transport along the polymer backbone ([001] direction) than along the π-π stacking ([010] direction). [83]

The absorption behaviour of P3HT, which can be used as a powerful tool to characterise the morphology, is well described in literature. [3, 132–134] In good solvents like chlorofrom, chlorobenzene or *o*-dichlorobenzene, P3HT is fully dissolved and the UV-vis spectrum (orange curve in Fig. 4.2 **a**) shows one broad absorption band at 460 nm. Upon aggregation and crystallisation, which is driven by the π-π interaction, the electronic structure of the polymer

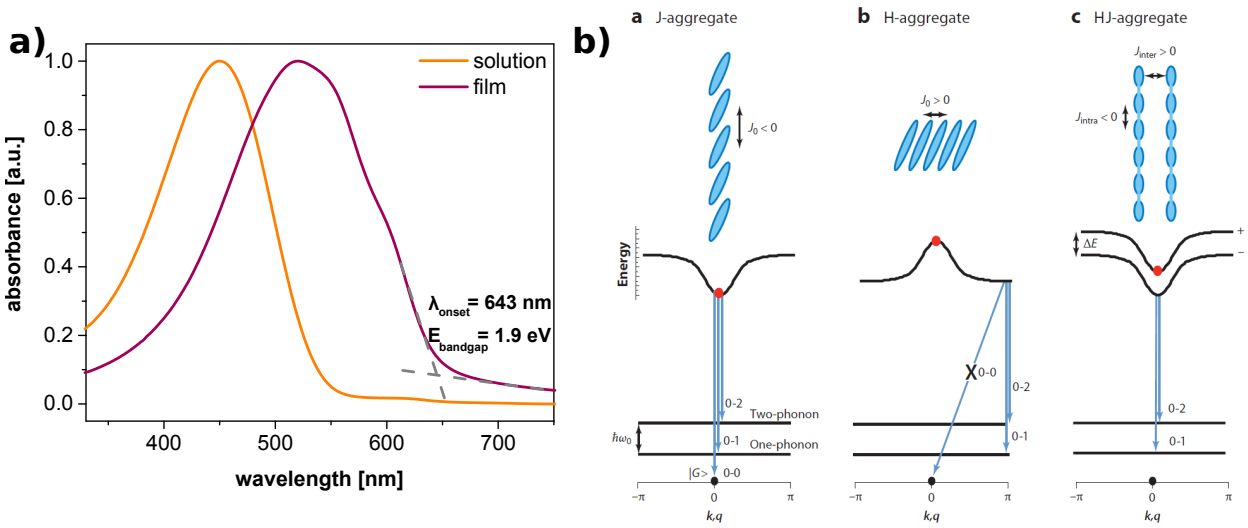

Figure 4.2: **a)** normalised UV-vis absorption spectra of a P3HT solution (orange) in chloroform ($5\,\mathrm{mg\,mL^{-1}}$) and a P3HT film (purple) spin coated from the same chloroform solution; **b)** schematic illustration of *J*-aggregates (left side) with an head-to-tail orientation of chromophores, *H*-aggregates with a side-by-side orientation of chromophores (middle) and *HJ*-aggregates in π-π stacked polythiophene chains (right side) (reprinted with permission from Spano et al. [3], Copyright (2014) Annual Reviews).

chains is strongly altered which causes a bathochromic shift of the absorption band accompanied by the formation of a fine structure. [3, 132–134] The UV-vis absorption spectrum of a P3HT film spin coated from chloroform solution (purple curve in Fig. 4.2 **a**) reveals a broad absorption band between 400 nm and 650 nm with a peak maximum at 520 nm and two shoulders at 550 nm and 610 nm respectively. The bathochromic shift and formation of the fine structure in the absorption spectrum of the P3HT film can be explained by the decreased polymer chain mobility in the solid state. In literature the absorption band at 600 nm - 610 nm is attributed to π-π stacking interaction due to planarisation of the chains during to the aggregation of P3HT. [84] The spectroscopic behaviour of P3HT can be described by the model of weakly interacting *H*-aggregates (see Fig. 4.2 **b**), developed by Spano and Silva. [3] This model was originally established to describe the interaction of chromophores which are oriented head-to-tail (*J*-aggregate, 0-0 transition allowed, schematic illustration in Fig. 4.2 **b** left side) or side-by-side (*H*-aggregate, no 0-0 transition due to rapid intraband relaxation, schematic illustration in Fig. 4.2 **b** middle). A single polymer chain

can be seen as a *J*-aggregate, while in multiple π-π stacked chains the intrachain electronic coupling (J) and interchain coupling (H) are combined. Therefore the crystalline domains in a P3HT film are described by a combined *HJ*-aggregate behaviour (schematic illustration in Fig. 4.2 **b** right side). The free exciton band width W, which can be used as a quantity for the crystallinity [92], can be calculated from the ratio of the first two vibronic peaks in the absorption or emission spectra of P3HT according to Eq. 16: [132]

$$\frac{A_{00}}{A_{01}} = \left(\frac{1 - 0.24\ W/E_\mathrm{p}}{1 + 0.073\ W/E_\mathrm{p}} \right)^2 \tag{16}$$

with A_{00} and A_{01} as intensities of the 0-0 and 0-1 transitions at 610 nm and 550 nm respectively and E_p as the energy of the symmetric $C{=}C$ stretching vibration (0.18 eV according to [132]). The smaller the exciton band width W, the longer the conjugation length of the polymer chains. [3, 84, 132, 135]

Absorption spectroscopy is also a versatile tool to determine the frontier orbital energy levels of organic semiconductors. Especially the HOMO energy level of P3HT is an important criterion for the fabrication of organic electronics like organic and hybrid solar cells [16, 17, 136, 137] since the HOMO level of the donor material has to fit to the LUMO level of the acceptor material to ensure effective power conversion efficiency. [138] Commonly the optical band gap, which corresponds to the $S_0 \longrightarrow S_1$ transition in the absorption spectrum, is determined from the low-energy onset wavelength which results in an underestimation of the band gap by approximately 0.2 eV to 0.3 eV. [2, 49, 139, 140] The UV-vis absorption spectrum of a P3HT film in Fig. 4.2 **a** (purple curve) reveals an onset wavelength of 643 nm which results in an optical band gap of 1.9 eV.

For the application in organic optoelectronics not only the band gap but also the individual frontier orbital energy levels, which are not accessible by absorption spectroscopy, are of interest. To determine the HOMO energy level of organic semiconductors, UPS (ultraviolet photoelectron spectroscopy) can be used. The LUMO energy level is only accessible through photoelectron spectroscopy in the gas phase [141] and low-energy inverse photoemission spectroscopy [142–144]. In literature HOMO energy levels between -4.5 eV and -4.65 eV and a LUMO energy level of -2.13 eV for spin coated P3HT are reported. [145–150] From these values a band gap between 2.37 eV and 2.52 eV can be calculated.

Another simple method to determine the frontier orbital energy levels and band gap is cyclic

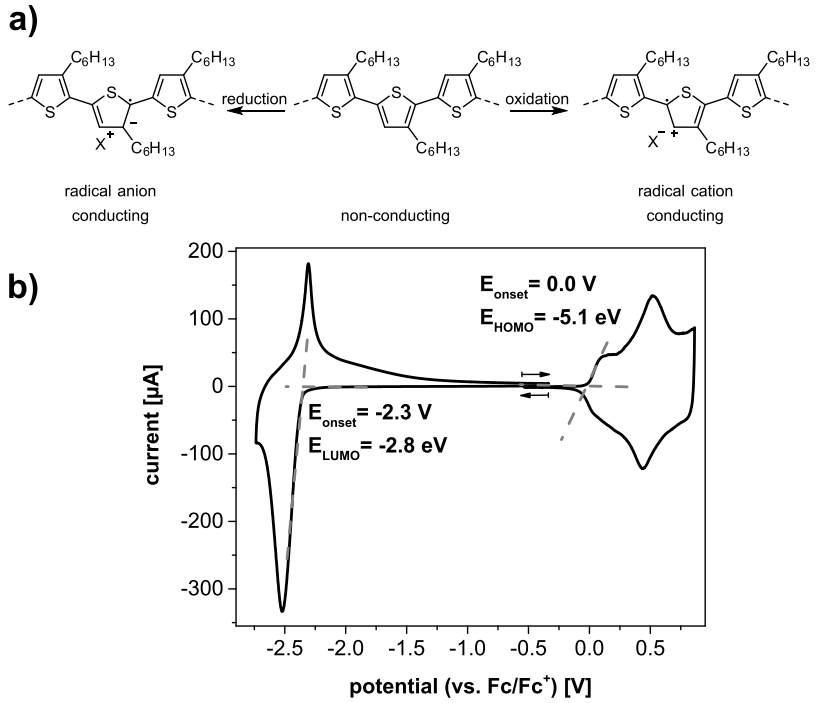

Figure 4.3: Redox behaviour of P3HT. **a)** chemical structures of the non-conducting neutral P3HT chain and the conducting radical anion and radical cation form; **b)** cyclic voltammograms of the oxidation and reduction of a P3HT film (spin coated from chloroform solution, $5\,\mathrm{mg\,mL^{-1}}$, thermally annealed at 80 °C) measured in 0.1 M NBu_4PF_6/ MeCN with a scan rate of $20\,\mathrm{mV\,s^{-1}}$; arrows indicate the scan direction of the separately measured anodic and cathodic scans.

voltammetry (CV). With this method the redox behaviour of the semiconductor is characterised and from the oxidation or reduction potentials the HOMO or LUMO energy levels can be calculated respectively. [151] In the optical band gap characterisation discussed above, the aggregation of P3HT caused a significant bathochromic shift of the absorption band which corresponds to a decrease of the band gap. Therefore a similar effect in the electrochemical behaviour is expected and solid state voltammetry is necessary to assess effects of the thin film morphology on the redox potentials. In Fig. 4.3 **b** the cyclic voltammograms of the first oxidation (from the neutral form to the radical cation) and first reduction (from the neutral form to the radical anion) of a P3HT film are shown. Being a classical semiconducting polymer, P3HT is isolating in its neutral form and conducting in both its radical cation and anion form (chemical structures shown in Fig. 4.3 **a**). In principle P3HT can be also oxidised to its dication at higher applied potential. The oxidative redox wave in Fig. 4.3 **b**

(right side, towards higher applied potential) is composed of broad overlapping waves while the reduction to the radical anion form (left side, towards more negative applied potentials) reveals a sharp, distinct redox wave. In Fig. 4.3 **b** the reduction wave is reversible but often the limited potential window of organic electrolytes, impurities in the electrolyte (traces of water or oxygen) and the type of the selected counter ions [152] lead to irreversible reduction behaviour of P3HT. From the cyclic voltammograms in Fig. 4.3 **b** HOMO and LUMO energy levels of $-5.1\,\mathrm{eV}$ and $-2.8\,\mathrm{eV}$ respectively can be calculated according to Equation 4 and 5, which results in an electrochemical band gap of $2.3\,\mathrm{eV}$.

Electropolymerisation of conjugated monomers like 3-alkylthiophenes is a versatile method to prepare films of semiconducting polymers. The polymerisation and deposition onto the electrode substrate take place concurrently. By variation of polymerisation parameters, the used electrode material and the monomer concentration the film thickness and morphology can be tuned. [153] Three different electrochemical methods; namely potentiostatic, galvanostatic and potentiodynamic; can by used to induce the anodic polymerisation. [154] Under potentiostatic control the potential is kept constant at or just below the peak potential of the monomer oxidation. Since the growing polymer film is always kept in its oxidised form (meaning without continuous charging-discharging cycles), a homogeneous film with precisely controlled film thickness is formed. Under galvanostatic control the applied potential is constantly modified to maintain a specified current density. Depending on the desired current density the applied potential can also reach extreme values. Thus, a galvanostatic deposition should be performed at rather low current densities and with high purity monomers to avoid overoxidation of the polymer film and side reactions. In addition, this method is unsuitable for copolymerisation of different monomers. [153] Potentiodynamic electropolymerisation is performed by multi-cycling the potential in a potential window in which the monomer oxidation occurs. This means that in each cycle the monomer is oxidised, the formed radical cation undergoes follow-up reactions to longer oligomers which have a lower oxidation potential. Therefore the oligomer species also become oxidised immediately. During the backward scan of the potential cycle the oligomer species become re-reduced to the neutral species. Therefore the polymer film growth is accompanied by continuously charging/ discharging which includes the movement of ions from the supporting electrolyte with their respective solvent shell. This results in mechanical stress for the polymer film

and possible overoxidation in case that the shift of the oxidation potential from monomer to polymer is large.

In 1987, Sato et al. observed different features in the voltammograms of electropolymerised poly(3-dodecylthiophene) (P3DDT) depending on the film preparation conditions. [155] The voltammogram immediately after electropolymerising (see Fig. 4.4 **a**) reveals a broad anodic redox wave with two subsignals at about 0.5 V and 0.75 V vs. Ag/Ag^+. After dissolving of the electropolymerised film from the original electrode and consequent drop-casting of the solution onto a new electrode the voltammogram (measured under the same conditions) reveals only the second subsignal at 0.75 V vs. Ag/Ag^+ (see Fig. 4.4 **b**). Since the films were prepared from the same polymer, the authors concluded that the different number of subsignals in the voltammograms results from different conjugation lengths in the polymer film rather than from different chemical structures. [155]

In 1998 Skompska et al. studied the deposition mechanism during the electropolymerisation of poly(3-methylthiophene) (P3MT) in detail. [156] The authors observed a two-step process depending on the current density. In the first step, at low current densities, thin polymer layers which consist of ordered fibres with large conjugation length are formed directly onto the electrode surface. [157] In the second step, at high current density, disordered P3MT layers with shorter conjugation length are formed. This is attributed to the formation of oligomers in solution in front of the electrode, followed by precipitation onto the electrode after the solubility limit is reached. [158] Skompska et al. also observed two subsignals at about 0.25 V and 0.4 V (see. Fig. 4.4 **b**) within the cyclic voltammogram of electropolymerised P3MT. [156] The two subsignals are attributed to domains of longer (lower oxidation potential) and shorter (higher oxidation potential) conjugation lengths respectively. This attribution is further supported by the scan rate to peak current dependency of both subsignals. The first subsignal, at lower oxidation potential, shows a dependency to the square root of the scan rate which is attributed to a diffusion controlled intercalation of counter ions in ordered, closer packed domains of the P3MT film while the second subsignal, at higher oxidation potential, reveals a linear dependency, indicating adsorption controlled fast ion transport into more porous domains. [156]

In contrast to electropolymerised poly(3-alkylthiophenes) which are rather ill-defined, chemical synthesis leads to well-defined polymers with controlled regioregularity, polydispersity

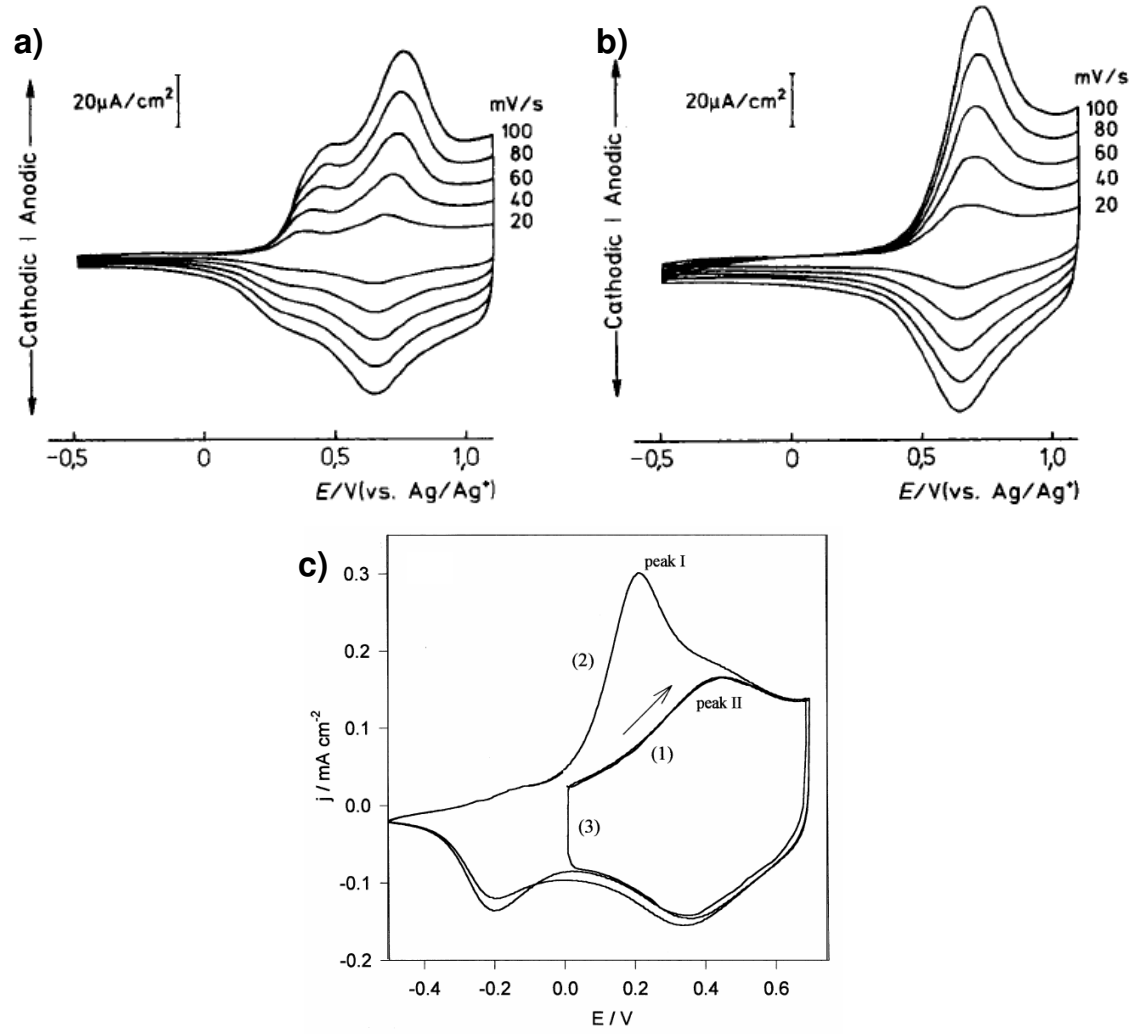

Figure 4.4: Cyclic voltammograms of electropolymerised poly(3-alkylthiophenes). **a)**, **b)** poly(3-dodecylthiophene) measured in 0.025 M NEt_4PF_6 in nitrobenzene on ITO electrodes, after electropolymerisation (**a**) and after drop casting of the dissolved electropolymerised film (**b**) respectively (reprinted with permission from Sato et al. [155], Copyright (1987) Wiley); **c)** poly(3-methylthiophene) measured in 0.1 M $LiClO_4$ in MeCN with a scan rate of 20 mV s^{-1} (reprinted with permission from Skompska [156], Copyright (1998) Elsevier).

and molecular weight which can be solution processed. [159–161] Regioiregular poly(3-alkylthiophenes) can be gained by oxidative coupling with $FeCl_3$ [162] while polymers with regioregularity larger than 97% are synthesised by Kumada and Negishi type cross-coupling reactions. [163, 164]

Since the 1990s Trznadel [165], Skompska et al. [166] and Jiang et al. [5] studied the influ-

ence of regioregularity of poly(3-alkylthiophenes) on the electrochemical behaviour. Jiang et al. compared the cyclic voltammograms of four P3HT batches of different regioregularities from regiorandom (54%), over medium regioregularities of 70% and 81% to highly regioregular (97%). [5] In Fig. 4.5 **a** the voltammograms are shown. The voltammogram of the regiorandom P3HT batch (54%) reveals only one anodic wave at 0.5 V vs. Ag/Ag^+, while the medium regioregular batches (81% and 70%) reveal an additional broad second anodic wave at about 0.25 V vs. Ag/Ag^+ and the highly regioregular batch (97%) an additional third anodic wave at 0.15 V vs. Ag/Ag^+. In the following these three anodic wave are labelled as I, II and III with increasing oxidation potential, respectively. Trznadel observed the same dependence of anodic subsignals on the regioregularity of poly(3-octylthiophene). [167]

The effect of regioregularity on the electrochemical behaviour of P3HT has also been studied by Trznadel et al. [165] In Fig. 4.5 **b** the voltammograms of regiorandom P3HT (synthesised by oxidative coupling with $FeCl_3$) and four soxhlet fractions of one regioregular P3HT batch are shown. The four regioregular P3HT fractions are: acetone ($M_n = 2300\,g\,mol^{-1}$, PDI = 1.38), *n*-hexane ($M_n = 4400\,g\,mol^{-1}$, PDI = 1.22), dichloromethane ($M_n = 8400\,g\,mol^{-1}$, PDI = 1.33) and tetrahydrofuran ($M_n = 17\,700\,g\,mol^{-1}$, PDI = 1.45). UV-vis absorption spectroscopy in THF solution and in solid state showed a bathochromic shift and a fine structure in the absorption band with increasing molecular weight, indicating longer conjugation lengths. The voltammograms of the regiorandom and acetone fraction, the regioregular fraction with the shortest conjugation length, reveal only one anodic redox wave at about 0.75 V vs. Ag/Ag^+. The regioregular fractions with longer conjugation lengths (*n*-hexane, dichloromethane and tetrahydrofuran) show three subsignals in the anodic redox wave at 0.6 V, 0.75 V and 0.9 V vs. Ag/Ag^+ which correspond to signals I, II and III observed by Jiang et al. (see Fig. 4.5 **a**). [5] The origin of these three subsignals has been controversially discussed in literature. In principal two models, which attribute the subsignals to different redox processes, have been proposed by Trznadel and Skompska. In the model established by Trznadel et al. subsignals I and III are attributed to the oxidation of defect-free domains of the neutral P3HT film to the radical cation and dication respectively. Subsignal II is attributed to the oxidation of disordered domains to the radical cation. [165, 168, 169] Skompska et al. proposed a model in which the three subsignals are all attributed to the oxidation

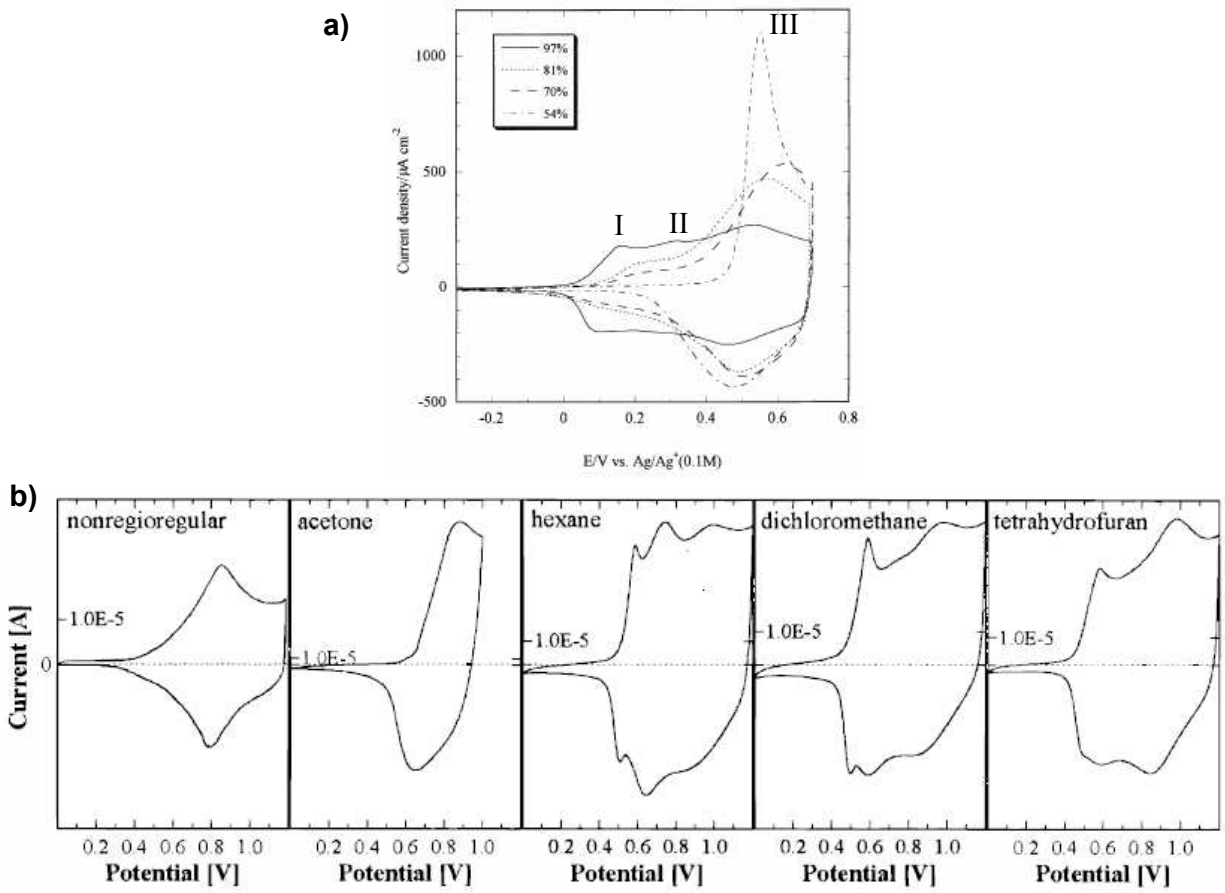

Figure 4.5: Cyclic voltammograms of chemically synthesised regioregular P3HT. **a)** P3HT batches of varying regioregularities, measured in 0.1 M NEt_4ClO_4 in MeCN with a scan rate of 100 mV s^{-1}, films prepared from chloroform solutions; reprinted with permission from Jiang et al. [5], Copyright (2002) Elsevier; labels *I*, *II* and *III* have been added to guide the eye **b)** comparison of regioiregular P3HT (synthesised with $FeCl_3$) and different soxhlet fractions (acetone, *n*-hexane, dichloromethane and tetrahydrofuran) of one regioregular P3HT batch, reprinted with permission from Trznadel et al. [165], Copyright (1998) American Chemical Society.

of neutral P3HT to the radical cation. According to Skompska et al. the origin of the subsignals in the voltammogram is due to the coexistence of morphological domains with different conjugation lengths. [166, 170] By studying the scan rate dependency of the subsignals in the cyclic voltammograms of poly(3-hexylthiophene) and poly(3-dodecylthiophene) of different regioregularities, Skompska et al. observed a decrease of the peak intensity ratio I/III and a

constant II/III ratio upon increasing scan rates. [166] The authors attribute this behaviour to two different counter ion intercalation processes due to different morphological domains in the polymer films. By studying the thermochromism of various poly(3-alkylthiophenes) of different regioregularities Holdcroft et al. identified three morphological domains coexisting in the polymer films. [171] The domains, namely ordered, quasi-ordered and disordered, vary in their packing density, π-π stacking distance and alkyl side chain alignment. Therefore, Skompska et al. attributes the formation of the three subsignals in the anodic redox wave in the voltammogram to the oxidation of the neutral P3HT to the radical cation form in the three morphological domains (I ordered, II quasi-ordered, III disordered). [166] In a second study, Skompska et al. observed a two-step swelling process during the oxidation of P3HT films. [170] During the oxidation in subsignal I the authors observed only a small increase of the film volume while during the oxidation in subsignal III a large volume increase is observed. This observation is interpreted by the intercalation of counter ions accompanied by a solvent molecule uptake into a compact structure with spatial constrains (I) and in an amorphous, more porous structure (III).

In summary, literature on the electrochemical behaviour of poly(3-alkylthiophenes) showed that the number of subsignal in the cyclic voltammogram depends on the regioregularity of the studied polymer. Regiorandom poly(3-alkylthiophenes), prepared by either electropolymerisation or oxidative cross coupling with $FeCl_3$, show only one subsignal in the voltammogram while with increasing regioregularity two additional subsignals at lower oxidation potentials arise. Thus, with increasing regioregularity the onset potential and therefore also the HOMO energy level are shifted towards lower oxidation potential or higher frontier orbital energy levels respectively. The origin of the subsignals in the anodic voltammetric scans is attributed to the coexistance of domains of different morphologies in the polymer films. Still, since the studies in literature are based on the comparison of different polymer batches and film preparation is typically performed by drop casting, which generally leads to inhomogeneous films, a direct comparison remains difficult and possible influences of the different molecular weight or polydispersity can not be ruled out.

4.2. P3HT Films of Different Deposition Methods

In order to establish a direct correlation between film morphology and redox behaviour in the cyclic voltammogram, P3HT samples of different, controlled morphologies but prepared from the same batch are studied in the following. First, the influence of the film deposition conditions is studied. In the second part three different crystallisation methods are used to control the film morphology and increase the degree of crystallinity in the polymer films. Since P3HT is usually used as the donor material in binary donor:acceptor blend systems, the influence of the addition of a fullerene acceptor material on the morphology and redox behaviour is studied thereafter.

4.2.1. As-cast P3HT Films

In the following, the influence of the film deposition conditions on the redox behaviour of P3HT is studied. As a first sample, an electropolymerised P3HT film is presented, since it can be seen as an amorphous extreme case. Afterwards the electropolymerised P3HT film is compared to P3HT films prepared from the same chemically synthesised, regioregular P3HT batch by different deposition methods.

The reaction mechanism of the anodic electropolymerisation of 3-alkylthiophenes is shown in Fig. 4.6 **a**. According to Heinze et al. [172] the mechanism is described via a cascade of oxidation steps of the neutral species to their respective radical cation forms, which is followed by dimerisation and proton elimination. A detailed study of the reaction kinetics by Heinze et al. showed a decrease in reaction rate of monomer addition to the polymer chain with increasing chain length, meaning that dimerisation reactions between chains of the same length are favoured (monomer-monomer, dimer-dimer, oligomer-oligomer and so forth). Therefore the electropolymerisation of 3-alkylthiophenes is described by the so-called *oligomer approach* as a step-growth mechanism. [49, 173] In general, electropolymerisation of 3-alkylthiophenes results in regiorandom head-to-tail coupling. [153]

For the preparation of an electropolymerised P3HT (labelled $P3HT_{electro}$) film a combination of galvanostatic and potentiostatic deposition is used. The corresponding potential (red) and current (blue) curves are shown in Fig. 4.6 **b**. For the polymerisation blank gold electrodes and a monomer concentration of 0.02 M in a supporting electrolyte of 0.1 M NBu_4PF_6 in MeCN was used. The anodic polymerisation was performed in the galvanostatic mode by

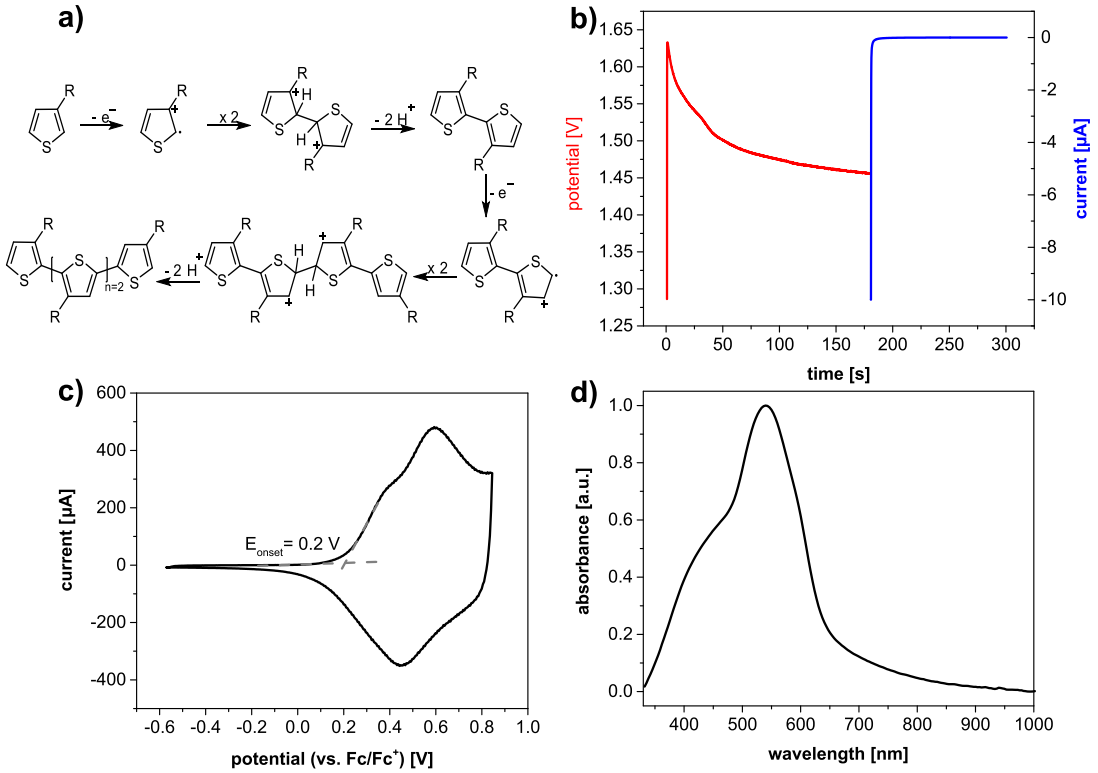

Figure 4.6: Electropolymerisation of P3HT. **a)** schematic reaction mechanism of the electrochemicaly induced oxidative coupling of 3-alkylthiophenes (R = alkyl chain); **b)** potential-time (red curve) and current-time (blue curve) curves of the galvanostatic polymerisation of 3-hexylthiophene onto gold electrodes with 0.5 mA cm^{-2} followed by potentiostatic discharging of the formed polymer film for 120 s at 0 V; **c)** cyclic voltammogram of the electropolymerised P3HT film measured in 0.1 M NBu_4PF_6 in MeCN with a scan rate of 20 mV s^{-1}; **d)** UV-vis absorption spectrum of the dry electropolymerised P3HT film measured in reflection.

applying a current density of 0.5 mA cm^{-2} for 90 s. The low current density has been chosen to avoid overoxidation of the formed P3HT film and high applied potentials which would exceed the potential window of the electrolyte solvent (for MeCN the potential window is about −2.2 V to 1.8 V vs. Fc/Fc^+). After the anodic polymerisation and deposition the P3HT film is oxidised. The discharging of the P3HT film is performed in potentiostatic mode at 0 V for 120 s to avoid uncontrolled increase of the reduction potential to maintain the desired current density. The potential-time curve of the galvanostatic polymerisation/ deposition shown in Fig. 4.6 **b** (red curve) reveals an initial increase of the potential to

1.63 V followed by a slow decrease to an almost constant potential plateau at about 1.45 V. This potential behaviour can be interpreted by an over-potential deposition due to the dismatch of the work function of the electrode material and the monomer oxidation potential. After the formation of an initial polymer layer at the electrode surface, whose work function matches the monomer oxidation potential, further deposition of additional polymer requires less energy, whereby the applied potential decreases. During the discharging (see blue curve in Fig. 4.6 **b**) the current initially increases to −10 µA, followed by a drop to 0 A indicating fast and complete discharging of the $P3HT_{electro}$ film.

Fig. 4.6 **c** shows the cyclic voltammogram of $P3HT_{electro}$, measured in monomer-free electrolyte. The voltammogram reveals a broad redox wave with an onset potential of 0.2 V vs. Fc/Fc^+. The broad anodic wave shows the superposition of two subsignals at about 0.35 V and about 0.5 V. The absorption spectrum in Fig. 4.6 **d** shows a broad absorption between 400 nm and 600 nm with a peak maximum at 540 nm and a well pronounced shoulder at 450 nm. The intense absorption shoulder at 450 nm and the lack of absorption at 610 nm indicate a predominantly amorphous structure of the $P3HT_{electro}$ film without distinct crystalline domains.

Fig. 4.7 shows the cyclic voltammograms of the electropolymerised P3HT film (**a**) and of a chemically polymerised, regioregular P3HT batch (M_w = 112 kg mol^{-1}, PDI = 2.4) after drop casting (**b**) and after spin coating (**c**) from chloroform solution (c = 5 mg mL^{-1}), labelled $P3HT_{electro}$, $P3HT_{drop}$ and $P3HT_{spin}$ respectively. The anodic wave of the $P3HT_{electro}$ film (Fig. 4.7 **a**; for polymerisation parameters see above) shows two subsignals at 0.35 V and 0.55 V and an onset potential of 0.2 V (all potentials vs. Fc/Fc^+) which corresponds to a HOMO energy level of −5.3 eV. In Fig. 4.7 **b** and **c** the voltammograms of a regioregular, chemically synthesised P3HT batch, but prepared by different casting methods, are shown as a direct comparison. As both films are prepared from the same polymer solution on identical electrodes and measured under the same conditions, differences in the redox behaviour can be attributed to the difference in the film morphology caused by the casting methods. During the drop casting the film thickness is uncontrolled which typically leads to inhomogeneous films while spin coating leads to thin, homogeneous films. The difference in film thickness is also displayed by the difference in the current intensity with similar electrodes geometry. The current of the anodic redox wave of the drop cast film (Fig. 4.7 **b**) is about

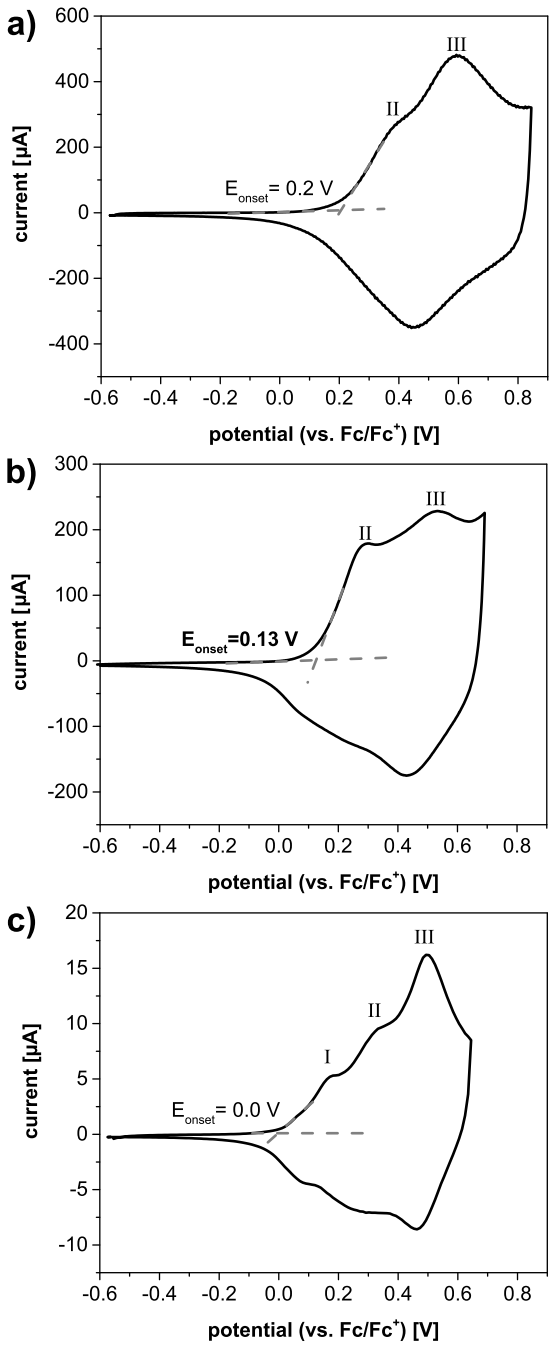

Figure 4.7: Comparison of the cyclic voltammograms of P3HT films prepared by electropolymerisation **(a)** and drop-casting **(b)** and spin-coating **(c)** of regioregular P3HT ($M_W = 112\,kg\,mol^{-1}$, PDI = 2.4); all voltammograms measured in 0.1 M NBu_4PF_6 with a scan rate of $20\,mV\,s^{-1}$.

10 times higher than in the spin coated film (4.7 **c**). Both film preparation methods result in dominantly amorphous P3HT films which can be seen from absorption spectroscopy, atomic force microscopy and electron diffraction (see below). Like for $P3HT_{electro}$, the voltammogram of $P3HT_{drop}$ exhibits two subsignals at about 0.25 V and 0.5 V, but the onset potential is shifted towards lower oxidation potential to 0.13 V. The two subsignals in $P3HT_{electro}$ and $P3HT_{drop}$ correspond to II and III described in literature. [5, 165, 166, 170] Subsignal I seems to be suppressed. In comparison, the anodic wave of $P3HT_{spin}$ consists of the superposition of three subsignals at 0.15 V, 0.25 V and 0.5 V. The onset potential is shifted to 0.0 V.
Since the deposition method of the very same P3HT solution already alters the number of subsignals and the onset potential of the cyclic voltammogram, careful control of the thin film morphology is crucial. A more detailed characterisation of $P3HT_{spin}$ is shown in Fig. 4.8. The AFM height (Fig. 4.8 **a**) and phase (**b**) images reveal a continuous, smooth and featureless film. The TEM bright field image (Fig. 4.8 **c**) is also featureless and the electron diffraction (inlet in Fig. 4.8 **c**) reveals only a faint halo at 3.8 Å which corresponds to the [020] reflex, indicating some π-π stacked chains in crystalline domains. Another characterisation method to gain information about the degree of crystallinity is absorption spectroscopy. The UV-vis absorption spectrum of $P3HT_{spin}$ in Fig. 4.8 **d** shows a broad absorption band between 400 nm and 650 nm with a peak maximum at 520 nm and shoulders at 550 nm and 610 nm respectively. The exciton band width W, calculated according to Equation 16 from the intensity ratio of the 0-0 (at 610 nm) to 0-1 (at 550 nm) transitions, can be used as a quantity for the degree of crystallinity. [3, 132] The lower W the longer the conjugation length of the P3HT chains. [84, 132, 174, 175] In case of $P3HT_{spin}$ W is 179 meV. A direct comparison of W values to literature is difficult since the polymer parameters like the molecular weight, regioregularity and molecular weight distribution also influence the degree of crystallisation, but W values in the range of 120 meV to 150 meV for samples prepared from chloroform solution and even up to 200 meV for samples prepared from *p*-xylene are reported in literature. [135, 175–177] In summary, structure resolved characterisation methods (AFM and TEM) as well as absorption spectroscopy reveal some crystalline domains in a predominantly amorphous thin film for $P3HT_{spin}$.
In addition $P3HT_{spin}$ has been studied by means of *in-situ* spectroelectrochemistry to directly correlate electrochemical information about redox processes to different chemical species.

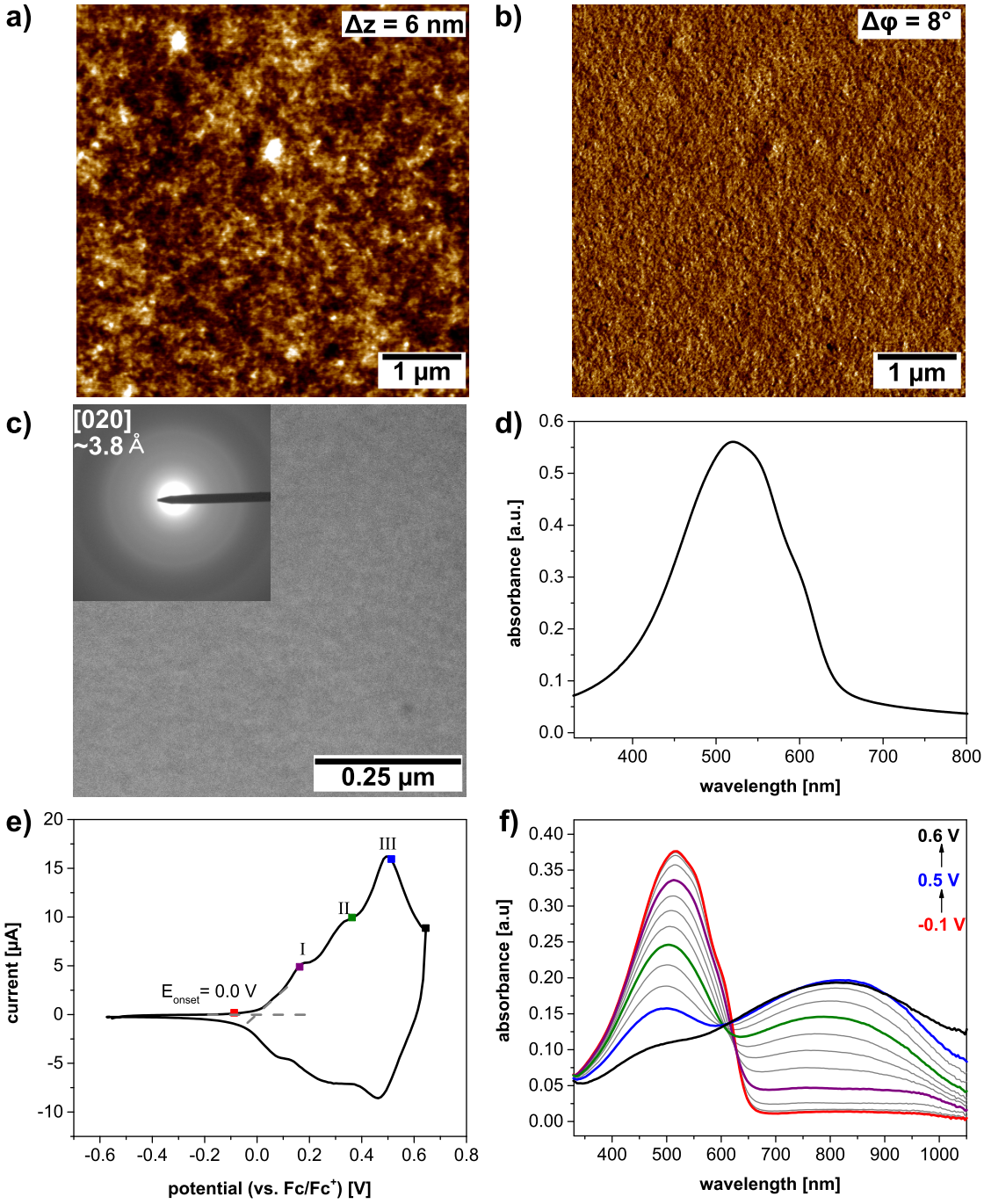

Figure 4.8: Morphological and electrochemical characterisation of a spin coated P3HT film (M_W = 112 kg mol^{-1}, PDI = 2.4), spin coated from chloroform solution (5 mg mL^{-1}) onto ITO electrodes. **a)** and **b)** AFM height and phase images, measured in tapping mode; **c)** TEM bright field image and electron diffraction pattern as inlet, measured with an acceleration voltage of 120 kV; **d)** UV-vis absorption spectrum of the dry film; **e)** cyclic voltammogram measured in 0.1 M NBu_4PF_6 in MeCN with a scan rate of 20 mV s^{-1}; **f)** corresponding UV-vis absorption spectra.

In Fig. 4.8 **e** and **f** the cyclic voltammogram and the corresponding potential dependent absorption spectra are shown. As discussed above the voltammogram consists of one broad anodic wave which is superimposed of three subsignals. In the absorption spectra the band of the neutral $P3HT_{spin}$ (red curve in Fig. 4.8 **f**) decreases and a new broad absorption band centred at 820 nm, attributed to the radical cation, arises with an isosbestic point at 640 nm. This evolution of characteristic absorption bands is maintained during all three subsignals (I: purple curve at 0.15 V; II: green curve at 0.35 V; III: blue curve at 0.5 V). Therefore, in accordance with Skompska et al. [166, 170], all three subsignals are attributed to the formation of the radical cation species of P3HT. At potentials higher than the peak potential of III (black curve at 0.6 V), the absorbance at wavelengths > 1000 nm increases, indicating the formation of the dication species. Potential dependent absorbance evolution curves (see appendix Fig. A.2 **a**) of the absorption bands of the neutral and radical cation species indicate an oxidation onset of 0.0 V which coincides with the value obtained from the voltammogram.

4.2.2. Controlled Crystallisation and Post-Treatment of P3HT Thin Films

In the following different post treatment methods are used to prepare P3HT thin films of controlled morphologies and to further study the influence on the cyclic voltammograms. For the electrochemical characterisation always the second voltammetric cycles have been used, to avoid memory effects which are usually observed in the first voltammetric cycles of polymer films.

As first post treatment method solvent vapour annealing is chosen. In this post treatment method the polymer film is mounted into a tailor-made cell (see Fig. 4.9 **a**) in which the temperature of the substrate and of the surrounding atmosphere can be controlled separately via a peltier element and a water bath, respectively. The composition of the surrounding atmosphere is set by intermixing of a dry nitrogen stream and a solvent saturated nitrogen stream via flow controllers (labelled *A* and *B* in Fig. 4.9 **a**). For the recrystallisation of $P3HT_{spherulite}$ the temperatures of the atmosphere and of the substrate were set to 22 °C and 19 °C respectively. Carbon disulphide (CS_2) was used as solvent due to its high vapour pressure and good solubility of P3HT herein. The overall volume stream (dry nitrogen and CS_2 saturated nitrogen) was set to 20 sccm. In Fig. 4.9 **b** the used annealing procedure as

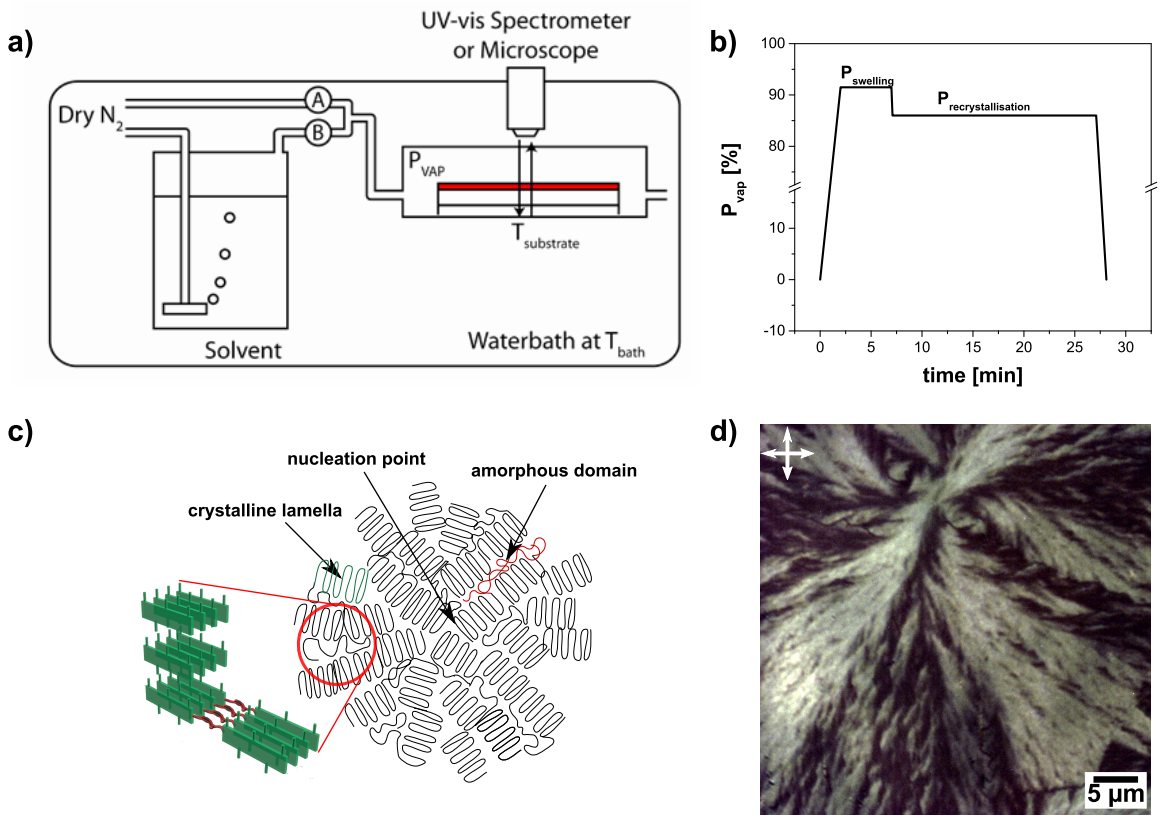

Figure 4.9: Preparation of P3HT spherulites by means of solvent vapour annealing **a)** schematic illustration of the solvent vapour annealing setup; adapted from [90] **b)** solvent vapour pressure (P_{vap}) as function of time for the swelling and recrystallisation of a spin coated P3HT film; **c)** schematic illustration of the polymer chain alignment in a spherulite with π-π stacking in the *edge-on* structure; image courtesy of *Florian Fischer* **d)** POM image with crossed polarisers of a P3HT spherulite prepared by solvent vapour annealing in CS_2.

function of CS_2 vapour partial pressure over time is shown. First the P3HT film is exposed to a high CS_2 pressure to ensure complete swelling of the polymer film to a solution-like state. Afterwards the CS_2 pressure is slightly reduced and kept constant to allow recrystallisation of the film. In the last step the recrystallised film is dried by reducing the CS_2 vapour pressure to zero.

Solvent vapour annealing of P3HT in CS_2 leads to the formation of spherulitic superstructures. Fig. 4.9 **c** illustrates schematically the structure of a P3HT spherulite. The central nucleation point is surrounded by the radial symmetric growth of *edge-on* textured π-π

stacked lamella which are interrupted by disordered, amorphous domains. In the POM image in Fig. 4.9 **d** the central nucleation point (upper middle), the radial symmetric growth of the spherulitic structure and the grain boundary between neighbouring spherulites (bottom right corner) can be seen.

The morphology of the spherulitic superstructure of CS_2 solvent vapour annealed P3HT is also shown in the AFM and TEM images in Fig. 4.10. The AFM height (**a**) and phase (**b**) images in Fig. 4.10 reveal fibre-like structures with a preferred direction. The TEM bright field image in Fig. 4.10 **c** also shows alternating lamella surrounding the central nucleation point in the middle of the image. The electron diffraction (inlet in Fig. 4.10 **c**) shows an intense [020] reflex at 3.6 Å for the π-π stacking in the semi-crystalline lamella, indicating an *edge-on* texture with the π-π stacking direction in plane. The UV-vis absorption spectra of the dry film (Fig. 4.10 **d**) reveals a well defined fine structure with 0-0 and 0-1 transition bands at 600 nm and 550 nm respectively. The exciton bandwidth W calculated according to Equation 16 is 129 meV. Compared to the spin coated film (179 meV, see Fig. 4.8 **d**) the exciton bandwidth is reduced which can be attributed to an increase in the conjugation length of the P3HT chains. [84, 132, 174, 175] The cyclic voltammogram of the spherulitic P3HT sample (Fig. 4.10 **f**) shows a broad anodic redox wave with three subsignals, which correspond to I, II and III described above, and an onset potential at 0.07 V, which is comparable to $P3HT_{spin}$. In comparison to the voltammogram of the spin coated sample (see 4.8 **f**) the current intensity of subsignal I is increased with respect to the peak current of subsignal III. In case of $P3HT_{spherulite}$ it is possible to determine not only the onset potential but also the first half wave potential which is electrochemically more reliable since it compensates kinetic effects. The half wave potential $E_{1/2}$ of $P3HT_{spherulite}$ is 0.13 V. The absorption spectra of the neutral $P3HT_{spherulite}$ measured *in-situ* to the cyclic voltammogram (red curve in Fig. 4.10 **e**) reveal the same fine structure with 0-0 and 0-1 transition bands at 600 nm and 550 nm as in the dry film (see Fig. 4.10 **d**). This is remarkable since the *in-situ* spectra are measured in wet state and during the second voltammetric scan, meaning the film morphology is preserved during the electrochemical charging/ discharging processes which includes intercalation/ expulsion of ions with their solvent shells. Upon oxidation of $P3HT_{spherulite}$ the neutral absorption band decreases and a new broad absorption band of the radical cation centred at 850 nm arises. The oxidation of neutral P3HT to its radical cation

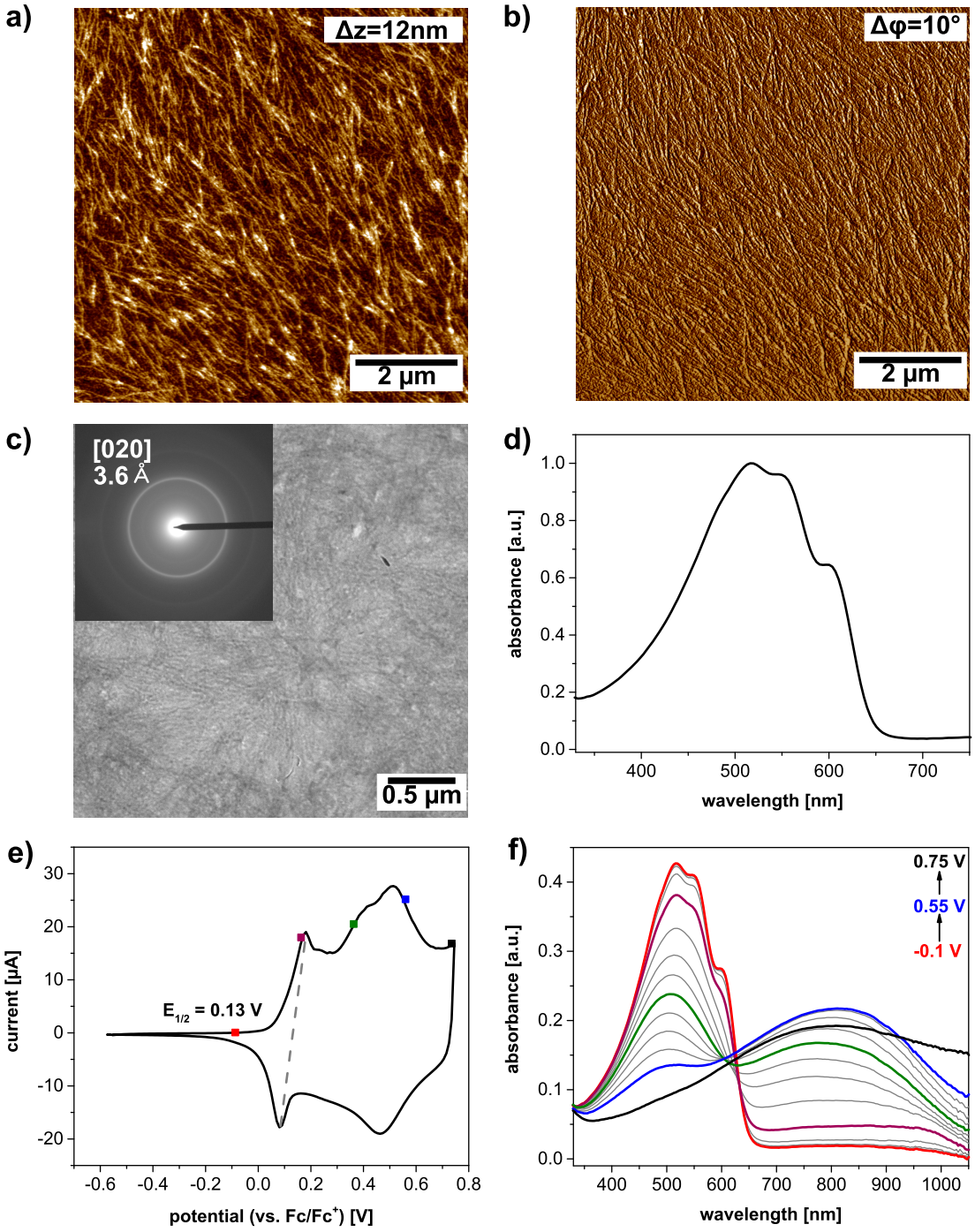

Figure 4.10: Morphological and electrochemical characterisation of P3HT (M_W = 112 kg mol^{-1}, PDI = 2.4) spherulites, spin coated from toluene solution (6 mg mL^{-1}) onto ITO electrodes, solvent vapour annealed in CS_2. **a)** and **b)** AFM height and phase images, measured in tapping mode; **c)** TEM bright field image and electron diffraction pattern as inlet, measured with an acceleration voltage of 120 kV; **d)** UV-vis absorption spectrum of the dry film; **e)** cyclic voltammogram measured in 0.1 M NBu_4PF_6 in MeCN with a scan rate of 20 mV s^{-1}; **f)** corresponding UV-vis absorption spectra.

can also be seen by the formation of an isosbestic point at 640 nm. At potentials higher than the peak potential of subsignal III (blue curve in Fig. 4.10 **e** at 0.55 V) the intensity of the radical cation band decreases and a new band with a wavelength >1000 nm (black curve in Fig. 4.10 **e** at 0.75 V) arises, indicating the beginning formation of the dication species. Potential dependent absorption evolution curves of characteristic absorption bands of the neutral and radical cation form of $P3HT_{spherulite}$ (see Fig. A.2 **c**) reveal restoration of the absorption intensities after the backward scan and indicate chemically reversible charging/ discharging behaviour.

The second method to prepare P3HT films of controlled thin film morphology is crystallisation from solution. The polymer is dissolved in a mixture of a good solvent (chloroform in case of P3HT) and a poor solvent (anisole). In the heat the polymer gets dissolved and upon controlled cooling P3HT starts to crystallise in form of nanowires in the *edge-on* texture with the π-π stacking direction along the fibre axis. [87] AFM height and phase images (Fig. 4.11 **a** and **b**) after spin coating of the nanowires onto ITO electrodes exhibit individual fibres with a diameter of 20 nm and length of up to a few micrometers. The individual fibres can also be seen in the TEM bright field image in Fig. 4.11 **c**. The electron diffraction pattern (inlet in Fig. 4.11 **c**) shows an intense [020] reflex at 3.8 Å for the π-π stacking distance, which indicates an *edge-on* texture with the π-π stacking direction in plane and increased crystallinity. In the UV-vis absorption spectra of the dry film (Fig. 4.11 **d**) again a well defined fine structure of the 0-0 and 0-1 transition bands at 600 nm and 550 nm is visible. The exciton bandwidth W is 124 meV, which is comparable to the other *edge-on* textured sample $P3HT_{spherulite}$, and indicates an increased conjugation length compared to the just spin coated sample $P3HT_{spin}$.

The cyclic voltammogram in Fig. 4.11 **f** exhibits a broad reversible redox wave with superimposed subsignals I, II and III. Similar to the voltammogram of $P3HT_{spherulite}$ not only the onset potential at 0.08 V but also the half wave potential of subsignal I at 0.13 V can be determined. While in case of $P3HT_{spherulite}$ the current intensity of subsignal I was just increased with respect to subsignal III, in the voltammogram of $P3HT_{wires}$ subsignal I becomes the dominant redox wave, indicating a direct correlation of I to the film morphology. The *in-situ* UV-vis absorption spectra shown in Fig. 4.11 **e** reveal similar behaviour as in $P3HT_{spherulite}$. The neutral spectra (red curve at −0.1 V) shows a well defined fine struc-

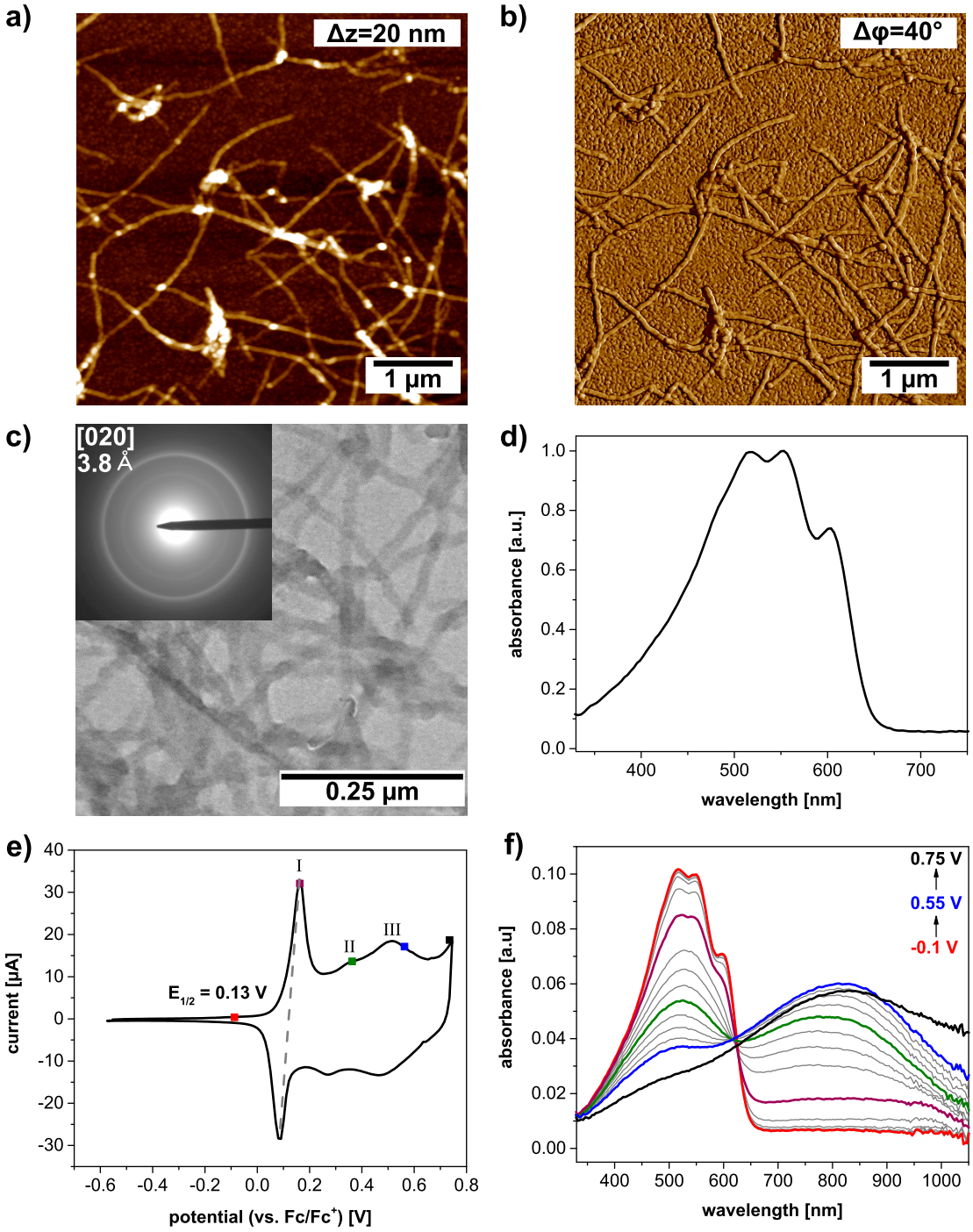

Figure 4.11: Morphological and electrochemical characterisation of P3HT ($M_W = 112\,kg\,mol^{-1}$, PDI = 2.4) nanowires, crystallised from anisole:chloroform (4:1) (c = 0.05 wt%) spin coated onto ITO electrodes. **a)** and **b)** AFM height and phase images; **c)** TEM bright field image and electron diffraction pattern as inlet, measured with an acceleration voltage of 120 kV; **d)** UV-vis absorption spectrum of the dry film; **e)** cyclic voltammogram measured in 0.1 M NBu_4PF_6 in MeCN with a scan rate of $20\,mV\,s^{-1}$; **f)** corresponding UV-vis absorption spectra.

ture with an intense 0-0 transition of the π-π stacked domains at 610 nm which is preserved even in wet state of the film and after a first charging/ discharging cycle. Upon oxidation of $P3HT_{wires}$ the neutral absorption band decreases and the absorption band of the radical cation centred at 820 nm arises with an isosbestic point at 640 nm. Beginning formation of the dication species is observed at 0.75 V (black curve) which is higher than the peak potential of subsignal III. Thus all three subsignals I, II and III correspond to the formation of the radical cation. Potential dependent intensity evolution curves of characteristic absorption bands, shown in Fig. A.2 **b**, reveal complete restoration of the intensities of the neutral and radical cation bands, indicating a reversible redox reaction.

High temperature rubbing is used as a third post treatment method. After the film deposition via blade coating, the polymer film is placed on a movable heat plate. The temperature is set to be just below the melting temperature of the polymer. When the desired temperature is reached, a rotating cylinder which is covered with a microfibre cloth, is pressed onto the polymer film and the film is moved laterally underneath the rotating cylinder. With this method P3HT films with large area alignment of the polymer chains mainly in the *face-on* texture are generated. [178]

AFM characterisation of rubbed P3HT films is difficult since, due to the mechanical stress during the rubbing process, the film surface is significantly roughened, which can lead to height differences of more than 100 nm (for the corresponding height image see Fig. A.1). In Fig. 4.12 **a** the AFM phase image shows oriented features. A better method for the morphological characterisation of rubbed polymer films is TEM. In the bright field image (Fig. 4.12 **b**) a periodic lamellar-like structure is observed with a periodicity of 20 nm and the lamellar orientation perpendicular to the rubbing direction. According to Hamidi-Sakr et al. the observed contrast is caused by the alteration of amorphous and crystalline domains. [92] The inlet in Fig. 4.12 **b** shows the electron diffraction pattern of $P3HT_{rubbing}$ with sharp [100], [200] and [300] reflexes at 17.3 Å, 8.3 Å and 5.5 Å, a ring-like reflex for the [020] reflex at 3.8 Å and an arc for the [002] reflex at 3.9 Å. The pattern is characteristic for a fibre-like P3HT texture and originates from a distribution of crystals which have the chain axis in parallel to the rubbing direction but varying contact planes. A similar pattern is also reported by Brinkmann et al. for epitaxial crystallisation of P3HT on 1,3,5-trichlorobenzene. [179] To study not only small area but large area alignment direction

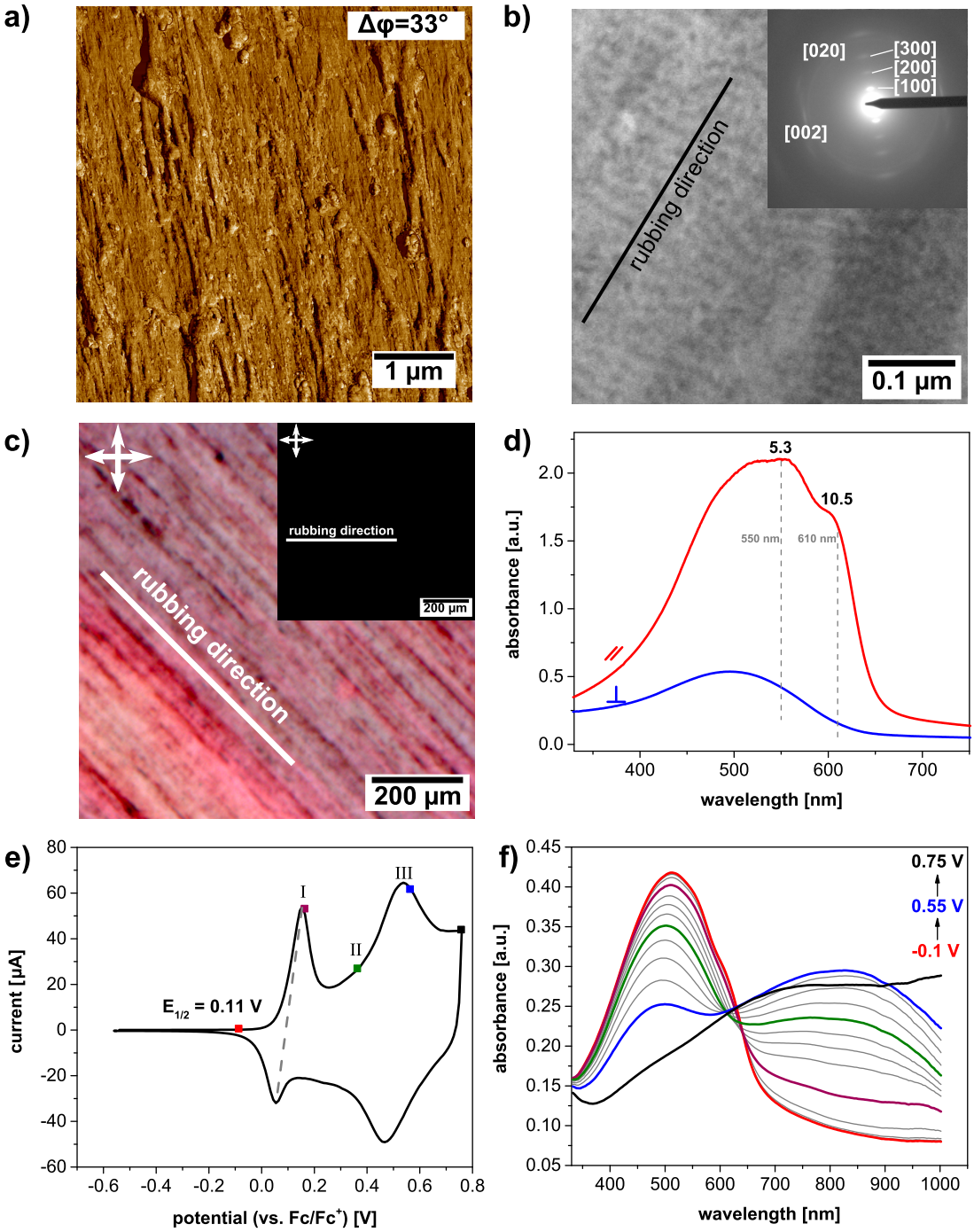

Figure 4.12: P3HT (M_W = 112 kg mol^{-1}, PDI = 2.4) after blade coating from *o*-dichlorobenzene solution (5 mg mL^{-1}) onto ITO electrodes and high temperature rubbing at 230 °C. **a)** AFM phase image; **b)** TEM bright field image and electron diffraction pattern as inlet; **c)** POM images with rubbing direction oriented in 45° and in 90° (inlet); **d)** polarised absorption spectra of the dry film with polarisers in parallel (red curve) and in perpendicular (blue curve) to the rubbing direction; **e)** cyclic voltammogram measured in 0.1 M NBu_4PF_6 in MeCN with a scan rate of 20 mV s^{-1}; **f)** corresponding absorption spectra.

dependent polarised optical microscopy has been performed. In Fig. 4.12 **c** the POM images with the polariser perpendicular (inlet) and at 45° angle to the rubbing direction are shown. With the rubbing direction perpendicular to the polariser the image appears black, while at 45° the image appears bright pinkish with stripe-like features along the rubbing direction, indicating macroscopic orientation of the polymer chains in the rubbed film. The same effect is observed with polarised absorption spectroscopy. The UV-vis absorption spectra of the dry $P3HT_{rubbing}$ film with polariser parallel (red curve) and perpendicular (blue curve) to the rubbing direction are shown in Fig. 4.12 **d**. The spectrum in parallel (red curve) reveals a typical spectrum of a semi-crystalline P3HT film with a fine structure and 0-0 and 0-1 transitions at 610 nm and 550 nm respectively. The absorption spectrum with the polariser perpendicular (blue curve) lacks the fine structure, it is blue shifted and the overall intensity is decreased. The dichroic ration, which can be used as a dimensionless quantity of the alignment, of 10.5 for the π-π stacking band at 610 nm shows successful alignment. Hamidi-Sakr et al. reported dichroic ratios up to 20 for rubbed P3HT of smaller molecular weight. [92]
The cyclic voltammogram of $P3HT_{rubbing}$ reveals a broad, reversible anodic wave with distinct subsignals at 0.1 V and 0.5 V, which can be attributed to I and III described above. Subsignal II at 0.35 V can be identified but is not well pronounced. The current intensity of subsignal I is comparable to subsignal III, meaning not only in the predominantly *edge-on* crystallised $P3HT_{spherulite}$ and $P3HT_{wires}$ but also in the predominantly *face-on* crystallised $P3HT_{rubbing}$ subsignal I is increased with respect to III. The onset potential and half wave potential can be determined to 0.07 V and 0.11 V respectively. The *in-situ* measured absorption spectra in Fig. 4.12 **e** and intensity evolution curves in Fig. A.2 **d** show similar behaviour to all other P3HT samples described above.
In summary the morphology of P3HT thin films has a significant influence on the electrochemical behaviour. With increasing regioregularity, from regiorandom electropolymerised P3HT to regioregular chemically synthesised P3HT, the number of superimposing subsignals in anodic redox wave increases from two to three. The newly observed subsignal in the regioregular P3HT is located at low oxidation potential, meaning the onset potential and HOMO energy level are shifted from 0.20 V to 0.00 V or −5.30 eV to −5.10 eV respectively. The oxidation onset potentials and corresponding HOMO energy levels, calculated with a correction factor of −5.1 [101], are summarised in Table 4.1. The three P3HT samples with

Table 4.1: Overview of the oxidation onset and half wave potentials of all studied P3HT samples with HOMO orbital energies calculated with the correction factor of −5.1 eV according to [101].

P3HT sample	E_{onset} [V]	$E^{HOMO}{}_{onset}$ [eV]	$E_{1/2}$ [V]	$E^{HOMO}{}_{1/2}$ [eV]
electro	0.20	-5.30	/	/
drop	0.13	-5.23	/	/
spin	0.00	-5.10	/	/
spherulite	0.07	-5.17	0.13	-5.23
wires	0.08	-5.18	0.13	-5.23
rubbing	0.07	-5.17	0.11	-5.21

controlled thin film morphology, prepared by solvent vapour annealing, crystallisation from solution and high temperature rubbing, reveal similar spectroelectrochemical behaviour. The cyclic voltammograms consist of three superimposing subsignals which correspond to the subsignals observed for the spin coated, regioregular $P3HT_{spin}$. The current intensity of the low oxidation potential subsignal (I) increases significantly with respect to subsignal III, which is usually the dominant redox wave. In case of $P3HT_{wires}$ subsignal I becomes the dominant redox wave. The two predominantly *edge-on* samples ($P3HT_{spherulite}$ and $P3HT_{wires}$) reveal onset potentials of 0.07 V and 0.08 V and the predominantly *face-on* sample $P3HT_{rubbing}$ of 0.07 V, which is in the range of the just spin coated $P3HT_{spin}$. In contrast to $P3HT_{spin}$, from which only the onset potential can be determined, for the three controlled morphology samples also the half wave potentials of subsignal I can be identified. The *edge-on* samples reveal a half wave potential of 0.13 V and the *face-on* sample of 0.11 V. The onset and half wave potentials of all P3HT samples as well as the corresponding HOMO energy levels are summarised in Table 4.1. By performing *in-situ* spectroelectrochemical characterisation of all P3HT samples, subsignal I, II and III are all attributed to the oxidation of neutral P3HT to the radical cation. At potentials higher than the peak potential of III also formation of the dication is observed. Intensity evolution curves of characteristic absorption bands indicate chemically reversible redox reactions. The absorption spectra of the neutral P3HT samples show defined fine structures with pronounced 0-0 transition bands of the π-π stacked

domains at 610 nm even in wet state and after multiple charging/ discharging cycles, indicating a preservation of the film morphology during the electrochemical characterisation. Morphological characterisation via various microscopy techniques and spectroscopy reveal unstructured semi crystalline $P3HT_{spin}$ with few π-π stacked domains. Applying of post annealing methods lead to successful growth of spherulitic structure ($P3HT_{spherulite}$), nanowires ($P3HT_{wires}$) and large area alignment ($P3HT_{rubbing}$) with decreased exciton bandwidths, indicating larger conjugation lengths and increased degrees of crystallinity. Therefore, in accordance with Skompska et al. [166, 170], subsignal I in the voltammograms is attributed to the first oxidation of crystalline domains in the P3HT films.

4.3. Binary P3HT:$PC_{61}BM$ Blends

P3HT is usually used with $PC_{61}BM$ ([6,6]-phenyl C_{61} butyric acid methyl ester) as binary donor:acceptor blend in organic solar cells. [50, 70, 72, 180, 181] Literature has shown that the blend morphology has a crucial influence on the power conversion efficiency of the solar cells. [6, 17] In the following, possible influences of the blend film morphology on the electrochemical behaviour of P3HT:$PC_{61}BM$ are studied.

In Fig. 4.13 **a** the cyclic voltammogram of $PC_{61}BM$ in solution reveals two reversible redox waves which correspond to the reduction of the neutral species to the radical anion and dianion respectively. The half wave potential of the first reduction is at $-1.02\,V$ which amounts to a LUMO energy level of $-4.08\,eV$. To identify redox signals and characteristic absorption bands in the binary blend system, first pure $PC_{61}BM$ films are studied by means of *in-situ* spectroelectrochemistry. The cyclic voltammogram of a $PC_{61}BM$ film, spin coated from chloroform solution onto ITO electrodes, in Fig. 4.13 **b** reveals three cathodic redox waves. All three cathodic redox waves are electrochemically irreversible, which can be seen by the hampered discharging signals in the backwards scan of the cyclic voltammogram. During the electrochemical experiment in thin films, dissolution of the fullerene film is observed, which might explain the irreversibility of the cathodic redox waves. Due to the irreversibility of the redox waves, not the half wave potential but the onset potential is determined. In Fig. 4.13 **b** the onset potential of $PC_{61}BM$ is at $-1.0\,V$ which corresponds to a LUMO energy level of $-4.1\,eV$. In Fig. 4.13 **c** the *in-situ* absorption spectra are shown. In the neutral state (red curve at $-0.5\,V$) $PC_{61}BM$ exhibits a narrow absorption band 335 nm. Upon reduction

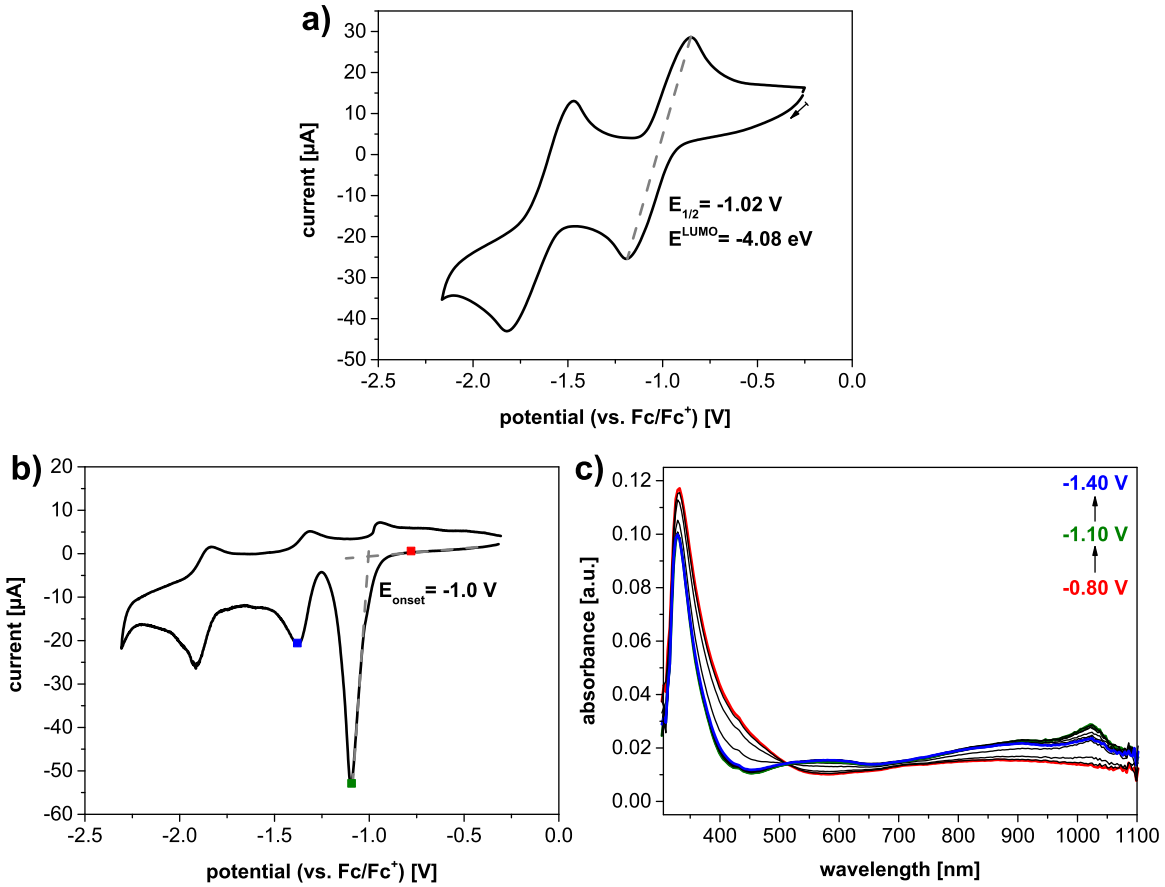

Figure 4.13: Electrochemical and *in-situ* spectroelectrochemical characterisation of $PC_{61}BM$; **a)** cyclic voltammogram of $PC_{61}BM$ in solution (0.02 M) measured in 0.1 M NBu_4PF_6 in THF with a scan rate of 50 mV s^{-1}; **b)** cyclic voltammogram of $PC_{61}BM$ spin coated from chloroform solution (5 mg mL^{-1}) onto ITO electrodes, measured in 0.1 M NBu_4PF_6 in MeCN with a scan rate of 50 mV s^{-1}; **c)** corresponding UV-vis absorption spectra of the $PC_{61}BM$ film.

the neutral band decreases and a new, broad band between 900 nm and 1050 nm with a peak maximum at 1025 nm of the radical anion arises. In addition there is a weak broad absorption band for the radical anion centred at 600 nm. Since it is only very weak and in the wavelength range of the P3HT neutral band, this particular absorption band will not be considered in the following discussion of the blend system.

The *in-situ* spectroelectrochemical characterisation of the binary blend films focuses on the oxidation behaviour of P3HT since the first reduction of $PC_{61}BM$ does not show an influence from the intermixing with the donor material. For sake of completeness, the cyclic

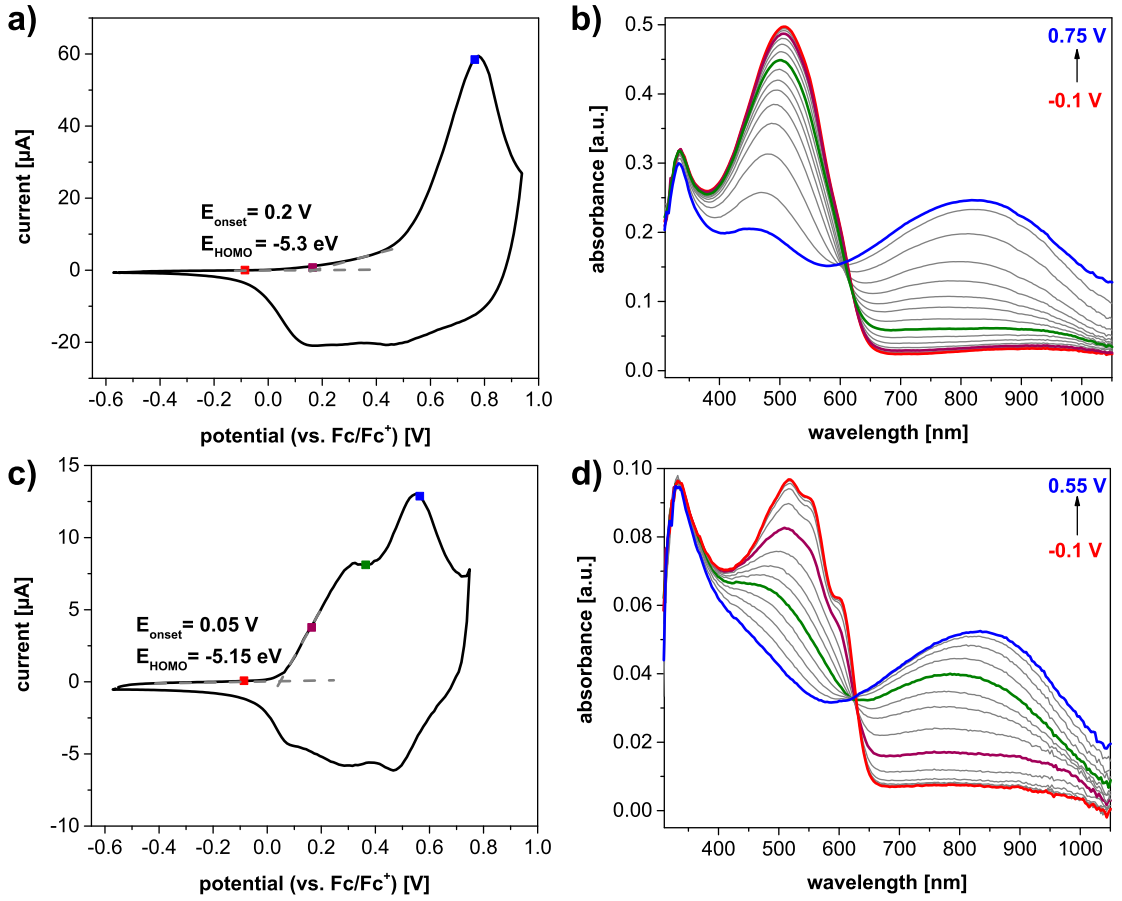

Figure 4.14: *In-situ* spectroelectrochemical characterisation of P3HT:$PC_{61}BM$ blend films (1:1 w/w) spin coated from chloroform solution (overall concentration 5 mg mL^{-1}) onto ITO electrodes; left column: cyclic voltammograms measured in 0.1 M NBu_4PF_6 in MeCN with a scan rate of 20 mV s^{-1}; right column: corresponding UV-vis absorption spectra; **a)**, **b)** after spin coating; **c)**, **d)** after thermal annealing at 150 °C for 1 h.

voltammograms of the P3HT:$PC_{61}BM$ reductions are shown in Fig. A.4 in the appendix.

In Fig. 4.14 **a** and **b** the cyclic voltammogram and the corresponding *in-situ* absorption spectra of a P3HT:$PC_{61}BM$ blend film (1:1 w/w, overall concentration of 5 mg mL^{-1}) are shown. The blend is prepared with the same P3HT batch (M_w = 112 kg mol^{-1}, PDI = 2.4) used above in the characterisation of the morphological influence on the cyclic voltammogram of neat P3HT. The film deposition conditions (solvent, concentration, electrode material, spin coating parameters) were chosen to be identical to $P3HT_{spin}$ described above, to ensure direct comparability of the blend system and the neat polymer films. The voltammogram

of the anodic scan of the P3HT:$PC_{61}BM$ blend film (Fig. 4.14 **a**) shows only one anodic wave with a peak potential of 0.7 V, which corresponds to subsignal III described above. Subsignals I and II, which are attributed to ordered, π-π stacked domains, are suppressed. Since it is difficult to determine if some oxidation already takes place at potentials lower than 0.5 V *in-situ* spectroelectrochemistry is a particularly valuable tool. From the potential dependent intensity evolution curves of the P3HT neutral (green curve, at 510 nm) and radical cation (violet curve, at 810 nm) absorption bands in Fig. A.5 **a** the proper onset potential of 0.2 V, which is in the range of electropolymerised P3HT, can be determined. The *in-situ* absorption spectra of the P3HT:$PC_{61}BM$ blend film during the oxidation are shown in Fig. 4.14 **b**. In the neutral state the absorption spectrum of the blend film (red curve at -0.1 V) reveals the bands of neutral $PC_{61}BM$ and neutral P3HT at 335 nm and 520 nm respectively. Upon oxidation the band of neutral $PC_{61}BM$ at 335 nm remains almost unchanged (the small decrease is due to overlapping with the neutral P3HT band) while the band of neutral P3HT at 520 nm decreases and the band of the P3HT radical cation at 800 nm arises with an isosbestic point at 615 nm. Thus, just as in case of neat P3HT, the anodic redox wave corresponds to the first oxidation of P3HT in the binary blend. An other interesting observation from the absorption spectrum of the neutral blend (red curve in Fig. 4.14 **b**) is that the typical fine structure of 0-0 and 0-1 transitions at 600 nm and 550 nm is suppressed, indicating lack of ordered P3HT domains in the blend film, which also correlates to the suppressed oxidation subsignals I and II in the voltammogram. Thus the formation of crystalline P3HT domains seems to be hampered by the intermixing with the fullerene acceptor material.

P3HT:$PC_{61}BM$ blends for application in organic solar cells are typically thermally annealed, since literature has shown that this simple post treatment leads to a better phase separation in the donor:acceptor blend and to increased power conversion efficiencies. [6, 17] In Fig. 4.14 **c** and **d** the *in-situ* spectroelectrochemical characterisation of a thermally annealed P3HT:$PC_{61}BM$ blend is shown. The blend is prepared similar to the blend described above with one additional post annealing step (150 °C for 1 h). In the cyclic voltammogram (Fig. 4.14 **c**) the oxidation waves at lower potential (subsignal I and II in case of neat P3HT) are regained and the onset potential is determined to be 0.05 V which is comparable to $P3HT_{spin}$. In the *in-situ* absorption spectra shown in Fig. 4.14 **d** the same spectroelectrochemical be-

Table 4.2: Overview of onset potentials, the frontier orbital energy levels and the effective band gap (E_g) of P3HT:$PC_{61}BM$ binary blend films (non-annealed and thermally annealed); calculated with the correction factor of −5.1 eV according to [101].

sample	$E_{ox.}$ [V]	E^{HOMO} [eV]	$E_{red.}$ [V]	E^{LUMO} [eV]	E_g [eV]
$P3HT_{spin}$	0.00	-5.10	/	/	/
P3HT:$PC_{61}BM$	0.20	-5.30	-1	-4.1	1.2
P3HT:$PC_{61}BM$ annealed	0.05	-5.15	-1	-4.1	1.05

haviour as in the non-annealed blend is observed, meaning the broad anodic redox wave in the voltammogram corresponds to the first oxidation of P3HT to its radical cation. In contrast to the non-annealed blend, the fine structure in the absorption band of the neutral P3HT (red curve in Fig. 4.14 **d**) is well pronounced in the thermally annealed blend film. In summary, the spectroelectrochemical data indicate that during spin coating of the binary P3HT:$PC_{61}BM$ blend film the formation of crystalline P3HT domains is hindered. By applying thermal post annealing, the crystalline domains in the blend film are regained due to the increased mobility of the polymer chains.

The frontier orbital energy levels and effective band gaps of the non-annealed and thermally annealed P3HT:$PC_{61}BM$ blends are calculated according to Equations 4 and 5 and are summarised in Table 4.2. The reduction potential (see voltammograms in Fig. A.4) and therefore the LUMO level of $PC_{61}BM$ is not influenced by the post annealing step. Regarding the HOMO energy levels, the thermally annealed blend (0.05 V or −5.15 eV respectively) is in the range of $P3HT_{spin}$, while the non-annealed blend is shifted towards higher potential and lower energy (0.20 V or −5.30 eV) respectively. The shift of the HOMO energy level of the non-annealed blend correlates to an increased effective band gap (from 1.05 eV to 1.2 eV) and therefore to a decreased efficiency in the P3HT:$PC_{61}BM$ solar cell.

5. Electrochemical Characterisation of the Oxidative Crosslinking of PVTPA-*co*-PS Copolymers

The synthesis of the studied PVTPA homopolymer and PVTPA-*co*-PS copolymers with various repeating unit ratios have been performed by *Corinne Rost-Schmidt*. Parts of the experimental work on the basic voltammetric characterisation, the *in-situ* spectroelectrochemical characterisation and the chemical doping have been performed by *Fabian Moczko*, *Lisa Eisele*, *Felix Goerigk* and *Lukas Stein* under my supervision within the scope of their bachelor thesis [182, 183] and research internship [184, 185] respectively.

5.1. State of the Art

The molecule family of triarylamines and their close relatives the carbazoles with all their derivatives are versatile materials for various organic electronic devices and have gained huge scientific and industrial interest in the last two decades. In the following, a brief overview of the most important properties and fields of application is given. The main focus is set on derivatives of triphenylamine since Chapters 5.2 to 5.4 are dedicated to the electrochemical, optical and electronic properties of polyvinyltriphenylamine (PVTPA) and its copolymers with polystyrene.

In 1987 Ohsawa et al. [85] introduced triphenylamine as a new conducting organic material and reported on the basic electrochemical and spectroscopic properties. Molecular triphenylamine has a high hole transport mobility and can be oxidised easily. Therefore triphenylamine and its derivatives are suitable hole transport materials for the application in organic electronic devices like organic light-emitting diodes (OLED) [23, 186], organic photovoltaics [187–189], electrochromic windows [190, 191], organic field effect transistors (OFET) [192] and as electrode material in organic batteries [86]. For the industrial production of such organic electronic devices, the polymeric derivatives, which contain the triphenylamine redox group in either the main or the side chain, are particularly interesting since they combine the promising electronic properties of the small-molecular derivatives with the possibility to use simple and cheap large-area deposition techniques like roll-to-roll or inkjet-printing. [186, 192, 193]

The most important application for triarylamine and carbazole derivatives is the organic

light-emitting diode. [23] In general OLEDs are of huge interest for both the scientific community and the industry, since they can be used for novel display applications. The advantage of OLED displays compared to the state-of-the-art liquid crystal displays (LCD) is that no back light is needed and therefore deeper black levels can be reached. This also means that OLED displays can be manufactured thinner and therefore light-weighted. In addition, OLED displays show a lower power consumption, a faster response time, a higher contrast ratio and wider viewing angles than LCD devices. Especially the so-called PLEDs (polymer light-emitting diodes) are promising for the large-scale industrial production, due to their processability by simple and cheap solution processes like printing techniques. For these devices polymeric derivatives of triarylamines and carbazoles are promising hole transport materials. [194] The two main reasons are, compared to other organic conducting materials, the fast charge transport and the formation of stable cations which decreases the air-sensitivity of these redox polymers in comparison to π-conjugated polymers significantly. [186]

Besides the application of triarylamines in OLED applications, they are also interesting materials for photovoltaic devices. In recent years the perovskite solar cells made a swift rise in the scientific community due to their exceptional high power conversion efficiencies of about 20% PCE. In these photovoltaic devices polytriarylamine is used as the hole transport layer material. [187, 188] Triarylamine derivatives are used for the application in all-organo solar cells too. Lindner et al. [189] used the nitroxide-mediated living radical polymerisation [195] for the synthesis of well-defined blockcopolymers with a hole transport block and an electron transport block. The basic concept is to use the microphase separation of these blockcopolymers to tune the inner structuring of the photo active layer. For the electron transport and hole transport blocks poly(perylene-bisimide-acrylate) and polyvinyltriphenylamine were used respectively. [189]

An other promising application for triarylamines are energy storage systems like organic batteries which utilise novel light-weight, flexible and non-toxic electrode materials. First attempts with π-conjugated polymers have failed due to cell potential fluctuation caused by the charge delocalisation on the conjugated polymer backbone. [196] In a recent approach the π-conjugated polymers have been replaced by redox polymers which possess stable cell potentials due to the electronic isolation of the charges on the redox groups. Hereby the main

focus has been spent on derivatives of triaryamines, carbazoles, arylnitroxides, nitroxides and ferrocene. [86]

An important property of triarylamines is their electrochromic behaviour, meaning the coupling of photo and electro activity. Electrochromic devices include devices like electrochromic windows, display applications and electronic paper. Since triarylamines are easily oxidised and form stable cations which involves a distinct colour switch herein, these molecules are promising materials for all sorts of electrochromic devices. In addition, due to their high charge carrier mobilities and the possibility to deposit thin layers in the nanometer range, the usage of triarylamines result in an increased switching time of electrochromic devices. [190, 191]

A rather exotic application of triarylamine derivatives is the development of new explosive detection sensors. The basic concept is to use conducting polymer based sensoring devices for the easy to handle, cheap and fast detection of nitroaromatics. The detection is based on an electron transfer reaction from an electron-rich polymer donor material to the electron-poor nitroaromatics. To increase the donor strength of the sensor material and therefore improve the detector sensitivity, triphenylamine or carbazole moieties are incorporated into conducting polymers. [197]

An other rather exotic application of triarylamine derivatives is the formation of so-called microporous polymer networks. These materials consist of highly cross-linked organic architectures, which possess high porosities and large surface areas as well as good chemical stability. These structures are interesting as host matrices for the intercalation of functional organic molecules which makes them promising materials for application in sensors, as gas storage materials and for catalysis. The synthetic challenge is to produce such cross-linked architectures under mild conditions and without expensive catalysts. Preis et al. presented a Friedel-Crafts-like route for the synthesis of various microporous polymer networks by using triarylamine moieties as the coupling groups. [198]

5.2. Synthesis and Polymer Characterisation

The studied PVTPA homopolymer and PVTPA-*co*-PS copolymers, the molecular structure is shown in Fig. 5.1, have been synthesised by *Corinne Rost-Schmidt* via free radical polymerisation with azobisisobutyronitrile (AIBN) as initiator. The detailed procedures for

the synthesis of the monomer and all polymers are shown in the appendix (Chapter A.3). In summary, seven polymers with varying repeating unit ratios were gained. The used monomer feed ratios of vinyltriphenylamine to styrene were varied in the range of 100:0 to 5:95 to obtain a series of copolymers with varying redox group density. The molecular weights and polydispersity indices (PDI) of the polymers were determined by gel permeation chromatography and are summarised in Table 5.1. To determine the ratio of the repeating units (polyvinyltriphenylamine to polystyrene) elemental analysis was performed and the ratios were calculated from the percentage portion of nitrogen to carbon, disregarding the respective end groups. The rounded values of the repeating unit ratios are listed in Table 5.1 as well.

From the ^{1}H and ^{13}C NMR spectra of the copolymers (see Chapter A.3) it is difficult to distinguish between a successful copolymerisation to random PVTPA-*co*-PS or homopolymerisation of the two monomers to a blend of PVTPA and PS. An alternative method to characterise the copolymers is differential scanning calorimetry (DSC). In case of a blend of the homopolymers or a blockcopolymer two separate glass transition temperatures are expected, while in case of a random copolymer only one T_g is expected. The DSC curves of all studied polymers (PVTPA-*co*-PS copolymers, PVTPA and PS homopolymers and a PVTPA:PS blend (1:1 w/w)) are shown in Fig. 5.2 **a** and the glass transition temperatures are summarised in Table 5.2. As expected, for the PVTPA and PS homopolymers one glass transition temperature at 141 °C and 91 °C respectively and for the blend of the two homopolymers two glass transition temperature at 91 °C and 140 °C, which matches the

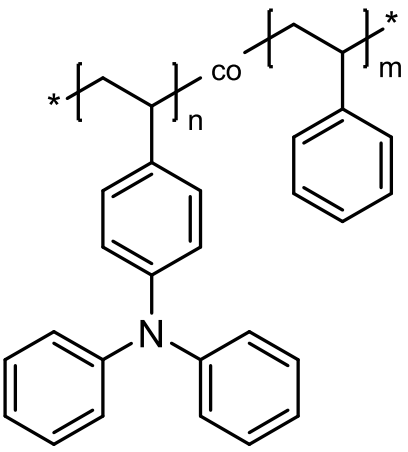

Figure 5.1: Molecular formula of the PVTPA-*co*-PS copolymers.

Table 5.1: Characteristic parameters (molecular weight and polydispersity indices (PDI)) of the polyvinyltriphenylamine homopolymer and polyvinyltriphenylamine-*co*-polystyrene copolymers.

monomer feed ratio (vinyltriphenylamine : styrene)	M_n [kg mol^{-1}]	PDI	repeating unit ratio [a]
100:0	19	1.66	100:0
50:50	25	1.54	50:50
25:75	20	1.57	30:70
20:80	15	1.67	25:75
15:85	15	1.59	20:80
10:90	21	1.60	15:85
5:95	15	1.62	10:90

[a] calculated from the nitrogen-to-carbon ratio determined by elemental analysis.

individual T_g of the homopolymers, are observed. For each of the PVTPA-*co*-PS copolymers only one T_g is observed. The glass transition temperatures of the copolymers vary with the repeating unit ratio between 134 °C and 105 °C; the lower the amount of PVTPA the lower the T_g. According to the Fox equation (Eq. 17) the T_g of a random copolymer can be calculated:

$$\frac{1}{T_g} = \sum_i \frac{\omega_i}{T_{g,i}} \tag{17}$$

with T_g the glass transition temperature of the copolymer, ω_i the mass fraction of monomer i and $T_{g,i}$ the glass transition temperature of the respective homopolymer. The measured glass transition temperatures of the PVTPA-*co*-PS copolymers, the PS and PVTPA homopolymers and the blend of the homopolymers as well as the calculated T_g (calculated according to Eq. 17) as function of the TPA amount are shown in Fig. 5.2 **b**. The T_g of the copolymers follow the progression of the Fox equation. Therefore, from the number of observed glass transition temperatures and the T_g progression according to the Fox equation, successful copolymerisation of styrene and vinyltriphenylamine to random PVTPA-*co*-PS copolymers can be assumed.

Table 5.2: Glass transition temperatures of the PVTPA-*co*-PS copolymers with varying vinyltriphenylamine:styrene repeating unit ratios, the polyvinyltriphenylamine and polystyrene homopolymers and a 1:1 (w/w) blend of the homopolymers.

repeating unit ratio (vinyltriphenylamine : styrene)	T_g [°C]
50:50	134
30:70	122
25:75	121
20:80	118
15:85	116
10:90	105
PVTPA homopolymer	141
PS homopolymer	91
blend (1:1 w/w)	91, 140

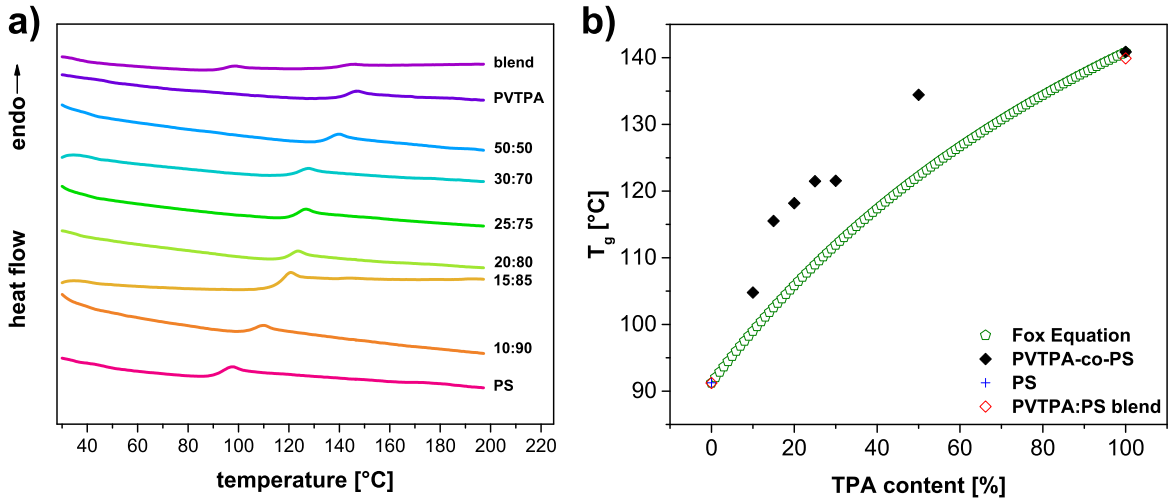

Figure 5.2: Differential scanning calorimetry characterisation of PVTPA-*co*-PS copolymers; **a)** DSC curves of the heating cycles measured with heating rates of $10\,\mathrm{K\,min^{-1}}$; **b)** glass transition temperatures (T_g) of PVTPA-*co*-PS copolymers (black dots), polystyrene (blue cross), polystyrene-polyvinyltriphenylamine blend (red diamonds) and calculated T_g according to the Fox equation (green pentagons) as function of TPA content.

5.3. Charging Behaviour of PVTPA-*co*-PS as Function of the TPA Content

5.3.1. Electrochemical Characterisation

Gold Electrodes

The basic electrochemical characterisation of the redox processes in the PVTPA-*co*-PS copolymer films is performed by means of cyclic voltammetry on planar gold electrodes. In Fig. 5.3 **a** the consecutive first (black curve) and second (red curve) voltammetric cycles of the PVTPA homopolymer are shown. In the forward scan of the first cycle a sharp anodic redox half wave with a peak potential of 0.62 V is observed. During the backward scan no respective cathodic redox half wave is observed, indicating an irreversible oxidation reaction. The backward scan reveals two cathodic half waves, which do not correspond to the anodic half wave in the forward cycle and can be interpreted as the two-step reduction of a redox active species generated in a follow-up reaction due to the irreversible oxidation of the PVTPA polymer. In the consecutive second voltammetric cycle (red curve in Fig. 5.3 **a**) only two reversible redox waves with half wave potentials of 0.43 V and 0.54 V are observed. The sharp anodic half wave from the first cycle is absent and the two cathodic half waves in the first and second cycle are identical. In Fig. 5.3 **b** the consecutive tenth to twenty-fifth cycles also only reveal the two reversible redox waves without the irreversible anodic half wave from the first cycle, indicating an electrochemical stable redox system which is generated after the anodic scan of the first cycle. The lower current values in the later CV cycles (5.3 **b**) compared to the second cycle (red curve in Fig. 5.3 **a**) is due to a repositioning of the working electrode in-between the measurements which result in dissimilar electro-active electrode areas (varied depth of polymer film immersion into the electrolyte).

The electrochemical redox behaviour of the PVTPA homopolymer observed in the voltammograms can be explained by the mechanism of oxidative cross-coupling of triphenylamine groups described in literature. [8, 199] The mechanism adapted from Yurchenko et al. is shown in Fig. 5.4. Upon oxidation of the triphenylamine (TPA) groups the respective radical cation is formed. The positive charge is located at the nitrogen atom and the spin-density of the unpaired electron is highest in the *para* position. As a chemical follow-up reaction the TPA radical cations dimerise under proton elimination in the *para* position to form a neutral

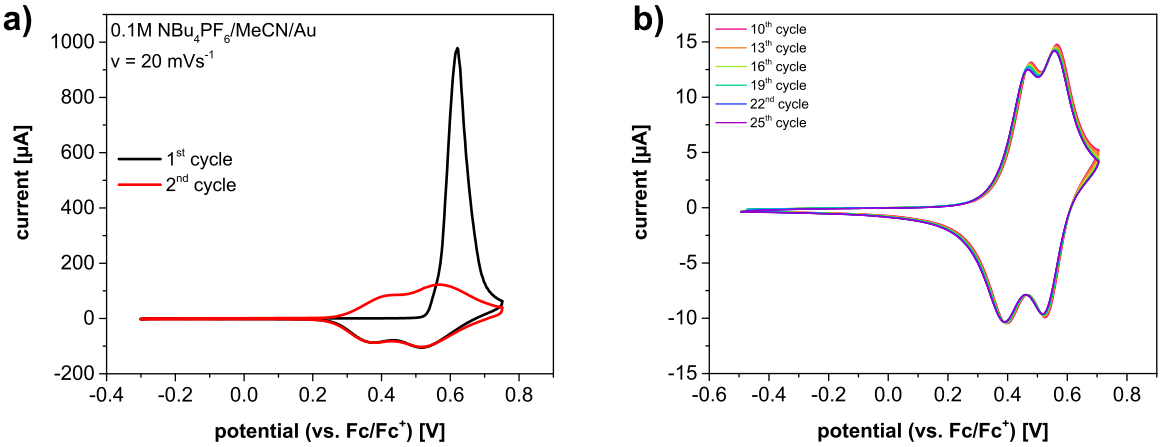

Figure 5.3: Electrochemical crosslinking and characterisation of PVTPA films spin coated onto gold electrodes. Cyclic voltammograms measured in 0.1 M NBu_4PF_6 in MeCN with a scan rate of 20 mV s^{-1}; **a)** first and second cycle; **b)** tenth to twenty-fifth cycle.

tetraphenylbenzidine (TPB) group. Since the conjugated π-system of the TPB is enlarged, the oxidation potential of TPB is lower than of TPA. Therefore the formed neutral TPB undergoes immediate oxidation via a radical cation form ($TPB^{+\cdot}$) to its dication (TPB^{2+}) in which the benzoid-like electronic structure is transformed into a quinoid-like structure. This electrochemical and chemical reaction cascade can also be described by the *ECE* mechanism (sequence of an electrochemical reaction with a chemical follow-up reaction and a subsequent electrochemical reaction) described by Speiser [97].

In summary the irreversible anodic redox half wave in the first cycle (black curve in Fig. 5.3 **a**) corresponds to the formation of the $TPA^{+\cdot}$ radical cation which then undergoes an irreversible dimerisation reaction under proton elimination. Since the oxidative dimerisation is initialised at a potential higher than the oxidation potential of the formed TPB groups, the TPB^{2+} dication is generated immediate. During the cathodic scan the two redox half waves correspond to the two reduction steps from the TPB^{2+} dication to the $TPB^{+\cdot}$ radical cation and the neutral TPB. In the second cycle the two redox waves of the two-step oxidation of the TPB groups reveal a 1:1 current ratio, indicating electrochemically reversible redox reactions. The potentials of all observed redox processes are summarised in Table 5.3.

Due to the dimerisation reaction of the TPA groups attached to the polymer backbone, PVTPA undergoes intermolecular and intramolecular cross-linking of the polymer chains.

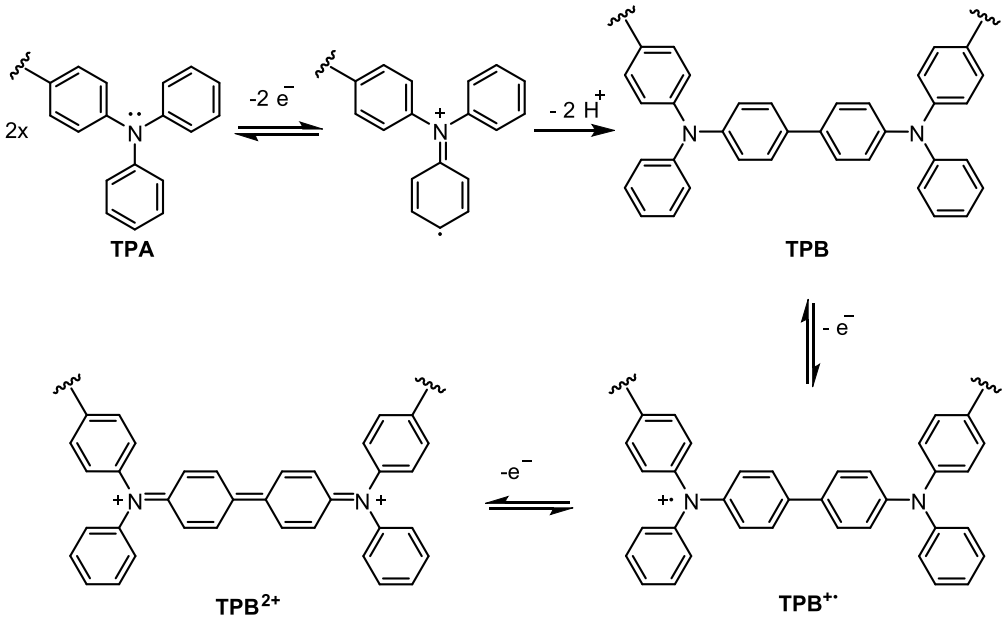

Figure 5.4: Mechanism of the electrochemically induced dimerisation reaction of triphenylamine (TPA) to tetraphenylbenzidine (TPB) groups with subsequent reversible two-step oxidation of the formed TPB groups; adapted from [8].

The cross-linking density can be reduced by the copolymerisation of vinyltriphenylamine with a chemically related but redox inactive monomer like styrene. To characterise the influence of the reduced cross-linking density on the electrochemical redox behaviour cyclic voltammograms of PVTPA-*co*-PS copolymer films spin coated onto planar gold electrodes were measured under the same conditions as the PVTPA homopolymer shown in Fig. 5.3. The voltammograms (first cycles in black and second cycles in blue) of the homopolymer as well as five additional copolymers with polyvinyltriphenylamine to polystyrene ratios in

Table 5.3: Potentials of all redox processes involved in the oxidative dimerisation of the PVTPA homopolymer; determined by means of cyclic voltammetry on planar gold electrodes measured with a scan rate of 20 mV min^{-1} in 0.1 M NBu_4PF_6.

redox process	parameter	potential (vs. Fc/Fc^+)
$TPA \rightarrow TPA^{\cdot+}$	E_{peak}	0.62 V
$TPB \rightleftharpoons TPB^{\cdot+}$	$E_{1/2}$	0.43 V
$TPB^{\cdot+} \rightleftharpoons TPB^{2+}$	$E_{1/2}$	0.54 V

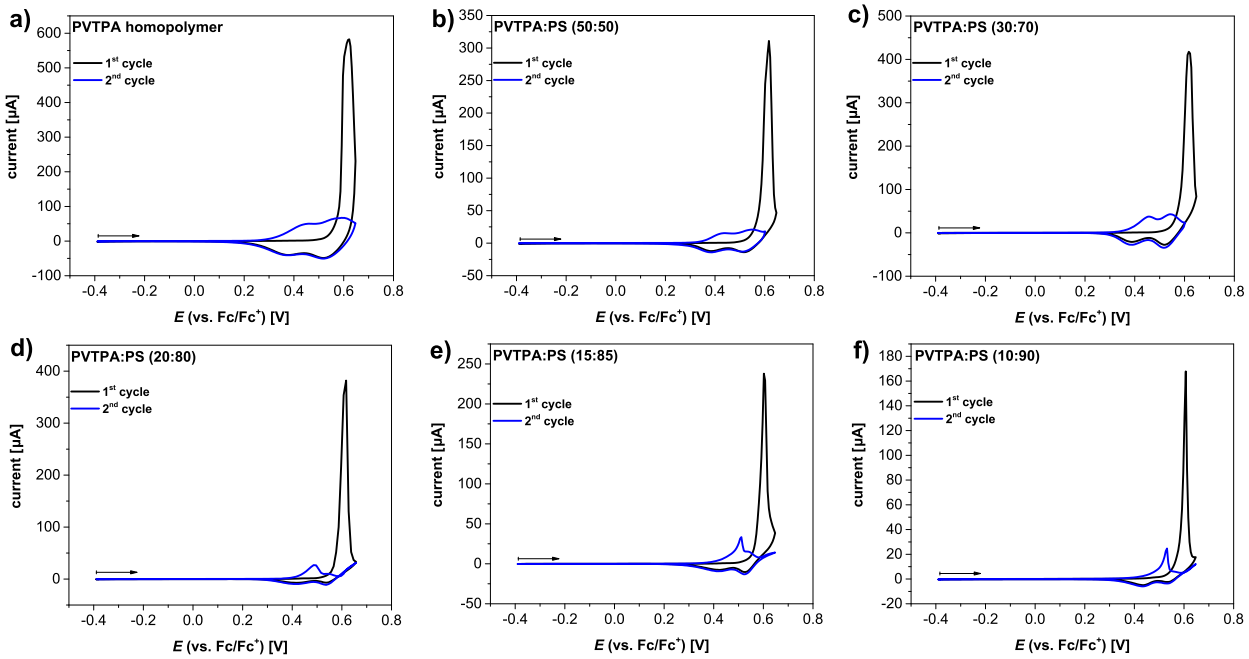

Figure 5.5: Cyclic voltammograms of PVTPA-*co*-PS copolymers; **a)** homopolymer, **b)** 50 mol%, **c)** 30 mol%, **d)** 20 mol%, **e)** 15 mol% and **f)** 10 mol%; first cycles in black and second cycles in blue respectively; measured in 0.1 M NBu_4PF_6/MeCN with a scan rate of 20 mV s^{-1} on gold electrodes.

the range of 50 mol% to 10 mol% are shown in Fig. 5.5. The first cycles of all investigated polymers reveal a sharp, irreversible anodic half wave associated to the oxidative dimerisation reaction indicating successive cross-linking even for the lowest TPA content polymers. The peak potentials of the dimerisation half waves are in the range of 0.60 V to 0.62 V. An overview of the potentials of all redox processes in all studied polymers is given in Table 5.4. The voltammograms of the second cycles of the polymers with high TPA content (homopolymer, 50 mol% and 30 mol%) shown in Fig. 5.5 **a-c** reveal similar reversible, two-step redox behaviour of the cross-linked polymers. The half wave potentials of the first and second redox step are at 0.41 - 0.42 V and 0.54 - 0.55 V respectively. Interestingly for the polymers with low TPA amount (20 mol%, 15 mol% and 10 mol%) the anodic half waves of the voltamograms of the second cycles (blue curves in Fig. 5.5 **d-f**) differ from their high TPA content analogues. While the backward scans of all voltammograms reveal the same reduction half waves as in the high TPA content polymers, the anodic half waves of the two-step oxidation process from neutral TPB to the TPB^{2+} dication species start to superimpose

Table 5.4: Potentials of all redox processes in PVTPA-*co*-PS copolymers with varying repeating unit ratios; determined by means of cyclic voltammetry on planar gold electrodes measured with a scan rate of 20 mV min^{-1} in 0.1 M NBu_4PF_6 in MeCN.

polymer	redox process	parameter	potential (vs. Fc/Fc^+)
homopolymer	TPA $\rightarrow$ $TPA^{\cdot+}$	E_{peak}	0.62 V
homopolymer	TPB $\rightleftharpoons$ $TPB^{\cdot+}$	$E_{1/2}$	0.41 V
homopolymer	$TPB^{\cdot+}$ $\rightleftharpoons$ TPB^{2+}	$E_{1/2}$	0.55 V
50 mol%	TPA $\rightarrow$ $TPA^{\cdot+}$	E_{peak}	0.62 V
50 mol%	TPB $\rightleftharpoons$ $TPB^{\cdot+}$	$E_{1/2}$	0.41 V
50 mol%	$TPB^{\cdot+}$ $\rightleftharpoons$ TPB^{2+}	$E_{1/2}$	0.54 V
30 mol%	TPA $\rightarrow$ $TPA^{\cdot+}$	E_{peak}	0.62 V
30 mol%	TPB $\rightleftharpoons$ $TPB^{\cdot+}$	$E_{1/2}$	0.42 V
30 mol%	$TPB^{\cdot+}$ $\rightleftharpoons$ TPB^{2+}	$E_{1/2}$	0.54 V
20 mol%	TPA $\rightarrow$ $TPA^{\cdot+}$	E_{peak}	0.62 V
20 mol%	TPB $\rightleftharpoons$ $TPB^{\cdot+}$	$E_{1/2}$	0.45 V
20 mol%	$TPB^{\cdot+}$ $\rightleftharpoons$ TPB^{2+}	$E_{1/2}$	0.54 V
15 mol%	TPA $\rightarrow$ $TPA^{\cdot+}$	E_{peak}	0.60 V
15 mol%	TPB $\rightleftharpoons$ $TPB^{\cdot+}$	$E_{1/2}$	0.46 V
15 mol%	$TPB^{\cdot+}$ $\rightleftharpoons$ TPB^{2+}	$E_{1/2}$	0.53 V
10 mol%	TPA $\rightarrow$ $TPA^{\cdot+}$	E_{peak}	0.61 V
10 mol%	TPB $\rightleftharpoons$ $TPB^{\cdot+}$	$E_{1/2}$	0.48 V
10 mol%	$TPB^{\cdot+}$ $\rightleftharpoons$ TPB^{2+}	$E_{1/2}$	n.d. [a]

[a] anodic half wave not determinable; cathodic half wave at 0.53 V.

and reveal one sharp half wave with the second half wave as associated shoulder instead of an individual half wave. In case of the 20 mol% and 15 mol% polymers the first oxidation half wave dominates. The shoulders representing the second half wave are still well pronounced which allows for the determination of the half wave potentials of the two-step oxidation process. The half wave potentials are at 0.45 - 0.46 V and 0.53 - 0.54 V respectively. In case of the 10 mol% polymer the half wave potential of the first oxidation to the $TPB^{+\cdot}$ radical

cation species is at 0.48 V but the shoulder which corresponds to the second anodic half wave is too poorly resolved to determine the half wave potential of the second oxidation step to the TPB^{2+} dication species.

Since the sharp anodic half wave in the second cycle is only observed for the copolymers with low amount of the cross-coupling redox groups, it comes to mind to relate this unusually shaped CV signal to non-complete cross-coupling during the first cycle and consecutive overlapping of the anodic half waves caused by the two-step oxidation of TPB groups and left over TPA groups being oxidised to their radical cations. However, after the sharp anodic half wave is completed, the current declines back to the current back ground in the potential range in which the cross-linking half wave is observed in the first cycle, which contradicts the idea of half wave overlapping with remaining non-cross-linked redox groups.

In general, the nature of the current-potential curve in a cyclic voltammogram is based on three main parameters: the formal redox potentials (thermodynamic parameter) and the electron transfer kinetics at the electrode surface and ion diffusion kinetics in the electrolyte (kinetic parameters). [96, 100] To be able to narrow down the cause of the sharp anodic half wave for the low TPA-amount copolymers, possible influences on these three basic parameters are discussed in the following.

For a thermodynamic explanation of the formation of the sharp anodic half wave, a shift of the formal redox potentials of the involved redox reactions caused by a changed electrochemical environment (e.g. due to the insulating polystyrene matrix) is required. However, such a shift of the formal redox potentials is expected to also influence the cathodic half waves. Since no such shift of the cathodic half waves is observed a thermodynamic cause of the formation of the sharp anodic half wave is unlikely.

The electron transfer kinetics is mainly influenced by contact resistances and the compatibility of the electrode work function and the sample redox potential. The work function of the electrode material is defined by the electrode composition and therefore unchanged. For the sample redox potential no significant changes but only a small shift in the $E_{1/2}$ values of the first redox step from 0.41 V to 0.48 V is observed. A change in the contact resistance e.g. due to partial de-wetting could be caused by different mechanical properties of the deposited copolymer films due to the increased polystyrene amount. However, in this case an effect on the anodic cross-linking half wave in the first voltammetric cycle is expected

too. Since the observed peak potential of this half wave remains almost constant (0.60 V to 0.62 V) over the whole series of copolymers, an influence of a changing contact resistance seems unlikely too and it is concluded that the sharp anodic half wave in the second cycle of the low TPA-amount copolymers is unlikely to be caused by an effect of the electron transfer kinetics.

The third main parameter influencing a cyclic voltammogram is the ion diffusion kinetics, which describes the mass transport of charged species in the electrolyte. In general the ion diffusion kinetics is influenced by the electrolyte parameters (conducting salt, solvent, concentration) as well as mechanical and energetic barriers due to porous electrode materials or generation of ionic double layers at the electrode surface. Since the same electrolyte was used for the successful measurements of the PVTPA homopolymer and the high TPA-amount copolymers, an incompatibility of the chosen solvent/ conducting salt couple is ruled out. The ionic double layers are generated at the electrode surface due to a mismatch of the electrode polarisation potential to the electrolyte equilibrium potential. By deposition of the copolymer films as a partially insulating intermediate layer between the electrode and the electrolyte the specific formation of the ionic double layers may be influenced by the chemical composition of the polymer layer.

Upon charging of the copolymer films the corresponding counterions from the electrolyte have to diffuse into the polymer films to counter balance the charges and restore electrostatic net neutrality. In the electrolyte, the ions are surrounded by a solvent shell which has to be intercalated into the polymer film alongside the ions and results in a swelling or shrinking of the polymer film upon charging or discharging respectively. Since the used electrolyte solvent is orthogonal with respect to the solubility of the polymer, the ion/ solvent intercalation into the bulk of the polymer film has to overcome this mechanical barrier which results in an impeded counterion diffusion process. An influence of the copolymer composition on the counter ion diffusion processes is plausible due to the increasing amount of insulation polystyrene in the low-TPA-content copolymers. To be able to evaluate the possible influence of the repeating units ratio on ion movement processes, the mass evolution of the copolymer films upon electrochemical charging/ discharging is studied in chapter 5.3.2 by means of electrochemical quartz crystal microbalance.

ITO Electrodes

For advanced *in-situ* spectroelectrochemical characterisation a transparent electrode material like indium tin oxide (ITO) is required. Unlike the gold electrodes used in the previous chapter, the ITO electrodes are not perfectly planar but consist of a porous packing of ITO nano-particles coated onto a glass substrate, which leads to a higher surface roughness. [200, 201]

At first basic cyclic voltammetry characterisation of the PVTPA-*co*-PS copolymer films on ITO electrodes has been performed to identify possible influences of the electrode material on the oxidative cross-linking of the TPA groups and reversible redox reactions of the TPB groups described above. In Fig. 5.6 **a** and **b** the first and second voltammetric cycles of the PVTPA homopolymer are shown. The experimental parameters (0.1 M NBu_4PF_6 in MeCN, scan rate of $20\,mV\,s^{-1}$) and the used setup with the respective pseudo-reference electrode are identical to the electrochemical characterisation on gold electrodes described above. In the first cycle (Fig. 5.6 **a**) the sharp anodic half wave with a peak potential of 0.63 V associated to the cross-linking reaction and consecutive two-step oxidation of the formed TPB units is observed. However in the backward scan of the first cycle almost no current flow is observed. Only a weak and broad current signal centred at about −0.3 V is visible. Since the oxidation potential of the formation of the TPA radical cation which afterwards undergoes the cross-linking reaction is similar on both gold and ITO electrodes, no significant shift of the reduction potentials of the two-step reduction of the formed TPB^{2+} dication to its neutral species is expected. The lack of the reductive half waves with only a broad current signal at lower potential indicates significant charge trapping in the polymer film on ITO electrodes. The second cycle (Fig. 5.6 **b**) which has been measured consecutively reveals only a steady current increase with an onset potential of about 0.4 V but no distinct anodic half wave which may be due to the residual trapped charges from the first cycle. In the backward scan two broad redox half waves centred at 0.2 V and −0.3 V respectively are observed, indicating some discharging of the TPB^{2+} dication species. Still the potential range of the observed reduction half waves do not match the reduction potentials measured on gold electrodes (0.52 V and 0.37 V respectively). This strong charge trapping behaviour was also observed for the 50 mol% copolymer but not for the lower TPA content copolymers. A common experimental problem with ITO electrodes is de-wetting of organic solvent poly-

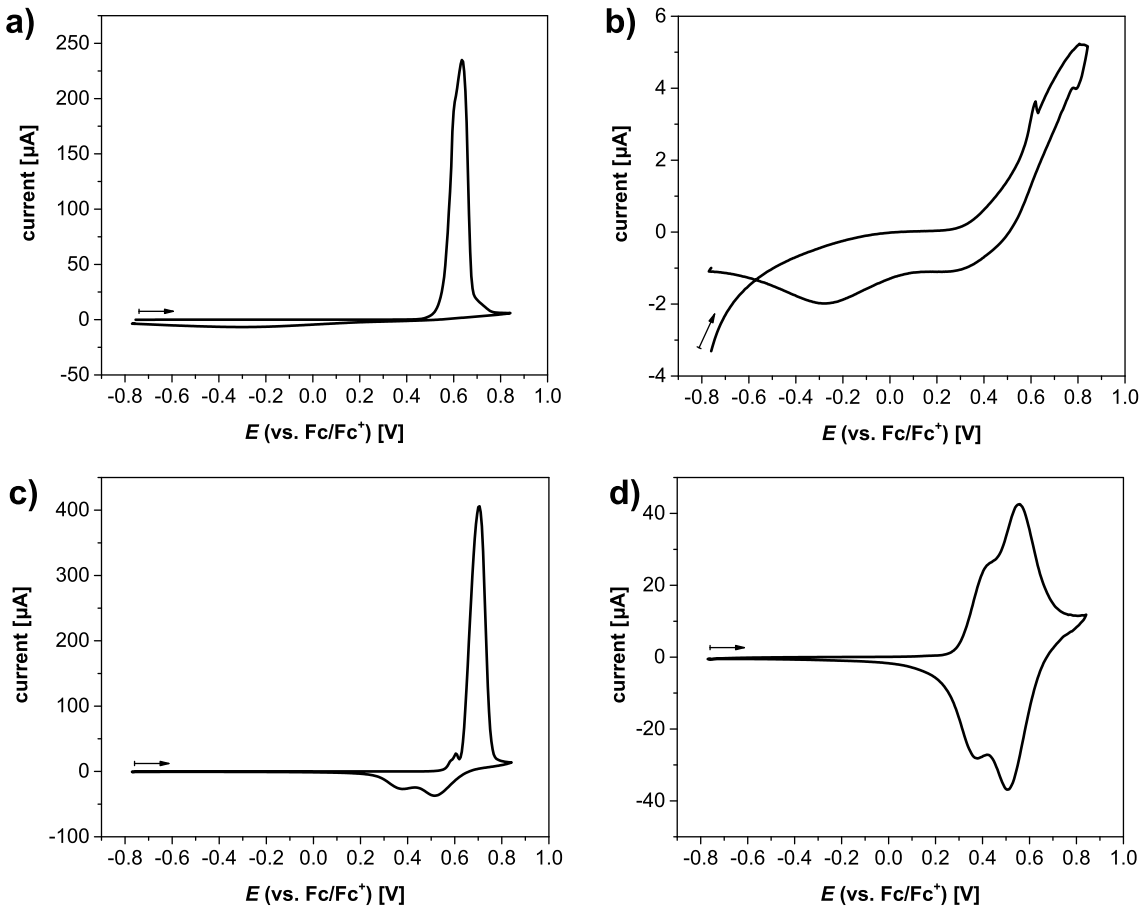

Figure 5.6: Cyclic voltammograms of PVTPA on ITO electrodes, measured in 0.1 M NBu_4PF_6 in MeCN with a scan rate of 20 mV s^{-1}. Left column: first cycles, right column: second cycles before (**a**, **b**) and after (**c**, **d**) thermal annealing for 1 h at 150 °C.

mer solutions during the spin coating process due to the highly polar ITO surface. Such de-wetting in combination to the generally rough surface of the ITO electrodes may lead to poor polymer-ITO contact and can therefore hamper the electron transfer at the polymer-ITO interface.

One possible procedure to improve the polymer-electrode contact is thermal annealing. In Fig. 5.6 **c** and **d** the first and second cycle of a thermally annealed PVTPA homopolymer film are shown. The sample preparation has been performed identically to the sample shown in Fig. 5.6 **a** and **b** with only an additional thermal annealing step at 150 °C for 1 h. The measurement was also conducted under the same conditions as in case of the non-annealed sample and the samples on gold. In the first cycle (Fig. 5.6 **c**) the anodic half wave of

the cross-linking reaction with a peak potential of 0.70 V is observed. During the backward scan the two cathodic half waves of the two-step reduction of TPB^{2+} to neutral TPB are visible. The peak potentials of the two reduction half waves are at 0.52 V and 0.38 V respectively, which matches the potentials measured on gold electrodes. After the two reduction half waves the current traces back to the base line indicating complete discharging of the PVTPA film. In the second cycle (5.6 **d**) two overlapping reversible redox waves with half wave potentials of 0.53 V and 0.40 V are observed, indicating unhampered charging and discharging of the PVTPA film. The half wave potentials are similar to the ones determined from measurements on gold electrodes. The improved charge transport can also be seen by the difference in the current values. The non-annealed and thermally annealed samples were prepared from the same polymer solution with the same spin coating parameters and the size of the polymer covered ITO electrodes was similar which means that the amount of redox active groups in both experiments are similar. Nevertheless the absolute current values are significantly higher in the thermally annealed PVTPA sample which again indicates a hampered charge transfer to the electrode in the non-annealed sample.
In general, please note that the small current signals at 0.6 V and at 0.5 V in Fig. 5.6 **c** and **b** are probably measurement artefacts due to a spike in the current input of the potentiostat or accidental movement of the electrolyte or electrodes rather than real redox half waves.
In summary, the cyclic voltammograms of non-annealed PVTPA on ITO electrodes reveal successful cross-linking but significant charge trapping which would hamper further electrochemical characterisation of PVTPA on ITO. By applying an additional thermal annealing step to the sample preparation the charge trapping can be prevented and the observed electrochemical behaviour with all characteristic redox potentials are similar to measurements on planar gold electrodes. This behaviour was only observed for the PVTPA homopolymer and the 50 mol% PVTPA-*co*-PS copolymer but not for the lower TPA content copolymers. This observation hints for a morphological or contact resistance problem at the polymer-electrode interface rather than a thermodynamic effect.

Electrochemical Impedance Spectroscopy

To gain deeper insights into the electron transfer at the polymer-ITO interface, electrochemical impedance spectroscopy (EIS) of non-annealed and thermally annealed PVTPA

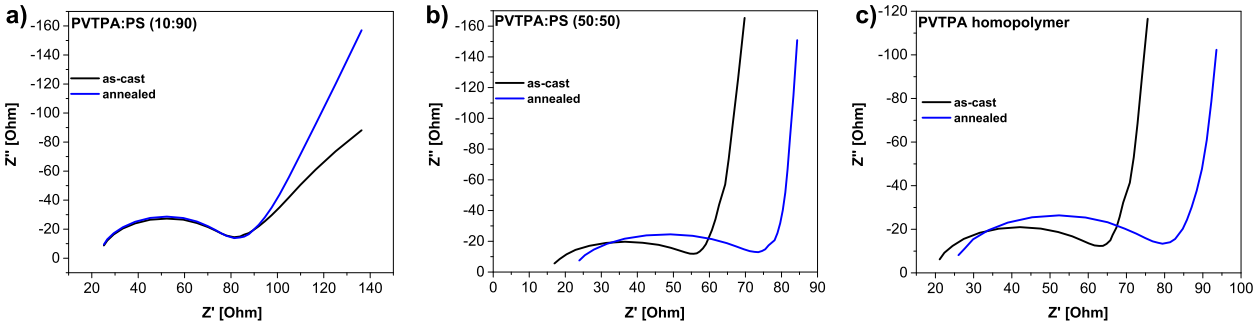

Figure 5.7: Nyquist plots of PVTPA-*co*-PS films before (black curves) and after (blue curves) thermal annealing for 1 h at 150 °C; **a)** 10 mol%, **b)** 50 mol% and **c)** PVTPA homopolymer; measured on ITO electrodes in 0.1 M NBu_4PF_6 in MeCN with an amplitude of 50 mV.

homopolymer and PVTPA-*co*-PS (50 mol% and 10 mol%) films has been performed. The experimental parameters were kept similar to the cyclic voltammetry experiment described above (0.1 M NBu_4PF_6 in MeCN, Ag/AgCl pseudo reference electrode). The EIS measurements were performed by applying an alternating external field with an amplitude of 50 mV and a frequency range of 100 mHz to 1 MHz. The applied amplitude is kept lower than the cross-linking potential to gain information of the initial electric circuit without any disturbance from a redox reaction. Therefore the EIS measurements provide information about contact resistances, ion diffusion in the electrolyte due to the polarisation of the electrode and ionic double layer capacitors at the interfaces. [109]

In Fig. 5.7 the *Nyquist* plots of the initial (black curves) and thermally annealed (blue curves) 10 mol% copolymer (**a**), the 50 mol% copolymer (**b**) and the homopolymer (**c**) are shown. According to Malev et al. [109] the Nyquist plot of electro-active polymer films can be described by the *Randles* equivalent circuit. From this, information about the electrolyte resistance (R_s), the electron transfer resistance (R_{ct}) at the polymer-electrode interface and the ionic double layer capacitance (C_{dl}) at the polymer-electrolyte interface can be gained from the high-frequency range. The left ending point and the diameter of the semicircle corresponds to R_s and R_{ct} respectively. The double layer capacitance can be calculated according to Equation 18: [109]

$$C_{\mathrm{dl}} = \frac{1}{\omega \cdot R_{\mathrm{ct}}} \tag{18}$$

with ω being the frequency of the semicircle vertex. The R_{ct} and C_{dl} values determined from

Table 5.5: Electrochemical impedance spectroscopy characterisation of the effect of thermal annealing of PVTPA-*co*-PS films; charge transfer resistance (R_{ct}) and double layer capacitance (C_{dl}) determined according to Malev et al. [109].

polymer	annealing	R_{ct}	C_{dl}
100:0	/	41.8 Ω	131 nF
	thermal	53.4 Ω	104 nF
50:50	/	38.6 Ω	142 nF
	thermal	49.7 Ω	110 nF
10:90	/	56.2 Ω	97 nF
	thermal	58.0 Ω	94 nF

the *Nyquist* plots presented in Fig. 5.7 are summarised in Table 5.5. For the low TPA-amount copolymer (10 mol%) the calculated charge transport resistance and double layer capacitance values are not influenced by the thermal annealing step. In contrast, the PVTPA homopolymer and the 50 mol% copolymer do show an influence of the thermal annealing to both R_{ct} and C_{dl}. The charge transfer resistance increases upon thermal annealing, indicating a higher contact resistance. Simultaneously the double layer capacitance, which is caused by the formation of an ionic double layer at the polymer-electrolyte interface due to a non-equilibrium potential between the polymer-modified electrode and the electrolyte, decreases. A pronounced ionic double layer acts as an energetic barrier for the counter ions, which are required to intercalate into the polymer film to counter balance the charges [100] and can therefore cause significant charge trapping in the non-annealed polymer films like shown in Fig. 5.6 **a** and **b** for the PVTPA homopolymer.

In-situ Spectroelectrochemistry

In-situ spectroelectrochemistry is a versatile tool to further characterise the electrochemically induced cross-linking reaction of to PVTPA-*co*-PS copolymers since this method combines the redox information from cyclic voltammetry with the chemical information derived from absorption spectroscopy. Since the electrochemical characterisation of the PVTPA-*co*-PS copolymers on gold electrodes showed similar redox behaviour for the high TPA content

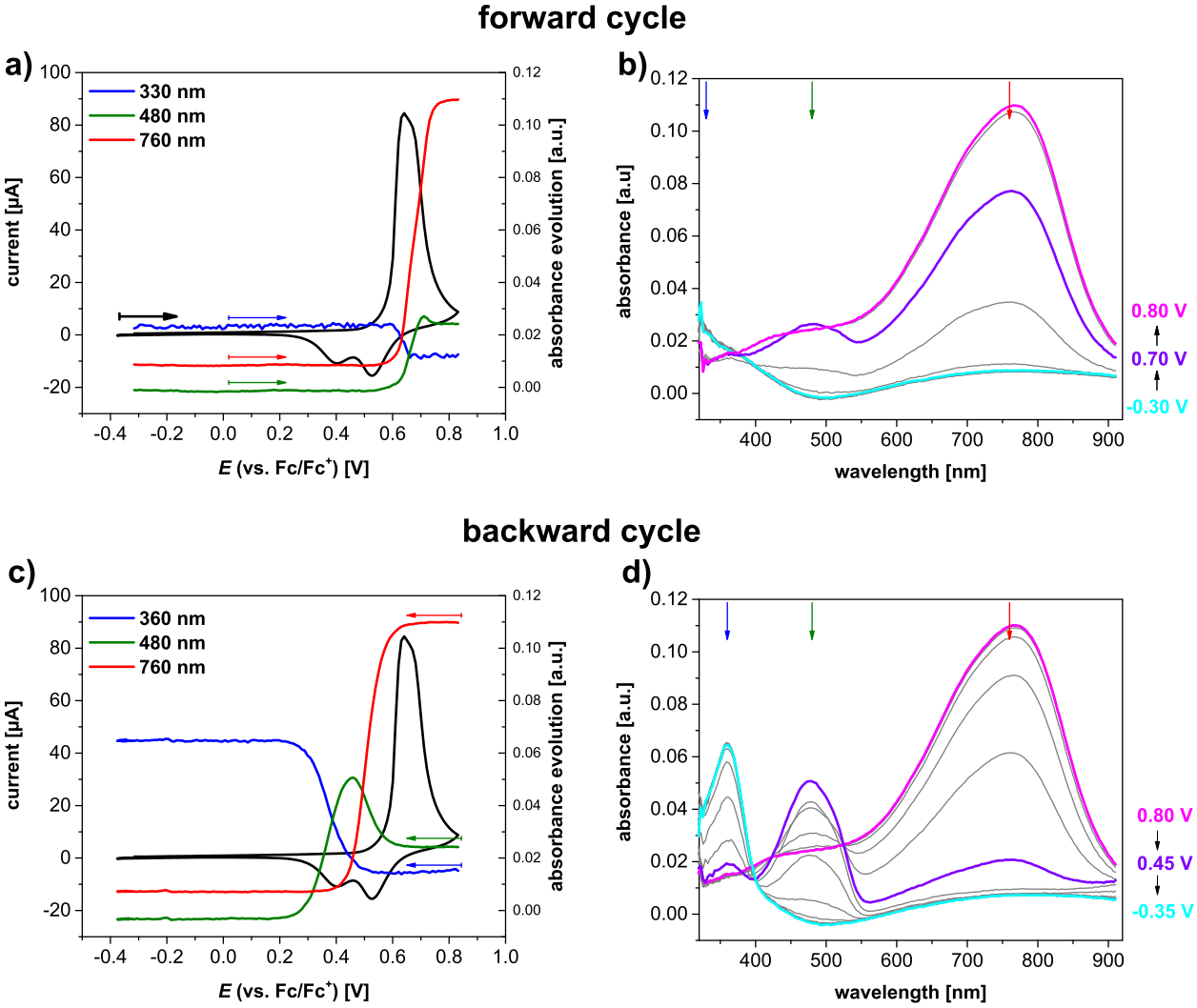

Figure 5.8: *In-situ* spectroelectrochemical characterisation of PVTPA-*co*-PS (30:70 mol%); measured in 0.1 M NBu_4PF_6 in MeCN with a scan rate of 20 mV s^{-1} on ITO electrodes. Left column: cyclic voltammogram of the first cycle with potential dependent absorbance evolution curves of characteristic absorption bands during the forward (**a**) and backward (**c**) scans; right column: corresponding UV-vis absorption spectra recorded during the forward (**b**) and backward (**d**) scans. The wavelengths of the shown absorbance evolutions in the spectra as well as the scan directions in the voltammograms are indicated by coloured arrows to guide the eye.

polymers (homopolymer down to 30 mol% TPA content) but slightly hindered charging behaviour in case of the low TPA content polymers (20 mol% to 10 mol%) while the char-

acterisation on ITO electrodes revealed hindered discharging for the homopolymer and the 50 mol% copolymer, the copolymer with 30 mol% of TPA redox groups is the polymer of choice for the *in-situ* spectroelectrochemical characterisation. In Fig. 5.8 the cyclic voltammogram (left column) of the first cycle of an PVTPA-*co*-PS (30 mol%) copolymer film with the respective UV-vis absorption spectra (right column) of the forward (top row) and backward (bottom row) scan are shown. In the forward scan (Fig. 5.8 **a**) an irreversible anodic half wave with a peak potential of 0.64 V associated to the cross-linking reaction is observed. The peak potential of the irreversible anodic half wave matches the peak potentials of all studied copolymers measured on gold electrodes (see Fig. 5.5 and Table 5.4). In Fig. 5.8 **b** the corresponding absorption spectra recorded during the forward scan are shown. The spectrum of the neutral, non-cross-linked PVTPA-*co*-PS film recorded at −0.30 V is shown in teal. Within the detector limits no obvious absorption band but an increasing intensity below 400 nm is observed. Please note, that the weak, broad absorption band centred at 750 nm is commonly observed on ITO electrodes and is caused by slight inhomogeneity of the polymer covered substrate and the bare ITO slice used for the background reference spectrum. Upon the electrochemical oxidation the intensity at the detector limit at 330 nm decreases while two new, broad absorption bands centred at 480 nm and 760 nm arise (violet curve at 0.70 V and magenta curve at 0.80 V in Fig. 5.8 **b**). For an easier attribution of the absorption bands to their corresponding redox signals, the potential dependent intensity evolution curves of the three characteristic absorption bands at 330 nm, 480 nm and 760 nm are shown in Fig. 5.8 **a** in blue, green and red respectively. The scan directions in Fig. 5.8 **a** and the wavelength positions in Fig. 5.8 **b** are indicated by correspondingly coloured arrows to guide the eye. Despite the bad signal-to-noise ratio, the intensity of the absorption signal at 330 nm (blue curve in Fig. 5.8 **a**) remains constant until the onset potential of the anodic half wave in the voltammogram is reached. Afterwards the absorption intensity at 330 nm decreases. Therefore this absorption signal is attributed to the neutral, non-cross-linked TPA units. At the oxidation onset potential the intensity of the absorption band at 480 nm and 760 nm (green and red curves in Fig. 5.8 **a**) increase significantly, indicating charged species. At higher applied potentials than the peak potential of the anodic half wave, the intensity of the absorption band at 480 nm decreases slightly, which can be explained by attribution of the 480 nm and 760 nm bands to two different charged species.

Table 5.6: Characteristic absorption bands of all redox active species involved in the oxidative cross-linking of TPA groups and the charging/ discharging of the generated TPB groups; determined by means of *in-situ* spectroelectrochemistry of PVTPA-*co*-PS (30 mol%) on ITO electrodes measured with a scan rate of 20 mV min^{-1} in 0.1 M NBu_4PF_6 in MeCN.

species	peak potential (V) [a]	wavelength (nm)
TPA	0.64	<330 [b]
TPB	/ [c]	360
$TPB^{+\cdot}$	0.40	480
TPB^{2+}	0.52	760

[a] of the redox half wave corresponding to the respective electrochemical species.
[b] peak of absorption band below the detector limit.
[c] electrochemically stable species at no applied potential.

In the backward scan of the voltammogram (Fig. 5.8 **c**) two cathodic half waves with peak potentials at 0.52 V and 0.40 V are visible. The corresponding absorption spectra are shown in Fig. 5.8 **d**. At the turning potential, which defines the beginning of the backward scan, the absorption spectrum (magenta curve in Fig. 5.8 **d**) reveals the band at 760 nm. During the reductive scan, from 0.80 V (magenta curve in Fig. 5.8 **d**) to 0.45 V (violet curve in Fig. 5.8 **d**), the intensity of the 760 nm band decreases while the 480 nm band increases. The consumption of the 760 nm band into the 480 nm band can also be seen in the isosbestic point at 525 nm. Upon further reduction, from 0.45 V to −0.35 V (teal curve in Fig. 5.8 **d**) the intensity of the 480 nm band decreases and a new absorption band at 360 nm arises. Again the consumption of the 480 nm band into the 360 nm band is also indicated by an isosbestic point at 395 nm. The potential dependent intensity evolution curves of the three observed absorption bands at 360 nm, 480 nm and 760 nm are shown in Fig. 5.8 **c** in blue, green and red curves respectively. Again, the scan directions in Fig. 5.8 **c** as well as the wavelength positions in Fig. 5.8 **d** are highlighted by correspondingly coloured arrows to guide the eye. At the onset potential of the cathodic half wave with the peak potential of 0.52 V the intensity of the 760 nm band (red curve) decreases while the intensity of the 480 nm band (green curve) increases. The curve of the 480 nm band reaches its peak intensity at 0.46 V,

which correlates to the local current minimum between the two cathodic half waves in the voltammogram. At the onset potential of the second cathodic half wave, centred at 0.40 V, the intensity of the 480 nm band (green curve) decreases and the 360 nm band (blue curve) increases and reaches a plateau when the current in the voltammogram reaches the baseline. From the potential dependent behaviour of the intensity evolution curves the absorption bands at 360 nm, 480 nm and 760 nm can be attributed to the neutral TPB, the $TPB^{+\cdot}$ radical cation and the TPB^{2+} dication respectively. The identified characteristic absorption bands of all redox active species involved in the electrochemical cross-linking and charging/ discharging of PVTPA-*co*-PS are summarised in Table 5.6.

5.3.2. Electrochemical Quartz Crystal Micro Balance

Technical Issues

As a second advanced electrochemical characterisation method the quartz crystal micro balance is used to gain deeper insight into the cross-linking and charging/ discharging behaviour of the PVTPA-*co*-PS copolymers as a function of their cross-linking densities. With this method the electrochemical redox information derived from a normal cyclic voltammogram is coupled with information about the relative weight of the studied sample, which is dependent on the interaction of the polymer film with the ions from the electrolyte upon oxidation or reduction. As described above, the cross-linking density does influence the electrochemical charging behaviour on gold electrodes which may be due to different counter ion uptake kinetics. The general operation principle of this method is described in Chapter 3.3.3 in detail. Albeit, in the following a few fundamental and experimental obstacles due to the cell design and the nature of the cross-linking reaction are discussed to allow for a better assessment of the limitations and inaccuracies of the presented EQCM data.

The used commercial EQCM cell from *Metrohm* is designed to be operated with aqueous electrolytes, mainly to study the electrochemical deposition of inorganic compounds. Therefore most parts of the cell which are in direct contact to the electrolyte had to be replaced by organic solvents inert, tailor-made analogues. Since all the compartments of the EQCM cell have to be set up around the working electrode for every individual experiment, the subsequent tailor-made parts have to fit perfectly and need to be fast tightened by a couple of screws to avoid electrolyte leakage. At the same time, the tightening of the screws applies

mechanical strain onto the quartz crystal which causes a threat of damaging the crystal as well as it increases the driving force, meaning the energy required to maintain the applied oscillation of the quartz crystal [202], during the measurement, which often results in an automatic abortion of the measurement by the potentiostat due to instrumentation limits. In other words, the cell needs to be set up as loose as possible but as tight as needed to keep the electrolyte from leaking. As a related obstacle, the O-rings which are essential to seal the bottom of the cell, tend to swell in the used acetonitrile based electrolyte, which not only causes leakage of the electrolyte but also applies a gradual increasing mechanical strain onto the working electrode which results in a gradually quartz equilibrium frequency increase and damage of the gold layer at the soldering joint to the electronic contact. Therefore, the measurements were usually performed as individual voltammetric cycles rather than multi-cycle stability tests and the frequency had to be re-equilibrated between the cycles. An other experimental obstacle which hampers multi-cycle analysis is that the EQCM cell can not be airtight sealed. As a consequence an argon stream was fed into the cell via a plastic tube to fill the cells atmosphere with an inert gas which is heavier than air and therefore acts as protection layer. Due to the open cell design in combination to the argon stream the solvent of the electrolyte tends to evaporate within the time frame of the electrochemical experiments. The decreasing electrolyte volume not only poses the risk of the reference and counter electrode to run dry, but also the changing weight of the electrolyte does change the driving force during the experiment. Consequently, the experiments have to be performed as single cycles with continuous replenishment of the electrolyte between the individual cycles. Another experimental challenge for the EQCM experiments is the usage of a fitting reference electrode. Due to the original cell design based on aqueous electrolytes, the corresponding reference electrode is also water based and can not be re-filled with an organic electrolyte. Therefore a silver chloride coated silver wire was used as pseudo reference. Since the absolute potential value of the pseudo reference versus the standard hydrogen electrode is dependent on the quality of the coating, the usage of the ferrocene/ ferrocenium redox couple as internal standard is required. The ferrocene reference measurement was performed after the electrochemical experiments and was conducted with a blank EQCM electrode. Nevertheless, the ferrocene measurement could not be performed successfully after some experiments wherefore the presented data of these experiments are referred to the used pseudo silver/

silver chloride reference instead of the ferrocene/ ferrocenium couple. As a consequence the absolute potential values derived from these experiments can not be compared to the potentials from the basic voltammetric characterisation described above.

Besides the experimental problems caused by the cell design, there are also two important obstacles caused by the nature of the studied polymer film to consider. Firstly, the geometry of the used quartz-gold working electrodes with the pins soldered tightly, which act as contacts towards the potentiostat, prohibit the film preparation by spin coating. Therefore the films were prepared by drop casting which results in inhomogeneous coatings. In addition, to avoid too high equilibrium frequencies, excess of the applied polymer on the bare quartz crystal had to be gently removed with a chloroform soaked cotton bud without harming the crystal. The inhomogeneity of the polymer films may lead to different ion intercalation quantities in zones of varying film thickness. The second and possibly largest experimental obstacle caused by the studied polymer films is the electrochemically induced cross-linking reaction during the first voltammetric cycle. The cross-linking of the polymers alters the mechanical characteristics of the polymer film, which most probably results in a change in the elastic modulus and therefore contributes to frequency changes during the experiment. Unfortunately with the available EQCM setup it is not possible to determine the proportion of frequency change being caused by the elastic modulus or the real mass change by ion (and solvent) uptake respectively.

In general the quartz crystal micro balance has been designed for the layer thickness determination of rigid, metal coatings measured in air. In the 1980s it has been shown that the quartz crystal micro balance characterisation method is also feasible in liquids which opened the field of the electrochemical quartz crystal micro balance technique. [203] Especially in the field of electro-active polymer characterisation, nowadays non-rigid coatings with viscoelastic properties are studied by means of EQCM. For such coatings the deposited material is not directly coupled to the quartz crystal oscillation but experiences a phase shift or an attenuation of the initial applied acoustic wave across the coating. [204] To characterise the mechanical properties of the coating, commonly the EQCM is coupled with an impedance spectrometer. From the interpretation of the electric impedance with the aid of elaborate equivalent circuits (e.g. the *Butterworth-van Dyke* model), the rheological loss and storage modulus can be extracted from the resistance and capacitive elements of the

equivalent circuits. [203, 204]

EQCM of the PVTPA Homopolymer

In the following, first a general discussion on the overall EQCM characteristics of the first and second voltammetric cycles of the PVTPA homopolymer and the attributed ion transport processes is given. Afterwards in the second part the influences of the cross-linking density and the ion size of the respective conducting salts is discussed.

In Fig. 5.9 the cyclic voltammograms (left column) and the corresponding potential dependent frequency curves (right column) of the first (top row) and second (bottom row) cycle of the PVTPA homopolymer, measured in a standard electrolyte of 0.1 M NBu_4PF_6 in acetonitrile, are shown. In the first cycle (Fig. 5.9 **a**) the voltammogram reveals the intense, sharp anodic half wave at 0.58 V associated to the oxidative cross-coupling of the TPA groups to TPB groups with consecutive charging to the dication species. In the backward scan of the voltammogram the two cathodic half waves with peak potentials at 0.37 V and 0.52 V corresponding to the two-step discharging of the TPB^{2+} dication to the neutral TPB groups are observed. In the second voltammetric cycle (Fig. 5.9 **c**) two overlapping reversible redox waves with half wave potentials of 0.40 V and 0.54 V are visible. The current increase at the turning potential (in the range of 0.7 V - 0.75 V) is attributed to the increasing current base line caused by the electrolyte rather than to non-cross-linked TPA groups since the onset potential of the current increase is shifted by about 0.2 V towards higher potential compared to the cross-linking signal in the first cycle. The peak potential of the cross-linking half wave in the first cycle as well as the half wave potentials of the reversible redox reactions in the second cycle are comparable to the values measured on planar gold electrodes (see Table 5.4) indicating similar electrochemical behaviour of PVTPA on the gold coated quartz electrodes.

The potential dependent frequency changes of the first and second voltammetric cycles of PVTPA are shown in Fig. 5.9 **b** and **d** respectively. At the start of the measurements the frequency is set to 0 Hz. In the first cycle (Fig. 5.9 **b**) the frequency remains constant until the onset potential of the anodic cross-linking signal at 0.55 V is reached. At the onset potential the frequency decreases by 565 Hz. According to the *Sauerbrey* equation (see Eq. 7) the frequency decrease relates to a mass increase of the polymer film. This mass

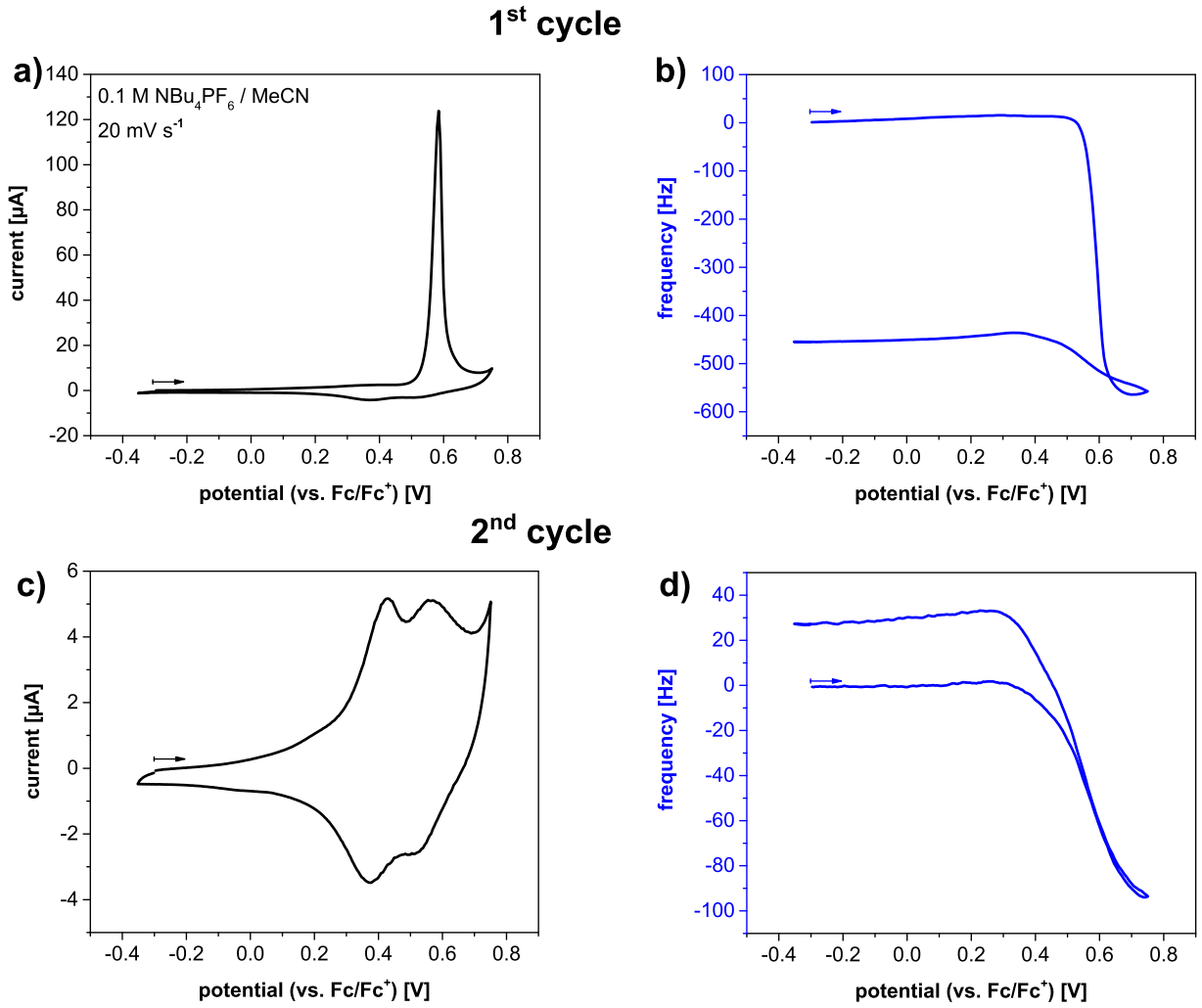

Figure 5.9: Electrochemical quartz crystal micro balance characterisation of PVTPA films; left column: cyclic voltammograms of the first (**a**) and second (**c**) cycles; right column: corresponding potential dependent frequency evolutions during the first (**b**) and second (**d**) voltammetric cycles; measured on gold covered quartz crystals in 0.1 M NBu_4PF_6 in MeCN with a scan rate of 20 mV s^{-1}; scan directions are indicated by arrows respectively.

increase is caused by the intercalation of the PF_6^- anions with their solvent shell to counter balance the cationic species in the polymer film ($TPA^{+\cdot}$, $TPB^{+\cdot}$ and TPB^{2+}). Interestingly, in the range of 0.70 V to 0.75 V, meaning between the end of the cross-linking half wave in the voltammogram and the turning potential, the measured frequency increases slightly by about 10 Hz. This can be interpreted as a small mass decrease e.g. from the proton elimination process. Another interpretation might be a change of the elastic modulus of the

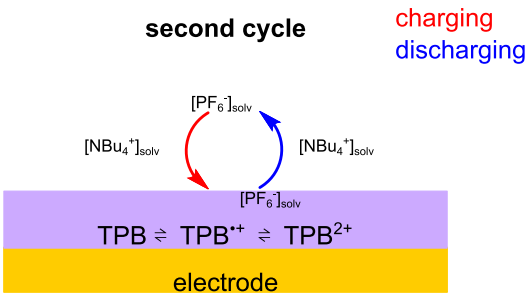

Figure 5.10: Schematic illustration of the possible ion intercalation/ expulsion processes and the associated solvent uptake during the reversible charging/ discharging of a cross-linked PVTPA film.

polymer film due to the cross-linking of the polymer chains. During the backward scan of the voltammetric cycle, the measured frequency increases until 0.3 V, which correlates to the end of the cathodic half waves, is reached. Afterwards the frequency remains constant at −450 Hz. Two plausible explanations for the frequency offset between the neutral polymer film prior and after the voltammetric cycle are a significant change of the elastic modulus of the polymer film or a permanent mass increase which could be for example trapping of ions from the electrolyte in the cross-linked polymer film. In the forward scan of the second cycle (see Fig. 5.9 **d**) again the frequency remains constant until the onset potential of the onset of the anodic redox half wave at about 0.2 V is reached. Towards higher applied potentials the frequency decreases by 95 Hz indicating a mass increase which can be explained by counter ion and solvent uptake. During the backward scan of the voltammetric cycle, the frequency increases and mass decreases again and reaches a plateau at about 0.25 V which correlates to the end of the cathodic half waves in the voltammogram.

In summary, the EQCM characterisation of the PVTPA homopolymer reveals a clear correlation of the current signals from the voltammograms and the frequency changes with complex ion intercalation and expulsion processes during the cross-linking and the reversible charging/ discharging of the polymer film. While the ion movement in the cross-linked state in the second cycle can be interpreted straightforward, the interpretation of the ion movement in the cross-linking reaction in the first cycle is complex and requires additional information about the mechanical properties of the original and the cross-linked polymer films. Therefore, in the following a possible interpretation of the ion movement processes in the first cycle, which neglects possible contribution of a change of the elastic modulus of the

polymer film, is given.

During the forward scan of the first cycle the TPA groups become oxidised to their radical cation species. To maintain charge neutrality the respective counter ion PF_6^- from the electrolyte is intercalated into the polymer film. During the discharging the intercalated anions get electrostatically repelled. Due to the cross-coupling of the polymer chains some PF_6^- anions are enclosed in the polymer film and therefore can not be expelled upon discharging of the PVTPA. To counter balance the residual PF_6^- ions in the polymer film, solvated NBu_4^+ cations are intercalated in a secondary process, which could explain the irreversible frequency offset concurrent to the complete discharging of the PVTPA at the end of the first voltammetric cycle. During the second cycle solvated PF_6^- anions are reversibly intercalated during the two-step oxidation of the PVTPA film and expelled during the re-reduction to the neutral polymer. The ion movement processes during the second voltammetric cycles are schematically illustrated in Fig. 5.10.

EQCM of PVTPA-co-PS Copolymers

To gain further insights into the cross-linking density dependency of the ion movement processes during the first and second charging/ discharging cycles, the EQCM data of PVTPA-*co*-PS copolymers with 50 mol% (**a**, **b**), 30 mol% (**c**, **d**) and 10 mol% (**e**, **f**) are shown in Fig. 5.11. Since the EQCM measurements suffer from a number of experimental obstacles described above, the cyclic voltammograms are taken as a measure to assess the quality of the gained EQCM data. In the first cycles (Fig. 5.11 **a**, **c** and **e**) the irreversible anodic half wave associated to the oxidative cross-linking of the TPA groups is observed. The peak potentials are at 0.57 V (50 mol%, **a**), 0.54 V (30 mol%, **c**) and 0.57 V (10 mol%, **e**) respectively. With exception of the 30 mol% copolymer the peak potentials of the cross-linking half wave of the studied PVTPA-*co*-PS copolymers match the peak potential of the PVTPA homopolymer (0.58 V, see Fig. 5.9 **a**). The peak potentials of all shown EQCM measurements as well as their respective analogues measured on planar gold electrodes are summarised in Table 5.7. The discrepancy of the peak potential of the 30 mol% copolymer (5.11 **c**) can be explained by the fact that both data curves (current in black as well as frequency in blue) reveal a spike in the range of the current peak which is most likely due to a measurement error.

In summary, the electrochemically induced cross-linking reaction of the TPA groups is ob-

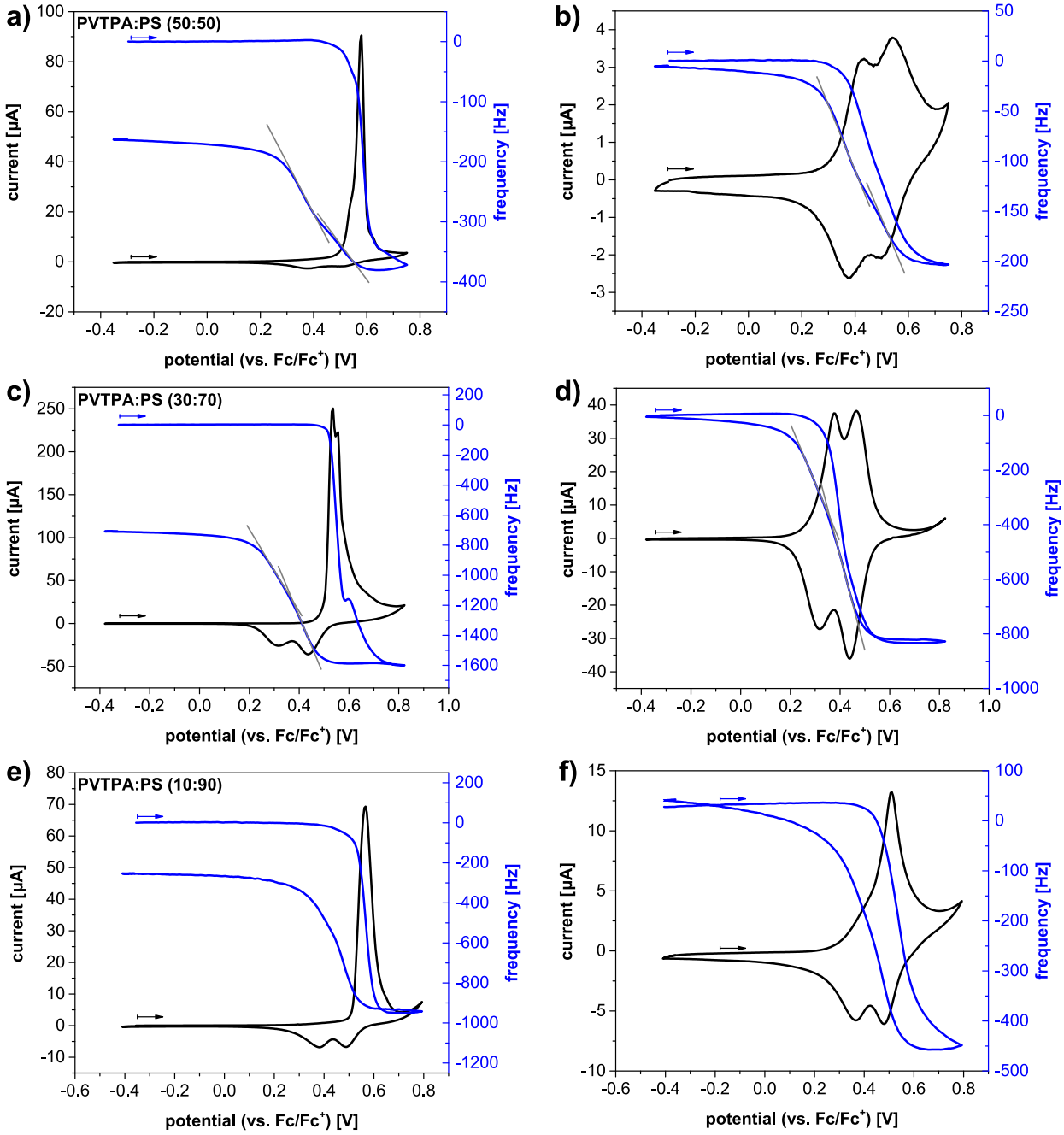

Figure 5.11: Electrochemical quartz crystal micro balance characterisation of PVTPA-*co*-PS copolymer films with varying TPA content; left column: first cycles; right column: second cycles; voltammograms (black curves) and potential dependent frequency evolutions (blue curves) of PVTPA-*co*-PS with 50 mol% (**a**, **b**), 30 mol% (**c**, **d**) and 10 mol% (**e**, **f**); measured in 0.1 M NBu_4PF_6 in MeCN with scan rates of 20 mV s^{-1}; scan directions are indicated by arrows respectively.

Table 5.7: Comparison of the peak potentials of the cross-linking half waves of PVTPA-*co*-PS copolymers; determined by means of basic voltammetry on gold electrodes and by electrochemical quartz crystal micro balance experiments on gold coated quartz electrodes; measured with a scan rate of 20 mV min^{-1} in 0.1 M NBu_4PF_6 in MeCN.

polymer	electrode	peak potential (V)
homopolymer	gold	0.62
homopolymer	quartz/ gold	0.58
50 mol%	gold	0.62
50 mol%	quartz/ gold	0.58 [a]
30 mol%	gold	0.62
30 mol%	quartz/ gold	0.54
10 mol%	gold	0.61
10 mol%	quartz/ gold	0.57

[a] spike in both recorded data curves (current and frequency); probably due to a measurement error.

served in all studied polymers during the EQCM measurements. In the backward scan of the first cycle all copolymers show the two cathodic half waves attributed to the two-step discharging of the formed TPB^{2+} dications. Charge trapping similar to the experiments on ITO electrodes is not observed. In the second cycles (Fig. 5.11 **b**, **d** and **f**) the copolymers show the two redox waves of the reversible two-step redox processes $TPB^{2+} \rightleftharpoons TPB^{+\cdot} \rightleftharpoons TPB$. Interestingly, just as in case of the basic electrochemical characterisation on planar gold electrodes, the second voltammetric cycle of the copolymer with low TPA-content (10 mol% in Fig. 5.11 **f**) differs from the homopolymer (5.9 **b**) and high TPA-content copolymers (50 mol% and 30 mol% in Fig. 5.11 **b** and **d**) in a way that the anodic current signal does not consist of two separate half waves but the low-potentials half wave at about 0.4 V gets suppressed. In general, despite the spike in Fig. 5.11 **c** and a slight noisy current signal in Fig. 5.11 **b** the voltammograms of the PVTPA-*co*-PS copolymers measured by means of EQCM are well resolved and reveal the same electrochemical behaviour as during the basic voltammetric characterisation on planar gold electrodes.

The potential dependent frequency curves of the first cycles of the three PVTPA-*co*-PS copolymers (Fig. 5.11 **a**, **c** and **e**) all reveal the same general frequency trend as the PVTPA homopolymer. The frequency remains constant until the oxidation onset potential of the cross-linking half wave is reached. During the oxidation of the polymer films the frequency drops due to the mass increase probably caused by the intercalation of PF_6^- counter ions. At the start of the backwards scan, again the frequency remains constant until the reduction onset potential of the $TPB^{2+} \rightleftharpoons TPB^{+\cdot}$ redox process is reached. During the reduction of the polymer films the frequency increases and reaches a plateau which is at a lower frequency than the starting value as soon as no further current flow is detected. The frequency offset in the neutral state is either caused by an irreversible mass increase due to trapping of the intercalated counter ions even in the copolymer with the lowest cross-linking density (10 mol% in Fig. 5.11 **e**) or the changing mechanical properties caused by the cross-linking of the polymer chains. Interestingly, the frequency curve increase during the discharging of the copolymer films consists of two steps with different slopes (best seen in Fig. 5.11 **a**) which correlate with the interception of the two reduction half waves in the voltammogram. In the second cycles (Fig. 5.11 **b**, **d** and **f**) the copolymer films show a frequency decrease during charging and increase back to the starting value during discharging, indicating reversible counter ion intercalation and exclusion. The onset values of the frequency changes match the onset potentials of both the anodic and cathodic current signals. For the two high TPA-content copolymers (50 mol% and 30 mol% in Fig. 5.11 **b** and **d** respectively) the frequency curves show two separate mass transfer processes each during both the charging and the discharging processes indicated by the different slopes of the frequency curves which match the potentials of the interceptions of the redox half waves. This effect is also observed during the discharging of the 10 mol% copolymer film (see Fig. 5.11 **f**) but not during the charging. This is in accordance with the suppressed anodic half wave in the voltammogram.

In general, the frequency curves of all studied polymers show direct response to the observed current flows. The potentials dependent frequency changes in the PVTPA-*co*-PS copolymers follow the same tendencies as in the PVTPA homopolymer; namely a frequency decrease during the first cycle and reversible ion intercalation and exclusion during the reversible two-step redox processes of $TPB \leftrightharpoons TPB^{+\cdot} \leftrightharpoons TPB^{2+}$. With exception of the 10 mol% copolymer sample the two-step redox process can also be identified by the coexistence of two

frequency ranges with different slopes indicating different ion movement speeds.

Influence of Conducting Salt

To gain deeper insights into the ion movement during cross-linking and charging/ discharging of the PVTPA-*co*-PS copolymers two additional conducting salts ($LiClO_4$ and KPF_6) with different anion and cation sizes are used. For these measurements the 30 mol% copolymer is used since it neither showed the hampered oxidation of the low TPA-content copolymers in the basic voltammetric characterisation on planar gold electrodes nor the hindered discharging of the PVTPA homopolymer and high TPA-content copolymer on ITO electrodes. In Fig. 5.12 the voltammograms (black curves) and potential dependent frequency curves (blue curves) of the first (left column) and second (right column) cycles of the 30 mol% PVTPA-*co*-PS copolymer are shown. All measurements were performed as individual cycles with a scan rate of $20\,\mathrm{mV\,s^{-1}}$ in electrolytes containing 0.1 M conducting salt in MeCN. As conducting salts NBu_4PF_6 (**a**, **b**), $LiClO_4$ (**c**, **d**) and KPF_6 (**e**, **f**) were used. Please note that the data presented in Fig. 5.12 **a** and **b** have already been shown and discussed in Fig. 5.11 **c** and **d** and are only re-presented here to facilitate the direct comparison with the two other conducting salts. As a second important remark, since the ferrocene measurements for the $LiClO_4$ and KPF_6 electrolytes failed, the potentials are plotted with respect to the Ag/AgCl pseudo reference electrode. Therefore only the general shapes of the voltammograms and the respective frequency response, but no absolute potential values of signals are discussed. In general the voltammograms of all shown first cycles (left column in Fig. 5.12) reveal the irreversible anodic half wave and two cathodic half waves attributed to the oxidative cross-coupling of TPA $\rightarrow$ TPB and the two-step discharging $TPB^{2+} \leftrightharpoons TPB^{+\cdot} \leftrightharpoons$ TPB. The second cycles (right column in Fig. 5.12) show two reversible redox waves attributed to the reversible oxidation of the neutral cross-linked polymer to its dication form. Therefore the general electrochemical behaviour of PVTPA-*co*-PS (30 mol%) is similar for all tested conducting salts. On a closer look, it is conspicuous that in case of the two PF_6^- anion containing conducting salts (in NBu_4PF_6 and KPF_6) the two redox waves in the second cycles are separated while in case of $LiClO_4$ the overlapping of the two oxidative half waves even prevent the determination of the half wave potential for the first oxidation step.

The frequency curves of the first cycles (left column in Fig. 5.12) all reveal the same general

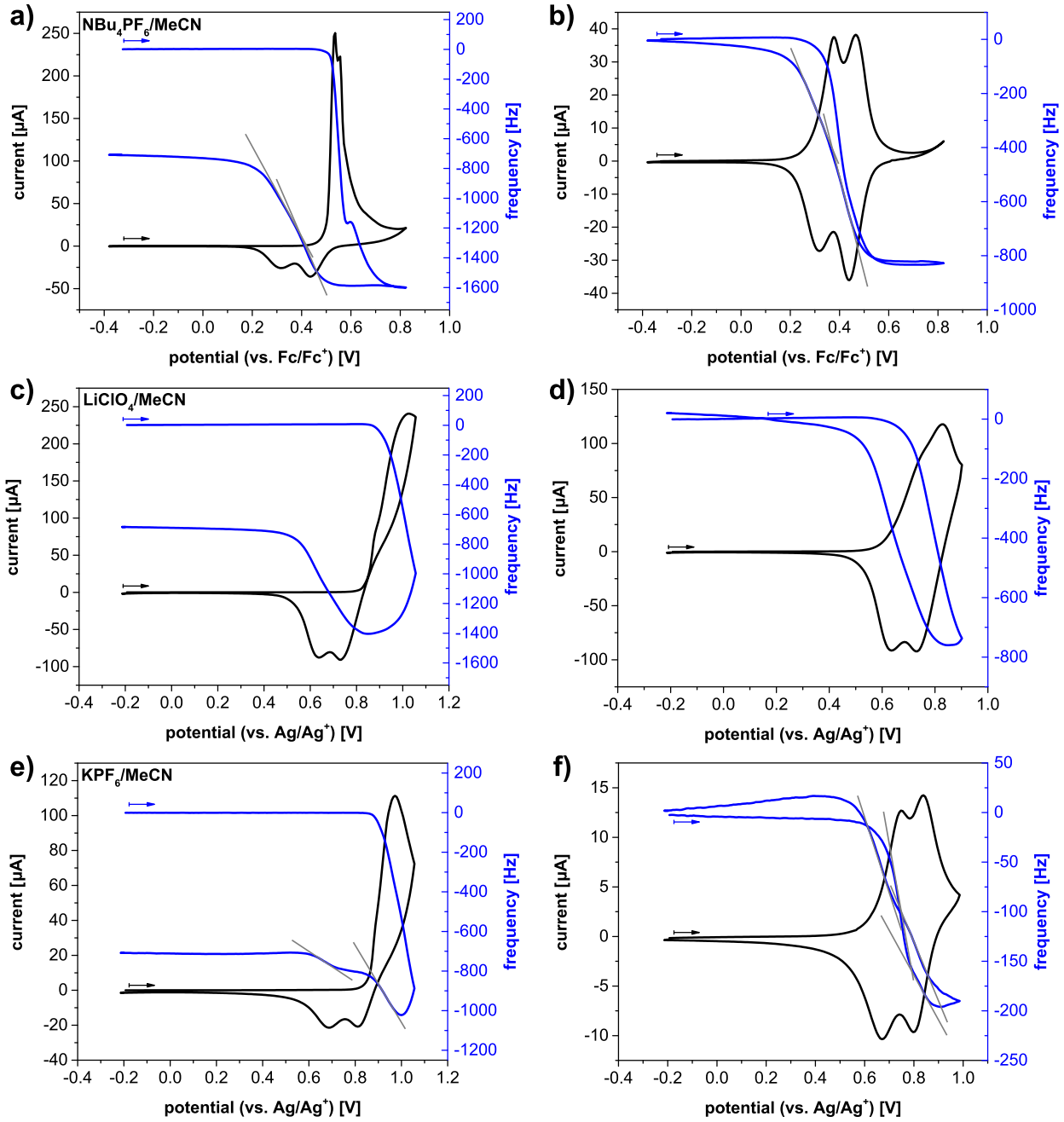

Figure 5.12: Electrochemical quartz crystal micro balance characterisation of PVTPA-*co*-PS (30 mol%) with varying conducting salts; **a)**, **b)** 0.1 M NBu_4PF_6 in MeCN; **c)**, **d)** 0.1 M $LiClO_4$ in MeCN; **e)**, **f)** 0.1 M KPF_6 in MeCN; voltammograms (black curves) and potential dependent frequency evolutions (blue curves); left column: first cycles with the oxidative cross-linking reaction; right column: second cycles with the reversible charging/ discharging of the cross-linked polymer.

tendency discussed above. The frequency remains constant until the onset potential of the anodic cross-linking half wave is reached. Upon oxidation of the polymer the frequency decreases which correlates to a mass increase. Upon the cathodic half waves the frequency increases but does not reach its initial value. As described above, two possible explanations for the frequency offset in the neutral state are an irreversible ion (and solvent) trapping and a change in the elastic modulus of the polymer film. In the second cycles (right column in Fig. 5.12) a reversible ion uptake and exclusion upon charging/ discharging is observed. The onset potentials of the frequency changes match the onset potentials of the current curves. Again, while in the measurements with PF_6^- anion containing electrolytes the two-step redox process (TPB $\leftrightharpoons$ $TPB^{+\cdot}$ $\leftrightharpoons$ TPB^{2+}) is also observed by a change in the slope of the frequency curves (best seen in Fig. 5.12 **e** and **f**), the frequency data obtained with $LiClO_4$ do not show such details. This finding supports the assumption of the merging and suppression of the anodic half waves in the reversible charging/ discharging of the cross-linked TPB groups being caused by a hindered ion diffusion kinetics.

5.4. Towards Electrochemical Devices

The PVTPA-*co*-PS copolymers are interesting materials for the application in organic electronic devices, since they combine the solution processability of the initial polymers with two reversible redox reactions and an increased film stability in the cross-linked films. In the following chapter, the general usability of PVTPA-*co*-PS as novel energy storage materials and transparent electrode materials is studied. In the first part, the charge storage properties of electrochemically cross-linked PVTPA-*co*-PS copolymer films are examined by means of supercapacitor tests. The supercapacitor device configuration has been chosen as a preliminary test system to evaluate the general usability of PVTPA-*co*-PS copolymers, since this device is easier producible than a battery device and does not necessarily require a *n*-conductor. In the second part, the chemical cross-linking and doping of PVTPA-*co*-PS copolymers with oxidative dopants is studied to exploit the usability of these copolymers as transparent electrode materials.

5.4.1. Charge Storage Capabilities — Supercapacitor Test

In the last 15 years, supercapacitors have gained a huge scientific and industrial interest due to their high power density, fast charging/ discharging times and good cycle lifetime in comparison to Li-ion batteries and fuel cells. Therefore they are promising devices to supply the demand of cheap, light weight, flexible and efficient energy storage devices for the application in portable electronic devices and electric vehicles. So far, the available supercapacitors suffer from low energy densities though. [32, 205, 206] The placement of supercapacitors regarding specific energy density and power density in comparison to other energy storage devices like fuel cells, batteries and capacitors is given by the *Ragone* plot and is shown in Fig. 5.13 **a**. [31, 32]

In general, the generic term of *supercapacitor* comprises three types of energy storage systems. In the so-called electrochemical double-layer capacitor (EDLC) the electric energy storage occurs in form of an electrostatic charge separation at the electrode-electrolyte interface. For this highly porous materials are necessary to maximise the charge storage capacity. The second type of supercapacitors are the so-called pseudocapacitors, which store energy in form of fast and reversible faradaic redox reactions. As a third type the so-called hybrid supercapacitors combine the properties of the other two types. [32, 205, 207] To improve the performance of supercapacitor devices, a lot of scientific effort has been spent in the development of new electrode materials like conducting polymers, carbonaceous materials and transition-metal-oxides in recent years. The most important requirements for new electrode materials are high conductivity and nano-porous structures to increase the electrode-electrolyte interface. [205–207] In principle conducting polymers are ideal candidates for the electrode material in supercapacitors since they comply all the mentioned requirements with their high conductivity in the doped state, fast electron transfer kinetics in the charging/ discharging reactions and a high specific capacity caused by the involvement of the whole bulk volume rather than only the surface for the charge storage. In addition, their straightforward synthesis and low production costs in comparison to transition-metal-oxides make them promising materials for large scale industrial application. [208, 209]

Even if significant progress has been made in the field of material development, there are still almost no film-state electrode materials available which limits the large scale production of commercial supercapacitors. The important advantages of film-state electrode materials are

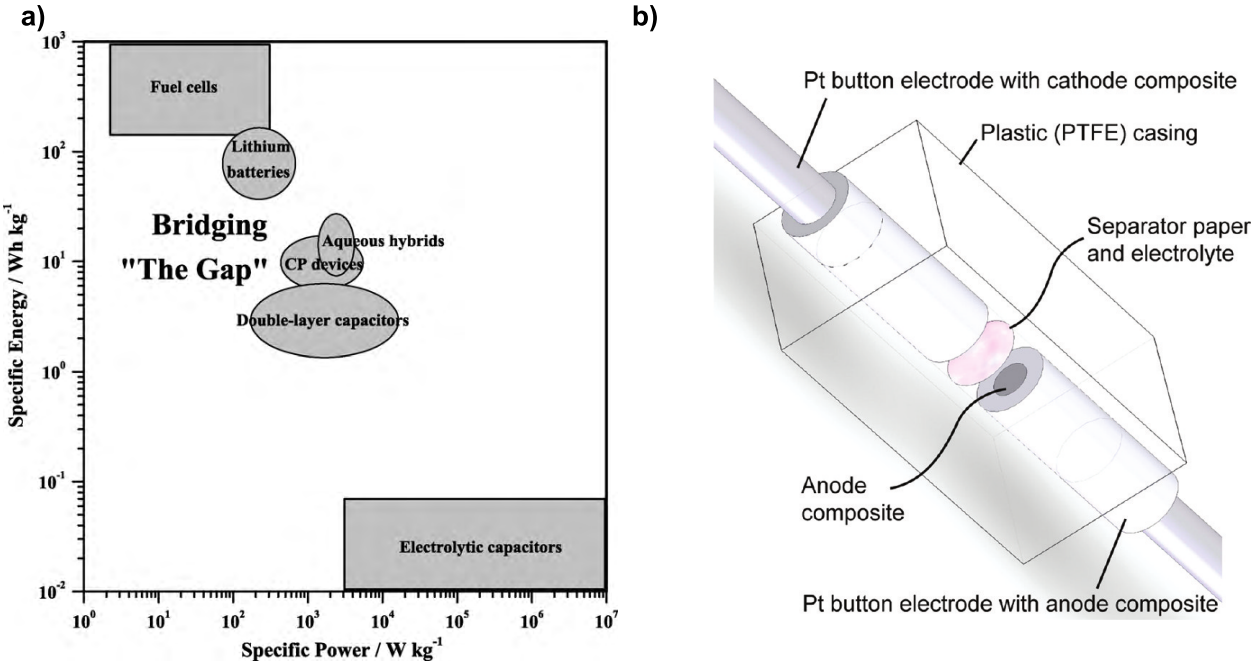

Figure 5.13: Electrochemical charge storage in supercapacitor devices. **a)** characteristic specific energy and specific power values of various energy storage devices like fuel cells, batteries and capacitors, reprinted with permission from Snook et al. [31], Copyright Elsevier (2011); **b)** schematic illustration of a supercapacitor setup, reprinted with permission from Rosario-Canales et al. [210], Copyright ACS (2012).

the flexibility and the possibility to integrate them directly into organic electronic devices resulting in a new generation of custom-made electronic devices. [205] First attempts with π-conjugated polymers like polythiophene and polypyrrole revealed poor cycle life stability due to volume changes of the polymer films during the charging and discharging reactions caused by the swelling and shrinking of the films as a result of counter ion intercalation and expulsion. [206] As one possible approach so-called conjugated microporous polymers were used, as they combine a π-conjugated skeleton with permanent nanopores. Although these polymers showed high specific capacitance and good cycle life stability, the rigid, cross-linked polymer skeleton inhibits the solution processing for film deposition whereby they are only usable as powder electrodes. [205, 211] The second approach is the usage of redox active, non-π-conjugated materials like carbazole derivatives. The important advantage is, that the material synthesis and film deposition can be performed simultaneously by means of

electropolymerisation. [205]

The general set-up of a supercapacitor device is rather plain and unsophisticated. Fig. 5.13 **b** shows the schematic illustration of such a common supercapacitor set-up. It consists of two current-collectors which are covered with the anode and cathode material respectively. The two electrodes are both in contact to an electrolyte soaked separator. [210] Depending on the anode and cathode material and doping state, supercapacitor devices are subdivided into three types referred to as *Type I*, *Type II* and *Type III*. For *Type I*, which has been used in this thesis, the same *p*- or *n*-type conducting material is used for both electrodes. Therefore the supercapacitor device is symmetric. In the asymmetric *Type II* a *p*-type conductor is used as anode material and a *n*-type conductor as cathode material respectively. *Type III* is based on *Type I* but the electrode material of the symmetric supercapacitor device is used in its *p*-doped state on one electrode and in its *n*-doped state on the other electrode. [31]

Even if sophisticated analysis techniques like the electrochemical quartz crystal micro balance can be used to characterise supercapacitor devices [212], usually the three electrochemical analysis methods of electrochemical impedance spectroscopy (EIS), cyclic voltammetry (CV) and galvanostatic charging/ discharging (GCD) are used. [213]

For the EIS characterisation of supercapacitors the *Nyquist* plot is recorded towards very low frequencies. From the slope of the imaginary part of the impedance in the low frequency region the specific capacitance (C_{sp}) can be calculated according to Equation 19: [213]

$$C_{\mathrm{sp}} = -\frac{1}{\pi \; f_{\mathrm{l}} \; Z^{\mathrm{II}}{}_{\mathrm{l}} \; m} \tag{19}$$

with f_l being the lowest frequency, $Z^{II}{}_l$ being the imaginary term of the impedance at f_l and m being the mass of the electrode material.

For ideal supercapacitor behaviour the CV characterisation of the device reveals a rectangular voltammogram with current plateaus between the turning potentials. From the current difference of the two plateaus (I) the specific capacitance can be determined according to Equation 20: [213]

$$C_{\mathrm{sp}} = \frac{2 \; I}{v \; m} \tag{20}$$

with v being the scan rate and m being the mass of the electrode material.

Even though EIS and CV are useful techniques to gain deeper insights into the electrostatic and redox processes in the device, galvanostatic charging/ discharging curves are the most

important characterisation of any charge storage device. They are recorded by applying a constant current for charging whose polarisation is simply reversed for discharging and recording the resulting time-dependent potential. To do so, either the duration of each current flow is set or the cut-off potentials at which the polarisation of the current is reversed are defined. From the galvanostatic charging/ discharging curves the specific capacitance is calculated as following: [213]

$$C_{\mathrm{sp}} = \frac{2\ I}{\frac{\Delta\ V}{\Delta\ t}\ m} \tag{21}$$

with I being the applied current, ΔV/Δt being the slope of the potential curve and m being the mass of the electrode material. Usually the discharging curves are used for the characterisation of energy storage devices.

The GCD curves can further be used for the determination of the specific energy density (E_{sp}) and the specific power density (P_{sp}) according to Equations 22 and 23: [213]

$$E_{\mathrm{sp}} = \frac{V\ I\ t}{m} \tag{22}$$

$$P_{\mathrm{sp}} = \frac{V\ I}{m} \tag{23}$$

PEDOT:PSS as Model System

In the following a commercial PEDOT:PSS is used as a literature-known, ideal supercapacitor material to test the custom-made measuring cell and to verify the correct application of the three mentioned analysis techniques by reproducing literature values. The experimental details are given in Chapter 3.2.7 and are inspired by Carlberg et al. [214] who reported values of 66 F g^{-1} for C_{sp}, 3600 - 14 400 J kg^{-1} for E_{sp} and 35 - 2500 W kg^{-1} for P_{sp} respectively. It is important to note that the polymer parameters as well as the preparation parameters significantly influence the charge storage parameters which leads to C_{sp} values as high as 100 - 120 F g^{-1} being reported in literature. [215] In the following supercapacitor characterisation of the PEDOT:PSS model system, the obtained specific capacitance, energy density and power density values are compared to values by Carlberg et al. [214], since the experimental details were chosen according to this reference.

Fig. 5.14 shows the electrochemical characterisation of a *Type I* PEDOT:PSS supercapacitor in 0.1 M $LiClO_4$ in MeCN. As the first analysis method, cyclic voltammetry with varying

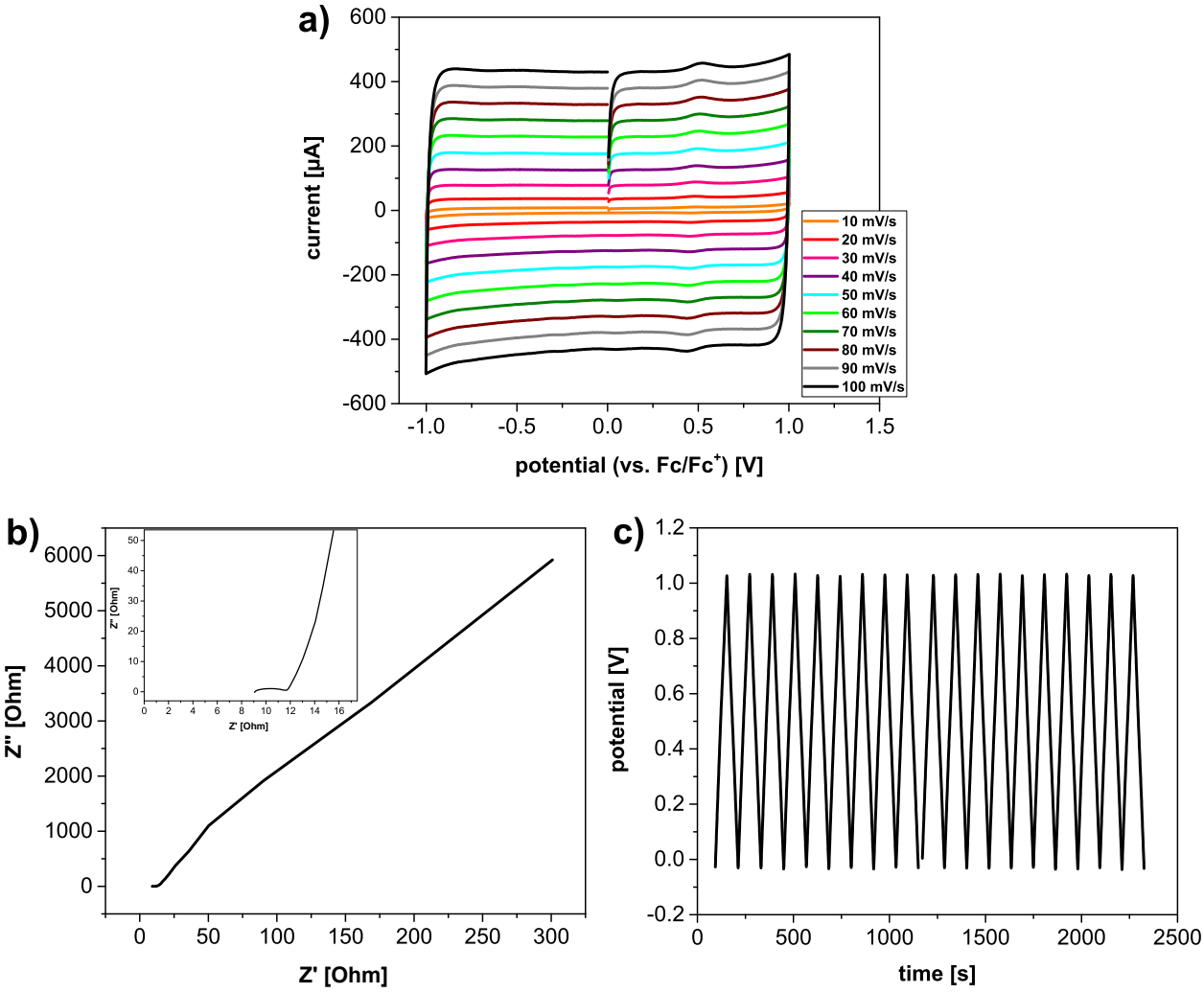

Figure 5.14: Charge storage capacity characterisation of a PEDOT:PSS supercapacitor measured in 0.1 M $LiClO_4$ in MeCN. **a)** scan rate dependent cyclic voltammograms; **b)** Nyquist plot from electrochemical impedance spectroscopy with an amplitude of 1 V (high frequency range shown as inlet) and **c)** galvanostatic charging/discharging curves with 100 µA and cut-off potentials of 0 V and 1 V.

scan rates is used as a control experiment to gain information about the redox processes in the supercapacitor. The CV measurements shown in Fig. 5.14 **a** have been recorded in the potential window between −1 V and 1 V with scan rates in the range of 10 mV s^{-1} to 100 mV s^{-1}. The observed voltammograms possess almost ideal rectangular shapes. The lack of distinct peaks indicates purely electrostatic behaviour without any faradaic redox reactions. The sudden current changes at the turning potentials indicate capacitive behaviour. With increasing scan rate the span between the current plateaus increases, which means that

Table 5.8: Supercapacitor characterisation of PEDOT:PSS, measured in 0.1 M $LiClO_4$ in MeCN by means of electrochemical impedance spectroscopy (EIS) and galvanostatic charging discharging (GCD).

parameter	method	value
C_{sc}	EIS	$9.8\,F\,g^{-1}$
C_{sc}	GCD	$10.3\,F\,g^{-1}$
E_{sp}	GCD	$5136\,J\,kg^{-1}$
P^{sp}	GCD	$90.9\,W\,kg^{-1}$

the specific capacitance of the PEDOT:PSS supercapacitor increases as well.

As second characterisation method EIS is used to gain additional information about possible electron impedance processes like contact resistance or the generation of ionic double layers. In Fig. 5.14 **b** the *Nyquist* plot of the PEDOT:PSS supercapacitor in a frequency range between 5 mHz and 100 kHz is shown. The EIS curve can be subdivided in three parts which correspond to characteristic electronic processes. [213] From the high frequency area (shown as inlet in Fig. 5.14 **b**) the contact resistance at the electrode/ electrolyte interface of 9 Ω (left end of semicircle) and the internal resistance of the electrode of 12 Ω (right end of semicircle) can be determined. The adjacent straight curve segment is caused by the combined resistive and capacitive behaviour of intercalating ions. As the third section, the straight line in the low frequency range describes the dominant capacitive behaviour of the generated charges in an ionic double-layer at the electrode surface. From the slope of the imaginary impedance term in this section the specific capacitance can be calculated according to Equation 21. For the studied PEDOT:PSS supercapacitor C_{sp} accounts for $9.8\,F\,g^{-1}$.

As the third and most important analysis technique galvanostatic charging/ discharging curves were recorded. In the presented PEDOT:PSS supercapacitor the GCD curves are recorded with cut-off potentials of 0 V and 1 V and current flows of 100 µA and −100 µA respectively. The second possibility would be to set the duration of each current flow under the risk of a significant over- or underpotential, which would lead to an automatic shut-down of the used potentiostat. In Fig. 5.14 **c** an extract of the recorded GCD curves is shown. The curves of the individual charging/ discharging cycles are uniform and show an evenly

time distribution which means that the charging and discharging times remain constant during the measurement. The shape of the individual curves comply with a triangle for each charging/ discharging cycle, indicating ideal charge storage behaviour of the PEDOT:PSS supercapacitor. From the slope of the discharging curve the specific capacitance, energy density and power density can be determined according to Equations 21, 22 and 23 respectively. The calculated values are $10.3\,\mathrm{F\,g^{-1}}$ for C_{sp}, $5136\,\mathrm{J\,kg^{-1}}$ for E_{sp} and $90.0\,\mathrm{W\,kg^{-1}}$ respectively. For the value calculation, 15 individual GCD curves have been analysed and averaged.
The determined values for the specific capacitance, the energy density and the power density, obtained by electrochemical impedance spectroscopy and galvanostatic charging/ discharging curves are summarised in Table 5.8. In comparison to the values from Carlberg et al. [214] the energy density and power density values are in range of the literature values but the specific capacitance is lower. Altogether the characterisation of the PEDOT:PSS supercapacitor results in reasonable values wherefore it can be assumed that the custom-build measurement cell is working and the used analysis techniques are applied appropriately.

*Cross-linked PVTPA-*co*-PS Copolymers*

In the next step the PVTPA-*co*-PS copolymers are studied. In Fig. 5.15 the schematic set-up of the measurement cell as well as the layer sequence of the used *Type I* supercapacitor are shown. For the separator cellulose soaked with 0.1 M LiBTFSI in MeCN is used. The film deposition was carried out by drop-casting and all electrodes were electrochemically cross-linked in an external three-electrode cell usually used for cyclic voltammetry measurements. Fig. 5.16 shows exemplarily the supercapacitor characterisation of the externally cross-linked PVTPA-*co*-PS copolymer with 20 mol% of PVTPA repeating units. The data of all other copolymers and the PVTPA homopolymer are shown in the Appendix in Chapter A.5. Analogous to the PEDOT:PSS supercapacitor, the characterisation of the redox polymers is carried out by CV, EIS and GCD.
The scan rate dependent cyclic voltammograms shown in Fig. 5.16 **a** reveal current plateaus with significant current in- and decrease at the turning potentials, indicating not purely capacitive behaviour but in addition faradaic redox processes in the range of the turning potentials. The impedance spectrum in Fig. 5.16 **b** shows similar progression as the PEDOT:PSS supercapacitor described above. From the slope in the low frequency range the

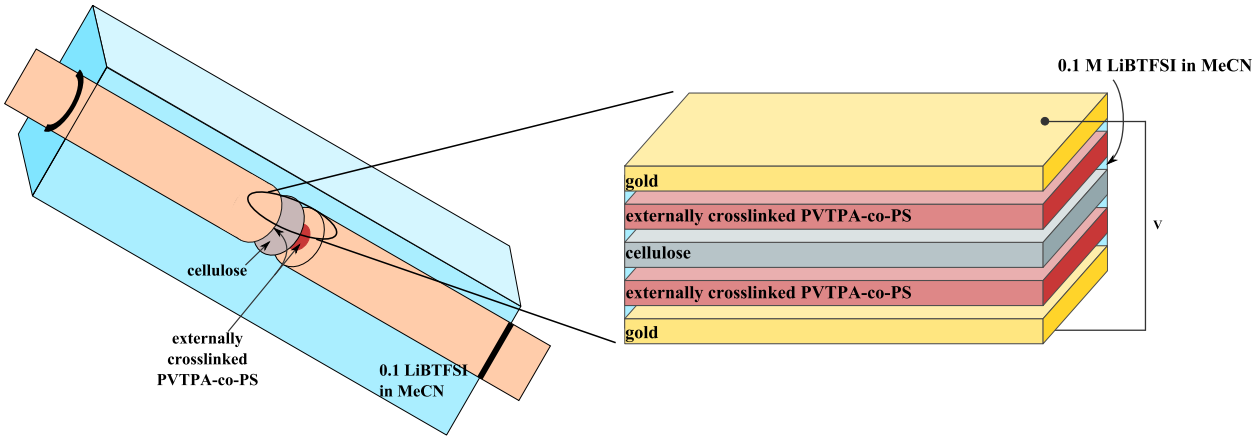

Figure 5.15: Schematic illustration of the custom-made supercapacitor setup based on a literature cell design by Rosario-Canales et al. [210]; the polymer films were prepared by drop casting onto disk electrodes and the oxidative cross-linking was performed externally in a three-electrode cell described in Chapter 3.4 prior to device assembly with cellulose paper used as separator material.

specific capacitance is calculated to be $58\,\mathrm{mF\,g^{-1}}$.

Fig. 5.16 **c** shows an extract of the recorded GCD curves. In contrast to the PEDOT:PSS supercapacitor, the discharging curves of the PVTPA-*co*-PS copolymer show a flattening slope towards lower potential values. This can be explained by the co-existence of two different charge storage processes. The initial potential decrease during the discharging scan is caused by fast, non-faradaic processes and the more gradual decrease towards the end of the discharging scan can be attributed to slower, faradaic redox reactions. [216] In accordance to literature [216] the calculation of the specific capacitance, the energy density and the power density are performed by using the average slope over the entire potential range of the discharging curve and with an average over 20 measurements. The obtained parameters are $4\,\mathrm{mF\,g^{-1}}$ for C_{sp}, $109.4\,\mathrm{J\,kg^{-1}}$ for E_{sp} and $11.8\,\mathrm{W\,kg^{-1}}$ for P_{sp}. All values obtained from all studied redox polymers are summarised in Table. 5.9 and are in the same range.

To be able to put the obtained values for the studied redox polymer supercapacitors into perspective an important limitation to the accuracy of the values has to be discussed. Since the m value is required for the calculation of all the characteristic supercapacitor parameters, the precise control of the mass of the electrode material is crucial. For this reason the polymer

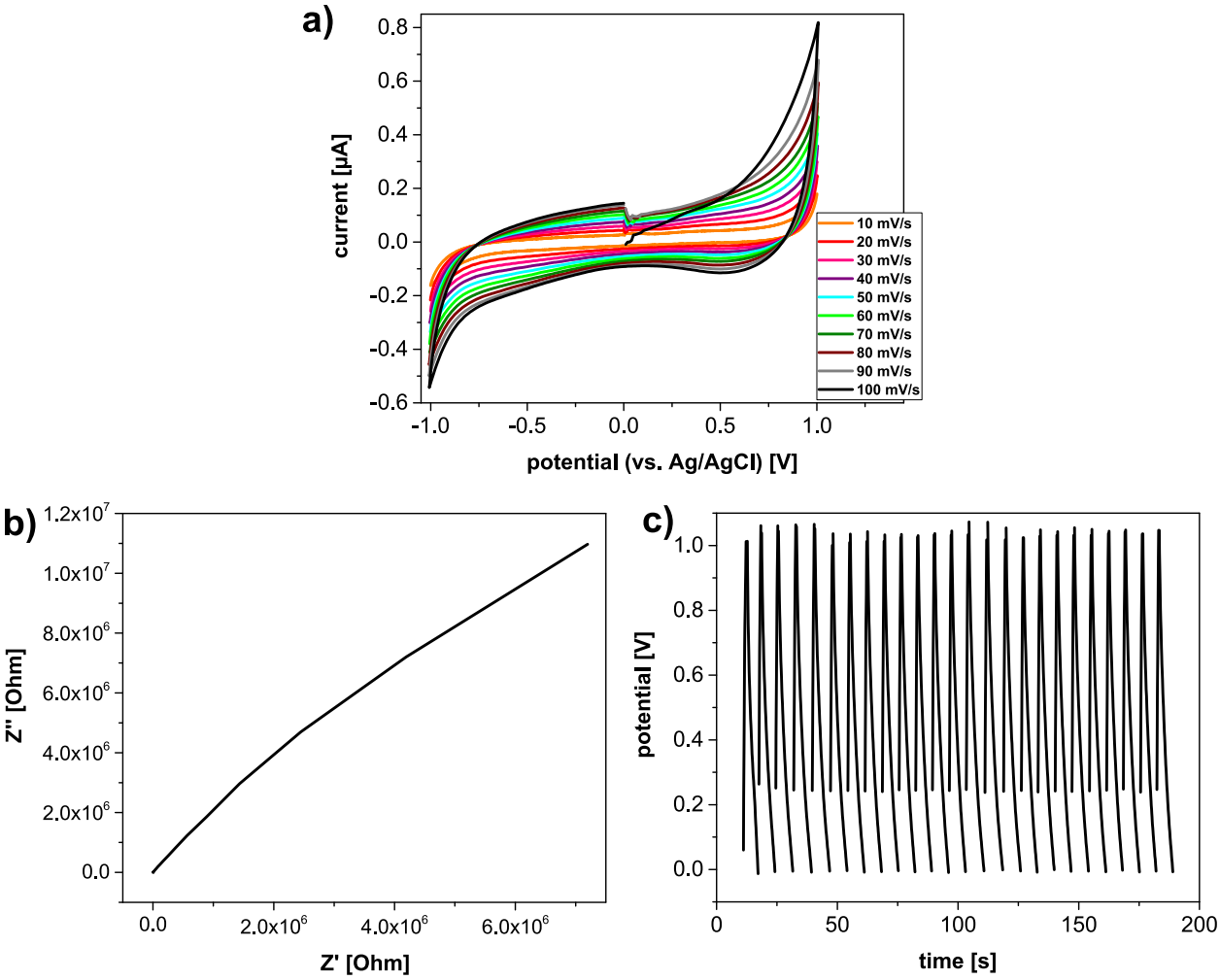

Figure 5.16: Charge storage capacity characterisation of an externally cross-linked PVTPA-*co*-PS (20 mol%) supercapacitor measured in 0.1 M LiBTFSI in MeCN. **a)** scan rate dependent cyclic voltammograms; **b)** Nyquist plot from electrochemical impedance spectroscopy with an amplitude of 0.5 V and **c)** galvanostatic charging discharging curves with 1 µA and cut-off potentials of 0 V and 1 V.

films had to be prepared by drop-casting. As a first consequence of this film deposition, no control over the homogeneity of the polymer film is possible. Secondly, there still remains a mass uncertainty of the electrode material. To avoid current short-cuts the used current-collectors are surrounded by an isolating teflon layer. Therefore it is essential to only deposit the polymer onto the free-standing disk electrode without spilling or leakage of the polymer solution onto the outer sheath. Even by drop-by-drop applying of the polymer solution it was not possible to prohibit some polymer deposition on the outer sheath, which results in

Table 5.9: Supercapacitor characterisation of cross-linked PVTPA-*co*-PS, measured in 0.1 M $LiBTFSI_4$ in MeCN by means of electrochemical impedance spectroscopy (EIS) and galvanostatic charging discharging (GCD).

PVTPA:PS ratio	$C_{sp,EIS}$ ($mF\,g^{-1}$)	$C_{sp,GCD}$ ($mF\,g^{-1}$)	E_{sp} ($J\,kg^{-1}$)	P_{sp} ($W\,kg^{-1}$)
100:0	58	2.0	43.4	10.0
50:50	230	2.0	90.0	10.0
30:70	152	2.3	60.5	11.0
25:75	30	10.0	32.1	9.4
20:80	58	4.0	109.4	11.8
15:85	49	2.5	10.3	6.1
10:90	45	2.0	114.1	11.4

some proportion of the polymer film not being electronically accessible. For this reason the energy density and power density values of the studied redox polymers are presented with their respective error bars obtained from a mass error propagation with a mass uncertainty of 50% of the absolute, applied mass in Fig. 5.17 **a** and **b** respectively. The used mass uncertainty of 50% has been chosen as a very cautious estimate and has most probably not been reached in the real experiments. But since no precise assessment of the electronically inactive polymer mass can be made, the uncertainty has been estimated rather too high than too low to cover a *worst-case scenario*. Since the resulting error bars become significant, only statements about orders of magnitude should be made. For the studied redox polymer supercapacitors the specific energy densities are in the range of 10^1 - $10^2\,J\,kg^{-1}$ and the specific power densities in the range of $10^1\,W\,kg^{-1}$. No dependency on the repeating unit ratio between PVTPA and PS is observed.

In general, the PVTPA-containing redox polymers do show charge storage properties and the stability of the cross-linked polymer films is good. Although, from the electrochemical characterisation of the supercapacitor devices, rather faradaic than capacitive behaviour is observed, which means that the application of these polymers in battery devices is expected to lead to higher charge storage efficiencies.

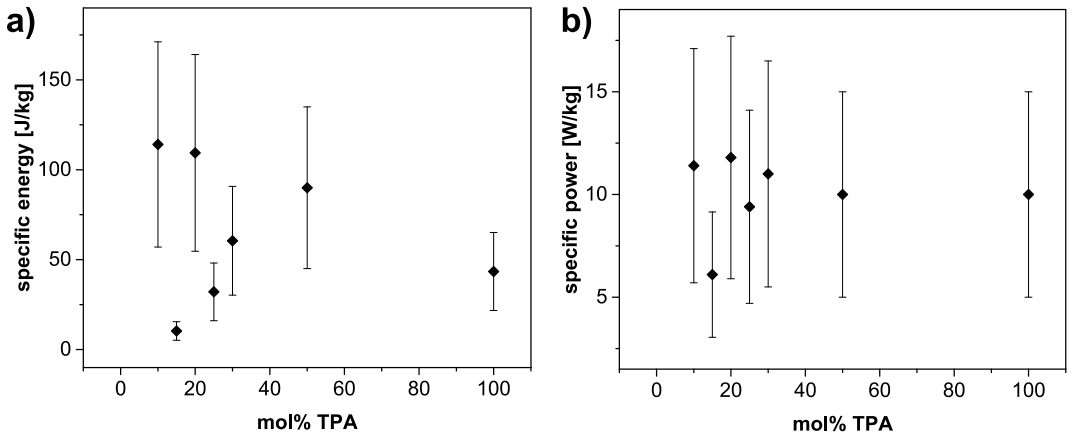

Figure 5.17: Overview of the specific energy (**a**) and specific power (**b**) of cross-linked PVTPA-*co*-PS copolymer supercapacitors measured in 0.1 M LiBTFSI in MeCN. Values were calculated from the galvanostatic charging discharging curves. Vertical bars indicate the error propagation of a mass uncertainty of 50% due to the film preparation by drop casting.

5.4.2. Conducting Films — Towards Novel Electrodes

TPA-containing polymers are promising new electrode materials to replace PEDOT:PSS due to their optical transparency, easy processability from solution and long term stability in the cross-linked state. For the utilisation in an industrial scale, electrochemical doping is uneconomical. Therefore, in recent years chemical doping of organic semiconducting materials has gained significant interest in literature. In particular, the chemical doping of *p*-type conducting polymers like P3HT with 2,3,5,6-tetrafluoro-7,7,8,8-tetracyanoquinodimethane (F4TCNQ) has been studied intensively, since it leads to polymer films of high conductivity and good long-term stability of the doped sample. [122, 217–219]

In a collaborative work with Reinold et al., we have studied the electrochemical and chemical doping behaviour of TPA-containing polythiophenes. [220] For the chemical doping of P3HT derivatives with side chain attached triphenylamine redox groups with F4TCNQ only doping of the polythiophene backbone was observed. To also initiate the oxidative cross-linking and charging of the TPA redox groups stronger dopants like $FeCl_3$ are needed. Therefore, the two dopants iron(III) chloride ($FeCl_3$) and iron(III) *p*-toluenesulfonate $Fe(Tos)_3$ are used to study the general usability of chemical doping for PVTPA and PVTPA-*co*-PS. The challenge for this particular study is to find the right conditions to successfully cross-link and charge the

redox polymers and to gain good conductivity values but meanwhile avoid overoxidation and side reactions like intramolecular cross-coupling of the triphenylamine groups to their phenyl-N-carbazole counter parts which has been reported by Olena Yurchenko for electrochemical doping at too high oxidation potentials. [221]

Chemical Dip Doping

As a first step, the general usability of $Fe(Tos)_3$ as a chemical dopant for triphenylamine containing redox polymers is studied. Therefore, a PVTPA homopolymer film, spin coated onto glass, is dipped into a solution of $Fe(Tos)_3$ in MeCN ($c = 0.5\,mg\,mL^{-1}$) under spectroscopic long time observation. In Fig. 5.18 **a** the evolution of the absorption spectra over a time period of 30 min are shown. In the wavelength range below 400 nm the signal-to-noise-ratio of all recorded spectra are poor, for which reason no information about the neutral TPA and TPB redox groups can be gained. For wavelengths above 400 nm the spectra are well resolved and the rise of characteristic absorption bands at 485 nm and 770 nm with a shoulder at 700 nm are observed. From the *in-situ* spectroelectrochemical characterisation in chapter 5.3.1 the observed absorption bands can be correlated to the $TPB^{+\cdot}$ radical cation and TPB^{2+} dication species. The shoulder at 700 nm has not been observed during the *in-situ* spectroelectrochemical characterisation but have been reported on by Yurchenko et al. and Reinold et al. and is attributed to non-cross-linked $TPA^{+\cdot}$ radical cations. [193, 220] As second difference in the chemical doping compared to the electrochemical, the generation of all charged species occurs concurrent, observed through the simultaneous arise of the characteristic absorption bands, while during the electrochemical doping the different redox species are generated in succession. This is caused by the oxidation potential of the dopant being constantly higher than the required potential for the cross-linking and charging reactions.
Unfortunately, no information about the neutral TPA and TPB redox groups can be gained from the *in-situ* spectra. For this reason the PVTPA sample was recovered, washed in pure MeCN to remove excess of the doping solution, dried in a nitrogen stream and afterwards transferred to a stationary spectrometer. Fig. 5.18 **b** shows the absorption spectra of the dry PVTPA before (black curve) and after (blue curve) chemical doping in $Fe(Tos)_3$ solution. In the initial PVTPA film only the absorption band of the neutral TPA redox groups at 310 nm is observed. After chemical doping two additional absorption bands at 360 nm and 485 nm of

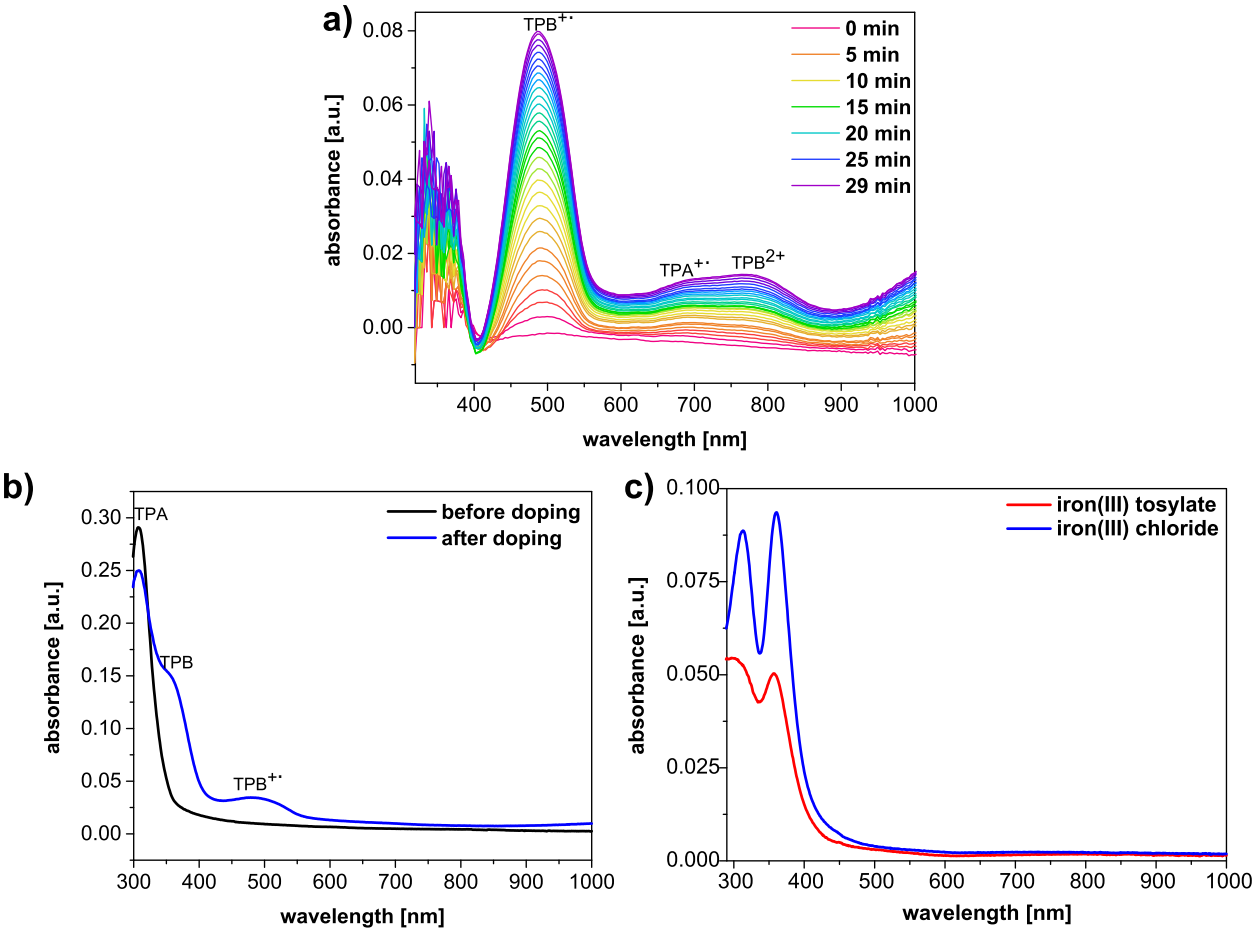

Figure 5.18: **a)** *in-situ* spectra recorded during the chemical doping of a PVTPA film in $Fe(Tos)_3$ solution in MeCN with a concentration of 0.5 mg mL^{-1} with an overall exposure time of 30 min; **b)** absorption spectra of the PVTPA film before (black curve) and after (blue curve) chemical doping, measured in dry state; **c)** absorption spectra of $Fe(Tos)_3$ (red curve) and $FeCl_3$ (blue curve) in MeCN with a concentration of 0.5 mg mL^{-1}.

the neutral TPB redox groups and the $TPB^{+\cdot}$ radical cation are observed respectively. The absorption bands of the $TPA^{+\cdot}$ radical cation and the TPB^{2+} dication at 700 nm and 770 nm respectively are not observed in the *ex-situ* spectra, which can be due to discharging caused by the washing and drying of the polymer film. An overview of all observed absorption bands during chemical doping of PVTPA with $Fe(Tos)_3$ is given in Table 5.10. In sum, from the *in-situ* and *ex-situ* spectra it can be concluded, that partial oxidative cross-linking of the TPA redox groups and consecutive two step-oxidation of the generated TPB redox groups to the respective dication are initiated by the chemical doping with $Fe(Tos)_3$ in solution.

Table 5.10: Overview of the absorption bands of PVTPA during chemical doping with $Fe(Tos)_3$ in MeCN with a concentration of $0.5\,mg\,mL^{-1}$.

wavelength (nm)	chemical species [a]
<400	/ [b]
485	$TPB^{+\cdot}$
700	$TPA^{+\cdot}$ [c]
770	TPB^{2+}
310	TPA [d]
360	TPB [d]

[a] identification of chemical species by means of *in-situ* spectroelectrochemical studies.
[b] absorption bands not identifiable due to noisy absorption signals.
[c] species identification according to Reinold et al. [220], Yurchenko et al. [193] on polymers containing similar redox groups.
[d] absorption bands observed in dry state.

For a better understanding of what causes the poor signal-to-noise ratio of the *in-situ* absorption spectra at wavelengths <400 nm and to avoid confusion of polymer absorption bands and dopant absorption bands, the spectra of the doping solution of both dopants $FeCl_3$ and $Fe(Tos)_3$ are shown in Fig. 5.18 **c**. Both $FeCl_3$ (blue curve) and $Fe(Tos)_3$ (red curve) solutions in MeCN possess two overlapping absorption bands at 310 nm and 355 nm with a sharp absorption intensity decline at 400 nm. Thus, the wavelength range of the poor signal-to-noise ratio observed in the *in-situ* spectra matches the wavelength range of the doping solution. Since the spectrum of a clean glass substrate emerged into the doping solution was used as the reference spectrum, intensity changes of the dopant absorption bands during the doping process result in a mismatch of the used reference spectrum to the actual background spectrum which might cause the intense signal noise. In addition, the TPA and TPB redox groups neutral bands may be disguised by excess of the dopant. Consequently, the following spectroscopic characterisation of the chemical doping processes of PVTPA-*co*-PS copolymer films has been performed on washed and dried films, taken into account the risk of de-doping. To verify the general usability of the chemical doping to generate conducting PVTPA-*co*-PS films and to study the influence of the cross-linking density Fig. 5.19 shows the absorption spectra of the PVTPA-*co*-PS copolymer films with varying repeat unit ratios after dip doping

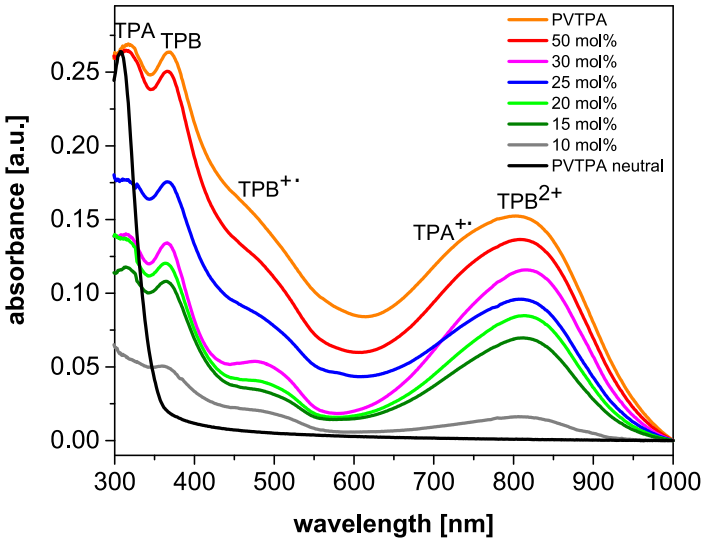

Figure 5.19: Absorption spectra of PVTPA-*co*-PS copolymer films after chemical doping with $FeCl_3$ solution in MeCN with a concentration of $5\,mg\,mL^{-1}$ and exposure times of 15 min each.

in $FeCl_3$ solution ($c = 5\,mg\,mL^{-1}$) for exposure times of 15 min each. The initial spectrum of a PVTPA homopolymer film is also inserted in Fig. 5.19 (black curve) to allow for a direct comparison. The absorption spectra of all studied copolymers reveal the characteristic absorption bands described above after chemical doping with $FeCl_3$, indicating successful cross-linking and charging of the copolymers. For all PVTPA-*co*-PS copolymers and the PVTPA homopolymer the TPA neutral and $TPA^{+\cdot}$ radical cation bands are still observed, meaning the cross-linking is incomplete regardless of the repeating units ratio. The influence of the repeating unit ratio can be seen as a general trend of increasing absorption intensity of all charged species with increasing PVTPA amount. For all studied polymer films, the intensity of the TPB^{2+} absorption band is higher than of the $TPB^{+\cdot}$ band, indicating an amplified generation of the dication with respect to the radical cation.

To avoid the risk of an overoxidation caused by the high oxidation potential of $FeCl_3$ which could result in decreased conductivity of the polymer films, the chemical doping with $Fe(Tos)_3$, which is a milder dopant, is also studied. In Fig. 5.20 the absorption spectra of the PVTPA homopolymer and PVTPA-*co*-PS copolymers after chemical doping in $Fe(Tos)_3$ solution ($c = 5\,mg\,mL^{-1}$) with an exposure time of 15 min each are shown. Again, to allow a direct comparison to the initial polymer film spectrum, the PVTPA neutral spectrum is

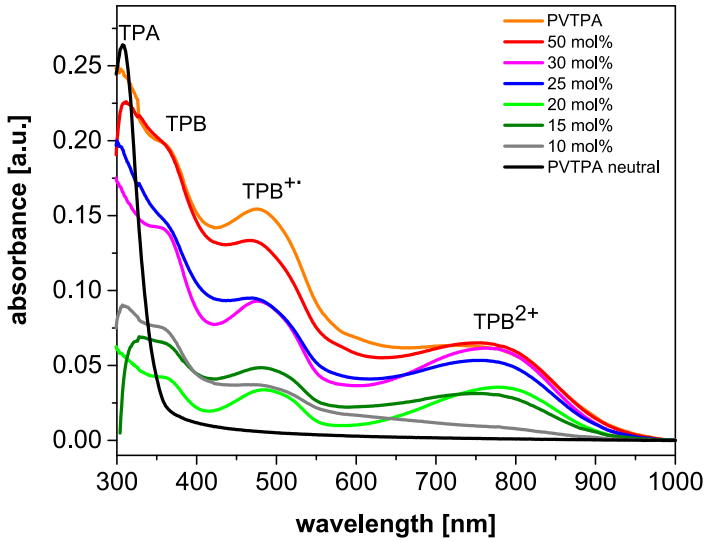

Figure 5.20: Absorption spectra of PVTPA-*co*-PS copolymer films after chemical doping with $Fe(Tos)_3$ solution in MeCN with a concentration of $5\,mg\,mL^{-1}$ and exposure times of 15 min each.

shown in Fig. 5.20 (black curve) as well. Similar to the chemical doping with $FeCl_3$, the characteristic absorption bands of the cross-linked and charged redox groups are observed after doping with $Fe(Tos)_3$ regardless of the PVTPA amount. Due to the preservation of the TPA neutral band at 310 nm after the doping process, again only partial cross-linking of the redox groups is observed. Again, the influence of the repeating units ratio can be seen as a general trend of increasing absorption intensity of the charged species with increasing PVTPA amount. In contrast to the chemical doping with $FeCl_3$ the absorption intensity of the TPB^{2+} dication is weaker than of the $TPB^{+\cdot}$ radical cation for the studied polymers, which leads to the interpretation that even with the oxidation potential of $Fe(Tos)_3$ being high enough to initiate the cross-linking reaction, the milder doping conditions result in a favoured preservation of the $TPB^{+\cdot}$ radical cation rather than generation of the TPB^{2+} dication.

The aim of the chemical doping of PVTPA containing polymers is to generate conducting polymer films which can be used as electrodes in organic electronic devices. The conductivity of such organic materials can be measured by means of the so-called *4-point-probe* (*4pp*) technique. The deposition of the organic semiconductor onto an isolating, square-shaped substrate and the knowledge of the exact film thickness are the two prerequisites therefore.

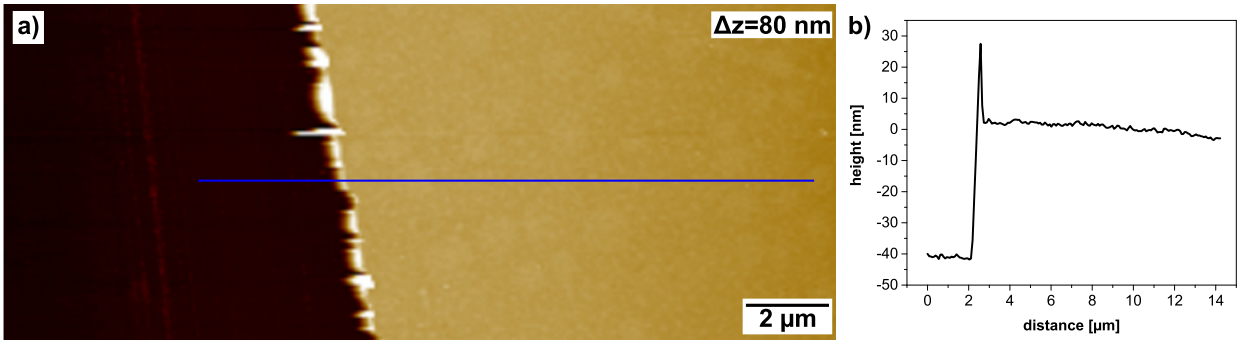

Figure 5.21: Determination of the PVTPA homopolymer film thickness; **a)** AFM height image measured in tapping mode and **b)** height profile extracted from the AFM image. The position of the extracted height profile is indicated by a blue line in **a)**.

The film thickness determination via atomic force microscopy of a PVTPA homopolymer film spin coated onto glass is shown in Fig. 5.21 exemplarily. The AFM hight image (Fig. 5.21 **a**) reveals an even, homogeneous polymer film (bright area to the right of the image) and the edge to a deliberate scratch (dark area to the left of the image), at which the polymer has been removed with a sharp cannula to expose the underlying glass substrate. By measuring the height profile (see Fig. 5.21 **b**) perpendicular to the scratch edge (position indicated by the blue line in Fig. 5.21 **a**) the average thickness of the polymer film can be determined. For the studied PVTPA films spin coated onto glass (5 mg mL^{-1} in chloroform, 180 s at 2000 rpm) the average film thickness, measured on multiple samples and at various positions per sample accounts to 40±5 nm.

Being a first test to introduce the field of chemically cross-linked and doped triphenylamine containing redox polymers as novel electrode materials, the following conductivity characterisation is restricted to the PVTPA homopolymer, the technique of dip-doping and $Fe(Tos)_3$ as dopant. Since PVTPA is not a π-conjugated semiconducting polymer with a broad conductivity plateau but a redox polymer with a literature-known conductivity profile with distinct maxima for electrochemical doping, the challenge is to find the optimal sample preparation parameters (dopant, concentration, duration) to achieve good conductivity values. [8] To determine the conductivity of the doped PVTPA films by means of *4pp* measurements, a defined current procedure is applied through the two outer pins of the probe head and the resulting potential between the two inner pins is recorded. In Fig. 5.22 **a** the used current

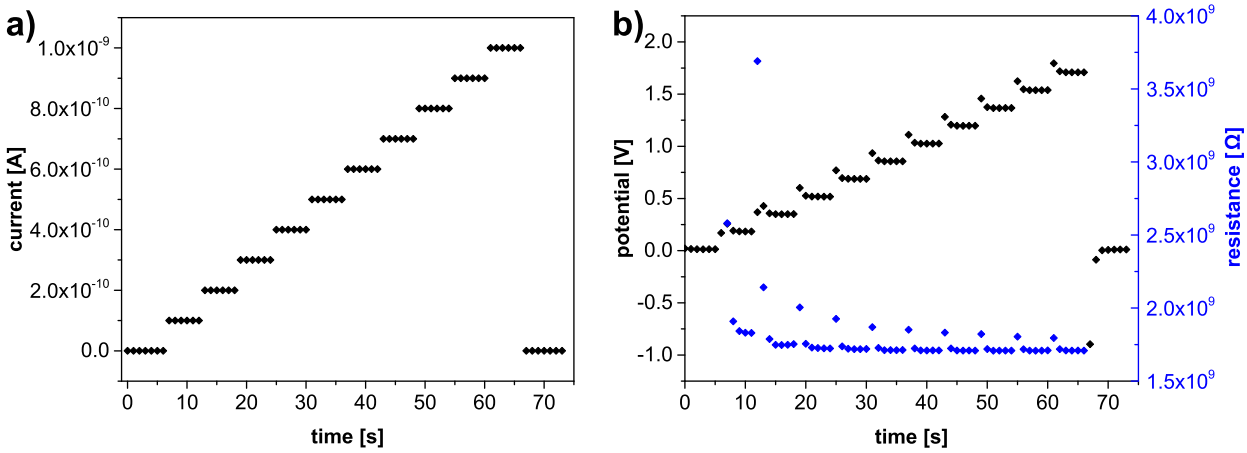

Figure 5.22: Conductivity measurement of PVTPA after doping with $Fe(Tos)_3$ in MeCN by 4-point-probe; **a)** current input as function of time; **b)** measured potential (black dots) and calculated resistance (blue dots) as function of time.

protocol is shown as a function of time. In every step the current is kept at a constant value for the duration of 6 s and then increased stepwise. The stepwise protocol of the applied current is used to assess the quality of the experimental data. In the linear, ohm'ic resistance regime, the recorded potential mirrors the applied current step-function. In Fig. 5.22 **b** the potential data points (black dots) follow the step-function of the applied current with exception of the first data point of each current step. The deviation of the first respective data point can be caused by a slow adjustment of the internal field equilibrium due to the sudden current modification. Since the other potential data points follow the current step-potential by forming a plateau, the respective first data points of each current step are neglected for further analysis and the conductivity calculation. From the measured potential the resistance (blue dots in Fig. 5.22 **b**) can be calculated according to Ohm's law. By using Eq. 14 the bulk conductivity of the polymer film can be calculated from the bulk resistance and the film thickness. In Fig. 5.23 the average conductivities with their standard deviation of the PVTPA homopolymer dip-doped in $Fe(Tos)_3$ solution with varying concentrations (0.5 mg mL^{-1} to 10 mg mL^{-1}) and doping duration times (5 min to 30 min) are shown. For each sample multiple measurements (at minimum four) at various positions on the polymer film were conducted. For the dip-doping of PVTPA with $Fe(Tos)_3$ conductivities in the range of 10^{-5} A V^{-1} cm^{-1} and 10^{-4} A V^{-1} cm^{-1} were reached over a wide doping solution concentration and doping duration time range. The highest conductivity value of

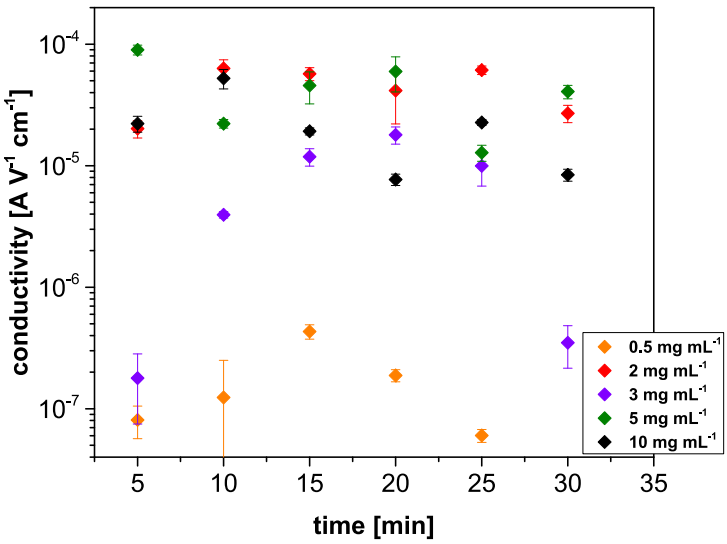

Figure 5.23: Overview of the conductivity of PVTPA films after dip-doping in $Fe(Tos)_3$ solutions in MeCN with varying dopant concentrations and exposure times.

$9 \times 10^{-5}\,A\,V^{-1}\,cm^{-1}$ was achieved for a $Fe(Tos)_3$ concentration of $5\,mg\,L^{-1}$ and doping duration of 5 min. For the chemical doping of PVTPA with $FeCl_3$ no conductivity values higher than $10^{-7}\,A\,V^{-1}\,cm^{-1}$ were recorded. Reasons for this low conductivity values in comparison to the doping with $Fe(Tos)_3$ can be non-optimised sample preparation parameters (doping concentration and duration) as well as possible over-oxidation due to the higher oxidation potential of the dopant.

Chemical Vapour Doping

An other chemical doping technique which has gained interest in the organic electronics community in recent years is vapour doping. This technique is often used for the chemical doping of *p*-type conducting polymers like P3HT with F4TCNQ. The main advantage of this method is, that the organic semiconductor can be doped in dry state. As a first task a vapour doping cell has been constructed according to a set-up described by Yamamoto et al. [94] in which the polymer film can be deposited onto a quartz glass disc via spin coating to allow for *in-situ* absorption spectroscopic characterisation during the vapour doping process. $FeCl_3$ and $Fe(Tos)_3$ have been used as dopants to test for proper operation of the set-up. Fig. 5.24 shows the *in-situ* absorption spectra of a PVTPA homopolymer film during the vapour doping process with $FeCl_3$ at a pressure of 10^{-3} mbar. The isolated, lowered spectrum in

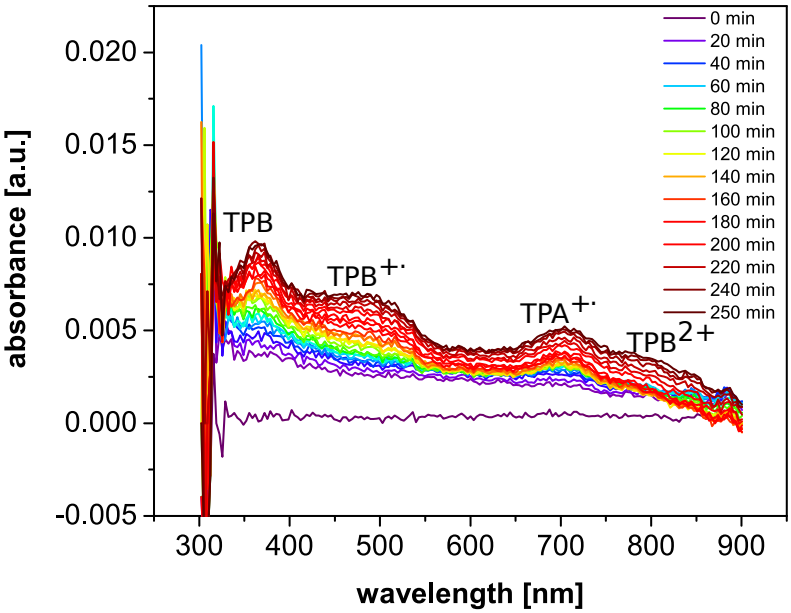

Figure 5.24: *In-situ* absorbtion spectra of a PVTPA film recorded during chemical vapour doping with $FeCl_3$ and an overall exposure time of 250 min.

Fig. 5.24 corresponds to the initial spectrum before the under pressure is applied which caused the dopant to transfer into the gas phase and therefore acts as a reference spectrum. In general, the intensity of the recorded spectra is low which leads to noisy signals especially at the edges of the detection range. Unfortunately in the range of 300 nm to 330 nm the signal-to-noise ratio is that poor that no information about the TPA neutral band can be gained. Upon the vapour doping of PVTPA with $FeCl_3$ the characteristic absorption bands of the neutral TPB redox groups, the $TPB^{+\cdot}$ radical cation, the $TPA^{+\cdot}$ radical cation and the TPB^{2+} dication species arise, indicating successful oxidative cross-coupling and charging of the polymer film. For the vapour doping of PVTPA with $Fe(Tos)_3$ no evolution of the characteristic absorption bands was observed. Possible reasons for this are a too low partial pressure of the dopant under the used experimental conditions or leakage of the custom-made set-up. To test if $Fe(Tos)_3$ vapour doping is usable for the oxidative cross-coupling and charging of PVTPA in general, further experiments with an improved set-up design are required.

6. Conclusion and Outlook

Within the scope of this thesis the electrochemical redox processes in two classes of conducting polymers, namely the π-conjugated poly(3-hexylthiophene) (P3HT) and the redox polymer polyvinyltriphenylamine (PVTPA), have been studied. Special focus has been set on the influence of the inner structure of the polymer films on the electrochemical redox behaviour. The film morphology of the semi-crystalline P3HT has been manipulated by the film deposition and post-treatment techniques to obtain a series of samples of different textures and of varying degrees of crystallinity. In case of the redox polymer PVTPA the inner structure of the polymer film is generated by an electrochemically induced cross-linking reaction of the polymer chains. By studying a series of PVTPA-*co*-PS copolymers with varying PVTPA-to-PS ratios, from the PVTPA homopolymer to just 10 mol% of redox-active repeating units, the influence of the cross-linking density on the electrochemical redox behaviour has been studied.

Influence of Controlled Thin Film Morphology on the Electrochemical Behaviour of P3HT

In this thesis, it has been shown, that the regioregularity, the morphology and the degree of crystallinity of semi-crystalline P3HT thin films have a significant influence on the electrochemical behaviour and the HOMO energy levels.

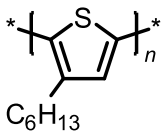

By comparing an electropolymerised, regioirregular P3HT sample with chemically synthesised, regioregular P3HT it could be shown, that the number of superimposing anodic subsignals in the voltammogram increases from two to three with increasing regioregularity (see also Fig. 6.1). The additional anodic subsignal is located at lower oxidation potential which results in a shift of the HOMO energy levels by 0.2 eV from -5.3 eV to -5.1 eV with increasing regioregularity. *In-situ* spectroelectrochemical characterisation has been performed to gain information about the chemical species attributed to the anodic voltammetric half wave. In Fig. 6.2 the *in-situ* spectroelectrochemical characterisation of a spin-coated P3HT film is shown exemplarily. From the potential dependent intensity evolution curves of characteristic absorption bands, all three superimposing subsignals of the anodic half wave can

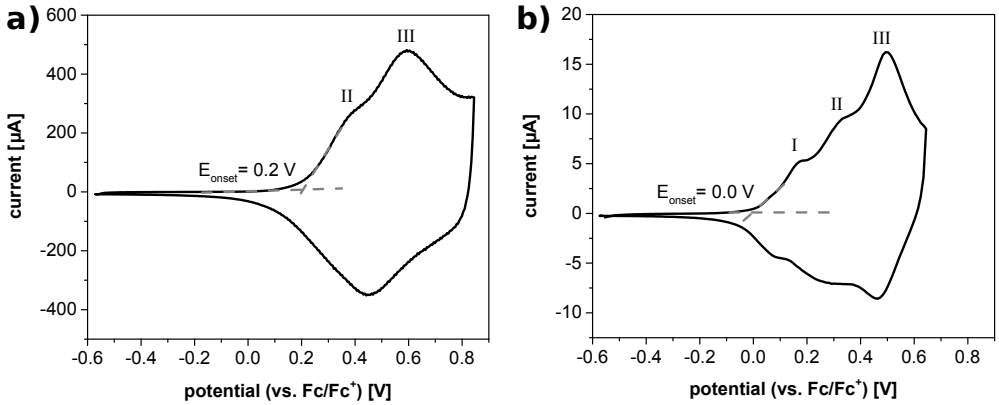

Figure 6.1: Cyclic voltammograms of electropolymerised (**a**) and chemically synthesised (**b**) P3HT film samples; measured in 0.1 M NBu_4PF_6 in MeCN with a scan rate of 20 mV s^{-1}.

be attributed to the first oxidation of neutral P3HT to the radical cation species. At potentials higher than the peak potential of the anodic half wave also an increasing absorption band of the dication species is observed (black curve in Fig. 6.2 **b** at 0.6 V).

The observed subsignals in the anodic half wave are in accordance with literature [5, 166, 170] in which they are assumed to correlate to the first oxidation step in coexisting domains of different morphologies, but no direct correlation could be made due to uncontrolled film morphologies of the studied samples. To be able to draw a direct correlation of P3HT film

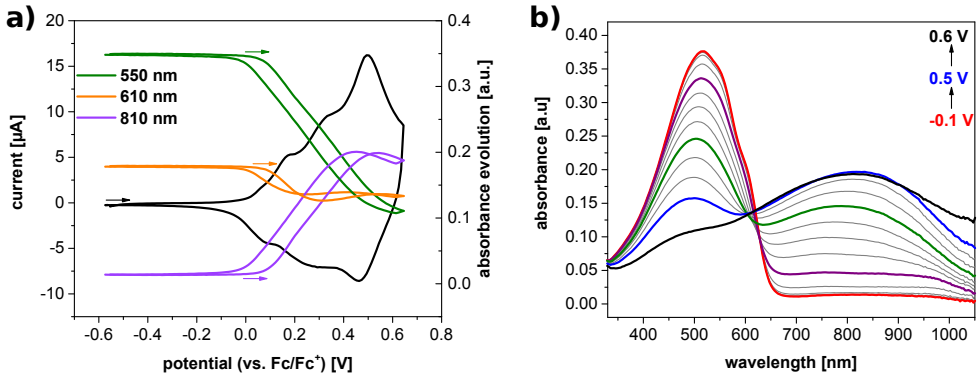

Figure 6.2: *In-situ* spectroelectrochemical characterisation of spin-coated, regioregular P3HT; **a)** cyclic voltammogram with intensity evolution curves of characteristic absorption bands; **b)** absorption spectra recorded during the forward scan of **a**; measured in 0.1 M NBu_4PF_6 in MeCN with a scan rate of 20 mV s^{-1}.

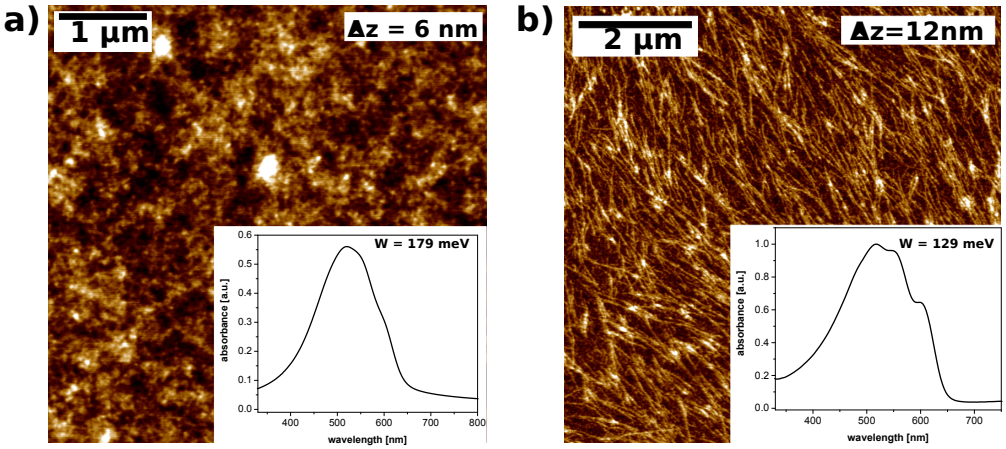

Figure 6.3: Morphological characterisation of spin-coated (**a**) and solvent vapour annealed (**b**) P3HT films by means of atomic force microscopy and absorption spectroscopy.

morphology to the superimposing anodic subsignals, P3HT samples of controlled morphologies in the *edge-on* and *face-on* textures with increasing degree of crystallinity have been prepared from the same chemically synthesised regioregular P3HT batch, by crystallisation from solution and post-annealing techniques like solvent vapour annealing and high temperature rubbing. The film morphologies have been characterised by means of atomic force microscopy, transmission electron microscopy, polarised optical microscopy and absorption spectroscopy. While non-annealed regioregular P3HT (see Fig. 6.3 **a**) forms predominately amorphous films with only few π-π stacked domains, the crystallisation and post-treatment methods result in successful growth of P3HT nanowires, spherulitic structures (see Fig. 6.3 **b**) and large-area alignment of the polymer chains, which show decreased exciton band widths, indicating larger conjugation lengths and higher degrees of crystallinity.

The anodic half waves of all crystallised P3HT films reveal three superimposing subsignals which match the potentials of the subsignals observed in the amorphous P3HT sample (see Fig. 6.4). The onset potentials of all crystallised P3HT samples are similar (0.07 V to 0.08 V), but the intensity of the first subsignal at low oxidation potentials increases with respect to the other subsignals, which enables the determination of the half wave potential of the first subsignal for the crystallised P3HT samples. The two predominately *edge-on* samples (nanowires and spherulitic structures) and the predominately *face-on* sample (high temperature rubbing) reveal half wave potentials of 0.13 V and 0.11 V respectively.

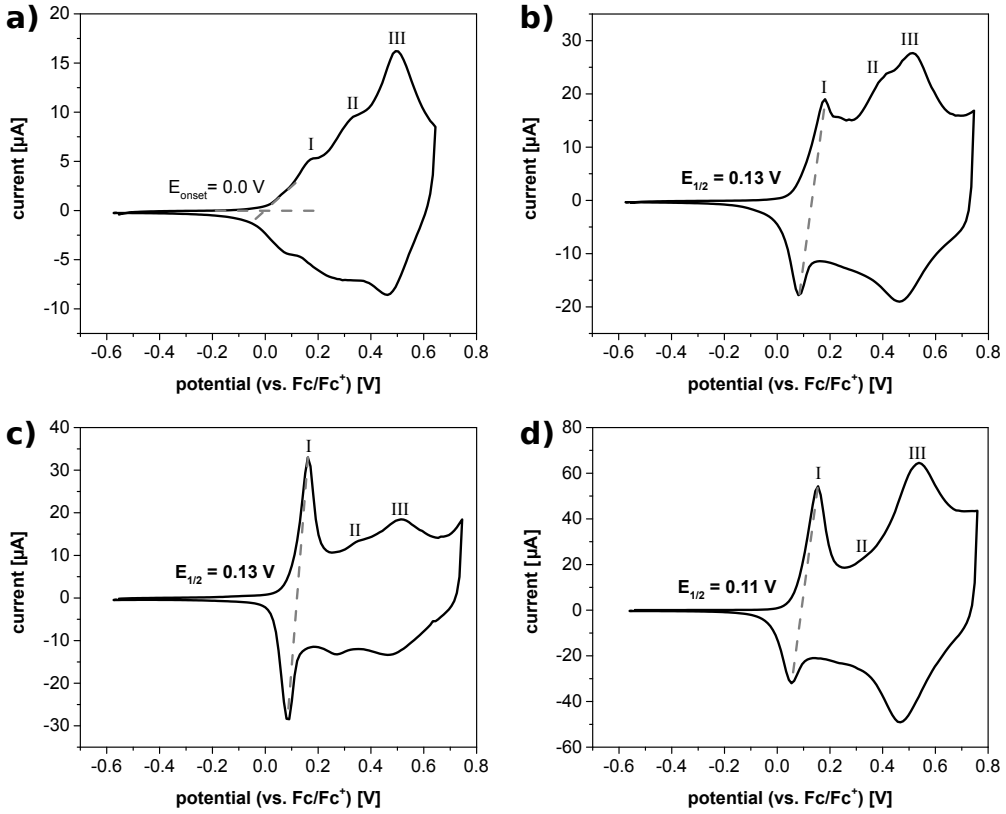

Figure 6.4: Electrochemical characterisation of P3HT films of controlled morphologies; **a)** spin-coated, non-annealed P3HT film; **b)** spherulitic P3HT sample after solvent vapour annealing; **c)** P3HT nanowires prepared by crystallisation from solution; **d)** large area aligned P3HT film prepared by high-temperature rubbing; measured in 0.1 M NBu_4PF_6 in MeCN with a scan rate of 20 mV s^{-1}.

The *in-situ* spectroelectrochemical characterisation of the P3HT samples of controlled morphologies reveal the same behaviour as the non-annealed, regioregular P3HT sample, whereby all subsignals of the anodic half wave are attributed to the oxidation of neutral P3HT to the radical cation species. In increasing intensity of the dication absorption band is only observed at potentials higher than the peak potential of the third subsignal. From the potential dependent intensity evolution curves of characteristic absorption bands and from the observed fine structure in the neutral spectra prior and after electrochemical charging/ discharging cycles, chemically reversible redox reactions under preservation of the film morphology is observed. In accordance with Skompska et al. [166, 170] the three superimposing subsignals in the anodic scan of P3HT are attributed to the formation of the radical cation in coexisting domains of different morphologies in the P3HT films. In addition, a direct correlation of the

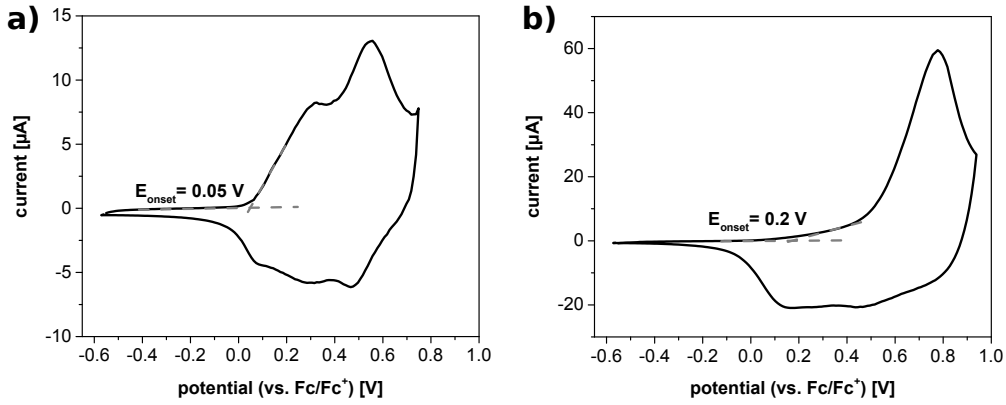

Figure 6.5: Cyclic voltammograms of non-annealed (**a**) and thermally annealed (**b**) binary P3HT:$PC_{61}BM$ donor acceptor blend films; measured in 0.1 M NBu_4PF_6 in MeCN with a scan rate of 20 mV s^{-1}.

intensity of the first subsignal at low oxidation potentials to the degree of crystallinity can be made and therefore the first subsignal is attributed to the first oxidation of crystalline domains of the P3HT films.

In the next step, the influence of the intermixing of P3HT with $PC_{61}BM$ on the electrochemical behaviour of the binary donor acceptor blend films has been studied. In Fig. 6.5 the cyclic voltammograms of a non-annealed (**a**) and a thermally annealed (**b**) P3HT:$PC_{61}BM$ film are shown. The anodic scan of a non-post-treated P3HT:$PC_{61}BM$ blend film shows a broad half wave which corresponds only to the third subsignal observed in pristine P3HT films. The absence of anodic subsignals at lower oxidation potentials and the lack of a fine-structure in the neutral absorption spectrum indicate hindered formation of crystalline P3HT domains in the blend film due to the intermixing with the acceptor material. Compared to undisturbed, pristine regioregular P3HT films, the HOMO energy is lowered by 0.2 eV in the binary blend. By applying of an additional thermal annealing step during sample preparation, both the fine-structure in the neutral spectrum as well as the anodic subsignals at lower oxidation potentials are regained, which is attributed to the formation of π-π stacked, crystalline domains due to the increased mobility of the polymer chains in the blend system during the thermal annealing step. The HOMO energy level of a thermally annealed P3HT:$PC_{61}BM$ blend film is similar to the HOMO level of pristine, regioregular P3HT. Since the reduction potentials of $PC_{61}BM$ are not influenced by the annealing, the shift of the HOMO level in the non-annealed blend film causes an enlargement of the effective band gap by 0.2 eV. An

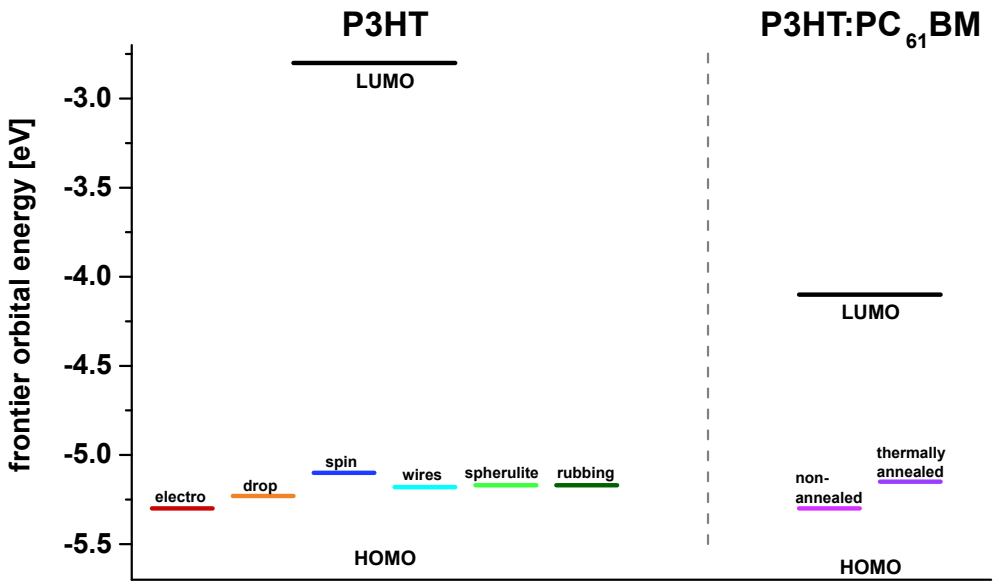

Figure 6.6: Overview of the frontier orbital energy levels of P3HT and P3HT:$PC_{61}BM$ film samples; determined by means of cyclic voltammetry.

overview of the frontier orbital energy levels of P3HT films of various morphologies as well as pristine and thermally annealed P3HT:$PC_{61}BM$ blend films are shown in Fig. 6.6.

In this thesis the focus was set on the characterisation and interpretation of the first, low-oxidation-potential subsignal in the anodic half wave of P3HT, since it can be unambiguously attributed to the first oxidation towards the radical cation species, while the high-oxidation-potential subsignals may overlap with the beginning formation of the dication species. In addition, a possible attribution to the crystalline domains as suggested by Ref. [166] is rather straightforward to investigate, since the preparation of P3HT thin films of controlled morphology and increased crystallinity is well known in literature.

To further study the correlation of π-π stacked, crystalline P3HT domains and the corresponding electrochemical response, film preparation by directional solidification (*epitaxy*) can be performed. Brinkmann et al. [179] could show, that P3HT solidified on 1,3,5-trichlorobenzene results in highly oriented and crystalline films with periodically alternating amorphous and crystalline lamellae.

In addition, the nature of the two other anodic subsignals, which Ref. [166] attributes to the first oxidation of quasi-ordered and amorphous domains respectively, should be further studied. Since the *in-situ* spectroelectrochemical characterisation indicates the beginning

second oxidation to the dication species at potentials higher than the peak potential of the third anodic subsignal, cyclic voltammetry coupled with electron paramagnetic resonance spectroscopy should be performed to study the potential dependent consumption of the radical cations and formation of dications.

Electrochemical Characterisation of the Oxidative Cross-linking of PVTPA-*co*-PS Copolymers

Within the scope of this thesis the optical, electrochemical and electronic properties of PVTPA and PVTPA-*co*-PS copolymers with varying repeating unit ratios have been studied. The focus was set on the characterisation of the influence of the cross-linking density on the redox behaviour.

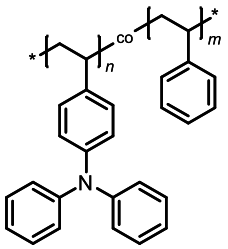

In the basic electrochemical characterisation on gold electrodes, it could be shown, that even for the lowest TPA-amount copolymer (10 mol%) successful oxidative cross-linking from TPA ⇌ TPB takes place and all polymers show reversible charging/ discharging behaviour in their cross-linked state. The cyclic voltammograms of the first and second cycles of the PVTPA homopolymer and the PVTPA-*co*-PS copolymer with the lowest PVTPA-to-PS ratio (10:90 mol%) are shown in Fig. 6.7 exemplarily. For the PVTPA homopolymer and the high TPA-amount copolymers (50 mol%, 30 mol% and 25 mol%) two reversible redox waves for the two-step redox process TPB ⇌ $TPB^{+\cdot}$ ⇌ TPB^{2+} are observed in the cross-linked state. In case of the low TPA-content copolymers (20 mol%, 15 mol% and 10 mol%) an overlapping of the anodic half waves in the cross-linked state is observed, while the cathodic half waves remain unimpaired. One possible explanation for this behaviour is a changing ion intercalation movement during the charging process.

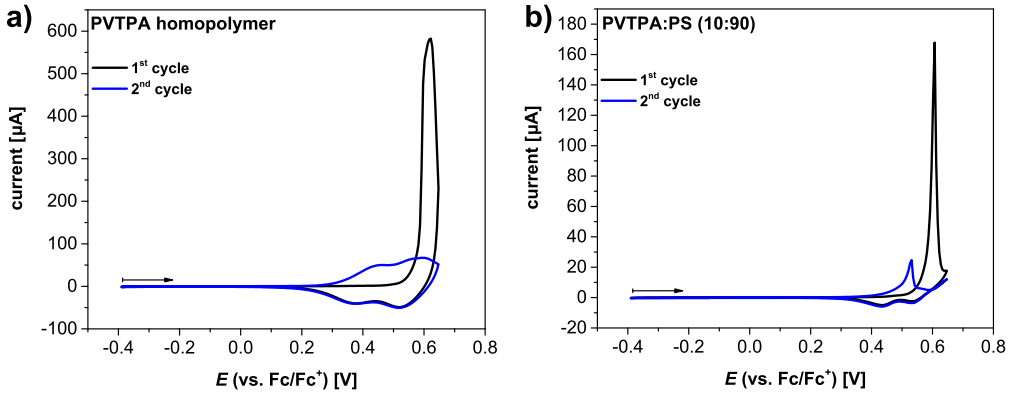

Figure 6.7: Cyclic voltammograms of the first and second cycles of the PVTPA homopolymer (**a**) and the PVTPA-*co*-PS copolymer with a PVTPA-to-PS ratio of 10:90 mol% (**b**); measured in 0.1 M NBu_4PF_6 in MeCN with a scan rate of 20 mV s^{-1}.

During the electrochemical characterisation of PVTPA and PVTPA-*co*-PS on ITO electrodes a hindered discharging behaviour after the cross-linking reaction has been observed for the PVTPA homopolymer and the high TPA-content copolymers (50 mol% and 30 mol%). By applying a thermal annealing step after the film deposition, the same discharging behaviour as observed on gold electrodes could be recorded. Electrochemical impedance characterisation of the initial and the thermally annealed polymer films on ITO revealed a reduced double layer capacitance after the annealing step for the homopolymer and the 50 mol% copolymer, which can be interpreted as a decreased energetic barrier for the counter ion movement at the polymer-electrolyte interface.

In-situ spectroelectrochemical characterisation has been used to confirm the cross-linking and charging mechanism described by Yurchenko et al. [8] and to identify characteristic absorption bands for the different charging states. In Fig. 6.8 the spectroelectrochemical characterisation of the two-step oxidation of cross-linked PVTPA-*co*-PS (30:70 mol%) is shown exemplarily. The identified characteristic absorption bands are essential for the identification of charged species after chemical doping.

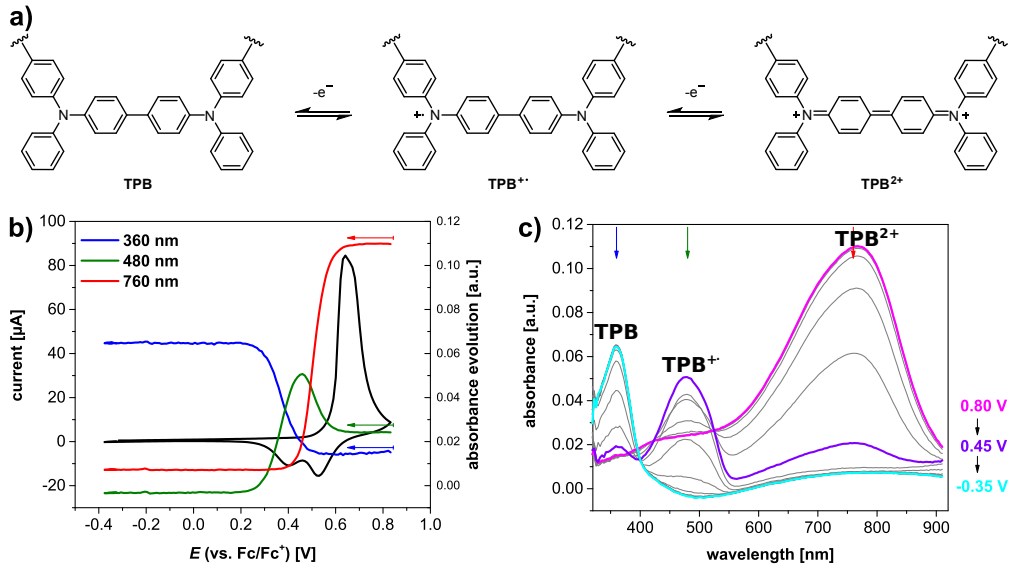

Figure 6.8: Identification of characteristic absorption bands by means of *in-situ* spectroelectrochemical measurements; **a)** mechanism of the reversible two-step oxidation of cross-linked PVTPA; **b)** cyclic voltammogram (first cycle) of PVTPA-*co*-PS (30:70 mol%) with intensity evolution curves of characteristic absorption bands; **c)** absorption spectra recorded during the backwards scan of **b**.

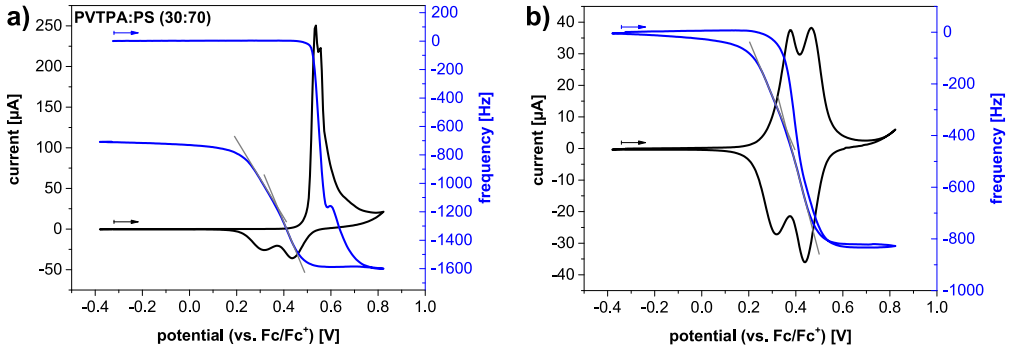

Figure 6.9: Electrochemical quartz crystal micro balance characterisation of the first (**a**) and second (**b**) cycle of PVTPA-*co*-PS (30:70 mol%); measured in 0.1 M NBu_4PF_6 in MeCN with a scan rate of 20 mV s^{-1}.

To gain a deeper understanding of the ion movements during the electrochemical induced cross-linking reaction and charging/ discharging processes, electrochemical quartz crystal micro balance measurements of the PVTPA homopolymer and the PVTPA-*co*-PS copolymers with different conducting salts have been performed. Fig. 6.9 shows exemplarily the EQCM characterisation of the first (**a**) and second (**b**) cycles of the PVTPA-*co*-PS copolymer (30:70 mol%) measured in 0.1 M NBu_4PF_6 in MeCN. In general, a direct correlation of redox half waves and frequency changes have been observed. Upon charging of the polymer films the frequency decreases, indicating a mass increase due to counter ion intercalation, while discharging of the polymer films lead to a frequency increase caused by the expulsion of ions from the polymer film into the electrolyte. In case of the cross-linking reaction an irreversible frequency offset in the neutral state is observed, which can be explained by ion trapping and a change in the elastic modulus caused by the cross-linking of the polymer chains. During the charging/ discharging of the cross-linked polymer films reversible ion intercalation and expulsion is observed. The two-step redox processes TPB $\rightleftharpoons$ $TPB^{+\cdot}$ $\rightleftharpoons$ TPB^{2+} can be identified by a changing slope of the frequency curves. In case of the low TPA-content copolymer with only 10 mol% of redox groups, the EQCM data reveal the superimposing of the anodic charging half waves which has also been observed during the basic electrochemical characterisation on gold electrodes.

First experiments to assess the general usability of PVTPA and PVTPA-*co*-PS copolymers as charge storage materials have been performed by means of supercapacitor tests. Cyclic voltammetry and electrochemical impedance spectroscopy have been used as control exper-

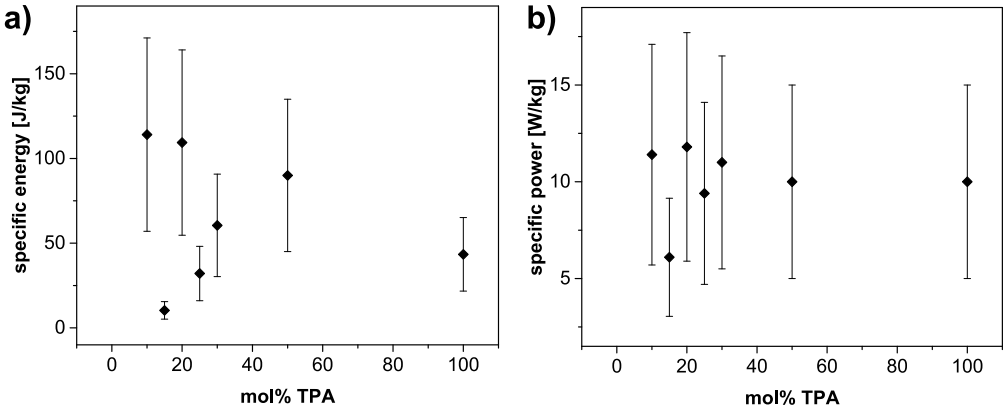

Figure 6.10: Overview of the specific energy densities (**a**) and specific power densities (**b**) of cross-linked PVTPA-*co*-PS copolymers; measured as symmetric supercapacitor devices in 0.1 M LiBTFSI in MeCN.

iments to gain deeper insight into the nature of the electronic processes and the state of the device, like contact resistances at the current collector-polymer or polymer-electrolyte interfaces, as well. Galvanostatic charging discharging curves have been recorded to determine the specific capacitance, energy density and power density. For all studied polymers capacitive and faradaic charge storage behaviour with specific energy densities and power densities of 10^1 - $10^2\,\mathrm{J\,kg^{-1}}$ and $10^1\,\mathrm{W\,kg^{-1}}$ respectively is observed. An overview of the specific energy and power density values of all studied redox-active polymers is shown in Fig. 6.10.

In addition, the usability of chemical dopants like $FeCl_3$ and $Fe(Tos)_3$ to induce the oxidative cross-linking and doping of PVTPA and PVTPA-*co*-PS has been studied. In Fig. 6.11 the absorption spectra of all studied triphenylamine-containing polymers (**a**) and the conductivity values of the PVTPA homopolymer (**b**) after chemical dip-doping in $Fe(Tos)_3$ solutions in MeCN are shown. For all polymers, partial cross-linking and the generation of charged species has been observed spectroscopically after dip doping with both $FeCl_3$ and $Fe(Tos)_3$ solutions. For the chemically cross-linked and doped polymer films also characteristic absorption bands of the neutral TPA and the $TPA^{+\cdot}$ radical cation species were observed. Conductivities of up to $10^{-4}\,\mathrm{A\,V^{-1}\,cm^{-1}}$ were recorded by means of 4-point-probe measurements. First experiments with $FeCl_3$ vapour doping of PVTPA also showed successful cross-linking and doping.

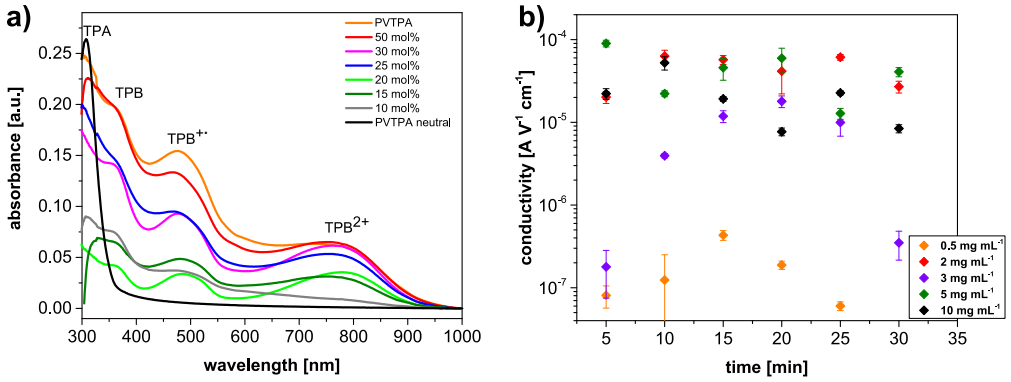

Figure 6.11: Chemical doping of triphenylamine-containing polymers with $Fe(Tos)_3$; **a)** absorption spectra of the PVTPA homopolymer and PVTPA-*co*-PS copolymers after dip-doping in $5\,mg\,mL^{-1}$ $Fe(Tos)_3$ in MeCN and exposure times of 15 min each; **b)** overview of the conductivity values of the PVTPA homopolymer after dip-doping in $Fe(Tos)_3$ solutions in MeCN with varying concentrations and exposure times.

For a better in-depth understanding of the cross-linking density influence on the ion movement processes in PVTPA-*co*-PS copolymer films, additional EQCM experiments are necessary. First and foremost, the influence of the elastic modulus on the frequency curves has to be investigated by means of EIS-coupled EQCM measurements to be able to distinguish between irreversible ion trapping and varied mechanical properties of the polymer films during the cross-linking reaction. In addition, a general optimisation of the EQCM set-up for organic electrolytes has to be performed to be able to gain more reliable data and a better reproducibility of the experiments. By combining the *Sauerbrey* equation with the charges (determined from the integrated CV signal over time) the "molecular mass of the transferred ionic species", which includes the ion and the surrounding solvent shell, can be calculated and the potential dependent swelling of the polymer films can be characterised as function of the cross-linking density.

The supercapacitor tests of the PVTPA homopolymer and the PVTPA-*co*-PS copolymers revealed faradaic charge storage processes, whereby the studied polymers are more suitable materials for the application in organic batteries or redox flow batteries than in supercapacitor devices. For future preparation and characterisation of PVTPA and PVTPA-*co*-PS containing battery cells the device preparation of standardised button cells has to be es-

tablished to be able to use standardised analysis instruments. In addition a fitting *n*-type conductor as the counter electrode material has to be used and the electrolyte (solvent, salt and concentration) needs to be optimised.

First experiments on chemical doping of PVTPA and PVTPA-*co*-PS with $FeCl_3$ and $Fe(Tos)_3$ showed successful cross-linking and charging of the polymer films leading to conductivity values up to $10^{-4}\,A\,V^{-1}\,cm^{-1}$. Nevertheless, the studied polymer samples were washed after the dip doping process to remove excess of the doping solution, which potentially causes de-doping of the polymer films and therefore reduces the measured conductivity values. Recent results in our research group indicate, that de-doping occurs upon washing of the polymer films and that excess of the doping solution does not influence the 4-point-probe measurements. Therefore by further optimisation of the sample preparation, the doping process (e.g. spin doping), the dopant and the doping parameters (time, concentration) higher conductivity values of PVTPA and PVTPA-*co*-PS samples might be reached. In addition, further optimisation of the custom-made vapour doping cell are needed to gain better control and stability of the under pressure in the cell.

As a closing remark, a brief outlook on a possible promising PVTPA-containing polymer for future works shall be given. Within the scope of this thesis only random PVTPA-*co*-PS copolymers were studied. By synthesising block copolymers with controlled block lengths a structuring of the copolymer films can be induced due to the microphase separation of the different blocks prior to the cross-linking of the polymer chains, to gain not only transparent but also structured electrode coatings. A similar concept of nanometer scale structured PVTPA block copolymer films has been reported by Lindner et al. [189] for the application as the photoactive layer in organic solar cells. Within this thesis a first attempt of the synthesis of a PVTPA-*block*-PS copolymer via nitroxide-mediated living radical polymerisation has been performed and the experimental details are given in the Appendix in Chapter A.3. Still, for a systematic study of the structuring and the influence on the cross-linking and doping of the redox groups, further optimisation of the synthesis route are needed to gain a series of block copolymers with varying block lengths.

7. Bibliography

[1] G. Li, R. Zhu, Y. Yang, *Nature Photonics* **2012**, *6*, 153–161.

[2] K. Tremel, S. Ludwigs in *P3HT Revisited - From Molecular Scale to Solar Cell Devices*, (Ed.: S. Ludwigs), Springer, Berlin, Heidelberg, **2014**, pp. 39–82.

[3] F. C. Spano, C. Silva, *Annual Review of Physical Chemistry* **2014**, *65*, 477–500.

[4] H. Sirringhaus, P. J. Brown, R. H. Friend, M. M. Nielsen, K. Bechgaard, A. J. H. Spiering, *Nature* **1999**, *401*, 685–688.

[5] X. Jiang, Y. Harima, K. Yamashita, Y. Tada, J. Ohshita, A. Kunai, *Chemical Physics Letters* **2002**, *364*, 616–620.

[6] X. Yang, A. Uddin, *Renewable and Sustainable Energy Reviews* **2014**, *30*, 324–336.

[7] S. Muench, A. Wild, C. Friebe, B. Ha, T. Janoschka, U. S. Schubert, *Chem. Rev.* **2016**, *116*, 9438–9484.

[8] O. Yurchenko, J. Heinze, S. Ludwigs, *ChemPhysChem* **2010**, *11*, 1637–1640.

[9] https://www.eia.gov/todayinenergy/detail.php?id=32912 (visited on 08/18/2018).

[10] http://www.consilium.europa.eu/en/policies/climate-change/2030-climate-and-energy-framework/ (visited on 08/18/2018).

[11] http://www.consilium.europa.eu/en/policies/climate-change/international-agreements-climate-action/ (visited on 08/18/2018).

[12] https://www.trade.gov/topmarkets/pdf/Semiconductors_Executive_Summary.pdf (visited on 08/18/2018).

[13] S. Khan, L. Lorenzelli, R. S. Dahiya, *IEEE Sensors Journal* **2015**, *15*, 3164–3185.

[14] C. Kapnopoulos, E. D. Mekeridis, L. Tzounis, C. Polyzoidis, A. Zachariadis, S. Tsimikli, C. Gravalidis, A. Laskarakis, N. Vouroutzis, S. Logothetidis, *Solar Energy Materials and Solar Cells* **2016**, *144*, 724–731.

[15] W. Cao, J. Xue, *Energy & Environmental Science* **2014**, *7*, 2123.

[16] P.-L. T. Boudreault, A. Najari, M. Leclerc, *Chemistry of Materials* **2011**, *23*, 456–469.

[17] N. D. Treat, M. L. Chabinyc, *Annual Review of Physical Chemistry* **2014**, *65*, 59–81.

[18] J. Yan, B. R. Saunders, *RSC Adv.* **2014**, *4*, 43286–43314.

[19] H. Sirringhaus, *Advanced Materials* **2014**, *26*, 1319–1335.

[20] G. Horowitz, *Advanced Materials* **1998**, *10*, 365–377.

[21] L. Torsi, M. Magliulo, K. Manoli, G. Palazzo, *Chemical Society Reviews* **2013**, *42*, 8612.

[22] N. Thejo Kalyani, S. Dhoble, *Renewable and Sustainable Energy Reviews* **2012**, *16*, 2696–2723.

[23] C. Sekine, Y. Tsubata, T. Yamada, M. Kitano, S. Doi, *Science and Technology of Advanced Materials* **2014**, *15*, 034203.

[24] R. Yue, J. Xu, *Synthetic Metals* **2012**, *162*, 912–917.

[25] D. K. Schroder, *Semiconductor Material and Device Characterization*, *Vol. 44*, **2006**, p. 790.

[26] R. Rauh, *Electrochimica Acta* **1999**, *44*, 3165–3176.

[27] R. Baetens, B. P. Jelle, A. Gustavsen, *Solar Energy Materials and Solar Cells* **2010**, *94*, 87–105.

[28] T. F. Otero, M. Broschart, *Journal of Applied Electrochemistry* **2006**, *36*, 205–214.

[29] E. Smela, *MRS Bulletin* **2008**, *33*, 197–204.

[30] C. Chan, S. Chang, H. E. Naguib, *Bioinsp. Biomim.* **2008**, *3*, DOI 10.1088/1748-3182/3/3/035004.

[31] G. A. Snook, P. Kao, A. S. Best, *Journal of Power Sources* **2011**, *196*, 1–12.

[32] C. Zhong, Y. Deng, W. Hu, J. Qiao, L. Zhang, J. Zhang, *Chemical Society reviews* **2015**, *44*, 7484–7539.

[33] P. Simon, Y. Gogotsi, *Nature materials* **2008**, *7*, 845–54.

[34] A. K. Dhingra, *Journal of Metals* **1986**, *38*, 17.

[35] L. A. Utracki, *Polymer Engineering and Science* **1995**, *35*, 2–17.

[36] H. Shirakawa, E. J. Louis, A. G. MacDiarmid, C. K. Chiang, A. J. Heeger, *J. Chem. Soc. Chem. Commun.* **1977**, 578–580.

[37] C. K. Chiang, C. R. Fincher, Y. W. Park, A. J. Heeger, H. Shirakawa, E. J. Louis, S. C. Gau, A. G. MacDiarmid, *Physical Review Letters* **1977**, *39*, 1098–1101.

[38] A. J. Heeger, *Angewandte Chemie (International ed. in English)* **2001**, *40*, 2591–2611.

[39] Y. Liang, Z. Chen, Y. Jing, Y. Rong, A. Facchetti, Y. Yao, *Journal of the American Chemical Society* **2015**, *137*, 4956–4959.

[40] Y. Liang, L. Yu, *Polymer Reviews* **2010**, *50*, 454–473.

[41] H. Klauk, *Chem. Soc. Rev.* **2010**, *39*, 2643–2666.

[42] H. Hoppe, N. S. Sariciftci, *Journal of Materials Research* **2011**, *19*, 1924–1945.

[43] P. Docampo, S. Guldin, T. Leijtens, N. K. Noel, U. Steiner, H. J. Snaith, *Advanced Materials* **2014**, 1–18.

[44] L. E. Chaar, L A, N. E. Zein, *Renewable and Sustainable Energy Reviews* **2011**, *15*, 2165–2175.

[45] C. G. Cameron, P. G. Pickup, *Chem. Commun.* **1997**, *0*, 303–304.

[46] A. J. Heeger, *Chem. Soc. Rev.* **2010**, *39*, 2354–2371.

[47] M. Rehahn, *Chemie in unserer Zeit* **2003**, *37*, 18–30.

[48] G. Tourillon, F. Garnier, *Journal of The Electrochemical Society* **1983**, *287*, 2042–2044.

[49] J. Heinze, B. A. Frontana-Uribe, S. Ludwigs, *Chemical reviews* **2010**, *110*, 4724–71.

[50] Y. Olivier, D. Niedzialek, V. Lemaur, W. Pisula, K. Müllen, U. Koldemir, J. R. Reynolds, R. Lazzaroni, J. Cornil, D. Beljonne, *Advanced Materials* **2014**, *26*, 2119–2136.

[51] J. Poater, J. Casanovas, M. Sola, C. Alema, *The Journal of Physical Chemistry A* **2010**, *114*, 1023–1028.

[52] H.-B. Bu, G. Götz, E. Reinold, A. Vogt, R. Azumi, J. L. Segura, P. Bäuerle, *Chem. Commun.* **2012**, *48*, 2677–2679.

[53] J. F. Ponder, A. M. Österholm, J. R. Reynolds, *Macromolecules* **2016**, *49*, 2106–2111.

[54] Z. Yu, Y. Xia, D. Du, J. Ouyang, *ACS Appl. Mater. Interfaces* **2016**, *8*, 11629–11638.

[55] J. F. Mike, J. L. Lutkenhaus, *Journal of Polymer Science Part B: Polymer Physics* **2013**, *51*, 468–480.

[56] K. Tremel, PhD thesis, Universität Stuttgart, **2014**.

[57] D. T. Trefz, PhD thesis, Universität Stuttgart, **2018**.

[58] R. Matsidik, A. Luzio, S. Hameury, H. Komber, C. R. McNeill, M. Caironi, M. Sommer, *J. Mater. Chem. C* **2016**, *4*, 10371–10380.

[59] J. L. Bredas, G. B. Street, *Accounts of Chemical Research* **1985**, *18*, 309–315.

[60] R. Hoffmann, C. Janiak, *Macromolecules* **1991**, *24*, DOI 10.1021/ma00013a001.

[61] R. Gracia, D. Mecerreyes, *Polymer Chemistry* **2013**, *4*, 2206.

[62] T. Janoschka, M. D. Hager, U. S. Schubert, *Adv. Mater.* **2012**, *24*, 6397–6409.

[63] H. Nishide, T. Suga, *Electrochem. Soc. Interface* **2005**, *14*, 32–36.

[64] Z. Song, H. Zhou, *Energy Environ. Sci.* **2013**, *6*, 2280–2301.

[65] Z. Song, T. Xu, M. L. Gordin, Y.-B. Jiang, I.-T. Bae, Q. Xiao, H. Zhan, J. Liu, D. Wang, *Nano Lett.* **2012**, *12*, 2205–2211.

[66] K. M. Coakley, M. D. McGehee, *Chem. Mater.* **2004**, 4533–4542.

[67] M. Skompska, *Synthetic Metals* **2010**, *160*, 1–15.

[68] S. E. Shaheen, D. S. Ginley, G. E. Jabbour, G. Editors, *MRS Bulletin* **2005**, *30*, 10–19.

[69] C. Deibel, V. Dyakonov, *Reports on Progress in Physics* **2010**, *73*, 096401.

[70] A. J. Heeger, *Advanced Materials* **2014**, *26*, 10–28.

[71] A. J. Pearson, T. Wang, D. G. Lidzey, *Rep. Prog. Phys.* **2013**, *76*, 022501.

[72] M. T. Dang, L. Hirsch, G. Wantz, *Advanced Materials* **2011**, *23*, 3597–3602.

[73] J. C. Hummelen, B. W. Knight, F. LePeg, F. Wudl, J. Yao, C. L. Wilkins, *J.Org. Chem.* **1995**, *60*, 532–538.

[74] N. Chandrasekaran, A. C. Y. Liu, A. Kumar, C. R. McNeill, D. Kabra, *J. Phys. D: Appl. Phys.* **2018**, *51*, DOI 10.1088/1361-6463/aa98fc.

[75] C. Sartorio, V. Campisciano, C. Chiappara, S. Cataldo, M. Scopelliti, M. Gruttadauria, F. Giacalone, B. Pignataro, *Journal of Materials Chemistry A* **2018**, *6*, 3884–3894.

[76] J. J. R. Arias, M. d. F. Vieira Marques, *Reactive and Functional Polymers* **2017**, *113*, 58–69.

[77] B. Kadem, A. Hassan, W. Cranton, *Journal of Materials Science: Materials in Electronics* **2016**, *27*, 7038–7048.

[78] A. Singh, A. Dey, P. K. Iyer, *ACS Applied Nano Materials* **2018**, *1*, 5646–5654.

[79] B. Kadem, A. Hassan, M. Göksel, T. Basova, A. Senocak, E. Demirbas, M. Durmus, *RSC Adv.* **2016**, *6*, 93453–93462.

[80] M. S. Whittingham, *Science* **1976**, *192*, 1126–1127.

[81] H. Nishide, K. Oyaizu, *Science* **2008**, *319*, 737–738.

[82] K. Nakahara, S. Iwasa, M. Satoh, Y. Morioka, J. Iriyama, M. Suguro, E. Hasegawa, *Chemical Physics Letters* **2002**, *359*, 351–354.

[83] E. J. W. Crossland, K. Tremel, F. Fischer, K. Rahimi, G. Reiter, U. Steiner, S. Ludwigs, *Advanced Materials* **2012**, *24*, 839–844.

[84] E. J. W. Crossland, K. Rahimi, G. Reiter, U. Steiner, S. Ludwigs, *Advanced Functional Materials* **2011**, *21*, 518–524.

[85] Y. Ohsawa, M. Ishikawa, T. Miyamoto, Y. Murofushi, M. Kawai, *Synthetic Metals* **1987**, *18*, 371–374.

[86] B. Häupler, R. Burges, C. Friebe, T. Janoschka, D. Schmidt, A. Wild, U. S. Schubert, *Macromolecular Rapid Communications* **2014**, *35*, 1367–1371.

[87] K. J. Ihn, J. Moulton, P. Smith, *Journal of Polymer Science: Part B: Polymer Physics* **1993**, *31*, 735–742.

[88] C. Sinturel, M. Vayer, M. Morris, M. Hillmyer, *Macromolecules* **2013**, *46*, 5399–5415.

[89] S. Ludwigs, G. Krausch, R. Magerle, A. V. Zvelindovsky, G. J. A. Sevink, *Macromolecules* **2005**, *38*, 1859–1867.

[90] F. S. U. Fischer, K. Tremel, M. Sommer, E. J. C. Crossland, S. Ludwigs, *Nanoscale* **2012**, *4*, 2138–2144.

[91] G. L. Schulz, S. Ludwigs, *Advanced Functional Materials* **2017**, *27*, 1603083.

[92] A. Hamidi-Sakr, L. Biniek, S. Fall, M. Brinkmann, *Advanced Functional Materials* **2016**, *26*, 408–420.

[93] M. Brinkmann, L. Hartmann, L. Biniek, K. Tremel, N. Kayunkid, *Macromolecular Rapid Communications* **2014**, *35*, 9–26.

[94] J. Yamamoto, Y. Furukawa, *J. Phys. Chem. B* **2015**, *119*, 4788–4794.

[95] J. F. Rusling, S. L. Suib, *Advanced Materials* **1994**, *6*, 922–930.

[96] J. Heinze, *Angewandte Chemie* **1984**, *96*, 823–840.

[97] B. Speiser, *Chemie in unserer Zeit* **1981**, *21*, 62–67.

[98] F. Harnisch, S. Freguia, *Chemistry an Asian journal* **2012**, *7*, 466–75.

[99] A. M. Bond, N. W. Duffy, S.-X. Guo, J. Zhang, D. Elton, *Analytical chemistry* **2005**, *77*, 186–195.

[100] D. Gosser, *Cyclic Voltammetry: Simulation and Analysis of Reaction Mechanisms*, VCH, **1993**.

[101] C. M. Cardona, W. Li, A. E. Kaifer, D. Stockdale, G. C. Bazan, *Advanced Materials* **2011**, *23*, 2367–2371.

[102] W. Kaim, J. Fiedler, *Chemical Society reviews* **2009**, *38*, 3373–82.

[103] A. J. Bard, L. R. Faulkner, *Electrochemical Methods - Fundamentals and Applications*, Wiley-VCH Verlag GmbH & Co. KGaA, New York, **2001**.

[104] F. Soavi, M. Mastragostino, A. May, *Phys. Chem. Chem. Phys.* **2000**, *2*, 2993–2998.

[105] R. Schumacher, *Angewandte Chemie* **1990**, *29*, 329–343.

[106] D. A. Buttry, M. D. Ward, *Chem. Rev.* **1992**, *92*, 1355–1379.

[107] D. Macdonald, *Transient Techniques in Electrochemistry*, Springer, **1977**.

[108] J. R. Macdonald, *Impedance spectroscopy: emphasizing solid materials and systems*, Wiley, **1987**.

[109] V. V. Malev, V. V. Kondratiev, *Russian Chemical Reviews* **2006**, *75*, 147–160.

[110] B.-Y. Chang, S.-M. Park, *Annual Review of Analytical Chemistry* **2010**, *3*, 207–229.

[111] F. M. Smits, *Bell System Technical Journal* **1958**, *37*, 711–718.

[112] E. Meyer, *Progress in Surface Science* **1992**, *41*, 3–49.

[113] G. Binnig, C. Quate, *Physical Review Letters* **1986**, *56*.

[114] R. Garcia, A. San Paulo, *Physical Review B* **1999**, *60*, 4961–4967.

[115] D. Fuoco, *Nanomaterials* **2012**, *2*, 79–91.

[116] D. B. Williams, C. B. Carter, *Transmission Electron Microscopy - A Textbook for Materials Science*, Springer, **2009**.

[117] G. R. Fulmer, A. J. M. Miller, N. H. Sherden, H. E. Gottlieb, A. Nudelman, B. M. Stoltz, J. E. Bercaw, K. I. Goldberg, R. Gan, H. Apiezon, *Organometallics* **2010**, *29*, 2176–2179.

[118] K. Bruchlos, D. Trefz, A. Hamidi-Sakr, M. Brinkmann, J. Heinze, A. Ruff, S. Ludwigs, *Electrochimica Acta* **2018**, *269*, 299–311.

[119] A. M. Crotty, A. N. Gizzi, H. J. Rivera-Jacquez, A. E. Masunov, Z. Hu, J. A. Geldmeier, A. J. Gesquiere, *The Journal of Physical Chemistry C* **2014**, *118*, 19975–19984.

[120] J.-J. Chao, S.-C. Shiu, C.-F. Lin, *Solar Energy Materials and Solar Cells* **2012**, *105*, 40–45.

[121] B. Conings, L. Baeten, C. De Dobbelaere, J. D'Haen, J. Manca, H.-G. Boyen, *Advanced Materials* **2014**, *26*, 2041–2046.

[122] D. T. Scholes, S. A. Hawks, P. Y. Yee, H. Wu, J. R. Lindemuth, S. H. Tolbert, B. J. Schwartz, *The Journal of Physical Chemistry Letters* **2015**, *6*, 4786–4793.

[123] W. Ma, J. Y. Kim, K. Lee, A. J. Heeger, *Macromolecular Rapid Communications* **2007**, *28*, 1776–1780.

[124] C. Nicolet, D. Deribew, C. Renaud, G. Fleury, C. Brochon, E. Cloutet, L. Vignau, G. Wantz, H. Cramail, M. Geoghegan, G. Hadziioannou, *The Journal of Physical Chemistry B* **2011**, *115*, 12717–12727.

[125] F. P. V. Koch, J. Rivnay, S. Foster, C. Müller, J. M. Downing, E. Buchaca-Domingo, P. Westacott, L. Yu, M. Yuan, M. Baklar, Z. Fei, C. Luscombe, M. A. McLachlan, M. Heeney, G. Rumbles, C. Silva, A. Salleo, J. Nelson, P. Smith, N. Stingelin, *Progress in Polymer Science* **2013**, *38*, 1978–1989.

[126] S. Lee, M. Lee, J. An, H. Ahme, C. Im, *Molecular Crystals and Liquid Crystals* **2013**, *578*, 68–72.

[127] O. Oklobia, T. Shafai, *Solar Energy Materials and Solar Cells* **2014**, *122*, 158–163.

[128] H. Hoppe, N. S. Sariciftci, *J. Mater. Chem.* **2006**, *16*, 45–61.

[129] X. Yang, J. Loos, *Macromolecules* **2007**, *40*, 1353–1362.

[130] L. H. Nguyen, H. Hoppe, T. Erb, S. Günes, G. Gobsch, N. S. Sariciftci, *Advanced Functional Materials* **2007**, *17*, 1071–1078.

[131] M. Brinkmann, *Journal of Polymer Science Part B: Polymer Physics* **2011**, *49*, 1218–1233.

[132] J. Clark, C. Silva, R. H. Friend, F. C. Spano, *Physical Review Letters* **2007**, *98*, 206406.

[133] F. C. Spano, *The Journal of Chemical Physics* **2005**, *122*, 234701.

[134] F. C. Spano, J. Clark, C. Silva, R. H. Friend, *The Journal of Chemical Physics* **2009**, *130*, 074904.

[135] J. Clark, J.-F. Chang, F. C. Spano, R. H. Friend, C. Silva, *Applied Physics Letters* **2009**, *94*, 163306.

[136] W. Lee, J. H. Seo, H. Y. Woo, *Polymer* **2013**, *54*, 5104–5121.

[137] Y. Wang, W. Wei, X. Liu, Y. Gu, *Solar Energy Materials and Solar Cells* **2012**, *98*, 129–145.

[138] A. W. Hains, C. Ramanan, M. D. Irwin, J. Liu, M. R. Wasielewski, T. J. Marks, *ACS Applied Materials & Interfaces* **2010**, *2*, 175–185.

[139] T. Johansson, W. Mammo, M. Svensson, M. R. Andersson, O. Inganäs, *J. Mater. Chem.* **2003**, *13*, 1316–1323.

[140] R. Kroon, M. Lenes, J. C. Hummelen, P. W. M. Blom, B. de Boer, *Polymer Reviews* **2008**, *48*, 531–582.

[141] B. W. Larson, J. B. Whitaker, X.-B. Wang, A. A. Popov, G. Rumbles, N. Kopidakis, S. H. Strauss, O. V. Boltalina, *The Journal of Physical Chemistry C* **2013**, *117*, 14958–14964.

[142] H. Yoshida, *Analytical and Bioanalytical Chemistry* **2014**, *406*, 2231–2237.

[143] W. Han, H. Yoshida, N. Ueno, S. Kera, *Applied Physics Letters* **2013**, *103*, 123303.

[144] H. Yoshida, *Journal of Physical Chemistry C* **2014**, *118*, 24377–24382.

[145] C. Tengstedt, W. Osikowicz, W. R. Salaneck, I. D. Parker, C.-H. Hsu, M. Fahlman, *Applied Physics Letters* **2006**, *88*, 053502.

[146] Q. Bao, X. Liu, S. Braun, F. Gao, M. Fahlman, *Advanced Materials Interfaces* **2015**, *2*, 1400403.

[147] W. E. Ford, D. Gao, N. Knorr, R. Wirtz, F. Scholz, Z. Karipidou, K. Ogasawara, S. Rosselli, V. Rodin, G. Nelles, F. von Wrochem, *ACS Nano* **2014**, *8*, 9173–9180.

[148] W. Osikowicz, M. P. de Jong, W. R. Salaneck, *Advanced Materials* **2007**, *19*, 4213–4217.

[149] C. Deibel, D. Mack, J. Gorenflot, A. Schöll, S. Krause, F. Reinert, D. Rauh, V. Dyakonov, *Physical Review B* **2010**, *81*, 085202.

[150] F. J. Zhang, A. Vollmer, J. Zhang, Z. Xu, J. P. Rabe, N. Koch, *Organic Electronics: physics materials applications* **2007**, *8*, 606–614.

[151] L. Micaroni, F. Nart, I. A. Hümmelgen, *Journal of Solid State Electrochemistry* **2002**, *7*, 55–59.

[152] G. Zotti, G. Schiavon, S. Zecchin, *Synthetic Metals* **1995**, *72*, 275–281.

[153] M. Skompska, *Electrochimica Acta* **2000**, *45*, 3841–3850.

[154] J. Heinze in *Electrochemistry IV*, (Ed.: E. Steckhan), Springer-Verlag, Berlin/Heidelberg, **1990**, pp. 1–47.

[155] M. Sato, S. Tanaka, K. Kaeriyama, *Makromolekulare Chemie* **1987**, *188*, 1763–1771.

[156] M. Skompska, *Electrochimica Acta* **1998**, *44*, 357–362.

[157] F. Chao, M. Costa, G. Jin, C. Tian, *Electrochimica Acta* **1994**, *39*, 197–209.

[158] A. Yassar, J. Roncali, F. Garnier, *Macromolecules* **1989**, *22*, 804–809.

[159] V. Senkovskyy, N. Khanduyeva, H. Komber, U. Oertel, M. Stamm, D. Kuckling, A. Kiriy, *Journal of the American Chemical Society* **2007**, *129*, 6626–6632.

[160] H. A. Bronstein, C. K. Luscombe, *Journal of the American Chemical Society* **2009**, *131*, 12894–12895.

[161] P. Sista, C. K. Luscombe in *P3HT Revisited - From Molecular Scale to Solar Cell Devices*, (Ed.: S. Ludwigs), Springer, Berlin Heidelberg, **2014**, pp. 1–38.

[162] K. Yoshino, S. Hayashi, R. Sugimoto, *Japanese Journal of Applied Physics* **1984**, *23*, L899–L900.

[163] R. D. McCullough, R. D. Lowe, M. Jayaraman, D. L. Anderson, *The Journal of Organic Chemistry* **1993**, *58*, 904–912.

[164] T. A. Chen, R. D. Rieke, *Journal of the American Chemical Society* **1992**, *114*, 10087–10088.

[165] M. Trznadel, A. Pron, M. Zagorska, R. Chrzaszcz, J. Pielichowski, *Macromolecules* **1998**, *31*, 5051–5058.

[166] M. Skompska, A. Szkurłat, *Electrochimica Acta* **2001**, *46*, 4007–4015.

[167] M. Trznadel, M. Zagórska, M. Lapkowski, G. Louarn, S. Lefrant, A. Pron, *Journal of the Chemical Society Faraday Transactions* **1996**, *92*, 1387.

[168] M. Trznadel, *J. Chim. Phys.* **1998**, *95*, 1165–1167.

[169] M. Trznadel, O. Chauvet, M. Lapkowski, A. Pron, *Synthetic Metals* **1999**, *101*, 6779199.

[170] M. Skompska, A. Szkurlat, A. Kowal, M. Szklarczyk, *Langmuir* **2003**, *19*, 2318–2324.

[171] C. Yang, F. P. Orfino, S. Holdcroft, *Macromolecules* **1996**, *29*, 6510–6517.

[172] C. C. Bof Bufon, J. Vollmer, T. Heinzel, P. Espindola, H. John, J. Heinze, *The Journal of Physical Chemistry B* **2005**, *109*, 19191–19199.

[173] J. Heinze, P. Tschuncky, A. Smie, *Journal of Solid State Electrochemistry* **1998**, *2*, 102–109.

[174] S. Thankaraj Salammal, S. Dai, U. Pietsch, S. Grigorian, N. Koenen, U. Scherf, N. Kayunkid, M. Brinkmann, *European Polymer Journal* **2015**, *67*, 199–212.

[175] M. Chang, J. Lee, N. Kleinhenz, B. Fu, E. Reichmanis, *Advanced Functional Materials* **2014**, *24*, 4457–4465.

[176] S. T. Turner, P. Pingel, R. Steyrleuthner, E. J. W. Crossland, S. Ludwigs, D. Neher, *Advanced Functional Materials* **2011**, *21*, 4640–4652.

[177] O. G. Reid, J. A. Nekuda Malik, G. Latini, S. Dayal, N. Kopidakis, C. Silva, N. Stingelin, G. Rumbles, *Journal of Polymer Science Part B: Polymer Physics* **2012**, *50*, 27–37.

[178] L. Hartmann, K. Tremel, S. Uttiya, E. Crossland, S. Ludwigs, N. Kayunkid, C. Vergnat, M. Brinkmann, *Advanced Functional Materials* **2011**, *21*, 4047–4057.

[179] M. Brinkmann, J.-C. Wittmann, *Advanced Materials* **2006**, *18*, 860–863.

[180] A. Ng, X. Liu, W. Y. Jim, A. B. Djurišić, K. C. Lo, S. Y. Li, W. K. Chan, *Journal of Applied Polymer Science* **2014**, *131*, DOI 10.1002/app.39776.

[181] F. C. Krebs, N. Espinosa, M. Hösel, R. R. Søndergaard, M. Jørgensen, *Advanced Materials* **2014**, *26*, 29–39.

[182] F. Moczko, Untersuchung elektrochemischer Vernetzung in triphenylaminhaltigen Polymersystemen, Universität Stuttgart, **2016**.

[183] L. Eisele, Dotierung von Triphenylamin-haltigen Polymeren, August, Universität Stuttgart, **2017**.

[184] F. C. Goerigk, electrochemical characterisation of triphenyl amine containing copolymer systems, Universität Stuttgart, **2015**.

[185] L. Stein, Chemical doping of Polyvinyltriphenylamine-co-polystyrene copolymers in thin films, Universität Stuttgart, **2017**.

[186] M. Behl, E. Hattemer, M. Brehmer, R. Zentel, *Macromolecular Chemistry and Physics* **2002**, *203*, 503–510.

[187] M. A. Green, A. Ho-Baillie, H. J. Snaith, *Nature Photonics* **2014**, *8*, 506–514.

[188] W.-H. Zhang, B. Cai, *Chinese Science Bulletin* **2014**, *59*, 2092–2101.

[189] S. M. Lindner, M. Thelakkat, *Macromolecules* **2004**, *37*, 8832–8835.

[190] S.-H. Hsiao, S.-L. Cheng, *Journal of Polymer Science Part A: Polymer Chemistry* **2015**, *53*, 496–510.

[191] K. Choi, S. J. Yoo, Y. E. Sung, R. Zentel, *Chemistry of Materials* **2006**, *18*, 5823–5825.

[192] P. Reiss, E. Couderc, J. De Girolamo, A. Pron, *Nanoscale* **2011**, *3*, 446–89.

[193] O. Yurchenko, D. Freytag, L. zur Borg, R. Zentel, J. Heinze, S. Ludwigs, *The Journal of Physical Chemistry B* **2012**, *116*, 30–39.

[194] D. Kröner, H. Krüger, M. W. Thesen, *Macromolecular Theory and Simulations* **2011**, *20*, 790–805.

[195] C. J. Hawker, A. W. Bosman, E. Harth, *Chem. Rev.* **2001**, *101*, 3661–3688.

[196] P. Novak, K. Müller, K. S. V. Santhanam, O. Haas, *Chem. Rev.* **1997**, *97*, 207–281.

[197] W. Dong, Y. Pan, M. Fritsch, U. Scherf, *Journal of Polymer Science Part A: Polymer Chemistry* **2015**, *53*, 1753–1761.

[198] E. Preis, C. Widling, U. Scherf, S. Patil, G. Brunklaus, J. Schmidt, A. Thomas, *Polymer Chemistry* **2011**, *2*, 2186.

[199] E. T. Seo, R. F. Nelson, J. M. Fritsch, L. S. Marcoux, D. W. Leedy, R. N. Adams, *J. Am. Chem. Soc.* **1966**, *88*, 3498–3503.

[200] N. R. Armstrong, P. A. Veneman, E. Ratcliff, D. Placencia, M. Brumbach, *Accounts of Chemical Research* **2009**, *42*, 1748–1757.

[201] Y.-H. Tak, K.-B. Kim, H.-G. Park, K.-H. Lee, J.-R. Lee, *Thin Solid Films* **2002**, *411*, 12–16.

[202] NOVA EQCM tutorial technical handbook.

[203] H. L. Bandey, S. J. Martin, R. W. Cernosek, A. R. Hillman, *Anal. Chem.* **1999**, *17*, 2205–2214.

[204] A. R. Hillman in *Encyclopedia of Electrochemistry*, (Ed.: A. J. Bard), Wiley, **2007**, pp. 230–289.

[205] H. Zhang, Y. Zhang, C. Gu, Y. Ma, *Advanced Energy Materials* **2015**, *5*, DOI 10.1002/aenm.201402175.

[206] M. Sun, Q. Tang, T. Zhang, G. Wang, *RSC Advances* **2014**, *4*, 7774.

[207] K. Yuan, Y. Xu, J. Uihlein, G. Brunklaus, L. Shi, R. Heiderhoff, M. Que, M. Forster, T. Chassé, T. Pichler, T. Riedl, Y. Chen, U. Scherf, *Adv. Mater.* **2015**, *27*, 6714–21.

[208] F. Marchioni, J. Yang, W. Walker, F. Wudl, *The journal of physical chemistry. B* **2006**, *110*, 22202–6.

[209] P. Sivaraman, S. P. Mishra, A. R. Bhattacharrya, A. Thakur, K. Shashidhara, A. B. Samui, *Electrochimica Acta* **2012**, *69*, 134–138.

[210] M. R. Rosario-Canales, P. Deria, M. J. Therien, J. J. Santiago-Avilés, *ACS Applied Materials & Interfaces* **2012**, *4*, 102–109.

[211] K. Yuan, P. Guo-Wang, T. Hu, L. Shi, R. Zeng, M. Forster, T. Pichler, Y. Chen, U. Scherf, *Chemistry of Materials* **2015**, *27*, 7403–7411.

[212] G. A. Snook, G. Z. Chen, *Journal of Electroanalytical Chemistry* **2008**, *612*, 140–146.

[213] R. Farma, M. Deraman, I. A. Talib, R. Omar, J. G. Manjunatha, M. M. Ishak, N. H. Basri, B. N. M. Dolah, *International Journal of Electrochemical Science* **2013**, *8*, 257–273.

[214] J. C. Carlberg, O. Inganäs, *J. Electrochem. Soc.* **1997**, *144*, DOI 10.1149/1.1837553.

[215] T. L. Kelly, K. Yano, M. O. Wolf, *ACS applied materials & interfaces* **2009**, *1*, 2536–43.

[216] P. M. DiCarmine, T. B. Schon, T. M. McCormick, P. P. Klein, D. S. Seferos, *The Journal of Physical Chemistry C* **2014**, *118*, 8295–8307.

[217] D. T. Duong, C. Wang, E. Antono, M. F. Toney, A. Salleo, *Organic Electronics* **2013**, *14*, 1330–1336.

[218] C. Wang, D. T. Duong, K. Vandewal, J. Rivnay, A. Salleo, *Physical Review B* **2015**, *91*, 1–7.

[219] I. E. Jacobs, E. W. Aasen, J. L. Oliveira, T. N. Fonseca, J. D. Roehling, J. Li, G. Zhang, M. P. Augustine, M. Mascal, A. J. Moulé, *Journal of Materials Chemistry C* **2016**, *4*, 3454–3466.

[220] P. Reinold, K. Bruchlos, S. Ludwigs, *Polymer Chemistry* **2017**, *8*, 7351–7359.

[221] O. Yurchenko, PhD thesis, Albert-Ludwigs-Universität Freiburg im Breisgau, **2010**.

A. Appendix

A.1. Spectroelectrochemical and Morphological Characterisation of P3HT Films with Controlled Morphologies

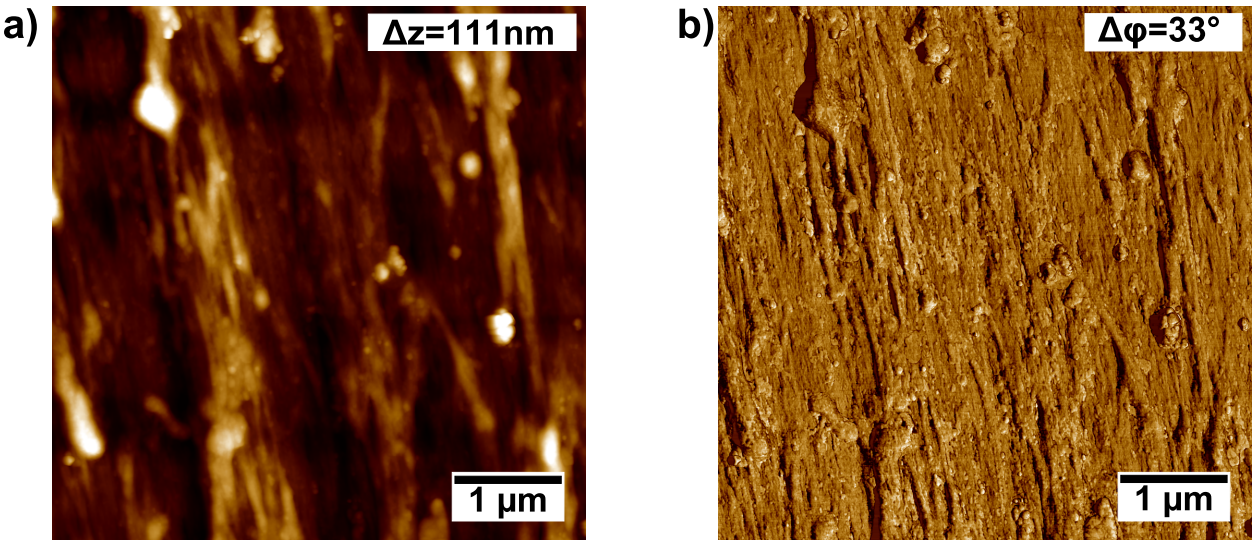

Figure A.1: AFM height **(a)** and phase **(b)** images of $P3HT_{rubbing}$ measured in tapping mode. Sample was prepared by blade coating from *o*-dichlorobenzene solution ($5\,mg\,mL^{-1}$) onto ITO electrodes and subsequent high temperature rubbing at 230 °C.

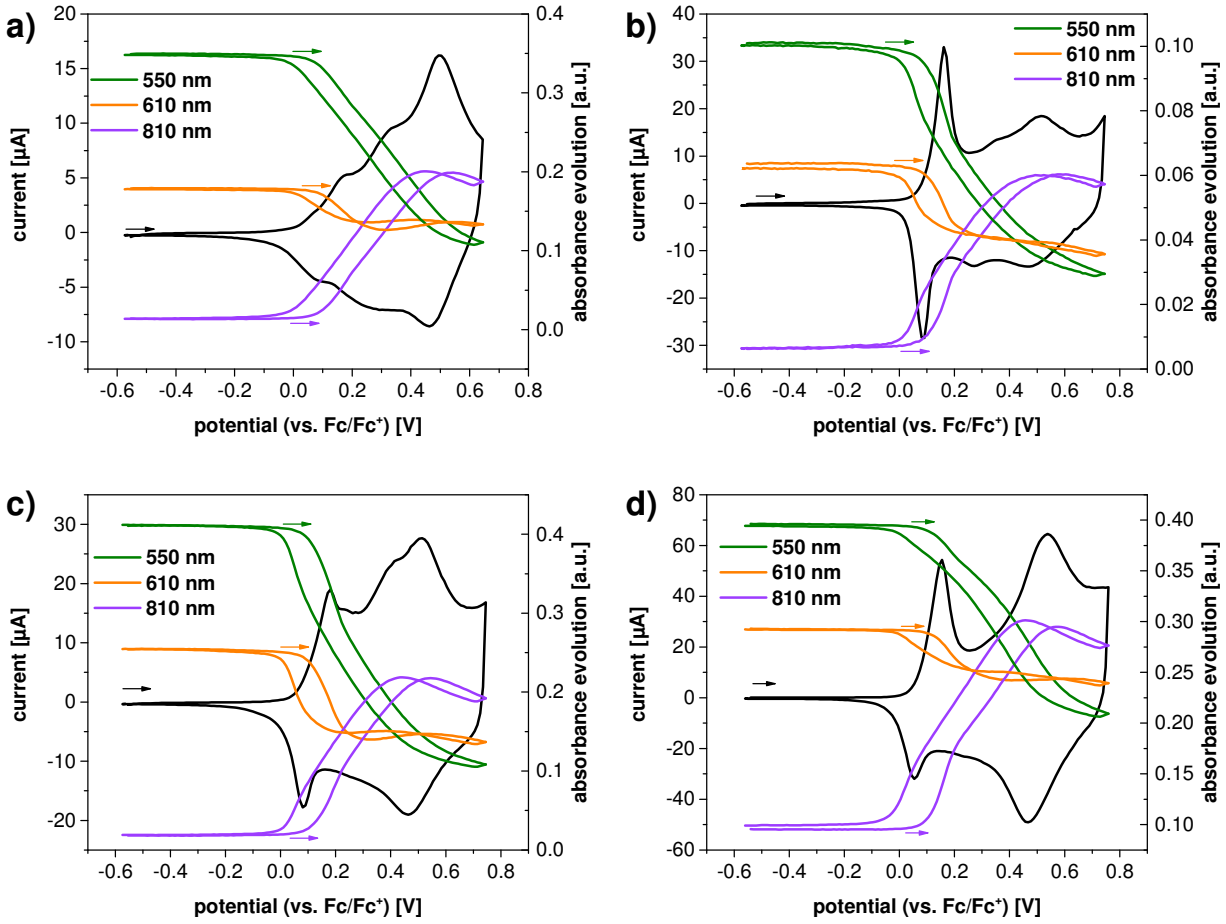

Figure A.2: Potential dependent absorbance intensity evolution curves of characteristiv absorption bands of $P3HT_{spin}$ (**a**), $P3HT_{wires}$ (**b**), $P3HT_{spherulite}$ (**c**) and $P3HT_{rubbing}$ (**d**). The intensity evolution curves of the neutral P3HT $\pi \longrightarrow \pi^*$ band at 550 nm, the π-π stacking band at 610 nm and the radical cation at 810 nm are highlighted in green, orange and violet respectively. The voltammograms were measured in 0.1 M NBu_4PF_6 in MeCN with a scan rate of 20 mV s^{-1}.

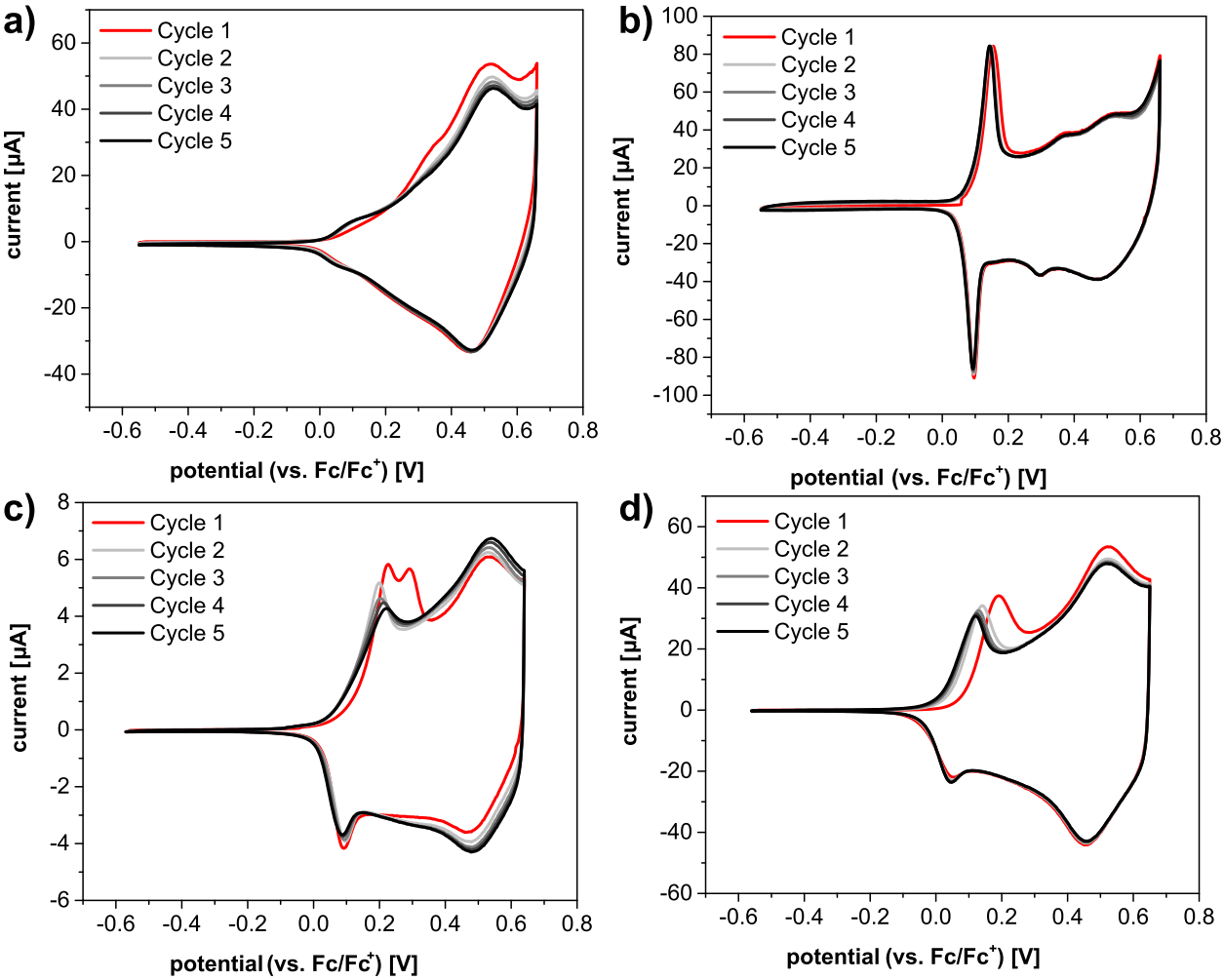

Figure A.3: Characterisation of memory effects in $P3HT_{spin}$ (**a**), $P3HT_{wires}$ (**b**), $P3HT_{spherulite}$ (**c**) and $P3HT_{rubbing}$ (**d**). The cyclic voltammograms were measured as continuous five cycles in 0.1 M NBu_4PF_6 in MeCN with a scan rate of 20 mV s^{-1}.

A.2. Spectroelectrochemical Characterisation of P3HT:$PC_{61}BM$ Blend Films

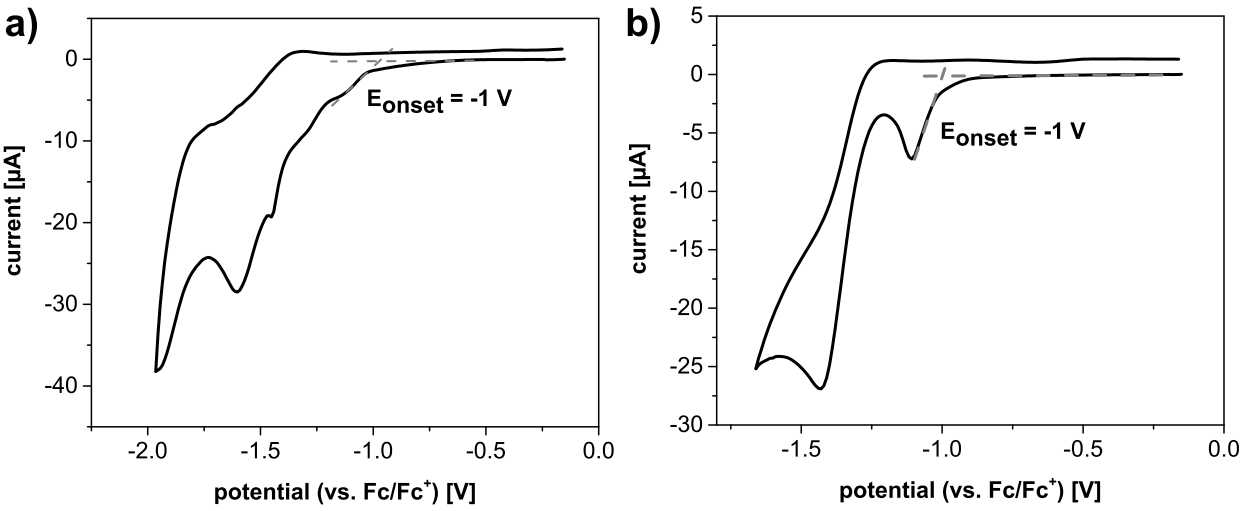

Figure A.4: Cyclic voltammograms of the reductions of the P3HT:$PC_{61}BM$ blends films after spin coating (**a**) and after thermal post annealing (**b**). The voltammograms were measured in 0.1 M NBu_4PF_6 in MeCN with a scan rate of 20 mV s^{-1}.

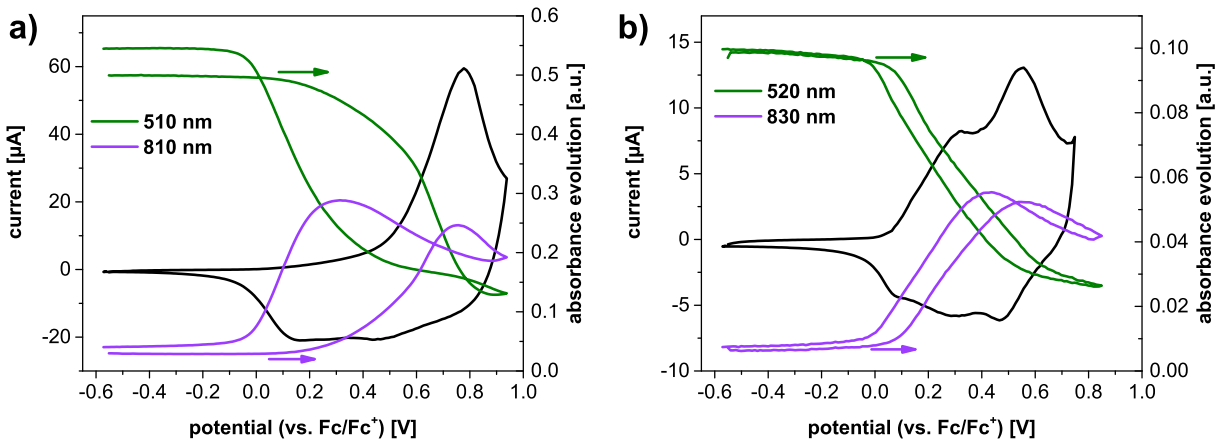

Figure A.5: Potential dependent absorbance evolution curves of P3HT:$PC_{61}BM$ blend films (1:1 w/w) prepared by spin coating from chloroform solution (overall concentration of $5\,mg\,mL^{-1}$) (**a**) and after thermal post annealing at 150 °C for 1 h(**b**). The intensity evolution curves of the neutral P3HT band and the P3HT radical cation are highlighted in green and violet respectively. The voltammograms were measured in 0.1 M NBu_4PF_6 in MeCN with a scan rate of $20\,mV\,s^{-1}$.

A.3. Synthesis of PVTPA-*co*-PS Copolymers

Vinyltriphenylamine

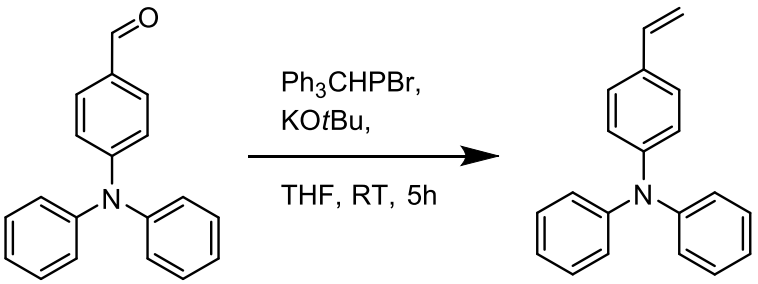

The synthesis procedure was adapted from Behl et al. [186] Methyltriphenylphosphoniumbromide (7.55 g, 21.1 mmol, 1.1 eq) was suspended in THF (50 mL) under argon atmosphere. Potassium-*tert*-butanolat (2.35 g, 20.9 mmol, 1.1 eq) was added slowly and the mixtures was stirred for 30 min in an ice bath. A solution of 4-(Diphenylamino)benzaldehyd (5.21 g, 19.1 mmol, 1 eq) in THF (20 mL) was added and the reaction mixture was stirred for 5 h at room temperature under argon atmosphere and then quenched with aq. HCl (2 N, 20 mL). The mixture was extraced with DCM (3 times) and the organic phases were combined and dried over $MgSO_4$. The solvent was removed under reduced pressure and the residual yellowish solid was purified by column chromatography (silica gel, cyclohexane:DCM (10:1)). 3.9 g (14.4 mmol, 75 % yield) of Vinyltriphenylamine were obtained.
^{1}H-NMR (250 MHz, CD_2Cl_2): δ(ppm) = 7.33-7.22 (m, 6H), 7.10-6.96 (m, 8H), 6.67 (dd, J=17.6, 10.9 Hz, 1H), 5.64 (dd, J=17.6, 1.0 Hz, 1H), 5.15 (dd, J=10.9, 0.9 Hz, 1H).

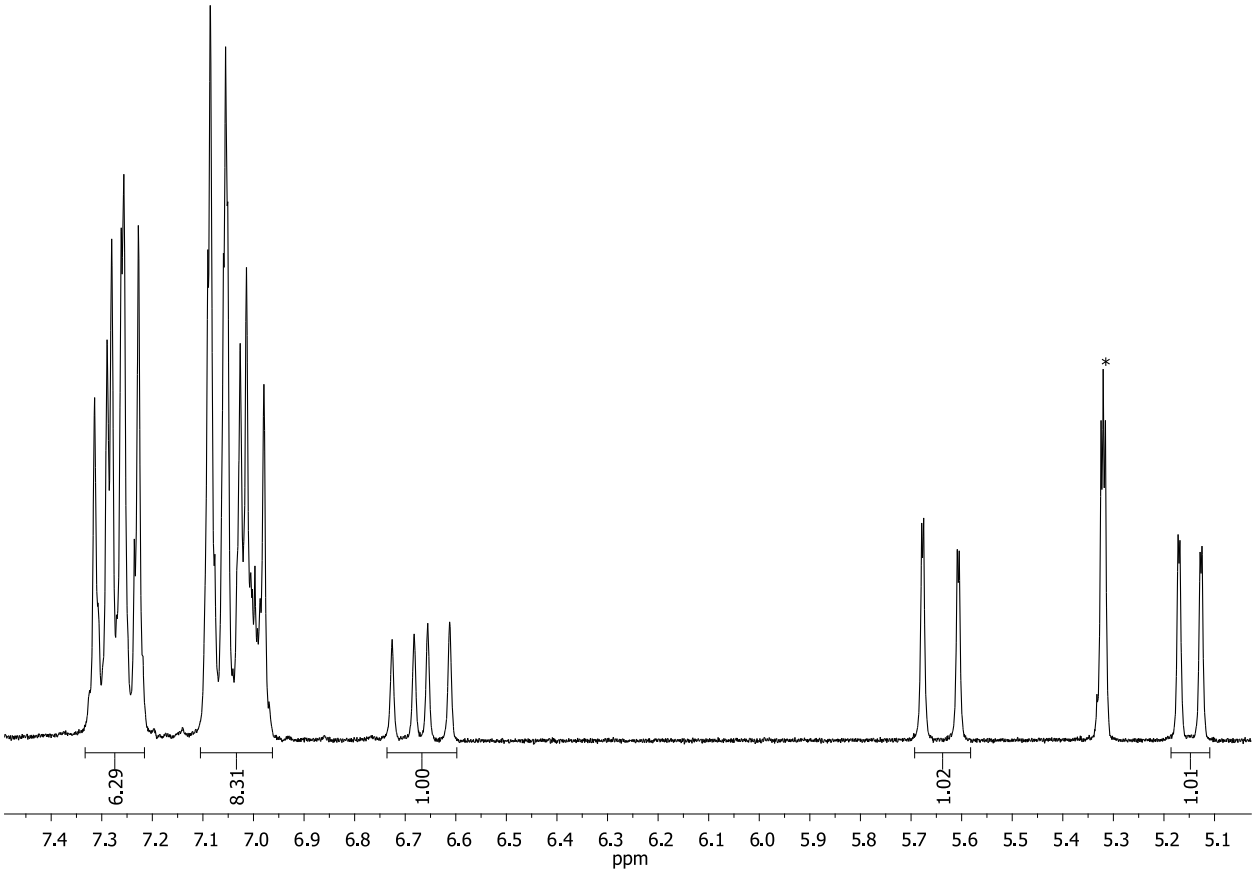

Figure A.6: ^{1}H-NMR of Vinyltriphenylamine in CD_2Cl_2.

Polyvinyltriphenylamine

The synthetic work has been performed by *Corinne Rost-Schmidt*.

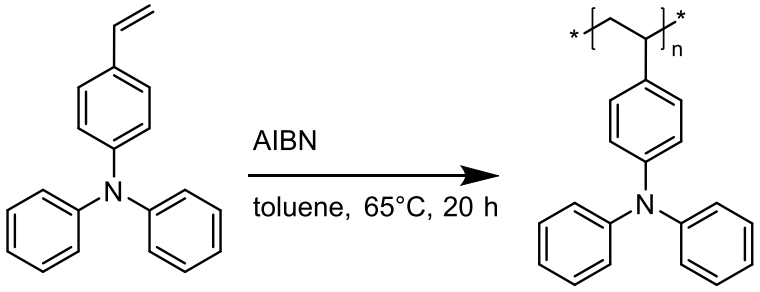

Vinyltriphenyl (500 mg, 1.85 mmol, 1 eq) and azobisisobutyronitrile (AIBN) (3 mg, 0.0185 mmol, 0.01 eq) were dissolved in toluene (3.5 mL) and degassed (3 times). The reaction mixture was stirred for 20 h at 65 °C. Poly-(vinyltriphenylamine) (0.196 g, 39 % yield) was obtained as a white solid after repeated precipitation in cold MeOH.

GPC (THF): $M_n = 19\,000\,g\,mol^{-1}$, PDI = 1.66

^{1}H-NMR (250 MHz, $CDCl_3$): δ(ppm) = 7.22-6.30 (m, 14H), 1.98 (s, 1H), 1.54 (s, 2H).

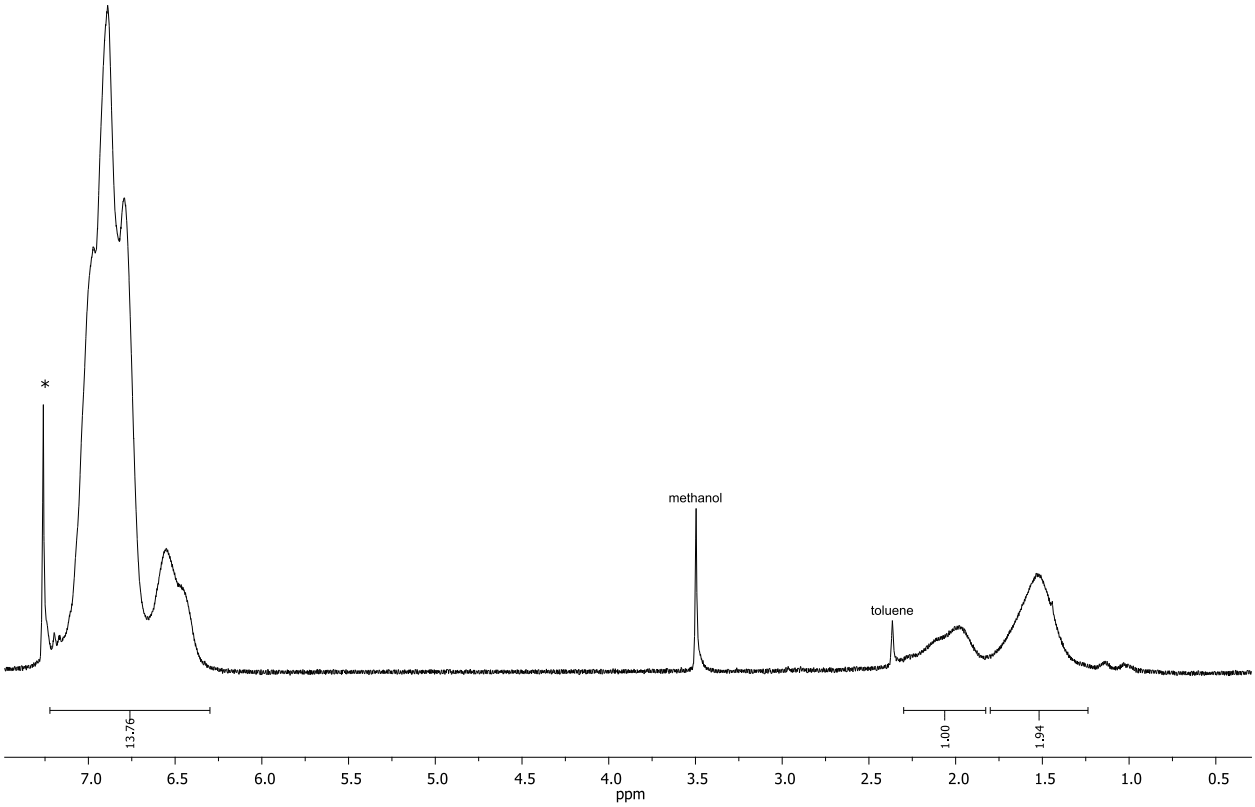

Figure A.7: ^{1}H-NMR of Polyvinyltriphenylamine in $CDCl_3$.

Polyvinyltriphenylamine-*co*-Polystyrene Copolymers

The synthetic work has been performed by *Corinne Rost-Schmidt*.

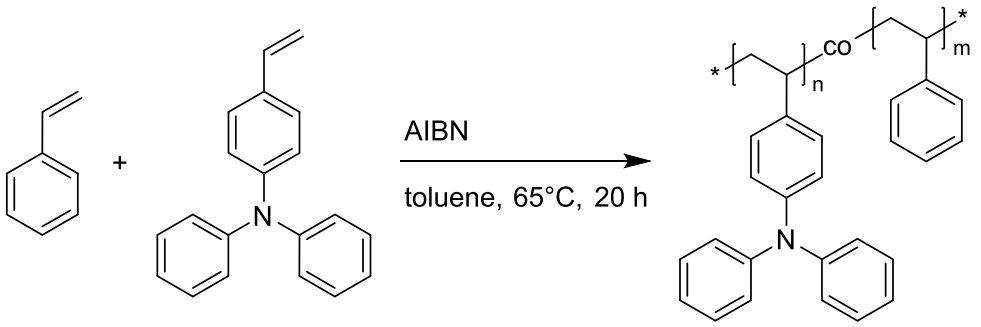

Vinyltriphenyl, Styrene (for the detailed amounts see Tab. A.1) and AIBN (0.01 eq) were dissolved in toluene and the reaction mixture was degassed (3 times). The reaction mixture was stirred at 65 °C. The Polyvinyltriphenylamine-*co*-Polystyrene Copolymers were obtained as white solids after repeated precipitation in cold MeOH. The reaction yields, molecular weights and polydispersity indices of all obtained copolymers are summarised in Tab. A.2.

Table A.1: Synthetic details for the free radical synthesis of Polyvinyltriphenylamine-*co*-Polystryrene with varying VTPA to styrene monomer ratios.

monomer ratio VTPA:styrene	vinyltriphenylamine	styrene	toluene	reaction time
50:50	0.75 g (2.8 mmol)	0.278 g (2.8 mmol)	3.5 mL	20 h
25:75	0.5 g (1.85 mmol)	0.576 g (5.54 mmol)	3.5 mL	20 h
20:80	0.5 g (1.85 mmol)	0.77 g (7.4 mmol)	5 mL	20.5 h
15:85	0.5 g (1.85 mmol)	1.09 g (10.48 mmol)	5 mL	20 h
10:90	0.25 g (0.925 mmol)	0.866 g (8.3 mmol)	5 mL	20 h
5:95	0.137 g (0.51 mmol)	1 g (9.61 mmol)	5 mL	21.5 h

^{1}H-NMR (250 MHz, $CDCl_3$): δ(ppm) = 7.24-6.84 (m, 9H), 6.84-6.16 (m, 5H), 2.28-1.68 (m, 2H), 1.66-1.21 (m, 4H).

Table A.2: Yields and characteristic polymer parameters (molecular weight and polydispersity indices (PDI)) of Polyvinyltriphenylamine-*co*-Polystyrene copolymers with varying monomer ratios.

monomer ratio	mass [mg]	yield [%]	M_n [g mol^{-1}]	PDI
50:50	436	42	25 000	1.54
25:75	543	50	20 000	1.57
20:80	260	20	15 000	1.67
15:85	400	24	15 000	1.59
10:90	436	39	21 000	1.60
5:95	400	35	15 000	1.62

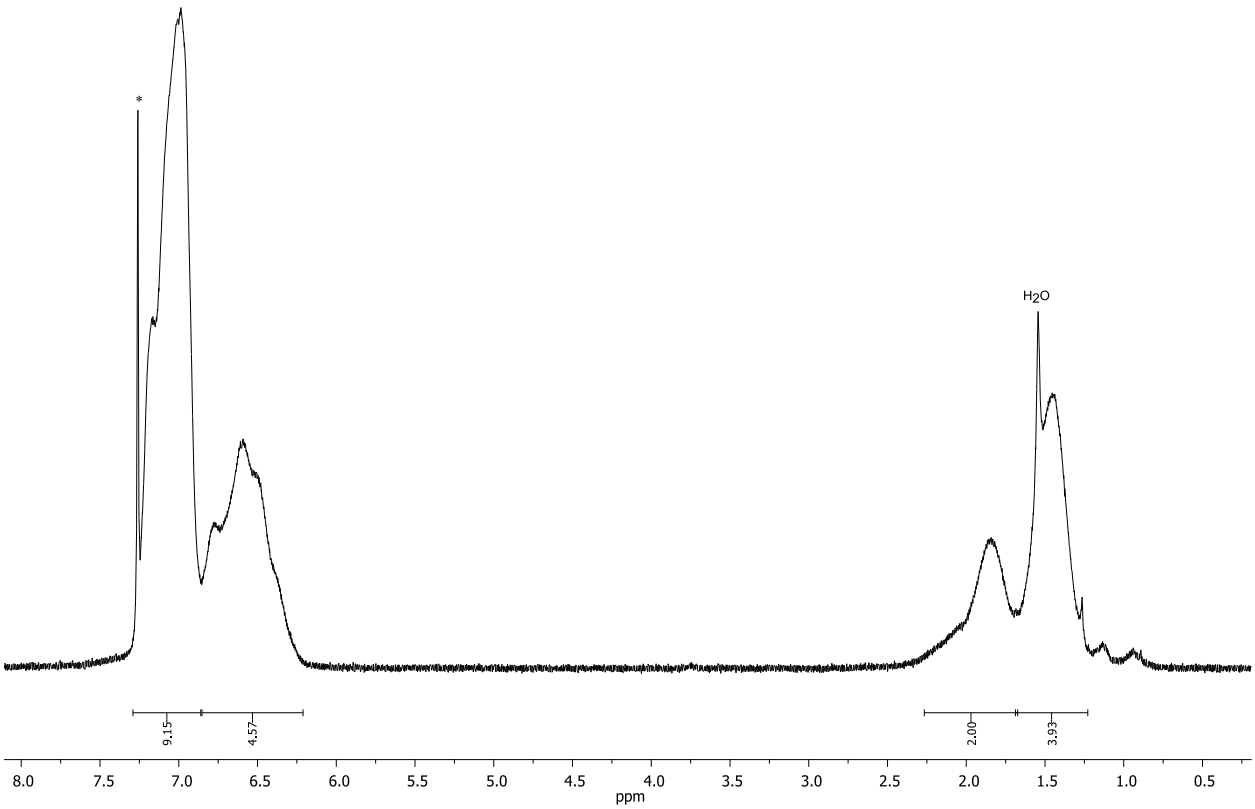

Figure A.8: Representative ^{1}H-NMR of Polyvinyltriphenylamine-*co*-Polystyrene (monomer ratio 20:80 TPA: Styrene) in $CDCl_3$.

Polyvinyltriphenylamine-*co*-Polystyrene Blockcopolymer

first block

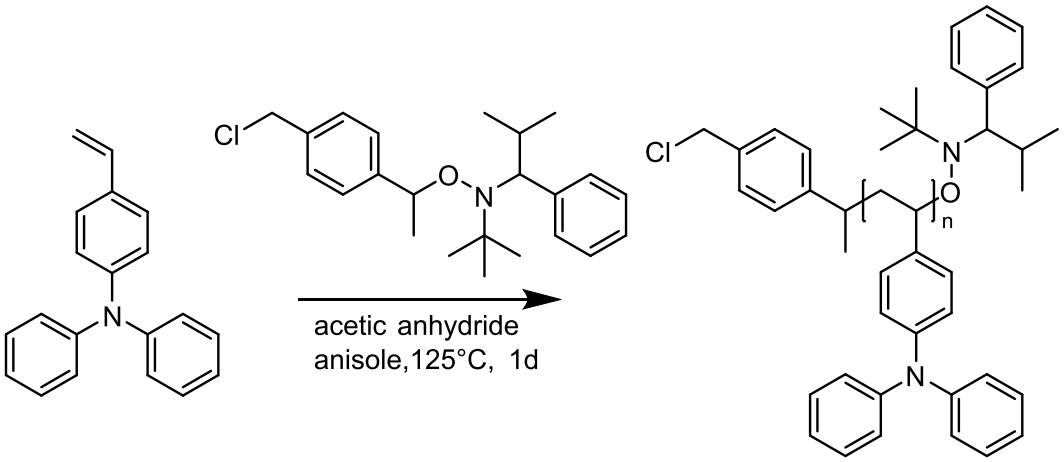

Vinyltriphenylamine (0.5 g, 1.84 mmol, 1 eq), TIPNO-Cl (1.6 mg, 7.4 µmol, 0.004 eq) and acetic anhydride (1.5 g, 14.7 µmol, 0.008 eq) were dissolved in anisole (1 mL) and the reaction mixture was degassed (5 times). The mixture was stirred at 125 °C for 9 h under argon atmosphere and quenched by immersing into liquid nitrogen. The solvent was removed under reduced pressure, the residual yellow solid was dissolved in DCM and precipitated in acetone. The obtained white solid was further purified by preparative size exclusion chromatography (self-packed column with polystyrenedivinylbenzene copolymer, 1% crosslinkage, bead size 40 - 80 µm, MW exclusion range 600 - 14 000 g mol^{-1}, chloroform as mobile phase). 167 mg (33% yield) of Polyvinyltriphenylamine was obtained as a white solid.

GPC (THF): M_n = 7000 g mol^{-1}, PDI = 1.25

^{1}H-NMR (250 MHz, CD_2Cl_2): δ(ppm) = 7.25-6.36 (m, 14H), 2.35-1.83 (m, 1H), 1.81-1.36 (m, 3H).

^{13}C-NMR (63 MHz, CD_2Cl_2): δ(ppm) = 148.41, 146.05, 129.68, 129.07, 124.44, 122.90, 40.85.

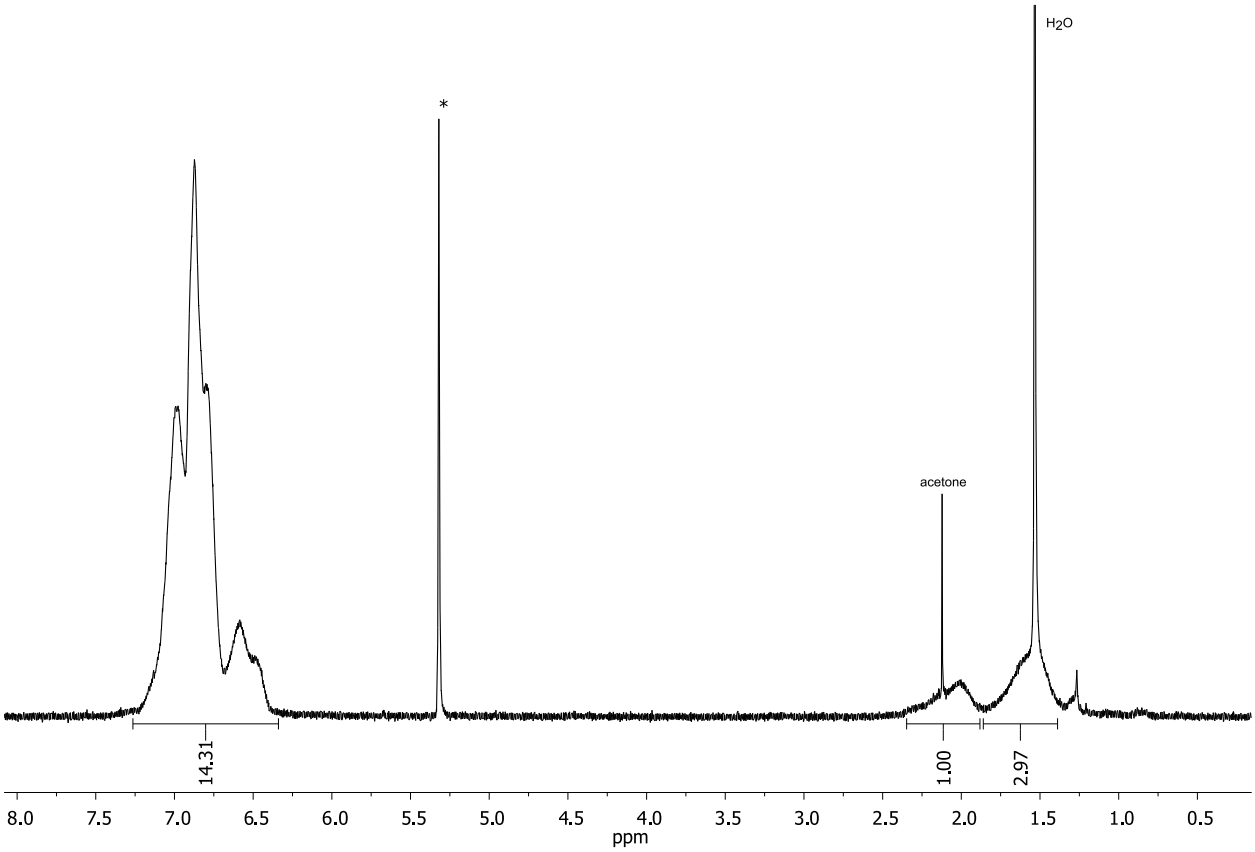

Figure A.9: ^{1}H-NMR of Polyvinyltriphenylamine in CD_2Cl_2.

second block

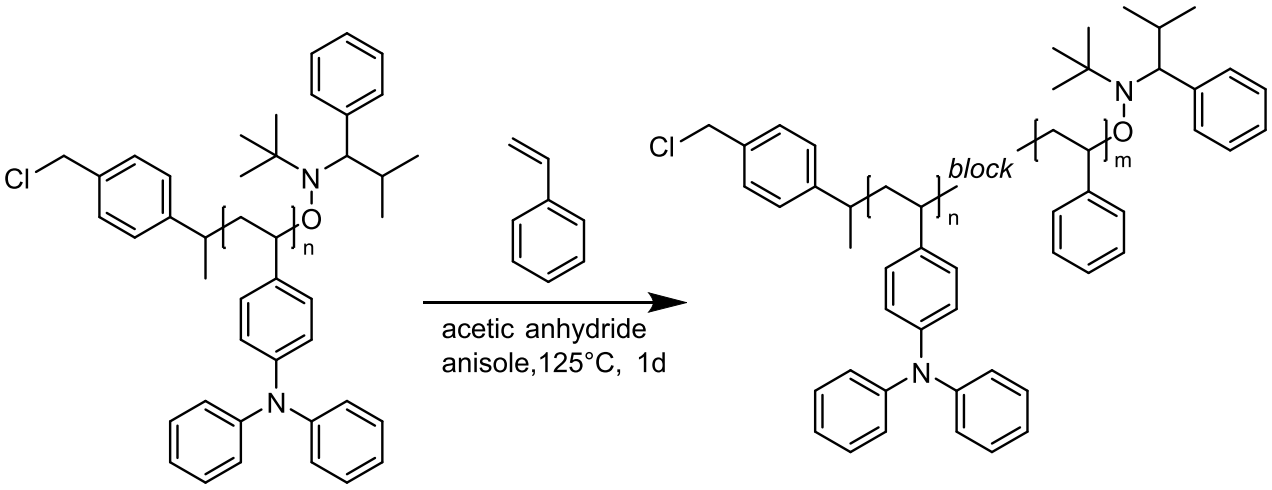

Polyvinyltriphenylamine (40 mg, 5.8 µmol, 1 eq), styrene (45.3 mg, 0.43 mmol, 75 eq) and acetic anhydride (1.08 mg, 0.016 mmol, 2.75 eq) were dissolved in anisole (0.5 mL) and degassed (5 times). The reaction mixture was stirred at 125 °C for 24 h under argon atmosphere and quenched by immersing into liquid nitrogen. The solvent was removed under reduced pressure, the residual yellowish solid was dissolved in DCM and precipitated in acetone. The obtained solid was further purified by preparative sive exclusion chromatography. 39 mg of Polyvinyltriphenylamine-*b*-Polystyrene was obtained as yellowish solid.

GPC (THF): $M_n = 10\,500\,g\,mol^{-1}$, PDI = 1.28

^{1}H-NMR (250 MHz, CD_2Cl_2): δ(ppm) = 7.22-6.33 (m, 14H), 2.36-1.85 (m, 1H), 1.82-1.34 (m, 4H).

^{13}C-NMR (63 MHz, CD_2Cl_2): δ(ppm) = 148.41, 146.05, 129.67, 129.09, 124.41, 122.91, 40.91.

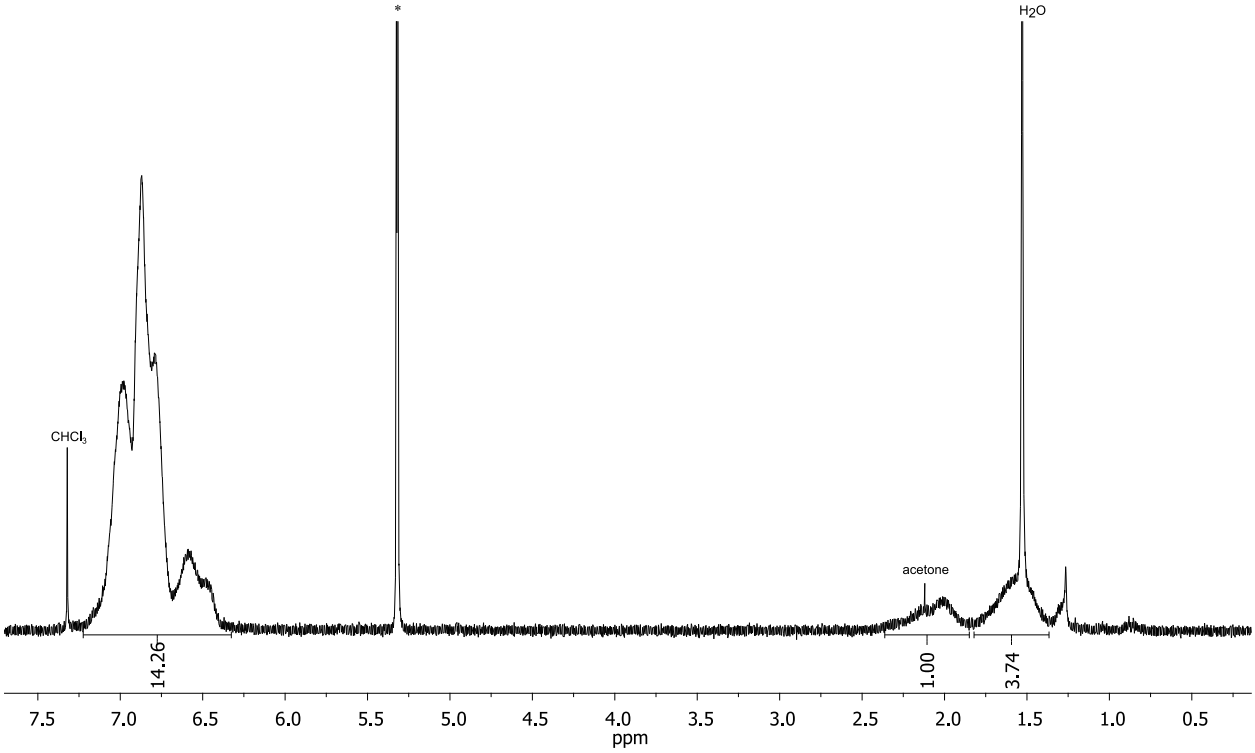

Figure A.10: ^{1}H-NMR of Polyvinyltriphenylamine-*b*-Polystyrene in CD_2Cl_2.

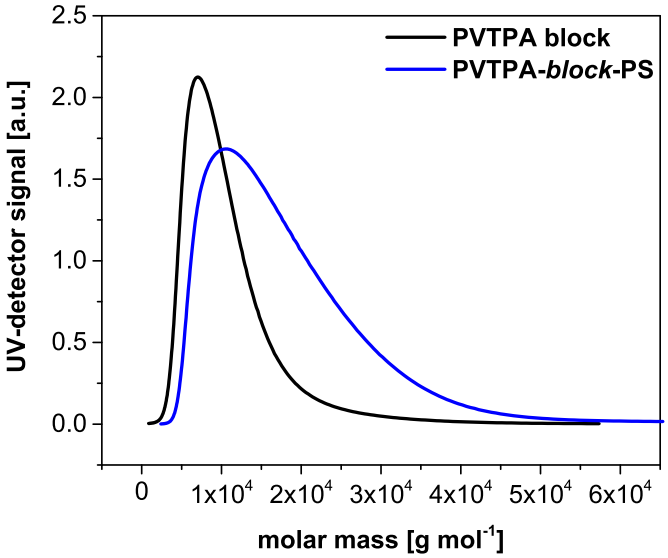

Figure A.11: Molecular weight distribution of the Polyvinyltriphenylamine block (black curve) and the Polyvinyltriphenylamine-*b*-Polystyrene blockcopolymer (blue curve) measured in THF.

A.4. Cyclic Voltammetry of PVTPA-*co*-PS with varying Conducting Salts

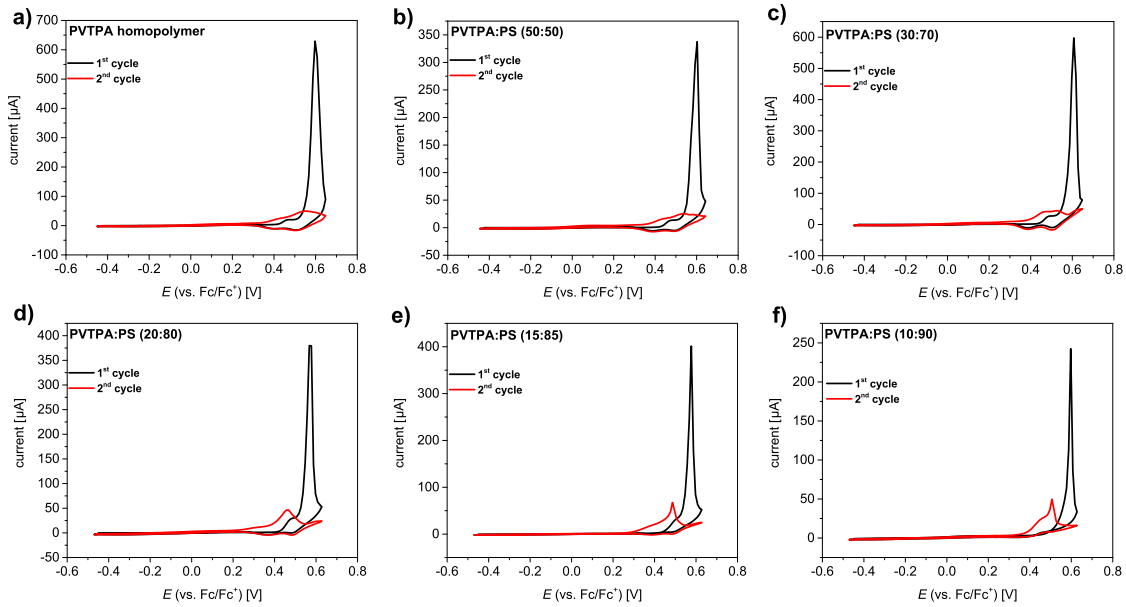

Figure A.12: Cyclic voltammograms of PVTPA-*co*-PS copolymers; **a)** homopolymer, **b)** 50 mol%, **c)** 30 mol%, **d)** 20 mol%, **e)** 15 mol% and **f)** 10 mol%; first cycles in black and second cycles in red respectively; measured in 0.1 M NBu_4BF_4/MeCN with a scan rate of 20 mV s^{-1} on gold electrodes.

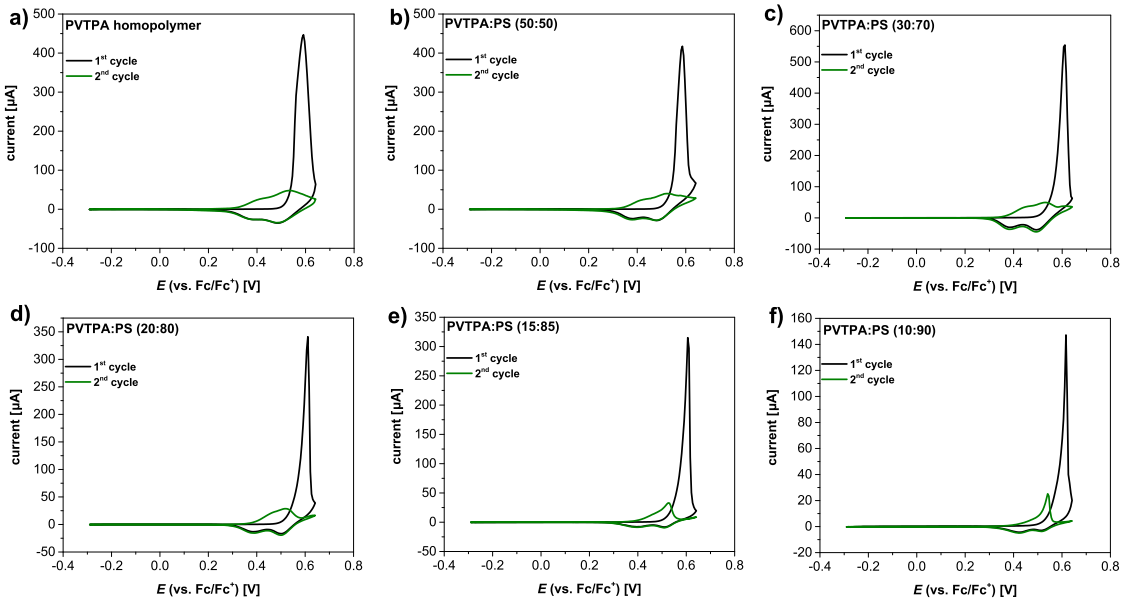

Figure A.13: Cyclic voltammograms of PVTPA-*co*-PS copolymers; **a)** homopolymer, **b)** 50 mol%, **c)** 30 mol%, **d)** 20 mol%, **e)** 15 mol% and **f)** 10 mol%; first cycles in black and second cycles in green respectively; measured in 0.1 M $LiClO_4$/MeCN with a scan rate of 20 mV s^{-1} on gold electrodes.

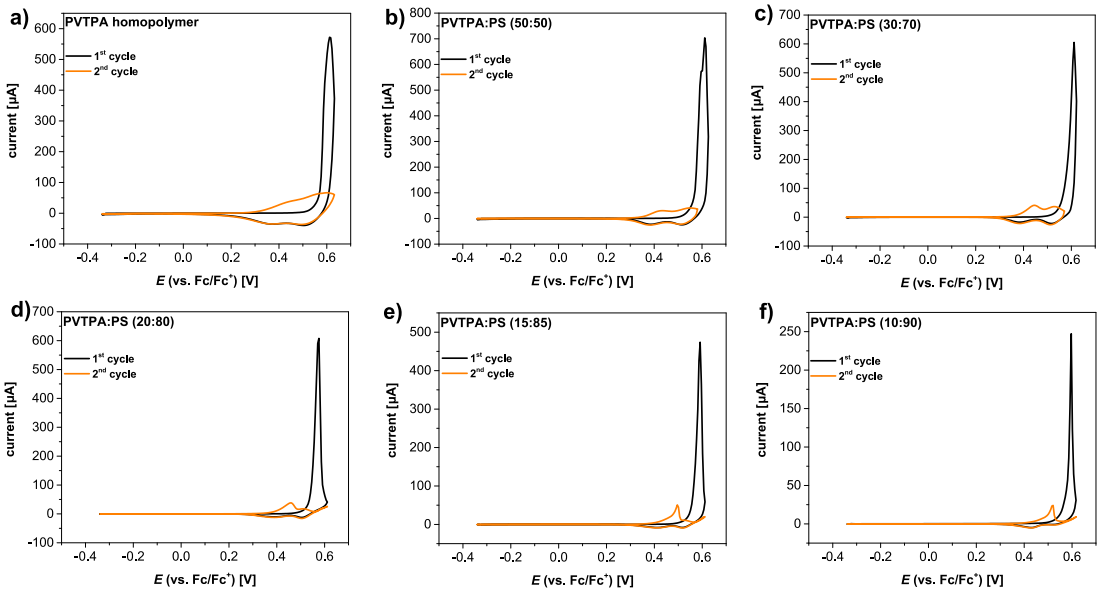

Figure A.14: Cyclic voltammograms of PVTPA-*co*-PS copolymers; **a)** homopolymer, **b)** 50 mol%, **c)** 30 mol%, **d)** 20 mol%, **e)** 15 mol% and **f)** 10 mol%; first cycles in black and second cycles in orange respectively; measured in 0.1 M KPF_6/MeCN with a scan rate of 20 mV s^{-1} on gold electrodes.

Table A.3: Potentials of all redox processes in PVTPA-*co*-PS copolymers with varying repeating unit ratios; determined by means of cyclic voltammetry on planar gold electrodes measured with a scan rate of 20 mV min^{-1} in 0.1 M NBu_4BF_4.

polymer	redox process	parameter	potential (vs. Fc/Fc^+)
homopolymer	TPA $\rightarrow$ $TPA^{\cdot+}$	E_{peak}	0.60 V
homopolymer	TPB $\rightleftharpoons$ $TPB^{\cdot+}$	$E_{1/2}$	0.42 V
homopolymer	$TPB^{\cdot+}$ $\rightleftharpoons$ TPB^{2+}	$E_{1/2}$	0.53 V
50 mol%	TPA $\rightarrow$ $TPA^{\cdot+}$	E_{peak}	0.60 V
50 mol%	TPB $\rightleftharpoons$ $TPB^{\cdot+}$	$E_{1/2}$	0.41 V
50 mol%	$TPB^{\cdot+}$ $\rightleftharpoons$ TPB^{2+}	$E_{1/2}$	0.52 V
30 mol%	TPA $\rightarrow$ $TPA^{\cdot+}$	E_{peak}	0.61 V
30 mol%	TPB $\rightleftharpoons$ $TPB^{\cdot+}$	$E_{1/2}$	0.43 V
30 mol%	$TPB^{\cdot+}$ $\rightleftharpoons$ TPB^{2+}	$E_{1/2}$	0.51 V
20 mol%	TPA $\rightarrow$ $TPA^{\cdot+}$	E_{peak}	0.57 V
20 mol%	TPB $\rightleftharpoons$ $TPB^{\cdot+}$	$E_{1/2}$	n.d. [a]
20 mol%	$TPB^{\cdot+}$ $\rightleftharpoons$ TPB^{2+}	$E_{1/2}$	0.48 V
15 mol%	TPA $\rightarrow$ $TPA^{\cdot+}$	E_{peak}	0.58 V
15 mol%	TPB $\rightleftharpoons$ $TPB^{\cdot+}$	$E_{1/2}$	n.d. [b]
15 mol%	$TPB^{\cdot+}$ $\rightleftharpoons$ TPB^{2+}	$E_{1/2}$	0.49 V
10 mol%	TPA $\rightarrow$ $TPA^{\cdot+}$	E_{peak}	0.60 V
10 mol%	TPB $\rightleftharpoons$ $TPB^{\cdot+}$	$E_{1/2}$	n.d. [c]
10 mol%	$TPB^{\cdot+}$ $\rightleftharpoons$ TPB^{2+}	$E_{1/2}$	n.d. [d]

[a] anodic half wave not determinable; cathodic half wave at 0.36 V.
[b] anodic half wave not determinable; cathodic half wave at 0.38 V.
[c] cathodic half wave not determinable; anodic half wave at 0.45 V.
[d] cathodic half wave not determinable; anodic half wave at 0.51 V.

Table A.4: Potentials of all redox processes in PVTPA-*co*-PS copolymers with varying repeating unit ratios; determined by means of cyclic voltammetry on planar gold electrodes measured with a scan rate of 20 mV min^{-1} in 0.1 M $LiClO_4$.

polymer	redox process	parameter	potential (vs. Fc/Fc^+)
homopolymer	TPA $\rightarrow$ $TPA^{\cdot+}$	E_{peak}	0.59 V
homopolymer	TPB $\rightleftharpoons$ $TPB^{\cdot+}$	$E_{1/2}$	0.40 V
homopolymer	$TPB^{\cdot+}$ $\rightleftharpoons$ TPB^{2+}	$E_{1/2}$	0.51 V
50 mol%	TPA $\rightarrow$ $TPA^{\cdot+}$	E_{peak}	0.59 V
50 mol%	TPB $\rightleftharpoons$ $TPB^{\cdot+}$	$E_{1/2}$	0.40 V
50 mol%	$TPB^{\cdot+}$ $\rightleftharpoons$ TPB^{2+}	$E_{1/2}$	0.50 V
30 mol%	TPA $\rightarrow$ $TPA^{\cdot+}$	E_{peak}	0.61 V
30 mol%	TPB $\rightleftharpoons$ $TPB^{\cdot+}$	$E_{1/2}$	0.42 V
30 mol%	$TPB^{\cdot+}$ $\rightleftharpoons$ TPB^{2+}	$E_{1/2}$	0.51 V
20 mol%	TPA $\rightarrow$ $TPA^{\cdot+}$	E_{peak}	0.61 V
20 mol%	TPB $\rightleftharpoons$ $TPB^{\cdot+}$	$E_{1/2}$	n.d. [a]
20 mol%	$TPB^{\cdot+}$ $\rightleftharpoons$ TPB^{2+}	$E_{1/2}$	0.51 V
15 mol%	TPA $\rightarrow$ $TPA^{\cdot+}$	E_{peak}	0.61 V
15 mol%	TPB $\rightleftharpoons$ $TPB^{\cdot+}$	$E_{1/2}$	n.d. [b]
15 mol%	$TPB^{\cdot+}$ $\rightleftharpoons$ TPB^{2+}	$E_{1/2}$	0.52 V
10 mol%	TPA $\rightarrow$ $TPA^{\cdot+}$	E_{peak}	0.62 V
10 mol%	TPB $\rightleftharpoons$ $TPB^{\cdot+}$	$E_{1/2}$	n.d. [c]
10 mol%	$TPB^{\cdot+}$ $\rightleftharpoons$ TPB^{2+}	$E_{1/2}$	0.53 V

[a] anodic half wave not determinable; cathodic half wave at 0.38 V.
[b] anodic half wave not determinable; cathodic half wave at 0.39 V.
[c] anodic half wave not determinable; cathodic half wave at 0.42 V.

Table A.5: Potentials of all redox processes in PVTPA-*co*-PS copolymers with varying repeating unit ratios; determined by means of cyclic voltammetry on planar gold electrodes measured with a scan rate of 20 mV min^{-1} in 0.1 M KPF_6.

polymer	redox process	parameter	potential (vs. Fc/Fc^+)
homopolymer	TPA $\rightarrow$ $TPA^{\cdot+}$	E_{peak}	0.62 V
homopolymer	TPB $\rightleftharpoons$ $TPB^{\cdot+}$	$E_{1/2}$	0.41 V
homopolymer	$TPB^{\cdot+}$ $\rightleftharpoons$ TPB^{2+}	$E_{1/2}$	0.54 V
50 mol%	TPA $\rightarrow$ $TPA^{\cdot+}$	E_{peak}	0.61 V
50 mol%	TPB $\rightleftharpoons$ $TPB^{\cdot+}$	$E_{1/2}$	0.41 V
50 mol%	$TPB^{\cdot+}$ $\rightleftharpoons$ TPB^{2+}	$E_{1/2}$	0.53 V
30 mol%	TPA $\rightarrow$ $TPA^{\cdot+}$	E_{peak}	0.61 V
30 mol%	TPB $\rightleftharpoons$ $TPB^{\cdot+}$	$E_{1/2}$	0.41 V
30 mol%	$TPB^{\cdot+}$ $\rightleftharpoons$ TPB^{2+}	$E_{1/2}$	0.52 V
20 mol%	TPA $\rightarrow$ $TPA^{\cdot+}$	E_{peak}	0.58 V
20 mol%	TPB $\rightleftharpoons$ $TPB^{\cdot+}$	$E_{1/2}$	0.42 V
20 mol%	$TPB^{\cdot+}$ $\rightleftharpoons$ TPB^{2+}	$E_{1/2}$	0.51 V
15 mol%	TPA $\rightarrow$ $TPA^{\cdot+}$	E_{peak}	0.59 V
15 mol%	TPB $\rightleftharpoons$ $TPB^{\cdot+}$	$E_{1/2}$	0.46 V
15 mol%	$TPB^{\cdot+}$ $\rightleftharpoons$ TPB^{2+}	$E_{1/2}$	n.d. [a]
10 mol%	TPA $\rightarrow$ $TPA^{\cdot+}$	E_{peak}	0.60 V
10 mol%	TPB $\rightleftharpoons$ $TPB^{\cdot+}$	$E_{1/2}$	n.d. [b]
10 mol%	$TPB^{\cdot+}$ $\rightleftharpoons$ TPB^{2+}	$E_{1/2}$	n.d. [c]

[a] anodic half wave not determinable; cathodic half wave at 0.52 V.
[b] anodic half wave not determinable; cathodic half wave at 0.43 V.
[c] cathodic half wave not determinable; anodic half wave at 0.52 V.

A.5. Charge Storage Capabilities of PVTPA-*co*-PS Copolymers

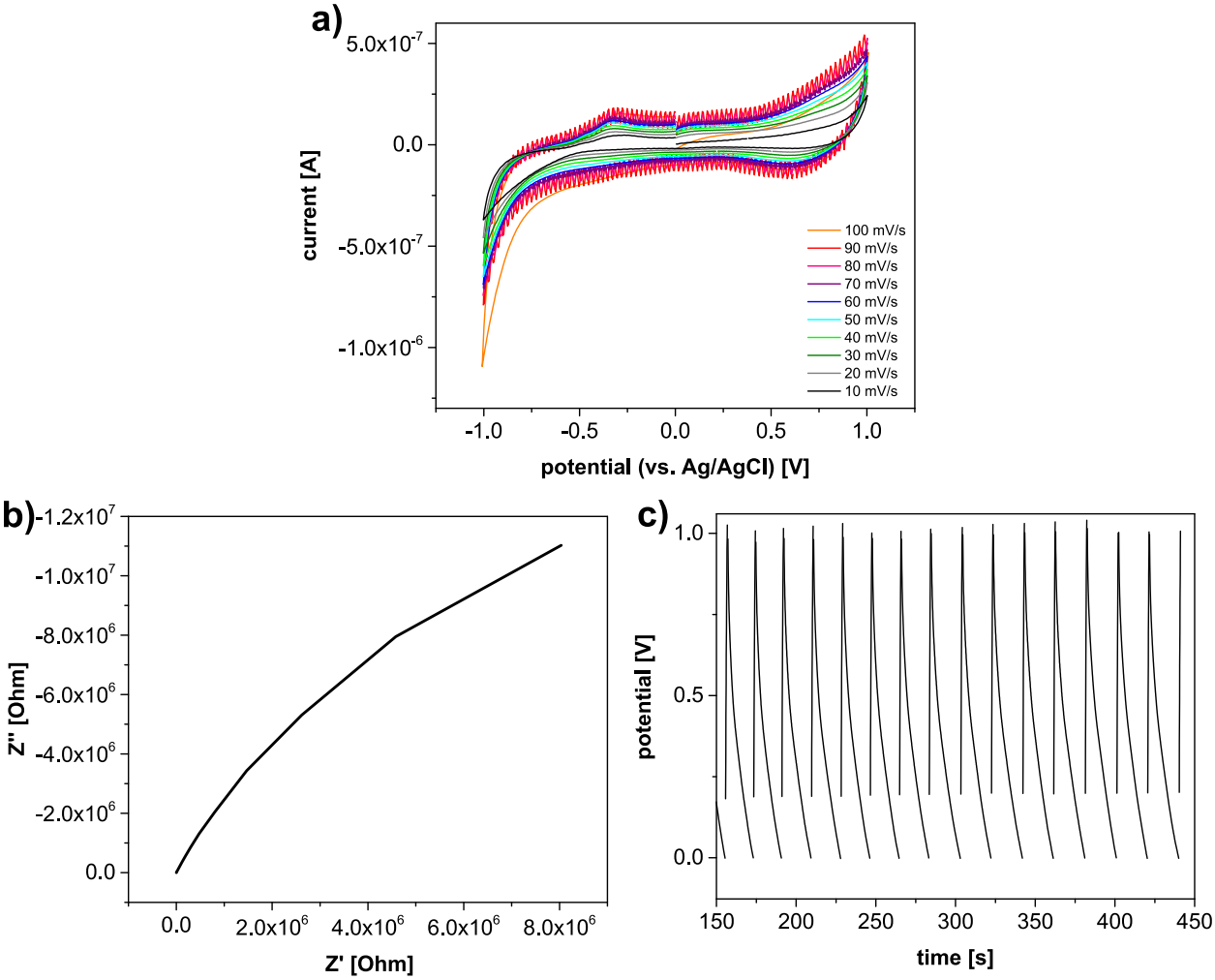

Figure A.15: Charge storage capacity characterisation of PVTPA homopolymer supercapacitor measured in 0.1 M LiBTFSI in MeCN. **a)** scan rate dependent cyclic voltammogramms; **b)** Nyquist plot from the electrochemical impedance spectroscopy with an amplitude of 0.5 V and **c)** galvanostatic charging/ discharging curves with 1 µA and cut-off potentials of 0 V and 1 V.

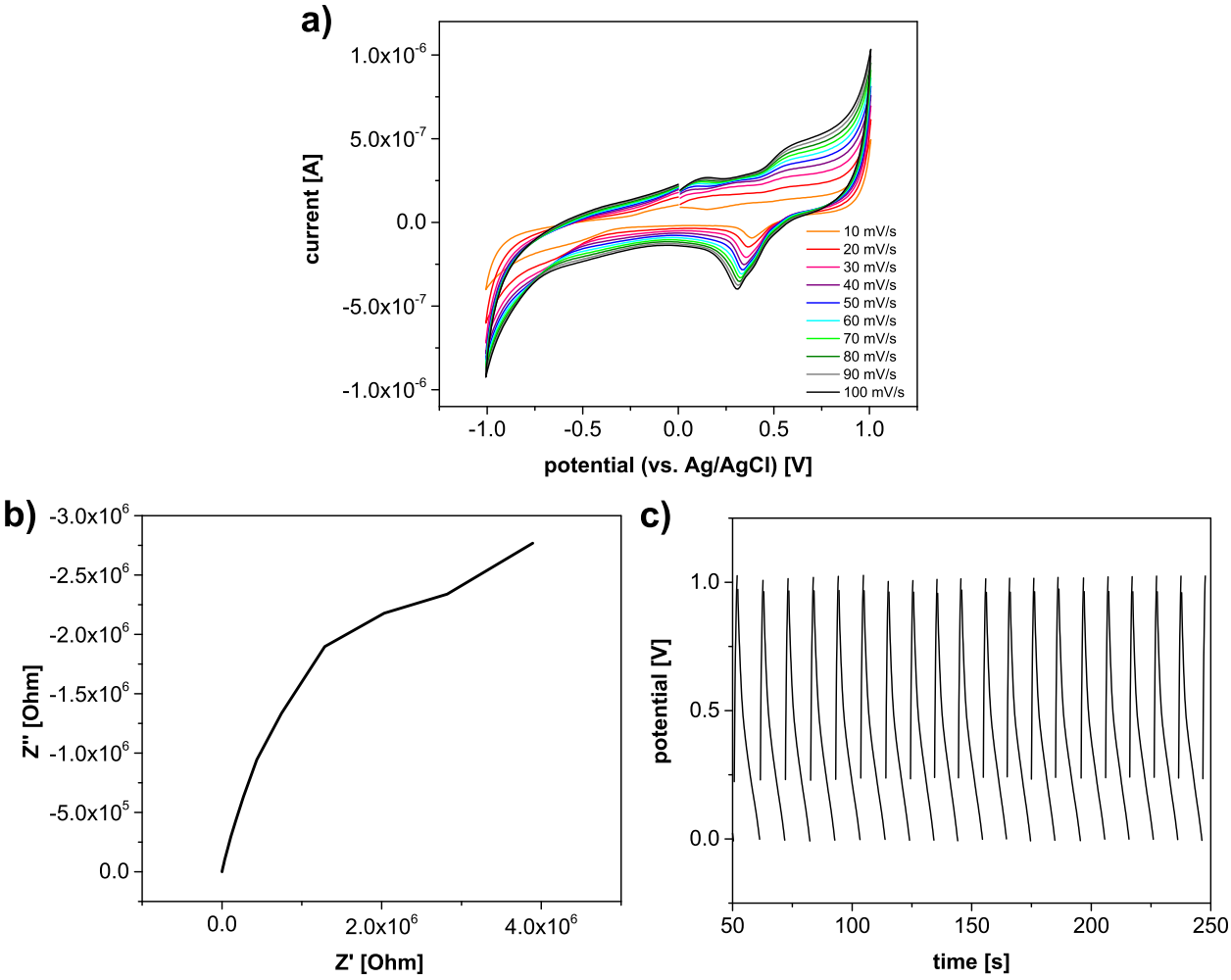

Figure A.16: Charge storage capacity characterisation of PVTPA-*co*-PS (50:50 mol%) supercapacitor measured in 0.1 M LiBTFSI in MeCN. **a)** scan rate dependent cyclic voltammogramms; **b)** Nyquist plot from the electrochemical impedance spectroscopy with an amplitude of 0.5 V and **c)** galvanostatic charging/ discharging curves with 1 µA and cut-off potentials of 0 V and 1 V.

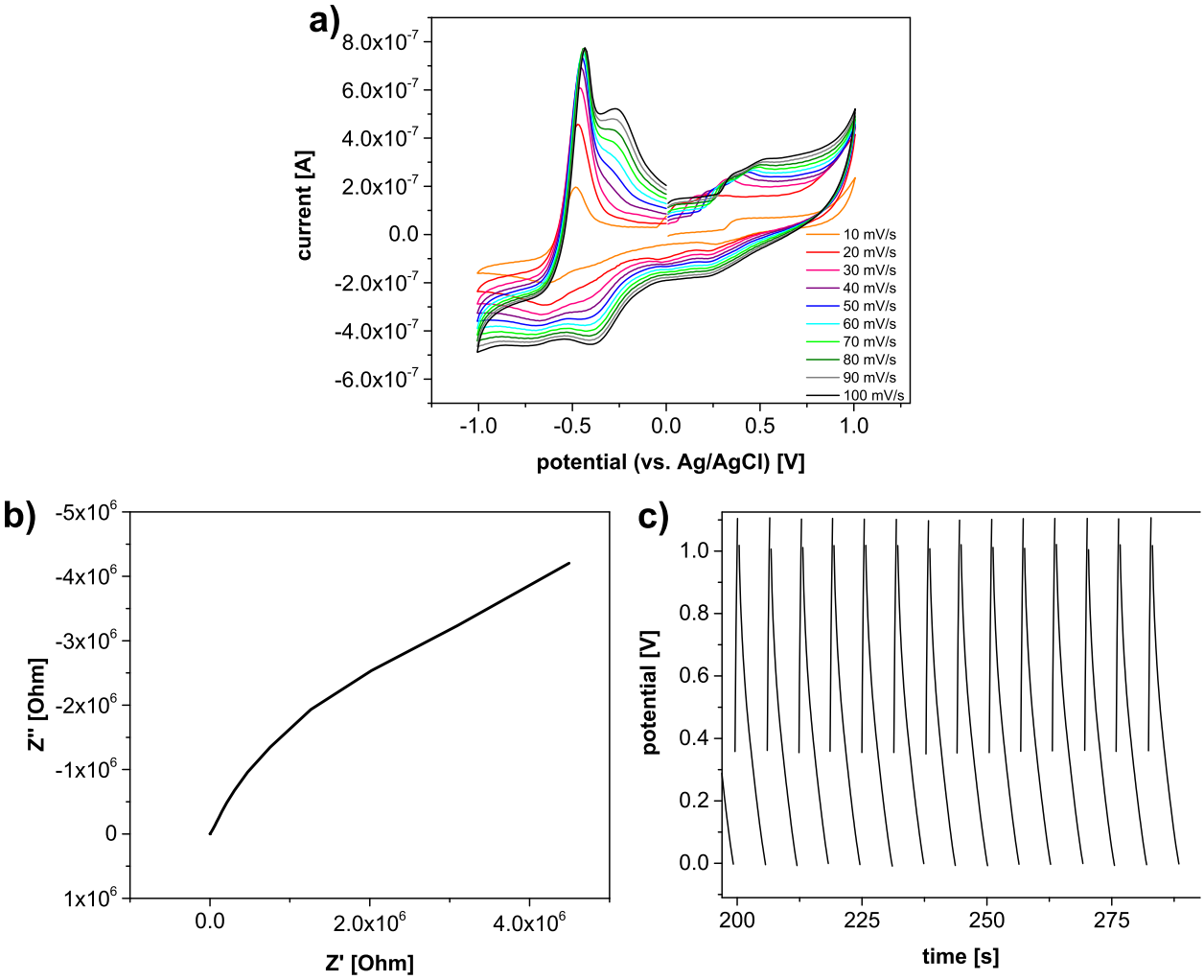

Figure A.17: Charge storage capacity characterisation of PVTPA-*co*-PS (30:70 mol%) supercapacitor measured in 0.1 M LiBTFSI in MeCN. **a)** scan rate dependent cyclic voltammogramms; **b)** Nyquist plot from the electrochemical impedance spectroscopy with an amplitude of 0.5 V and **c)** galvanostatic charging/ discharging curves with 1 µA and cut-off potentials of 0 V and 1 V.

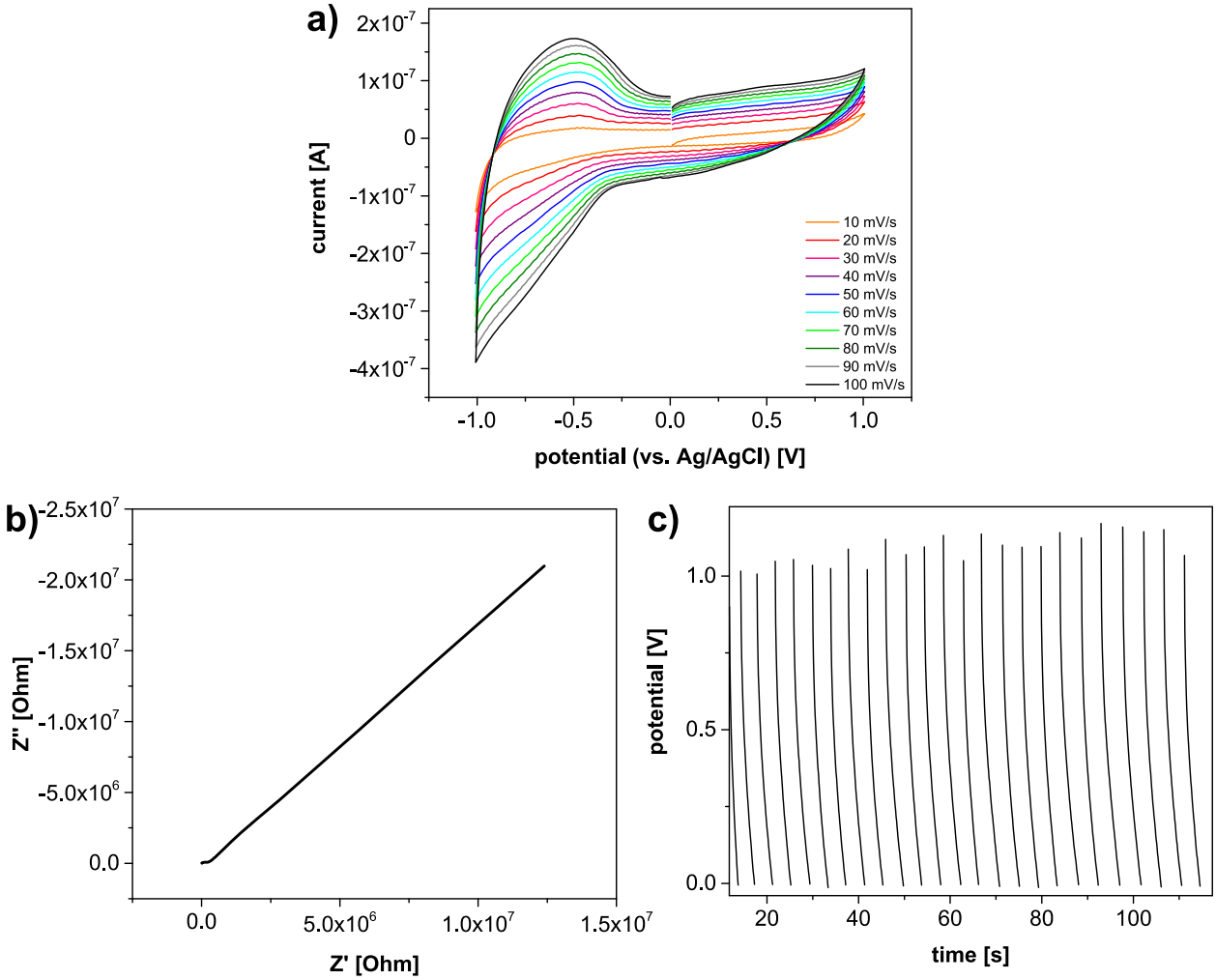

Figure A.18: Charge storage capacity characterisation of PVTPA-*co*-PS (25:75 mol%) supercapacitor measured in 0.1 M LiBTFSI in MeCN. **a)** scan rate dependent cyclic voltammogramms; **b)** Nyquist plot from the electrochemical impedance spectroscopy with an amplitude of 0.5 V and **c)** galvanostatic charging/ discharging curves with 1 µA and cut-off potentials of 0 V and 1 V.

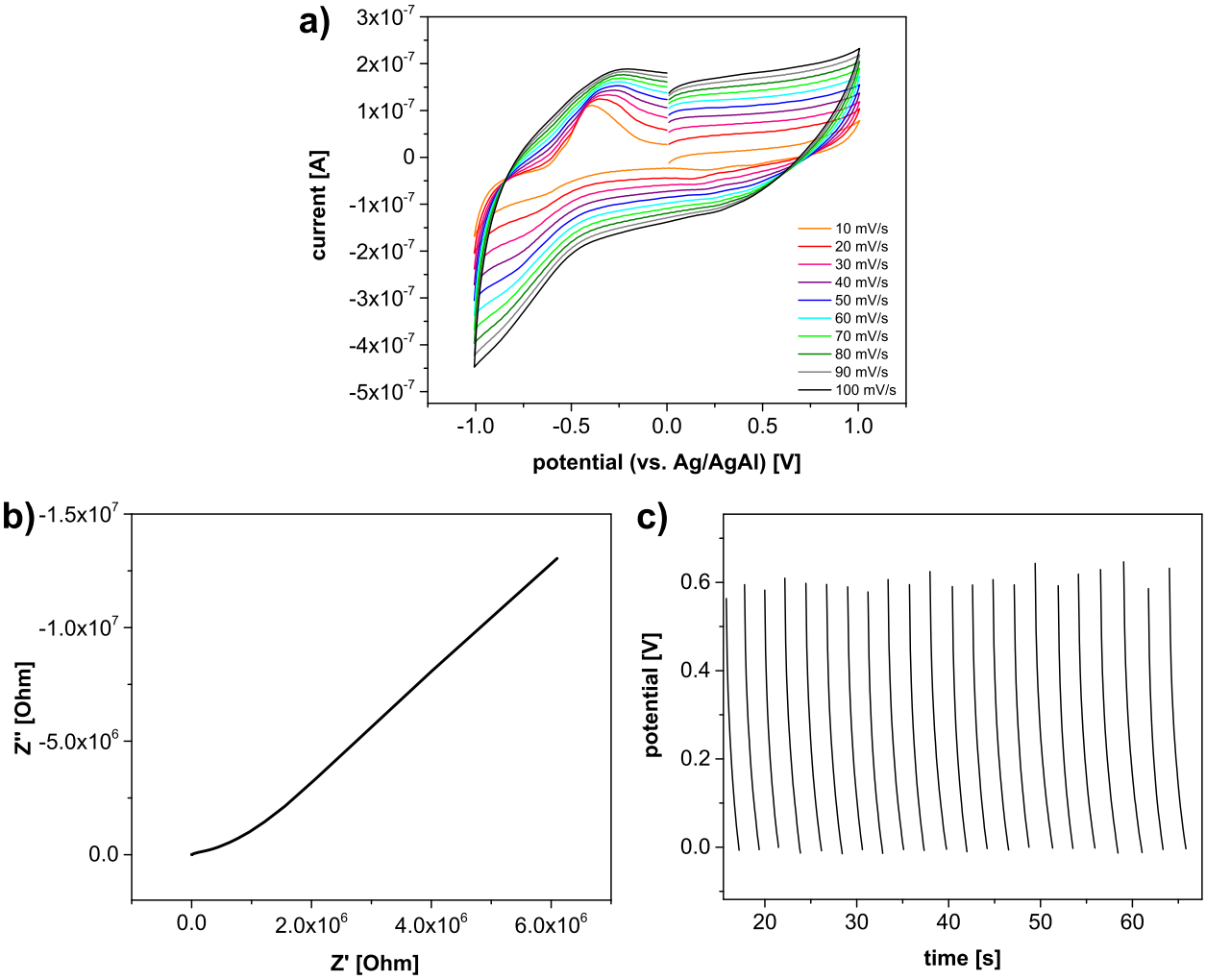

Figure A.19: Charge storage capacity characterisation of PVTPA-*co*-PS (15:85 mol%) supercapacitor measured in 0.1 M LiBTFSI in MeCN. **a)** scan rate dependent cyclic voltammogramms; **b)** Nyquist plot from the electrochemical impedance spectroscopy with an amplitude of 0.5 V and **c)** galvanostatic charging/ discharging curves with 1 µA and cut-off potentials of 0 V and 1 V.

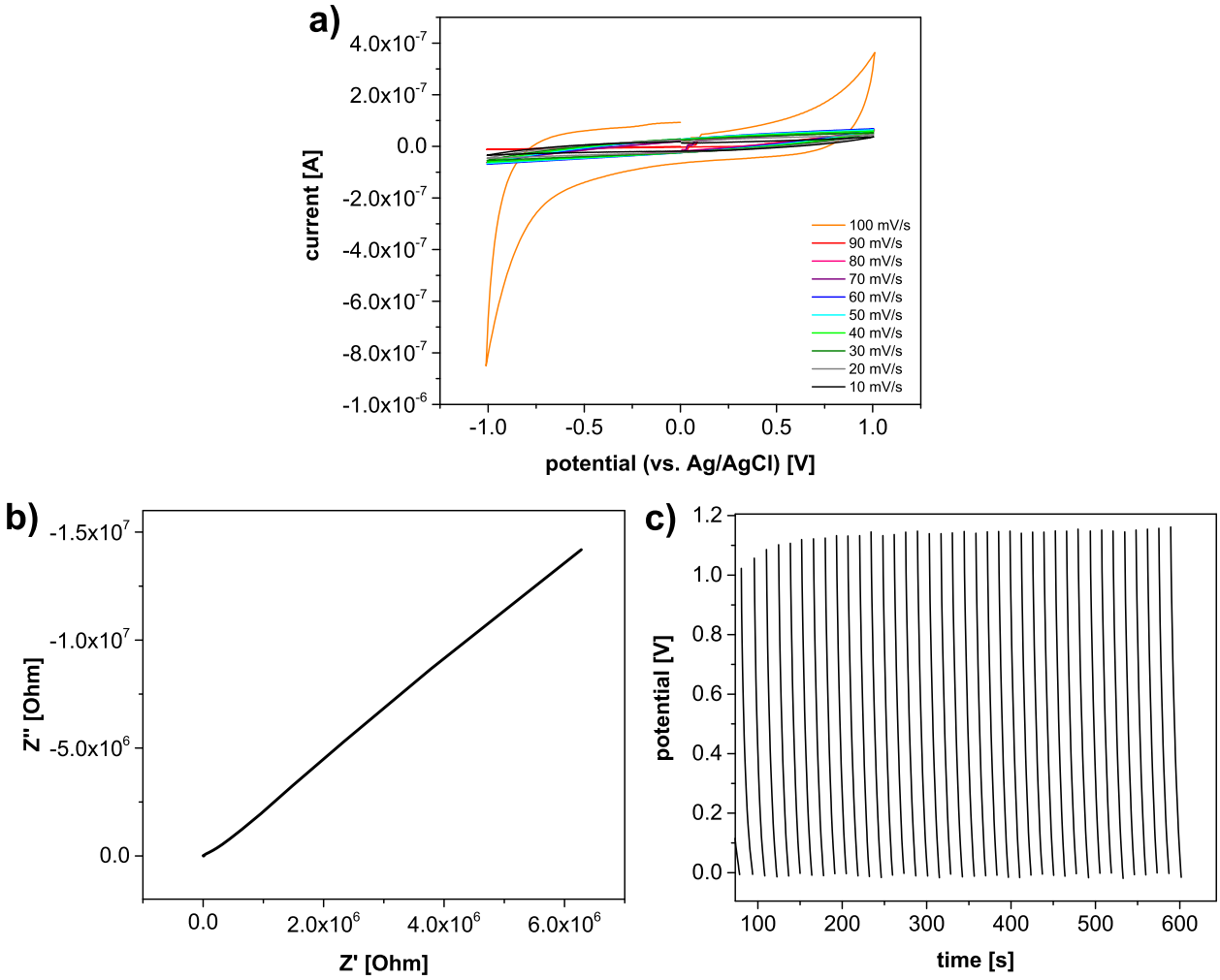

Figure A.20: Charge storage capacity characterisation of PVTPA-*co*-PS (10:90 mol%) supercapacitor measured in 0.1 M LiBTFSI in MeCN. **a)** scan rate dependent cyclic voltammogramms; **b)** Nyquist plot from the electrochemical impedance spectroscopy with an amplitude of 0.5 V and **c)** galvanostatic charging/ discharging curves with 1 µA and cut-off potentials of 0 V and 1 V.